Multi Cornered Thin Wall Sections for Crashworthiness and Occupant Protection

A thesis submitted in fulfilment of the requirements for the degree of Doctor of Philosophy (Mechanical and Manufacturing Engineering)

Biddala Reddy Sekhar Reddy

School of Aerospace Mechanical and Manufacturing Engineering

College of Science Engineering and Health

RMIT University

February 2015

Declaration

I certify that except where due acknowledgement has been made, the work is that of the author alone; the work has not been submitted previously, in whole or in part, to qualify for any other academic award; the content of the thesis/project is the result of work which has been carried out since the official commencement date of the approved research program; any editorial work, paid or unpaid, carried out by a third party is acknowledged; and, ethics procedures and guidelines have been followed.

Biddala Reddy Sekhar Reddy

16 February 2015

Multi Cornered Thin Wall Sections for Crashworthiness and Occupant Protection

A thesis submitted in fulfilment of the requirements for the degree of

Doctor of Philosophy (Mechanical and Manufacturing Engineering)

Biddala Reddy Sekhar Reddy

School of Aerospace, Mechanical and Manufacturing Engineering

College of Science, Engineering and Health

RMIT University, Melbourne, Australia

25 June 2014

DECLARATION

I certify that except where due acknowledgement has been made, the work is that of the author alone; the work has not been submitted previously, in whole or in part, to qualify for any other academic award; the content of the thesis is the result of work which has been carried out since the official commencement date of the approved research program; and, any editorial work, paid or unpaid, carried out by a third party is acknowledged.

Biddala Reddy Sekhar Reddy

25 June 2014

ACKNOWLEDGEMENTS

Foremost, I would like to express my sincere gratitude and thanks to my research supervisor and advisor, Dr. Mohammad Fard, for his continuous support and guidance all through my PhD study and research. His patience, motivation, enthusiasm, and knowledge have significantly contributed to my research. Besides my supervisor, I would also like to thank Prof. Reza Jazar, Dr. Monir Takla and Dr. Stefanie Feih at RMIT University for their encouragement, insightful comments and suggestions in the completion of this thesis.

My sincere thanks also go to Prof. Aleksandar Subic, Dean of Engineering and Head of School, Aerospace, Mechanical and Manufacturing Engineering, RMIT for his motivation and encouraging me to take up this research in the first place. I would also thank Peter Tkatchyk at RMIT for his support in getting complex test samples and experimentations. I would also like to extend my thanks to Milad Abbasi and Zhengqing Liu, research students for their support in my research and publications.

I would like to extend my special thanks to my colleagues at Ford Motor Company of Australia, Tom Spencer for support on design aspects, and Ross McBride for testing and Adam Frost, Head of Crash & Safety Dept., Digital innovation Group for his support and facilitation. I would also like to thank John Cooper, Head of CAE Crash & Safety, Tesla Motors, for providing support and my time facilitation to complete this research.

Finally I would like to thanks my parents for their support and best wishes. Special thanks goes to my wife and sweet kids who supported me immensely to complete my research in spite of my heavy work commitments, cheering me up and standing by me in times of good and bad.

Contents

ABSTRACT

The desire to improve crashworthiness of a passenger vehicle for enhanced occupant safety has been a major challenge for decades. When a crash is unavoidable, it is the crash energy and the manner in which vehicle occupants experience the associated forces that will determine the extent of injury to those occupants. The major energy management comes from the upfront crash energy absorption which can be designed to fit into the available packaging space without affecting the cost- weight effectiveness. Axial collapse of the thin walled structures has been studied in detail over decades and the understanding was limited primarily to circular tubes. It was later refined and extended to square sections. This research extended the knowledge beyond Square/Cylindrical shapes towards complex sections along with further exploratory works in practical applications. The hands on tools for designers to act as comparators for exercising flexibility in design decisions that are missing is addressed in this research study. The instigated ideas of this research study bridge the missing link and extend it further towards more robust energy absorption in automotive world. Since axial crush mode is dominant in vehicle frontal crash and rear impact, dynamic and quasi-static, axial crush characterization has been developed with various cross-sections across different designs within the constrained packaging space. With linear methods being insufficient to describe the plastic collapse process, nonlinear treatment combined with theory of plasticity with hardening models was employed. A new strategy has been proposed to improve energy absorption efficiency of thin-walled columns by introducing extra stable corners in the cross-section. Several profiles of multi-corner thin-walled columns obtained through this strategy were presented and their crashworthiness capacities under axial crush loading were investigated analytically, experimentally, and numerically which are well define in the main body of this research study. Super Folding

Element (SFE) concept was used in characterizing the collapse behaviour and parameters acting as comparators for designers were developed.

Utilizing the existing research methods from pioneering research of Wierzbicki and Abramowicz , the initial focus was put on re-visiting their works on Square sections and extending it further to Hexagon and Octagon sections. The methodology was then utilized to develop a new 12-Edge section with better packaging at edge corners for robust collapse in asymmetric/inextensional mode with good corner angle and high energy absorption capacity. Available domains of material through range of steels along with Aluminium were investigated to further the advancement with material characterization using series of static and dynamic tests. This material characterization was fed into the analytical and numerical models for establishment of crush performances of the intended sections in consideration both in quasi-static and dynamic modes. The results fed directly into the CAE models for correlation and robust predictions. Thorough analysis of the results data from the crush tests both physical and numerical lead to an important conclusion that the maximation of edge corners with right packaging and favourable corner angles provided higher capacity to absorb the initial crash kinetic energy with good weight effectiveness which in this study is the 12-edge sectional thin walled member. Its dominance over the pack of other sections was widely analysed and established through the crush responses. A new methodology of design sensitivity analyses using DOE (design of experiments) based on Taguchi method was proposed and performed to identify dominant characteristics and further multi objective optimization was done to extract the optimum values for the responses. Analytical expressions for design parameters like Mean crushing force (P_m), Specific Energy Absorption(SEA), Solidity ratio(ϕ)and Collapse Efficiencies are derived while new design parameters of Weight effectiveness (W_E), and structural effectiveness (η) along with their application are proposed.

The understanding and characterization of thin walled structural columns with multi cornered sections developed at component and subsystem level fit well into the domain of upfront energy absorption motive and would not be complete if their ultimate responses are analysed at a full vehicle level in terms of their capacitance for crash energy absorption. The intended test vehicle subjected to a velocity of 56kph to impact into a rigid wall as per FMVSS 208 standard and assessments for the effectiveness of the energy absorbing devices in terms of chest deceleration and dash intrusion, which is indicative of tibia/femur loading were considered.

The foundational dominance of 12-edge section at component level maturity and as applied to full automotive dynamic vehicle crash test resulted in achieving overall reduction in parameters reflecting Femur and chest injury of the occupants. Inspite of very small package space for the energy absorbing device, the 12-edge specimen showed 38% higher dynamic energy absorbtion than conventional square members. The specific energy absorbtion data also leans heavily towards 12-edge crush can with a value 20.21kJ/kg which is 39% higher than conventional square members. The dynamic dash intrusion measured at centerline of brake pedal on firewall into the occupant compartment reduced by 23% with 12-edged crush cans which is direct reduction on femur/tibia loading of the occupant.The occupant chest deceleration reduced by 4% inspite of very small package space for the crush can within the front-end structure. Thus indicative of the potential of the multi-cornered sections for enhancement in crashworthiness of Automtive vehicles and reduction in occupant fatalities in severe crash events.

PUBLICATIONS

The work arising from the PhD project has been published in the journal and conference papers listed below:

Under Review:

1. **Sekhar Reddy,** Mohammad Fard, Milad Abbasi, *Multi-cornered thin walled sheet metal members for enhanced crashworthiness and occupant protection*. Journal of Thin walled structures –TWST-S-15-00053-Elsevier 2014

2. **Sekhar Reddy,** Mohammad Fard, Milad Abbasi, *Multi-cornered thin walled sheet metal members for enhanced energy absorption and Crashworthiness.* Journal of Non-linear Engineering 2014

Published:

3. Milad Abbasi**, Sekhar Reddy** , Mohammad Fard, *Multiobjective crashworthiness optimization of multi-cornered thin-walled sheet metal members*, Journal of Thin walled structures –TWST-D14-00230R3-Elsevier 2014

4. Milad Abbasi, Ali Ghafari-Nazari, **Sekhar Reddy**, Mohammad Fard, *A new approach for optimizing automotive crashworthiness*, Journal of Structural and Multidisciplinary optimization – DOI 10.1007/s00158-013-0986-6; ISSN 1615-147X; Springer

5. M. Kajtaz, **S. R. Biddala Reddy**, A. Subic, M. Takla, *Crashworthiness Validation in Early Stages of a Design and Conceptualization ICRASH* ; International Crashworthiness Conference - Kyoto July 22 – 25 2008

LIST OF FIGURES

LIST OF TABLES

NOMENCLATURE:

C	Total side length
t	Wall thickness
α^*	Switching parameter
ϕ	Central angle of SFE
σ_0	Plastic flow stress
$\dot{\varepsilon}$	Strain rate tensor
Pm	Mean crushing force
$P_{\max}$	Peak Crush force
$2H$	Plastic folding wave length
M_0	Plastic bending moment
V_t	Rate of stretching
ψ_0	Central Folding angle
r	Rolling radius
δ_{eff}	Effective crush
σ_u	Ultimate Tensile Strength
σ_u^s	Specific ultimate tensile Strength
σ_y	Material yield strength
E_s^c	*SEA* Specific Energy Absorption
A_s	Sectional Area of the specimen
V	Volume of the specimen
ρ	Material Density
η	Structural Effectiveness
ϕ	Solidity ratio
S_E	Crush efficiency
$\boldsymbol{A_E}$	Crush force efficiency
$\boldsymbol{E_E}$	Energy efficiency
E	Young's Modulus of Material
υ	Poison ratio of the material
δ_m	Crush
E_{abs}	Total energy
W_E	Weight Effectivenes
ESW	Equivalent Square Wave
DAF	Dynamic Amplification Factor
v_0	Initial impact velocity
ω	Acoustic natural frequency
f	Restraint natural frequency
t^*	Time of occupant to restraint contact
δ_r	Restraint slack
δ_c	Maximum dynamic crush
t_m	Time of maximum dynamic crush
A	Occupant Chest deceleration
TL	Total Langrangian formulation
S/N	Signal to noise ratio

CHAPTER 1

1.0 Introduction

The birth, evolution and progression in understanding the intricate process of vehicle collisions originated at the start of this century at about year 1935 with recorded accidents starting from the first one in New York city in 1889.Vehicle collision is a consequence of a situation that produces an extreme abnormality wherever it occurs and in whatever mode it occurs whether with moving vehicle or with stationary one. It subjects the vehicle structure to very high forces and deformations depending upon the mode and velocity of the collision. If these collision forces exceed the energy absorbing capacity of vehicle structure in action the effect is directly felt on the Occupants and might lead sever injuries and fatalities. Understanding the process of collision and its effect of occupants of a vehicle is thus very important and this underlying need has led to the birth of the field of Crashworthiness and occupant safety. This aspect of design has become the inherent requirement for all the ground mobility vehicles. This requirement was perceived very early by the manufacturers and realized the need for incorporation of occupant protection even before the general public could consider using their products for their mobility needs.

The early periods from the year 1935 to 1966, focus was on the basic things like adoption of steel material for making vehicle structures, windshields for reducing facial lacerations, tire blowout reductions and other improvements in safe operating conditions of vehicles. From the year 1966 the focus was on basic crash avoidance through turn signals, windshield wiper, Headlamps etc., coupled with some rudimentary vehicle crash test of a vehicle into a rigid wall by General Motors. Performance evaluations of the crushed vehicle were made observing the heavily deformed vehicle post crush test. The most important step in safety was initiated in 1956 in terms of introduction of

Seat belts for occupants of a vehicle. The most important step in vehicle safety was initiated in the year 1966, when the National Highway Traffic Safety Administration (NHTSA) was formed and introduction of mandatory safety standards which are popularly known as Federal Motor Vehicle Safety Standards (FMVSS). These standards established a precedence to regulate various aspects of vehicle design and have become a foundational step for the safety of ground transportation vehicles all around world. It has become so mandatory that OEM (Original Equipment Manufacturers) of the vehicle have integrated these FMVSS standards into their design philosophies to develop safe vehicle structures. Over the past few decades the predominant focus has been on vehicle safety improvements through crash avoidance technologies coupled with structural crash performances, and occupant protection systems. The confluence of these improvements compounded with highways improvement along with better driver education has contributed to good reduction traffic fatalities.

Inspite of continuous decline in the fatality rates over a period of last few decades still the statistics of traffic injuries and death remain high. The data from NHTSA [1] for the year 2007 indicates an estimated 6,024,000 police-reported traffic crashes, in which 41,059 people were killed and 2,491,000 people were injured. The data also indicates an average of 112 people getting killed each day in motor vehicle crashes in 2007 which leads to one every 13 minutes in USA. The fatality rate for the year was about 1.37 per 100 million miles travelled (Figure.1.1).

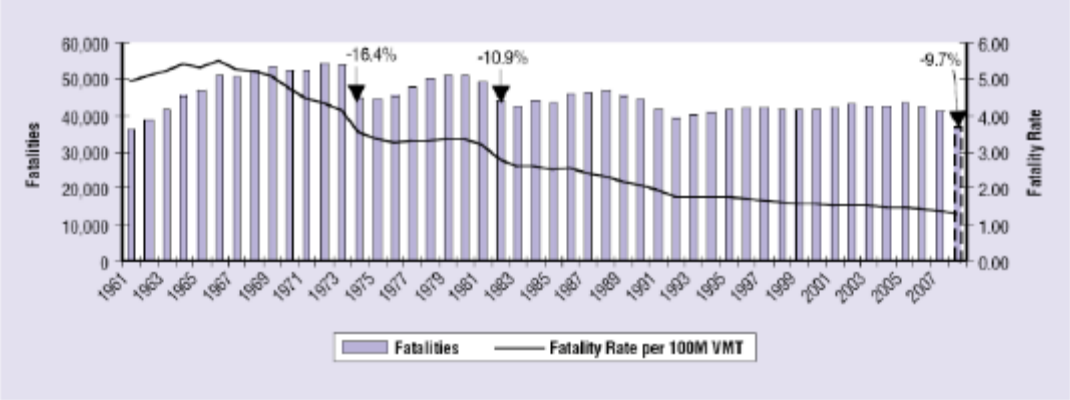

Fig 1.1Fatalities and Fatality Rates per 100 million from 1961-2008 [1]

During the same period the fatalities for every 100,000 residents in five developed countries also look staggering (Figure.1.2). The median fatality stands at 8 for every 100,000 residents. Even in Australia with a lowest population of 22 million the fatalities are on the higher side.

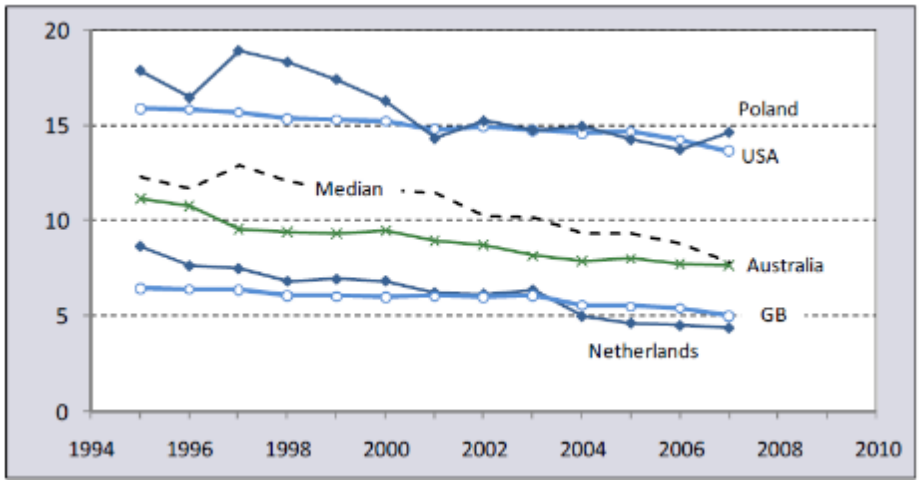

Fig 1.2 Fatalities for every 100,000 residents

Further from the safety facts of NHTSA data for the year 2007 the fatal distribution on different type of crashes including single and multiple vehicle crashes majority of them happening in a head on fashion typically termed as frontal impacts. The distribution of the fatalities indicates a phenomenal value of 53% towards drivers of the vehicles while 22% is attributed to passengers.

Asymmetric or concentrated loading across the vehicle front along with lack of enough structural capacity to specifically take these loads is the main reason for high intrusions into passenger compartments and associated injuries. When these injuries attributed to intrusions, NHTSA's injury data shows many occupants had serious chest injuries than any other injury type. These chest injuries are found to be on higher level when old passengers above 60 are involved. It is for this reason chest injury performance is considered in this research for evaluating the design responses on full vehicle level simulations.

To address the high percentages of fatalities in frontal impacts a large number of frontal crash tests have been studied by regulatory bodies like NHTSA, ECE and ADR along with public domain institutes like IIHS, SINCAP, ENCAP, ANCAP etc., to represent real frontal crash situations. Proposed tests like 56kph full frontal rigid wall impacts and 40% offset barrier impacts are the most powerful ones for the OEMS to relate their design performances to that of the real world frontal impacts which fall under majority of the distribution.

In most of the new car development projects, the car body would be developed to comply with the compulsory crash tests and would demonstrate decent level of performances in collisions that match or closely resemble those simulated which ultimately, determines the passive safety performance of the car. Given the scenario of the regulatory and public domain requirements with their constant refinements over the time the designs need to be constantly upgraded. The next chapter discusses the motivation for such design upgrades covering the wide scope of the research in its coverage of such aspects.

CHAPTER 2

2.0 Motivation and Scope

The desire to improve crashworthiness of a passenger vehicle has been for occupant safety has been a major challenge for decades. There were there were 40,000 fatalities and 3 million injuries resulting from motor vehicle crashes per year as per recent statistics by the National Highway Traffic Safety Administration in the United States. They burden society with $140 billion in annual economic losses [2]. Although passenger safety has improved significantly since 1966, when federal motor vehicle standards were first legislated, new challenges exist with consumer and legislative pressure to develop "green", low-emission, fuel-efficient cars. The direction most of the OEMs prefer to take for reduction in fuel consumption is by making designs lighter. It is estimated that a fuel saving of 0.3L /100 km and 0.7L /100 km can be achieved for every 100 kg reduction of mass in the case of highway and city driving conditions respectively [3]. In view of this potential, the need for light and advanced structures has been on high priority for the OEMs. Often this lightening exercise aggravates the risks for occupant protection and this needs to be addressed as it is shown in the previous studies that lighter vehicles tend to aggravate the fatality rates of occupants by two to three times on an average than that of the occupants of the heavier vehicle when involved in multivehicle collisions [4]. The increased incorporation of both passive and active energy absorbing devices gives rise to an increase in weight of the vehicle. This is evidenced by the fact that, historically for a specific car model, the ratio of overall vehicle mass to "body-in-white" mass has increased [3].

Moreover, when a crash is unavoidable, it is the crash energy and the manner in which vehicle occupants experience the associated forces that will determine the extent of injury to those occupants. So improving the vehicle crashworthiness reduces the magnitude of the forces experienced by the occupants, with the goal of reducing them to below the threshold for severe

injury. Solutions to these competing design goals of safety and fuel efficiency through light weight structures lie in the origination of innovative upfront energy absorption designs involving innovative designs which can be compounded by new materials, such as High Strength Low Alloy (HSLA), Dual Phase steels (DP), as well as composite structures.

From a public health perspective as well, the data indicate that motor vehicle crashes stand fourth in the top five leading causes of death after cardiac, cancer and stroke. It is imperative from the accident data [1] and human fatalities that there is quite a good need for continuous research on improving the safety of occupants in ground transport vehicles especially of the passenger cars which is in the majority of the mobility mode. The proportion of these fatalities attributed to type of vehicles from NHTSA data of 2007 (Figure-2.1) also indicates a majority of 56% with the passenger cars where most of primary means of ground transportation involving human personnel.

It's thus a major motive for this research on enhancing the safety of occupants of the passenger cars and any outcomes so implemented could potentially save many lives and families along with reducing the socio-economic burden on the society in terms insurance & Health costs.

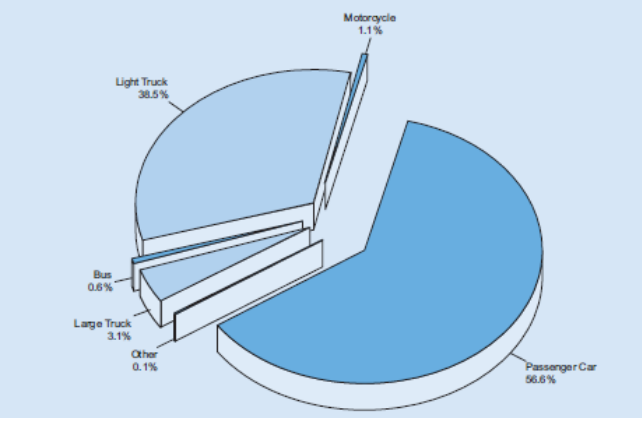

Fig. 2.1 Proportion of Vehicles involved in Traffic Crashes [1]

This thesis describes the methodology of structural collapse in corner angle element perspective and proposes an alternative design philosophy towards new frontal vehicle structure that directly deals with the asymmetric crash load of a frontal collision. This frontal collision is resisted predominantly by both longitudinal members through a progressive folding pattern called dynamic progressive buckling which has enough energy absorbing potential to prevent an aggressive deformation into the passenger compartment. It is most sort mode for energy absorption than global bending or Euler-type buckling. Figure-2.5 depicts the dynamic progressive buckling mode and the angular element or in short Super folding element (SFE) [5]

Fig. 2.2 Dynamic Progressive buckling and focus of corner element [29]

The objective of this thesis is to study the basic factors to enhance the energy absorption behaviour of front end automotive structures using crush tubes with a dominant variable of number of multi-corner including cross-sectional geometry under both quasi-static and dynamic loading conditions.

The methodology is further extended to full vehicle study to ascertain the effect on occupant injury performance. Both numerical and analytical studies are performed, with the former conducted using explicit code LS-DYNA.

The content presented in this thesis includes:

Chapter-3 describes an automobile structure and Crashworthiness emphasising the front end crash energy management and basic understanding of crashworthiness with steel as focus material.

Chapter-4 emphasises on the nonlinear mechanics and analytical capabilities of commercially available codes with highlights for each viable analytical code and finally the selection of appropriate coded for the analytical work in this research.

Chapter-5 focuses on some of the basic aspects of non-linear finite element analysis, continuum mechanics, and contact mechanics, nonlinearities arising from geometry, material and boundaries with explanation on numerical solution technique.

Chapter-6 focuses predominantly on the analytical aspects of crushing mechanism with special focus of super folding element theory proposed by Abramowicz and Wierzbicki to investigate the crush characteristics of single angular SFE through the formation and progression of the collapse mechanism along with basic derivation for mean crushing force.

Chapter-7 works on the natural extension of the singular SFE to multi corner member with different cross sections and this thesis author's further extension to higher edge members with derivations for mean Crushing force for individual shapes considered along with derivation for physical measures and design comparators for practical usage.

Chapter-8 deals with specific to Ls-Dyna Shells elements before ascertaining its use in

Numerical assessments using finite elemental simulations for the thin walled sheet metal sections. It also contains the formulation of numerical and physical tests for quasi-static and dynamic crush tests with discussion on the strain rate sensitivity and material effects.

Chapter-9 is related to the new methodology for dominant characteristics sampling using design sensitivity studies with Taguchi methods of DOE and optimisation using Pareto charts. This chapter presents the dominant effects of cross-sections in the responses under crush loading for energy absorption.

Chapter-10 is dedicated to material characterisation for all the Steel range and Aluminium first with quasi-static uni-axial tensile testing and the dynamic testing to ascertain the strain rate effects. The data from these tests are presented in graphical and tabular formats for representation and usage downstream for simulations and testing.

Chapter-11 focuses on the designs and manufacturing of physical samples for further testing and highlights the test set-ups for quasi-static and dynamic crush tests to characterise the crushing process in a controlled manner.

Chapter-12 is consolidation of analytical responses, numerical responses using finite element investigations, responses from physical tests both quasi-static and dynamic at sub-system level. Detailed data analyses and it depicts response characterisations with design comparators at force level and energy levels with discussions on result trends.

Chapter-13 discusses the extension of the subsystem level matured designs to a challenging full vehicle and investigations to study the ultimate responses of occupant injury with in tight package space to ascertain the dominance of the section in consideration for high performance.

Chapter-14 provides the consolidation of all the result trends and concludes the study with summary of findings.

Chapter-15 discusses the recommendations for the designers and analyst some salient points to consider for the effective design of energy absorbing structures taking into account of all the outcomes of this research. It also provided a brief note for future work on triggering mechanisms and further extension of this research towards triggered collapses under multitude of load cases

2.1 Existing works and Literature survey

Thin-walled structures are widely used as kinetic energy absorbers, since they are cheap, have high energy absorbing capacity, and are weight efficient. They can dissipate a large amount of kinetic energy through plastic deformation in the case of collisions. Such members must appear as major energy-absorbing components in automotive structures and absorb a substantial amount of crash energy at the time of impact occurrence. Front rail and front cross member in automotive are typical thin-walled energy absorbers which dissipate the kinetic energy by longitudinal and transverse deformations. Wdlentowitz, H. and Adam, H [3] discussed on the Energy absorption capabilities of such components that are very effective and weight-efficient approach in improving vehicle crashworthiness. Such a quest for lighter and more efficient energy absorbing components in various transportation systems has led to an increased interest in thin-walled sections. Many research articles have studied impact responses and crash performance of thin-walled structures. The major milestones in the research on thin walled sections starting from the first conceptualization from Alexander in 1960 until its extensions onto complex sections of today's modern day structures is as below in the chronological order of time.

- Thin-walled section collapse as an efficient mechanism for energy absorption – Alexander , 1960; Pugsley and Macauly 1960 [30,42]
- First theoretical analysis and analytical model with one folding wave and stationary hinge line assumption to characterise plastic collapse –Alexander 1960 [30]
- Practical industrial research effort driven by Magee and Thornton, at Ford Research labs

1978 on comparators for designers [41]

- Modifications to Alexander's theory with concertina folding mechanism with moving hinge lines by Wierzbicki and Bhat, Abramowicz and Jones -1986 [23,38]
- First FE codes for crashworthiness applications such as PAM-CRASH (Haug er al) and DYNA-3D (Hallquist and Benson) reproducing the actual crushing process 1986 [70-71]
- Extension of the approach to circular tubes to rectangular tubes Abramowicz ,Wierzbicki and Jones 1989 [23,43]
- Detailed Experimental studies of the Collapse modes - Normal Jones -1989 [7,29]
- Formulation of Super folding theory by combing theory of plasticity with moving hinge lines - Wierzbicki and Abramowicz and Jones 1989[31, 36]
- Detailed experimental study on single and double hat in both static and dynamic loading conditions- WhiteMD and Jones N 1999 [23-28]
- Collapse of thin-walled high-strength steel top hat sections-Tarigopula 2006 [34]
- Focus predominantly was on Cylindrical, Square and their derivative sections.
- **Extension beyond Square/Cylindrical shapes towards complex sections is missing**
- **Comparators for design flexibility is lacking**
- **Exploratory works towards practical applications is lacking**

The collapse process of the thin walled sections is of elasto-plastic in nature and conventional linear methods fail to describe it. The plastic collapse process needs nonlinear treatment and has to be combined with theory of plasticity with hardening models. The non-linearity arises from geometry, material and boundary (contact) which needs to be addressed analytically. David Hibbitt, Klaus-Jurgen Bathe, Pedro Marcal and John Swanson [8] were the some major players

in the early development of nonlinear finite element methods. Pioneering researches from the University of California, Berkeley researchers like Thomas J.R. Huges, Robert Taylor, Juan Simo, Bathe, Carlos Felippa, Pal Bergan, Kaspar Willam, Ekerhard Ramm and Michael Ortiz [8,9,10,11,16,17] lead to the solution methods which can address static and dynamic load cases using implicit methods. A major milestone in the advancement of nonlinear analytical work with explicit finite element codes was by John Hallquist's work in 1975 [70] and commercialisation through PAMCRASH in 1980 and Ls-Dyna in 1989. The rapidly decreasing cost of computers and the robustness of explicit codes have revolutionized design in the past decade which lead to extensive adaption by automotive domain in crashworthiness and proliferated to more industries. With the advent, adaption and maturation of these nonlinear explicit methods new challenges of design in the form of optimization towards crashworthiness improvement came to fore front. It is almost impossible to conduct crashworthiness design optimization using a high-fidelity finite element crash simulation directly. C.A.C. Coello, D.A. Van Veldhuizen, G.B. Lamont [48] provided the basis for multiobjective optimisation through DOE and surrogate models to construct the approximation on the exploratory design space. This was further enhanced with The Taguchi robust design method using fuzzy logics [47, 50] for multi-objective optimization in combination and Pareto-optimal criteria for design decisions in achieving an optimal solution. Moving further from the design space to application phase lot of studies were done on applying the collapse of thin walled columns collapse in the domains of automotive industry where vehicle crashworthiness and occupant safety remain among the most tangible, important and challenging design considerations.

The safety facts from NHTSA data for the year 2007 provides the fatal distribution on different type of vehicle crashes where it can be observed that majority of the crashes are happening in a head on fashion typically termed as frontal impacts. The distribution of the fatalities indicates a

phenomenal value of 53% towards drivers of the vehicles while 22% attributed to passengers. Many occupants had serious chest injuries followed by Femur injuries than any other injury type and forms the final metric for the effectiveness of the energy absorbers in full vehicle crashes.

Reports from IIHS(Insurance institute of Highway safety) [44] indicates that the overall driver death rate in midsize cars is 23% lower than in small cars which show the vulnerability of small cars with light bodies towards frontal crashes. Elaborate literature from the NHTSA and FMVSS (Federal Motor Vehicle Safety Standards) in particular FMVSS 208 provide the requirements for injury metrics and their subsequent treatments in the assessment of effectiveness of energy absorption in the energy absorbing devices. The dominant ones as per them are the chest deceleration and dash intrusion, which is indicative of Femur/Tibia Loading [45]. These injury metrics form the ultimate targets and any reduction due to the performance of the energy absorption methodology of this research would be greatly beneficial.

2.2 Research Objectives

The aspect of extending the knowledge beyond square and cylindrical section shapes instigate the idea for this study and formulate the objectives which are as below.

- **High energy absorption within the constraints of mass and space with better material utilization**
- **Stable collapse with prismatic sections having even corners**
- **Efficient usage of cross-sectional space for maximum corner elements packaging**
- **Development of a section outperforming the existing designs across material ranges**
- **Robust performance in static and dynamic load cases across wide range of chosen materials**
- **Adaption to full vehicle designs and reduce Occupant Injury**

2.3 Research Methodology

The methodology followed in this research starts with re-connect of the pioneering research works of Wierzbicki and Abramowicz in characterizing a Single Folding Element (SFE) and its application to Square sections. The plastic collapse process was analysed and relevant expressions for Peak mean force and plastic wave lengths were derived. The analytical methodology and understanding was further used towards ideation of multi cornered prismatic sections within constant packaging space and their characteristics under crush loading. The characterization was done in three ways starting analytically with expressions for design comparators and relevance to design applications. The next characterization was done numerically through nonlinear Finite element analysis using Ls-Dyna as the code and the generated design from ideations. The designs were thoroughly analysed and the concepts were matured to refine designs and tested quasi-statically and dynamically.

The FE validations would not be complete if they are validated with physical experiments. The third characterization was done using range of physical tests both statically and dynamically complimented further by material characterizations using uni-axial tensile tests and strain rate dependent tests. The material data so obtained was fed into the numerical models for better correlations and upfront robust predictions which pave further way for more design experiments. Design sensitivity analyses using Taguchi method was performed for understanding the dominant characteristics and design optimization was performed over the dominant characteristics to get optimum values. The data of the results were analysed and extended to full vehicle validations through transient dynamic analyses of crash at 56kph. The design responses were analysed and the occupant metrics were extracted to provide final conclusions. The Research methodology followed for this research is as per flow chart shown in the Figure -2.3.

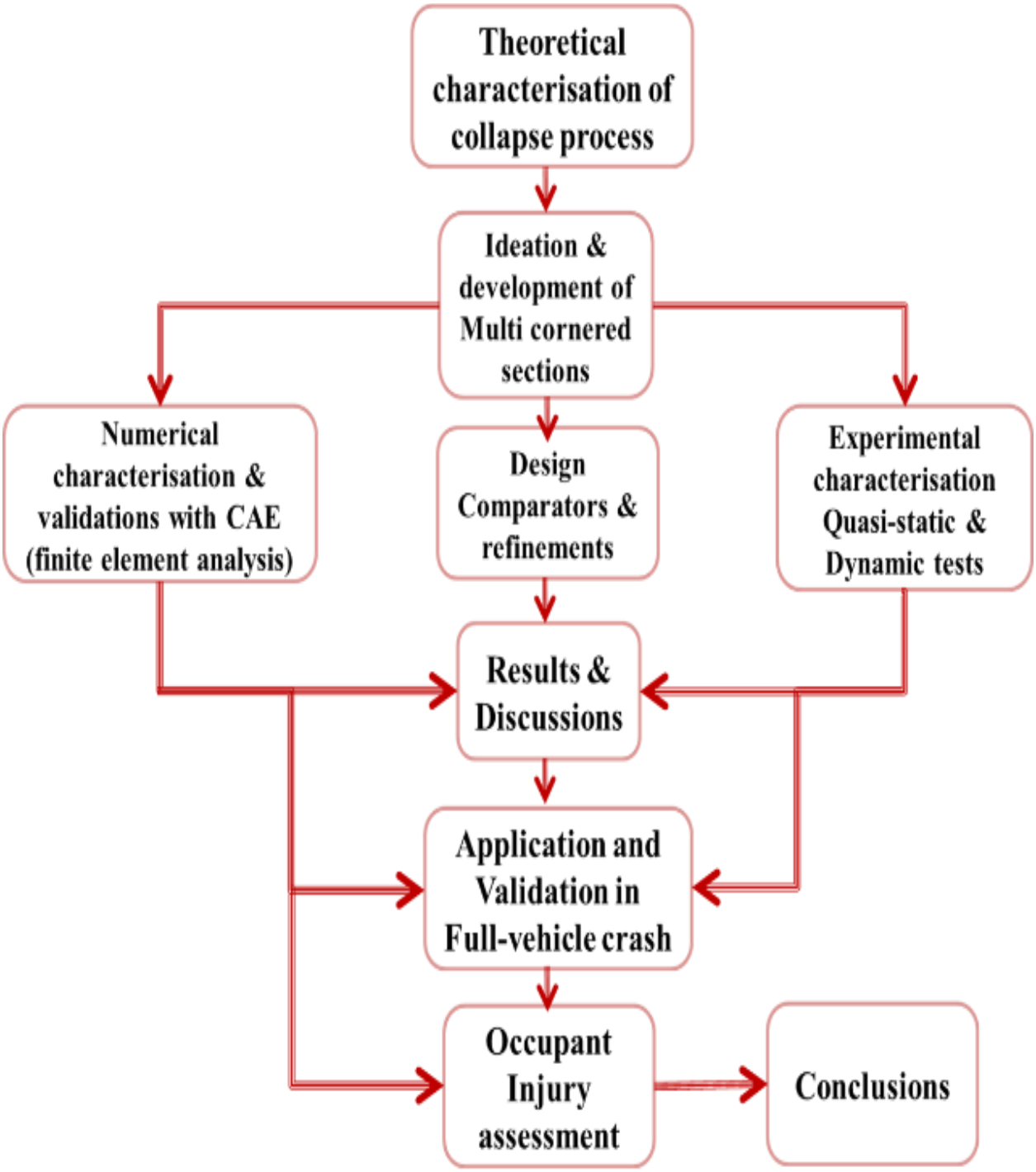

Fig. 2.3 Research Methodology Flow Chart

The methodology of the current research would not suffice if the basic aspects of crashworthiness with respect to the automobile are not understood. The next chapter provides a detailed know how on these important aspects and their application into the research subject.

CHAPTER 3

3.0 Automobile structure and Crashworthiness

The structure of an automobile has evolved over last seven decades meeting the needs of customers with complex conflicting requirements such as cost and weight, performance and materials, and energy management and package, markets and safety regulations, economics and competition, new technology and manufacturing capabilities. In addition to designing the vehicle structure for service loads under static and dynamic conditions which are anticipated during the vehicle's life cycle, it also need to be developed to sustain its integrity during collisions and provide adequate protection for occupants in inevitable crash scenarios.

Unit-body structural designs (Figure 3.1) are the most widely used amongst the passenger cars and were first introduced in the U.S. in early 1980's. These designs combine the structures of the body, chassis frame, and frontend frame and rear-end structure into a single unit from stamped sheet metal parts. The assembly so formed is connected predominantly by spot welding while other fastening methods like that of bolts, screws etc., are used in some localised locations. This style of construction of the unit body structure provides unique advantage in terms of whole vehicle rigidity in bending and torsion.

The material typically used in unit body structures is Steel, which is widely available and produced across the world which also enables economic mass production. It also forms the primary choice of the material for its unique characteristics of good formability, corrosion resistance, and recyclability while also meeting the requirements of body structure for an adequate strength, light weightiness to

reduce fuel consumption, well defined elasto-plastic zones in a stress-strain response and ease of manufacturing with joining

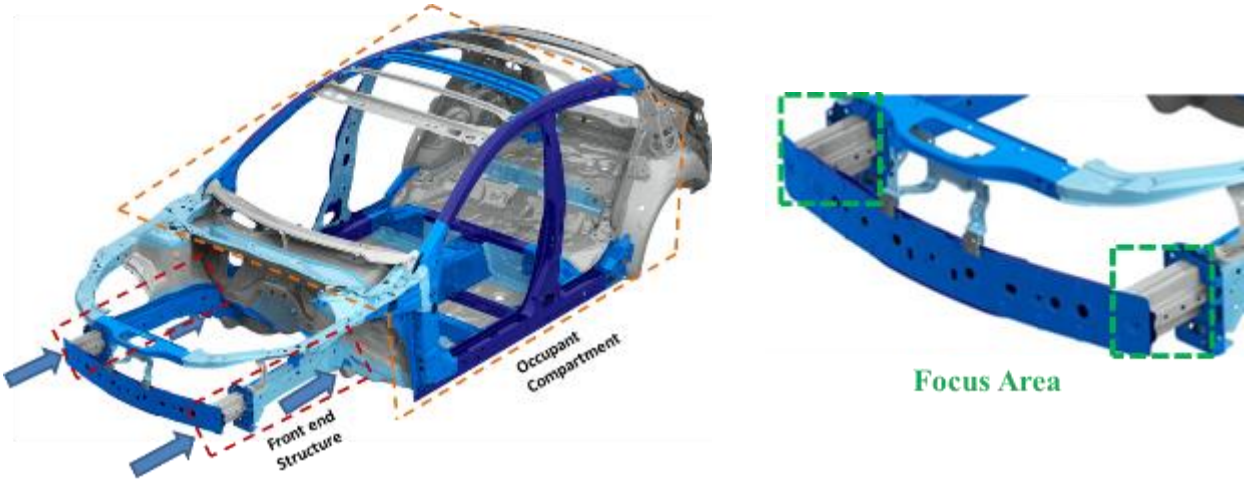

Fig. 3.1 Unit-body structure

.

Although modern day manufacturing is looking for Aluminium and composite the versatility and importance of steel cannot be overridden. The range of its availability from low strength to ultra-high strength [6] is commanding which gives this research a choice of material to investigate in low, mid and high strength ranges. Figure-3.2 provides the range distribution and grade availability of steel

Increased density and intensity of traffic coupled with stringent legislations along with growing concern of the public safety have made vehicle safety one of the major research areas in automotive engineering. Especially when fatalities occur due unfavourable large deformation of passenger compartments in collisions it becomes even more relevant to enhance the understanding of intricacies in the mechanics of collisions.

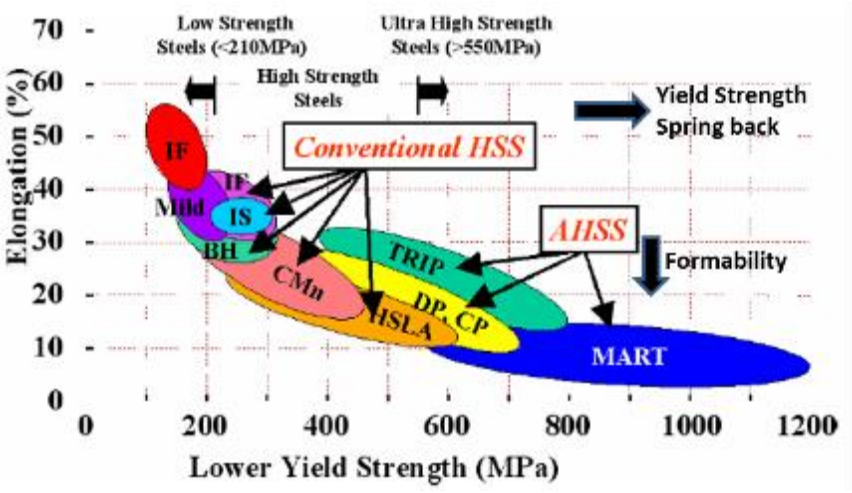

Fig. 3.2 Range distribution and grade availability of steel [6]

Though the term **"Crashworthiness" [19]** was first used by the aerospace industry in early 1950's it became more applicable to auto motive structures for its shear relevance. It has also received a wide attention and also been extended for design of all kinds of vehicles (cars, buses, trains, aircrafts, ships, etc.), for the design of devices that have to withstand collisions with moving objects (e.g. offshore structures, space structures) and for a wide range of safety components (including retention mechanisms in vehicles).

It can be defined as "*The ability of a vehicle structure to plastically deform and yet maintain integrity with reasonable deceleration loads and occupant survival space when involved in crashes"*. It is used to describe the impact performance of a structure when it collides with another object [7] to assess the damage and the survivability of passengers in vehicles. An important aspect of crashworthiness is to deal with impact energy absorption and dissipation of energy through specially designed zones. The main goal of vehicle crashworthiness as established in many auto OEMS is to develop a *vehicle structure which minimises the load transfer to the occupants by absorbing energy through vehicle deformations that are controlled and with adequate survival space so that the residual crash energy can be managed by the restraint systems.* Many efforts and

resources are put into achieve this goal and maintains the most important and challenging design considerations in the automotive industry.

The general practice for designers in automotive industry is to develop vehicle structures that provide high occupant protection by targeting integrity of the passenger compartment with simultaneous control of the deceleration pulse resulting from the crash to fall below the upper limit of human tolerance. Foremost the biggest challenge for vehicle structure developers is to address wide range of real world collision events which are uniquely dynamic happening in micro or milli seconds where the vehicle may collide with multitude of modes front, side or rear involving either moving vehicle pf stationary, different shape, stiffness and mass. Furthermore, the collisions can be of a single impact or multiple impact types with a wide range of speeds, different sizes of occupants and different modes of collisions. In automotive domains while developing the vehicle structure, for collisions, experts classify the modes of collisions as frontal, side, rear and rollover crashes to accumulate the responses of structure and its occupants. Achieving this balance between the structural response and occupants reactions to that response is very important as it can seriously affect the fatalities. In order to reach this balance the requirements for the vehicle crashworthiness [6] can be stated as below but not limited to them:

- Sufficiently stiff under bending and torsion from general service loads with proper ride handling.
- Avoid harshness and minimize high frequency fore-aft vibrations.
- Reasonable deceleration pulse that takes into consideration the range of occupant sizes, ages, and crash speeds
- Deformable and reasonably stiff front and rear structures capable of plastically deforming and absorb the crash kinetic energy.

- Intrusion prevention into the passenger compartment, while involved offset and small overlap crashes with narrow objects
- Roof crush and rollover protection with good roof structure.
- Optimal ride down and protection capability with good restraint systems that work in harmony with the vehicle structure

The tasks involved in achieving the crashworthiness are unique and differ from traditional structural analysis where elastic analysis within linear range of a material to withstand general service loads without yielding is considered. Linear analysis covers the development spectrum of the vehicle structure for service loads which could be static and dynamic. However when it comes to the crash - worthiness of the vehicle structure, it must deform plastically within a short period of time (milli seconds) and absorb the impact energy in a controlled manner. The critical thing in this process is that the controlled collapse must be limited to areas away from the passenger compartment there by ensuring that critical load are not transmitted ensuring that the human occupants are exposed to less aggressive deceleration levels.

A generic pattern of load-deformation of the structure to dissipate the kinetic energies in a controllable manner and provide safe occupant zones can be obtained by carefully laying out the stiffness stack up of the members starting from the front of the structure and progressing toward the occupant compartment as presented in Figure-3.3.

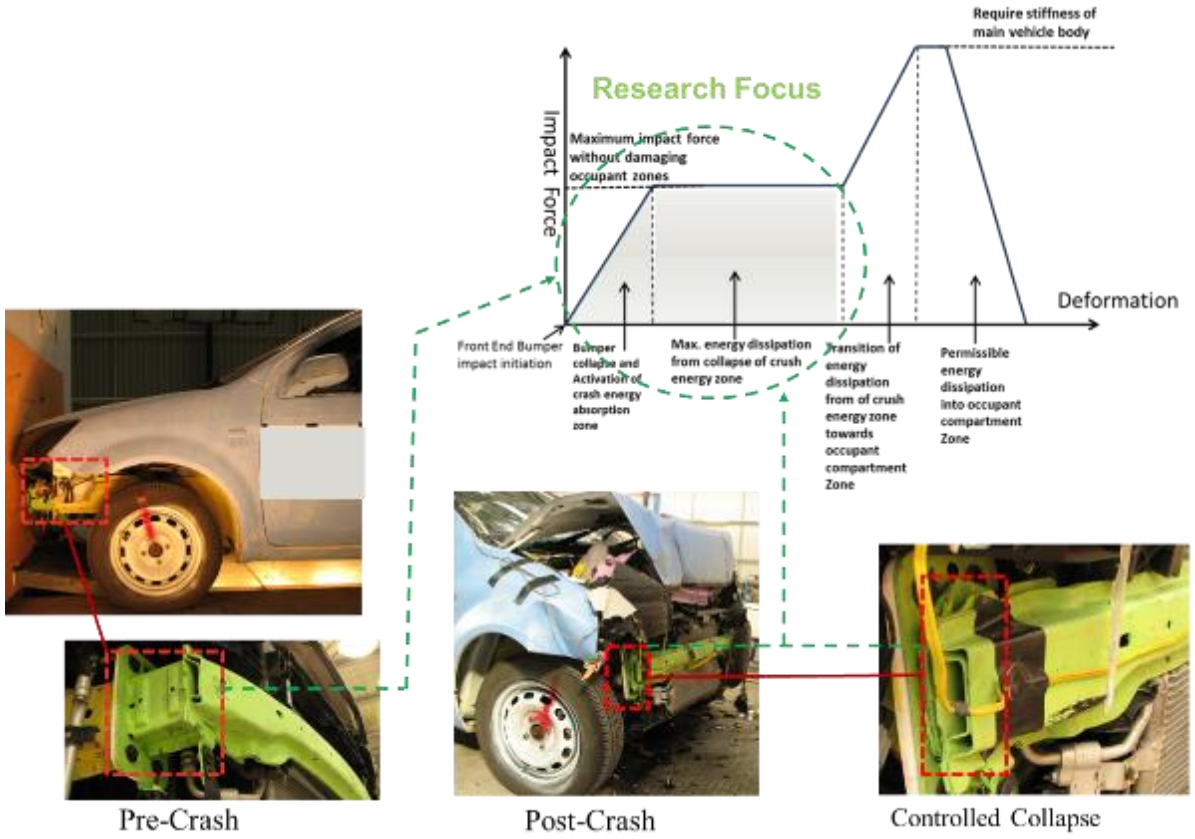

Fig. 3.3 Ideal front structure stiffness stack up in Force-deformation domain for a frontal impact event

The stiffness stack up of the structural members in front end structure of to dissipate the large kinetic energies of the collision in a controllable manner is generally obtained with assemblage of members composed of thin-walled structures that deform plastically leading to efficient energy dissipation in defined and localized regions. Figure-3.3 demonstrates the degree of complexity that is present in the front end crash absorbing structures of a modern day vehicle. It shows the front-structure as marked with red boxes, which exemplifies the main energy absorbing zone which are generally longitudinal sections made of high-strength steel. For crashworthiness to be effective 70 to 80% of the energy has to be taken care by this structure for conventional vehicle while remaining would be kept under permissible transition into occupant zone without causing aggravation of occupant injuries. This scenario can be more stringent when it comes to electric/hybrid vehicles where there is an absolute need for absorbing most of the crash energy by front structure alone, as

the safety of the battery modules packaged under occupant compartment become more dominant in addition to the occupant safety. This type of frontend structure is the result of amalgamation of conflicting requirements such as energy absorption, occupant safety and structural integrity sufficing at high speed collisions, low repair costs, pedestrian protection and compatibility with other vehicles.

To accomplish the toughest challenge of developing such frontend structures with minimum decelerations transmitted to the occupants which are within the range of human tolerance aided by restraints systems, designers have to rely on advanced mathematical tools going beyond simple strength of materials calculations.

With ever increasing demands on vehicle design year by year to satisfy safety regulations, fuel consumption requirements, low cost manufacturing and shortened design cycle times, there is a great impetus on the development of a methodology for crashworthiness evaluations with practical application sense.

With rapid progressions in computing power coupled with advancements in Finite element methods a combination of robust analytical and numerical methods can be used in evaluating the crashworthiness of vehicle structures. These methods matured from initial simple mass-spring models with few degrees of freedom to high fidelity articulate finite element models with millions of degrees of freedom. The following chapter would describe in more the details of these methodologies and available commercial tools with judicial comparison for their selection.

CHAPTER 4

4.0 Nonlinear Analysis and FEA codes

Nonlinear analysis involves very complex issues that pose series challenges for the analyst. The issues of convergence, choice of nonlinear solution algorithm and proper material modeling must be considered to get the proper and meaningful results from the nonlinear analysis. Unless the analyst is completely aware of these complex issues it is very difficult to predict accurate and reliable solution from the nonlinear simulations. A complete understanding of continuum mechanics, finite element method, structural mechanics, plasticity, stability theory and numerical method is required to carry out successful nonlinear finite element analysis. The analyst should be aware of how these topics are handled in a finite element program and its limitations. This chapter makes a brief survey of the history of nonlinear mechanics with a particular attention on the progress of the nonlinear finite element codes for the last three decades. Different types of nonlinearities and the general approach used for nonlinear analysis are explained in this paper. This chapter also presents important features and applications of three popular finite element codes NASTRAN, ABAQUS and LS-DYNA3D.

Nonlinear analysis is used in many practical engineering applications whenever the engineer wants to take full advantage of material capacity. Often, designs based on linear analysis are too conservative and cannot be competitive in today's international markets. An engineer must take full advantage of material ductility and toughness as many materials have significant capacity beyond their initial yield strength. On the other hand, thin shell structures and components made of materials such as rubber and elastomers show little resistance at small deformation and more resistance as they are subjected to more and more deformation. With linear analysis, no useful results can be obtained for these applications. Similarly nonlinear analysis is required to model creep deformation, which is important for high polymer plastics and machine elements at high temperatures. Contact analysis is

another most important type of nonlinear analysis that is commonly used in many engineering applications.

For analysts who are unfamiliar with nonlinear effects it might deter his predictive abilities due to broad range of issues which are generally masked by sensitive factors that can make a simulation quite misleading. Under generic load conditions structures can experience instabilities, can exhibit sensitiveness to imperfections with responses depending on material parameters but, once nonlinearity creeps into the model, the issues of convergence, choice of nonlinear solution algorithm, etc. take the precedence while the uniqueness and stability of the solution may be lost. Misinterpretation and inability to judge the trends in simulation results is quite a possibility unless the analyst is aware of these phenomena. Certain events like crash simulation of vehicle structures in automotive domains and metal forming cannot be analysed without considering nonlinearity.

Linear static analysis is the most commonly used type of analysis in the finite element applications. The term 'linear' means that the calculated response (either displacement or stress) is linearly related to the applied load. The finite element equilibrium equations for the linear and nonlinear analyses are given below, Bathe KJ [8].

$$[K]\{d\} = \{f\} \quad \ldots (4.1)$$

where {d} is the displacement matrix and {f} is the force matrix. The stiffness matrix [K] is defined as:

$$[K] = \int_V [B]^T [D][B] dV \quad \ldots (4.2)$$

$$\{\varepsilon\} = [B]\{d\}$$

$$\{\sigma\} = [D]\{\varepsilon\}$$

where [B] is the strain-displacement matrix and [D] is the constitutive matrix that relates the stresses and strains. For the linear analysis with infinitesimal displacements and strains the

strain-displacement matrix [B] is assumed to be linear. For the linear elastic materials, the constitutive matrix [D] is linear. Hence this leads the stiffness matrix [K] to be linear.

The above discussion of the linear analysis suggests the meaning for nonlinear analysis. If either the strain-displacement matrix [B] or the constitutive matrix [D] is nonlinear, the resulting stiffness matrix is nonlinear. Changes in boundary condition during the course of application of load also introduce nonlinear behaviour in structures.

4.1 History of nonlinear mechanics

David Hibbitt, Klaus-Jurgen Bathe, Pedro Marcal and John Swanson [8] were the some major players in the early commercial development of nonlinear finite element software. The first nonlinear program NONSAP was evolved from the linear program SAP developed by Bathe at Berkeley and later this has grown to present popular program ADINA. Pedro Marcal has developed the first nonlinear commercial finite element program MARC in 1969. At about the same time John Swanson has developed ANSYS that focused more on nonlinear material than the complete nonlinear problem and it dominated for many years in the commercial nonlinear finite element scene. Hibbitt and Marcal in 1972 founded HKS, to develop ABAQUS and this program had substantial impact, as it was one of the first finite element programs to introduce gateways for researches to add elements and material models.

The commercial finite element programs marketed until 1990 were capable of static solutions and dynamic solutions by implicit methods with more advancement in the 1970s, mainly by University of California, Berkeley researchers like Thomas J.R. Huges, Robert Taylor, Juan Simo, Bathe, Carlos Felippa, Pal Bergan, Kaspar Willam, Ekerhard Ramm and Michael Ortiz [8,9,10,11,16,17]. It was undoubtedly the main incubator in the early years of finite elements. Explicit finite element methods in their early years were strongly influenced by of the work of

DOE laboratories. In 1964, Costanino developed the first explicit finite element program at the IIT Research Institute in Chicago and it was limited to linear materials and small deformations. In 1969, Ted Belytschko developed a 2-D explicit program SAMSON which used by US defence industries for over a decade and was later updated to WRECKER in 1972, with capabilities for nonlinear three-dimensional transient analysis of structures.

A major milestone in the advancement of nonlinear analytical work with explicit finite element codes was by John Hallquist's work at Lawrence Livermore Laboratories. He started his work in 1975, and the first release of DYNA code was in 1976. Hallquist's works in developing the one-point quadrature and effective contact-impact algorithm with high degree of vectorization made a striking break-through in the world of engineering simulations [70]. The DYNA codes were first commercialized by a French firm, ESI, in the 1980s and called PAMCRASH. [71] In 1989, John Hallquist started his own firm to further develop the code with brand name Ls-Dyna, a commercial version of DYNA which has become a core tool in the world of crash mechanics.

The rapidly decreasing cost of computers and the robustness of explicit codes have revolutionized design in the past decade. The first major area of application was automotive crashworthiness, but it proliferated rapidly. In more and more industries, proto type tests are being replaced by nonlinear finite element simulations. Products such as cell phones, laptops, washing machines, chain saws and many others are designed with the help of simulations of normal operations, drop-tests and other extreme loadings. Manufacturing processes, such as forging, sheet metal forming and extrusion are also simulated by finite elements. For some of these simulations, implicit methods are becoming more powerful and it is clear that both capabilities are necessary.

4.2 Classification of nonlinear analysis

In a finite element analysis if either the strain-displacement matrix or the constitutive matrix is nonlinear, the resulting stiffness matrix is nonlinear. Changes in boundary condition during the course of application of load also introduce nonlinear behavior in structures. Based on the type of nonlinear effect, the nonlinear analyses are classified into three categories as below and discussed in next chapter in detail

1. Geometric nonlinear analysis
2. Material nonlinear analysis
3 Boundary nonlinear (Contact) analysis

4.3 General approach to nonlinear analysis

The most important aspect in a nonlinear analysis is to decide which type of nonlinear effect is to be considered for the analysis. Any combination of the three nonlinear effects discussed above can occur in combinations or simultaneously together. In many cases, the analyst will be able to decide which type of nonlinearities to be considered based on the response from the linear analysis. Hence, it is a good practice to proceed for linear analysis prior to the nonlinear analysis. The results from the linear analysis indicate the region where geometric nonlinearity may be significant and when the material exceeds it elastic limit [13].

In linear static analysis, the stiffness matrix [K] is constant and can be developed independently of the current displaced state of the structure. In nonlinear static analysis, the stiffness matrix is a function of the current displaced state of the structure and, therefore, can only be developed from the displaced configuration. Since the purpose of nonlinear analysis is the determination of an unknown displaced state, a stiffness matrix that depends on the unknown displaced state leads us

to a situation with no solution. We need to know the stiffness matrix to determine the displaced state, but the stiffness matrix cannot be computed "exactly" without the displaced state of the structure, since the stiffness matrix is dependent on the displaced state. The way out of this insolvable situation is to solve the equilibrium equation using iterative solution schemes. We start with the linear stiffness matrix [K] to obtain the displaced state {d}, assuming the structure behaves according to linear theory. Based on this initial displaced state {d}, we obtain [K(d)]. The equilibrium equation is now solved using [K(d)] to obtain an improved value of {d}, and the iteration continues until convergence is achieved.

The basic solution methodology to nonlinear problems is through incremental methods where in the load is applied in incremental way and a solution is predicted in each increment using the current state of stiffness and load increment. A residual force imbalance is then created during iteration where nonlinear behaviour occurs depending on the type of nonlinearity. The equilibrium with unbalanced forces is provided by the solution iterations and will continue until the convergence criterion is satisfied. The solution proceeds to next load increment only when the convergence for the current increment is satisfied and solution is obtained.

In the case of nonlinear dynamic analysis, the equation of motion is solved by time integration schemes such as Implicit or Explicit time marching. Explicit scheme is used for problems involving high frequency loadings, since these problems require small time-step to capture the associated phenomena and this scheme is stable for small time steps only. Implicit schemes are used for structural dynamics problems having moderate frequency contents since these problems are of longer duration and characteristically slow hence allows larger time step to be used. All commercial programs have algorithms to compute the time-step, which is a function of amount of nonlinearities and element sizes.

4.4 Finite element codes for nonlinear analysis

4.4.1 MSC/NASTRAN

MSC Nastran is the most widely used structural analysis tool by engineers worldwide in multiple disciplines. It is predominantly used to evaluate the basic strength, stiffness and life of structures under excess of stress, resonance, buckling etc., which might degrade the function and safety in simple to complex structures.

Components:

Linear Domain

- Linear statics
- Normal modes
- Linear buckling

Nonlinear Domain

- Short-duration dynamics
- Geometric and material non-linearity
- Fluid-structure interaction
- Multi body contacts

Dynamics

- Direct frequency response
- Modal frequency response
- Transient response
- Complex Eigenvalue analysis
- Random analysis
- Flutter analysis
- Aero elastic analysis
- Imbalance responses analysis
- Multi rotor system analysis

Thermal

- Linear and non-linear steady state Heat transfer
- Transient heat transfer
- Conduction
- Free or forced convection

- Radiation and coupled advection
- Thermal contact
- Coupled thermal & structural

Composites

- Composite laminate analysis
- Composite honeycomb sections
- Failure analysis of fiber, matrix and interlaminate plies

Fatigue

- Life and damage analysis
- Stress-life or strain-life methods for life calculations

Advanced

- Interior or exterior acoustic analysis
- Multi-physics code coupling
- Dynamic design analysis for shock loads
- Automated component Model synthesis
- Adaptive meshing
- Creep and relaxation analysis

Optimization

- Size and shape optimizations
- Topology optimizations
- Topography optimization

High performance Computing

- Parallel jobs with multi core
- Unsymmetric matrix solutions
- Parallel scalability

Major Applicability:

The majority usage of MSc Nastran is focused on linear statics for general load analysis, frequency responses and dynamics in NVH and for topology optimizations. Although advanced features are getting added to its contents, the evolution of this tool is based on linear domains and its application to nonlinear transient crash simulations is limited

4.4.2 ABAQUS

Abaqus is a powerful general purpose FEA tool to perform complex analysis. It has been predominantly developed for performing non-linear analysis and is very popular in the industry for wide range of applications. The strength of this tool is in its implicit method of solutions. It uses high performance, sparse, multi front equation solver to address both symmetric and unsymmetric equations. This tool is equipped with powerful automatic controls of the time incrementation to provide convergence without extensive experience in dealing the problems.

Features:

On top of all the capabilities which Nastran provides Abaqus has the following features which provides to the users.

Linear and Nonlinear

- Statics and low speed dynamic
- Linear responses with pre-loaded nonlinear history
- All Vibration response analyses
- Seismic loading

Multi-physics

- Transient steady state or dynamic heat transfer
- Coupled thermal and mechanical loading
- Thermal-Electrical coupling
- Low frequency Electro magnetics
- Structural acoustics
- Mas diffusion analysis
- Fluid flow through porous media
- Incompressible fluid flow
- Medical stents
- Bio-mechanics
- Hydrostatic fluid cavity
- Advanced material library

High performance computing

- Distributed memory parallel direct solver
- Good scaling and robust solution
- Direct cycling

Major applicability:

The strength of this tool comes from its implicit solution methodology. Over the years this method has been robust developed and is best in the class for multi-physics and generic non-linear applications. Although recent version of this tool comes with explicit methods but it maturity is yet to establish which limits the scope for its usage in short duration large deformation crash applications.

4.4.3 LS-DYNA

Ls-Dyna is a general purpose FEA tool to simulate complex real world problems. The tool itself originated from highly nonlinear, transient dynamic finite element analysis using explicit time marching scheme of solution. It is by far the most modern day code for capable of solving day to day engineering problems whether linear and non-linear, static and dynamic, multi-physics, multi stage, multi-scale and multi-processing. Its decked with distributed and shared memory solvers to provide short turnaround times for large problems with millions of degrees of freedom on desktops and clusters with Windows, Linux or Unix operating systems. It is aptly suited to investigate phenomena involving large deformations, complex material models, sophisticated contact conditions and for problems with disparate combinations. The development of code is concurrent with liaison with worldwide research institutes, universities and industry partners.

It has become an indispensable tool for many automotive companies and suppliers to understand the collapse mechanisms and associated occupant injuries at the design stages there by reducing significantly the developmental time with good cost savings on expensive crash prototypes. The usage of this tool is in most of the large car manufacturers including Ford, GM, Toyota, Honda, Nissan, Mercedes etc., for their crash and Safety applications. The variety and robustness of 25 contact algorithm helps in simulating complex interfaces and it also provides comprehensive library of materials along with high fidelity bio-mechanical systems like dummies in different categories and sizes. The strength in its application comes in predictions of failure and post failure

coupled with manufacturing history of parts generated through simulated environment of the manufacturing process. It is a heavily desired tool in metal forming mainly in stamping, hot forming, welding, rolling etc. The incremental approach allows simulating the multistage manufacturing process with secondary responses like trimming and spring back.

Ls-Dyna is also decked with an efficient optimizing tool for DOE studies and generates optimal solutions using advanced methods using response surfaces, Genetic algorithms, stochastic analysis using monte-carlo investigations, generic multi-disciplinary and multi objective optimizations. The extensive results data generated are highly compatible with numerous post-processors capable of binary and ascii processing.

Analytical capabilities

Linear:

- Linear statics
- Normal modes
- Linear Buckling
- Eigenvalue analysis
- Modal and transient
- Real-time acoustics

Non-Linear

- Non-linear buckling
- Non-linear statics
- Nonlinear dynamics
- Quasi-static simulations
- Fluid-structure interactions
- Dynamic relaxation
- Rigid body and coupled rigid body

CFD analysis

- Heat transfer both linear and nonlinear
- Structural-thermal coupling
- Conduction, convection and radiation
- Fluid analysis with Navier-Stokes
- Arbitrary Lagrangian Eulerian (ALE)
- Eulerian capabilities
- Shockwaves propagation

Structural failure analysis

- Crack propagations
- Rupture and catastrophic
- Multi-level failure
- Multi-event /contact failures
- Multi-physics coupling

Manufacturing

- Metal forming-stamping, machining, blanking etc.,
- Adaptive re-meshing
- Rezoning

Advanced

- Discrete and Boundary element method
- Mesh or element free methods
- Rigid to deformable switching
- Smoothened Particle Hydrodynamics (SPH)
- Explicit and Implicit combinations
- Bio mechanics and safety

Material Models

Ls-Dyna is with exhaustive library of different material models at about 150 in number for various analyses which involves non-metal and metals with multi directional failures.

- Metals
- Glass
- Foams
- Composites
- Plastics
- Fabrics
- Honeycombs
- Biomedical models
- Viscous fluids
- Visco-elastic
- Elastomers and rubbers
- High explosives
- Elasto-viscoplastic
- Concrete and soils
- User-defined materials

Element Library

Ls-Dyna has both under integrated and fully integrated elements, lower order and higher order formulations with tight controls on spurious energy modes.

- Discrete Elements
- Springs & dampers
- Beams- 13 types of formulations
- Shells- 37 types of formulations
- solid elements-24 types of formulations
- Weld element formulations
- SPH elements
- Sensor elements
- Safety Elements (Sensors, Pretensioners, Retractors & slip rings)
- Lumped mass elements
- Eulerian elements
- User-defined elements

Contact Algorithms

Ls-dyna has 63 different of contacts with both constraint based and penalty based algorithms and has been refined for robustness over last two decades. They can be categorised into flexible to flexible, flexible to rigid, Rigid to rigid and Edge to edge:
Some of the algorithms which are predominantly used are:

- Rigid wall contacts
- Surface contacts
- Edge contacts
- Eroding contact
- Geometric contacts
- Tied contacts
- Weld contacts
- Airbag Contacts
- 2D contacts
- Fluid-structure interface contacts
- User-defined contacts

Major applicability:

Ls-Dyna is the most sought code of the Automotive and manufacturing domain especially for crash and safety. Its wide range of capabilities extend its applicability to Aerospace for complex simulations like bird strike, Engine blade damage and failure analysis. It also got prominence in defence industries of r analysis on explosives, missile strikes and shock wave propagation studies. It is also being explored widely in Medical, sports and heavy machinery industries.

4.5 Selection of the nonlinear code:

Nonlinear finite element programs are widely used in aircraft, nuclear, automobile and offshore industries and also in the simulations of general manufacturing. While the 'Black-box syndrome' can lead to wrong results for linear analysis, it is far more dangerous in the case of nonlinear analysis and it can lead to totally misleading results, if the nonlinear finite element programs are not used in proper way. Judicious selection has to be made for the applicability of the right code to the current problem and the following comparative schematic provides the needed details.

Implicit ←	→ Explicit
• **Steady-State/Quasi-Static events** • **Solution: Iterative** • **Linearization necessity** • **Few Large time/load steps** • **unconditionally stable** • **Equilibrium/Convergence**	• **Pressure/stress Wave propagation effects** • **Solution: Direct** • **Decoupled: efficient, fast** • **Conditionally stable (courant)** • **Many Small Time steps**
Low velocity or long time events e.g. -Low frequency response -Gravity load of structure -vibration	High velocity or short time events e.g. -High frequency response -Explosions/chaotic flow -Impact/Crash

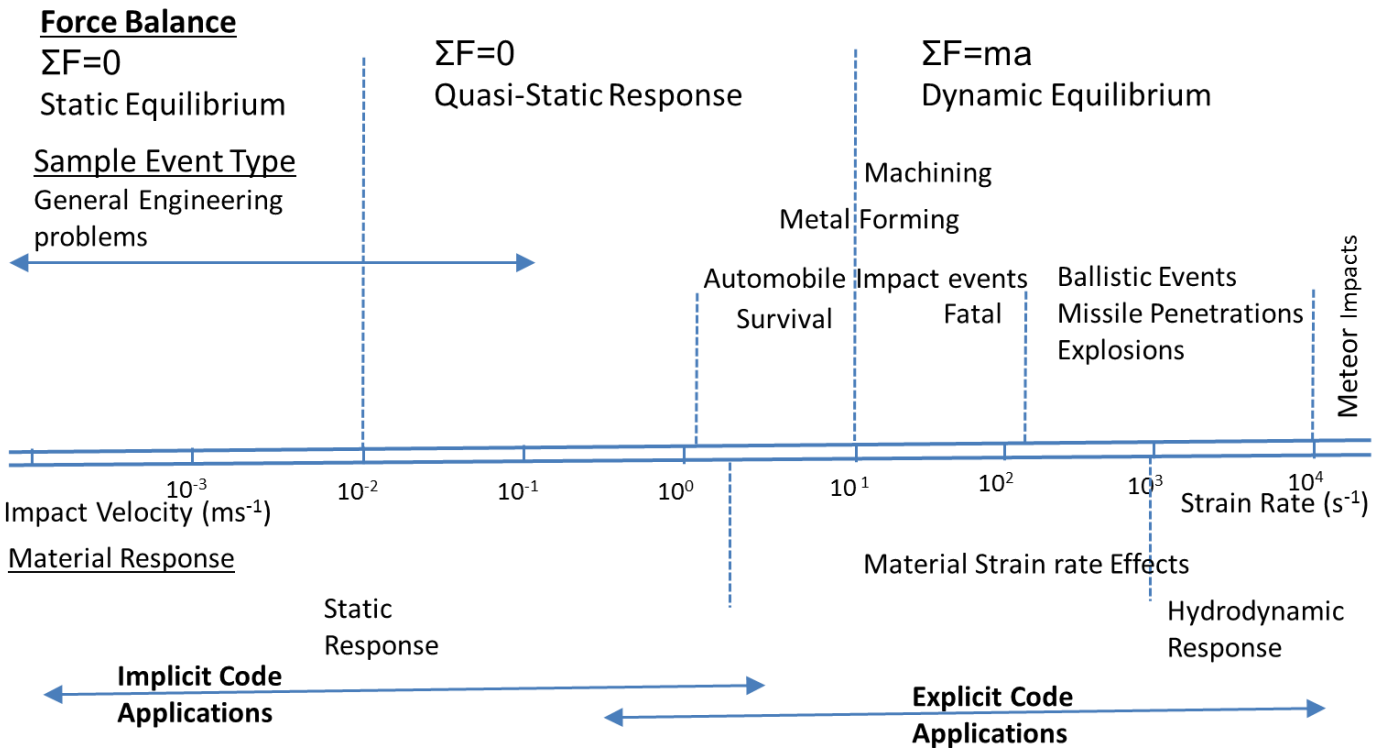

With the genetics of modern day numerical computational advancements using explicit methods, vast library of material models, robust contact treatment algorithms and its dominance in the adaption by automotive industry towards crash simulations **Ls-Dyna is the chosen explicit FEA code for simulation for this research.** With selection of code comes the need for understanding of the interlying complex domain of continuum mechanics along with essential formulations for explicit dynamic finite element analysis incorporating geometric, material and boundary non-linearities which are discussed to an elaborate level in the next chapter.

CHAPTER 5

5.0 Structural Nonlinearity and Finite Element Analysis

Linear static analysis is the most commonly used type of analysis in the finite element applications. The term 'linear' means that the calculated response (either displacement or stress) is linearly related to the applied load. The finite element equilibrium equations for the linear and nonlinear analyses are given below.

$$[K]\{d\} = \{f\} \quad \ldots (5.1)$$

where {d} is the displacement matrix and {f} is the force matrix. The stiffness matrix [K] is defined as:

$$[K]=\int_V B]^T[D][B]\, dV \quad \ldots (5.2)$$

$$\{\varepsilon\} = [B]\{d\} \quad \ldots (5.3)$$

$$\{\sigma\} = [D]\{\varepsilon\} \quad \ldots (5.4)$$

where [B] is the strain-displacement matrix and [D] is the constitutive matrix that relates the stresses and strains. For the linear analysis with infinitesimal displacements and strains the strain-displacement matrix [B] is assumed to be linear. For the linear elastic materials, the constitutive matrix [D] is linear. Hence this leads the stiffness matrix [K] to be linear.

The above discussion of the linear analysis suggests the meaning for nonlinear analysis. If either the strain-displacement matrix [B] or the constitutive matrix [D] is nonlinear, the resulting stiffness matrix is nonlinear. Changes in boundary condition during the course of application of load also introduce nonlinear behaviour in structures.

Based on the type of nonlinear effect, the nonlinear analyses are classified as Crisfield MA, Kleiber M [13, 14]:

1. Geometric nonlinear analysis
2. Material nonlinear analysis
3. Boundary nonlinear analysis

5.1 Geometric Nonlinear Analysis

When a structure undergoes large displacement, its stiffness changes significantly during the loading process and the assumption of linear strain-displacement relation is no longer valid. In such situations higher order terms in the strain equations should be considered. This type of nonlinearity arising due to the changes in geometry is called geometric nonlinearity. As an example, in plate bending problems if the maximum displacement exceeds 10 to 20% of plate thickness, geometric nonlinear effects become significant. An important feature that a structural problem can have geometrical nonlinearity is that the unknown equations of equilibrium with respect to deformed geometry must be written, in advance. The large displacement problem may be associated with small strain or large strain and the stress-strain relation may be either linear or nonlinear. The effect of follower force is another related feature of geometric nonlinear analysis. In a small displacement analysis, initial orientation is always maintained by the force, but in the case of large displacements, the follower force changes its orientation as the structure deforms and the applied force depends on deformation.

5.2 Material nonlinear analysis

Most metals at the low strain rates have a fairly linear stress-strain relation, but at higher strains the material yields at which point the stress-strain relation becomes nonlinear. Materials like rubber exhibit the nonlinear behaviour even for the low strain values. This type of nonlinearity arising due to the nonlinear effects in the constitutive equations is called material nonlinearity. This may be associated with time-independent or time-dependent (creep) phenomena and the strain-displacement relation may be either linear or nonlinear. For the material nonlinear analysis, the current state of deformation and the past history of deformation is needed to evaluate the response for the additional loads and it is very important to select proper material data (stress-strain relation and type of strain hardening) to simulate the actual problem.

5.3 Boundary Nonlinearity

Another common form of nonlinearity is boundary nonlinearity. This occurs if the boundary condition changes during the analysis. Typical case is of contact problems where in portions of structure can interact with each other either by sliding or slipping. Boundary nonlinearity is extremely discontinuous and when contact occurs during a simulation, there is a

large and instantaneous change in the response of the structure. The analysis of this interaction should be able to detect when the contact is happening and the constraints are applied accordingly. Similarly, the analysis must be able remove the contact constraints when it detects the separation of the two surfaces. In contact analysis, a force normal to the contacting surface acts on the two bodies when they touch each other and if there is a friction between the surfaces, shear forces may be created that resists the sliding of the bodies.

5.4 Kinematics of Deformation

Description of motion

Motion is a single parameter series of positions occupied by particles moving in space. It is described by displacement of particles w.r.t a reference or base state in which a particle P is labelled P0. Motion is kinematically admissible if:

1. Continuity of particles is preserved so that no gap or void occurs.
2. Kinematic constraints on motion are preserved. Eulerian (Spatial description)

The reference co-ordinate frame remains fixed in space and the motion of the boundary of the deformable solid is described w.r.t this frame. Hence it is computationally difficult to trace the moving boundary undergoing large displacement.

Lagrangian(Material description)

Reference frame is attached with material to follow the motion of material particles. Suitable for tracing the boundary motion of solids and structures.

Deformation gradient

$$\left[{}^{t}_{0}\mathrm{X} \right] = \frac{\partial^{t} X_i}{\partial^{0} X_j} \qquad \text{.....(5.6)}$$

- The term in left hand side represents the change in deformation from configuration at time 0 (undeformed) to configuration at time t.

Definition of stress measures

Second –Piola Kirchoff stress

Components of forces in deformed configuration at time t and acting on area on configuration at time zero.

It is represented by ${}^{t}_{0}S_{ij}$

Cauchy stress

Components of forces in deformed configuration at time t and acting on deformed area at time t. It is represented by ${}^{t}\sigma_{ij}$. Graphical representation of relation between Cauchy and Second Piola

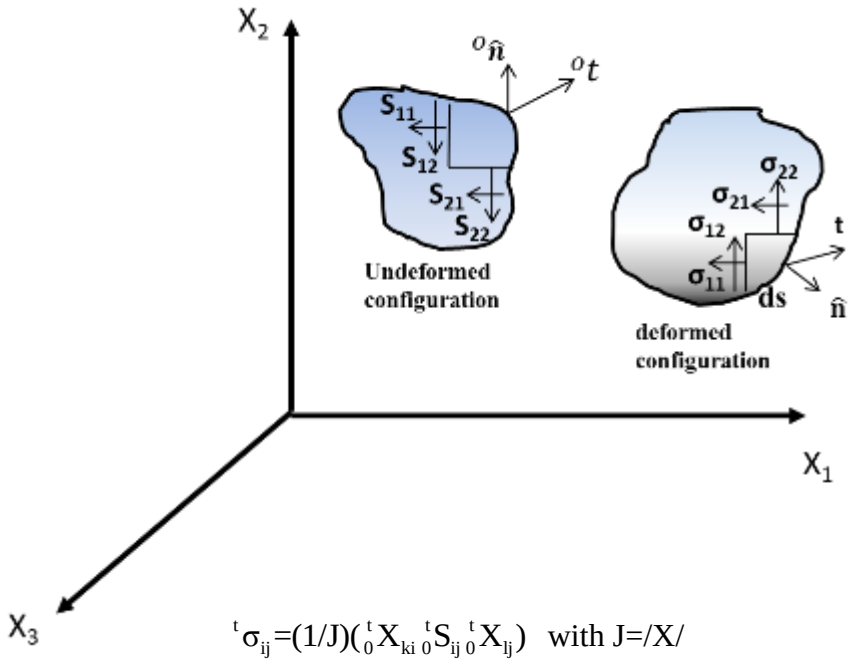

$${}^{t}\sigma_{ij}=(1/J)({}^{t}_{0}X_{ki}\,{}^{t}_{0}S_{ij}\,{}^{t}_{0}X_{lj}) \quad \text{with } J=/X/$$

Fig. 5.1 Graphical representation of relation between Cauchy and Second Piola

Physically Piola Kirchoff stress is Cauchy stress pulled back to the undeformed configuration and referred to area elements there.

Definition of Strain measures

Green-Lagrangian strain: ${}^{t}_{0}\varepsilon_{ij}=0.5([{}^{t}_{0}X]^{T}[{}^{t}_{0}X]^{-I})$ …(5.7)

Almansi Strain= $A_i= 0.5(L^2 - L_0^2) / L$ …(5.8)

Log strain or Hencky strain or True strain: $\varepsilon_L = \ln(L/L_0)$ ...(5.9)

5.5.0 Formulation of the problems

Similar to linear problems the principle of virtual work is used to establish the equilibrium equation for the solids.

$$\delta W = {}_V\sigma_{ij}\,\delta\varepsilon_{ij}\,dV \qquad ...(5.10)$$

The basic problem is to evaluate the quantities in above equation in current configuration which is not known a priori. Hence the large displacements and large strain problems need to be solved incrementally starting from a known configuration. This also includes the history dependence nature of the problems. So Lagrangian formulations are suitable.

5.5.1Total Lagrangian formulation (TL)

The kinematic variables at current configuration are measured w.r.t the undeformed configuration Crisfield MA, Kleiber M [13,14].

Virtual Work equation is written in current configuration.

$$\text{So } \delta W = V_0{}^{t+\Delta t}S_{ij}\,\delta_0{}^{t+\Delta t}\varepsilon_{ij}(dV_0) = V_0{}^0 f_i(\delta_0{}^{t+\Delta t}U_i)dV_0 + V_0{}^0 P_i(\delta_0{}^{t+\Delta t}U_i)dS_0 \qquad ...(5.11)$$

p and *f* are traction and body forces acting on undeformed configuration. The above equation is non- linear.
By incrementally decomposing the quantities, the above Virtual Work equation is linearized as:

$${}^{t+\Delta t}_{0}S_{ij} = {}_0{}^{t}S_{ij} + \Delta S_{ij} \qquad .... (5.12)$$

$${}^{t+\Delta t}_{0}U_{ij} = {}_0{}^{t}U_{ij} + \Delta U_{ij} \qquad ...(5.13)$$

$${}^{t+\Delta t}_{0}\varepsilon_{ij} = 0.5(\overline{U}_{i,j} + \overline{U}_{j,i} + \overline{U}_{k,i}\,\overline{U}_{k,j}),\ i=1,3 \text{ and } j=1,3 \qquad ...(5.14)$$

$${}^{t+\Delta t}_{0}\varepsilon_{ij} = {}_0{}^{t}\varepsilon_{ij} + \Delta\varepsilon_{ij} \qquad ...(5.15)$$

$$\overline{U} = {}^{t+\Delta t}_{0}U \qquad ...(5.16)$$

By substituting the above quantities in Virtual Work equation, basic continuum mechanics equation is obtained. This means, Virtual Work = $f(\Delta u, \delta u)$

Linear stiffness matrix

$$[K_L] = [B_L]^T\,[{}_0C][B_L] \qquad ...(5.17)$$

and $[{}_0C]$ is the constitutive matrix evaluated at undeformed configuration

F.E Discretization of the Virtual Work equation

$$\{\varepsilon\} = [B_L + 0.5B_{NL}]\{U\} \qquad ...(5.18)$$

$$d_i = \partial N_i / \partial x_i \qquad . . .(5.19)$$

$$[B_L] = f(\partial N_i / \partial x_i) \quad ...(5.20)$$

$$[B_{NL}] = f[U_i^k, f(d_i, d_i^2, d_i d_j)] \quad ...(5.21)$$

Large displacement stiffness matrix

$$[K_{LD}] = {}_{v_0}\{[B_L]^T [{}_0C][B_{NL}] + [B_{NL}]^T [{}_0C][B_{NL}] + [B_{NL}]^T [{}_0C][B_L]\}dV_0 \quad ...(5.22)$$

Geometric stiffness matrix

$$[K_\sigma] = [G]^T [S][G]dV_0 \quad ...(5.23)$$

$${}_{v_0}[G] = f(\partial N_i / \partial x_i) \quad ...(5.24)$$

Tangent stiffens matrix

$$[K_T] = [K_L] + [K_{LD}] + [K_\sigma] \quad ...(5.25)$$

Internal load vector

$$\{f_i\} = V_0 [B]^T \{{}^{t+\Delta t}_0 S_{ij}\} dV_0 \quad ...(5.26)$$

5.6 Updated Lagrangian formulation (UL)

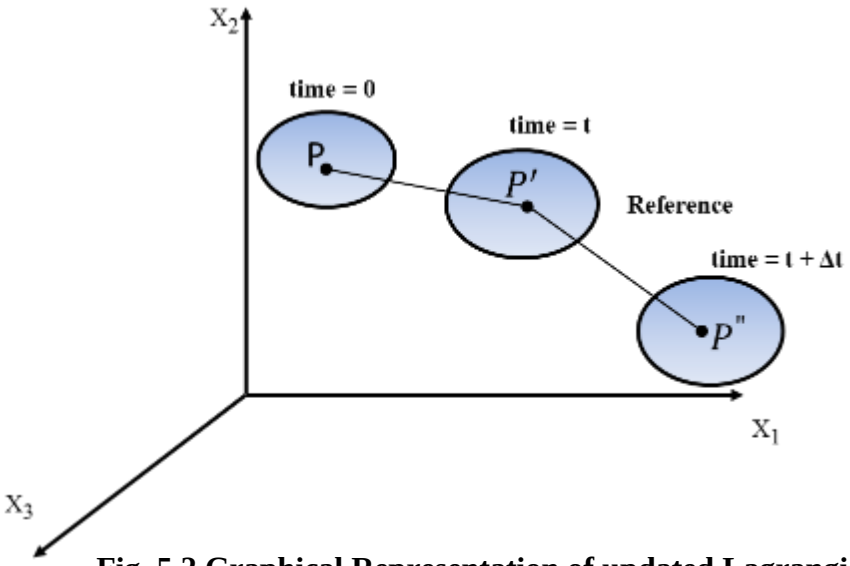

Fig. 5.2 Graphical Representation of updated Lagrangian

The last equilibrium configuration is taken as reference configuration for stress, strain to be measured. This reference is updated at the end of the time increment.

$${}^{t+\Delta t}_{t}S_{ij} = {}^{t}_{t}S_{ij} + \Delta S_{ij} \quad ... (5.27)$$

$$ {}^{t+\Delta t}_{t}\varepsilon_{ij} = {}^{t}_{t}\varepsilon_{ij} + \Delta\varepsilon \quad \ldots (5.28)$$

$$ [K_L] = {}_V[B_L]^T [{}_t C][B_L] dV \quad \ldots(5.29)$$

$$ {}^{t+\Delta t}_{t}\varepsilon_{ij} = {}^{t}_{t}\varepsilon_{ij} + \Delta\varepsilon_{ij} \quad \ldots(5.30)$$

$$ {}^{t}_{t}\varepsilon_{ij} = 1/2(U_{i,j} + U_{j,i} + U_{k,i} + U_{k,j}) \quad \ldots(5.31)$$

$$ [K_\sigma] = {}_V [G]^T [\sigma][G] dV \quad \ldots(5.32)$$

$$ [K_T] = [K_L] + [K_\sigma] \quad \ldots(5.33)$$

For evaluating internal load vector, same equation that used for TL formulation is used. But S is replaced by Cauchy stress, σ_{ij}

Observation

In UL formulation the large displacement matrix need not be calculated. Hence it is simpler and elegant to use for large displacement and large rotation problems with small or large strain with marginal cost of updating the reference frame.

5.7 Detailed Analysis of Geometric Nonlinearity

Stiffness of structures depends on its geometry and material. For small displacements, the changes in geometry are small and the linear analysis is adequate to predict the displacement. However for the large displacement problems, changes in geometry alter the stiffness of the structure significantly and for accurate determination of displacement, the effect of geometric nonlinearities should be taken into account in analysis. In the case of plate bending problem, stress due to membrane action is normally neglected in linear analysis. However, when the plate undergoes large bending deformation, the membrane tensile stress induced in the plate stiffens it and produces less bending deformation. This stiffening action in plate due to large displacement effect is shown in Figure-5.3. An exactly opposite effect can also be observed for some cases where in the stiffness of the structure decrease with the increase in load. Figure-5.4 shows the example of softening action due to effect of large displacement. The compressive stress induced in the cylindrical shell due to pressure reduces the stiffness of the structure and at high pressure load this reduction is significant and geometric nonlinear analysis will predict more displacement for the same load compared to that of linear analysis.

Several topics related to geometric nonlinear analysis are discussed in this chapter. The terminology associated with the load-deflection curves and some important locations in the load deflection curves are discussed. The finite element formulations for total and updated lagrangian concepts of geometric nonlinear problem are explained. The procedure for evaluating the large displacement and geometric stiffness matrices are explained for a simple 2D-truss element. The concept of linear and nonlinear stability analysis and the procedure for evaluating the buckling load are discussed. The role of imperfection in the pre and post buckling range is also covered in this chapter.

5.7.1 Load Deflection Curves

The overall nonlinear behaviour of many structures can be characterized by a load - deflection curve. A typical load-deflection (f–d) curve is shown in Figure-5.5. The terminology associated with the f–d curves are discussed below:

Equilibrium path

A smooth curve in the f–d chart is called a path and if this path represents a static equilibrium configuration it is called an equilibrium path. Each point in equilibrium path is equilibrium point.

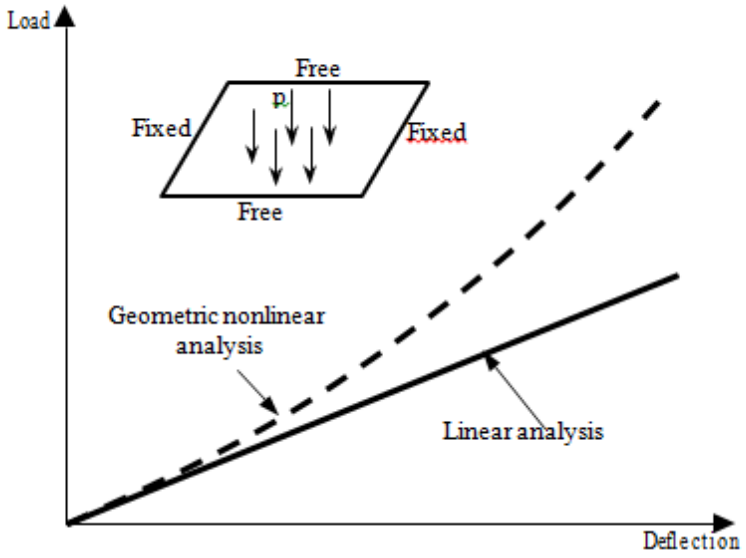

Fig. 5.3 Central deflection of clamped square plate under uniform pressure (Stiffening behaviour)

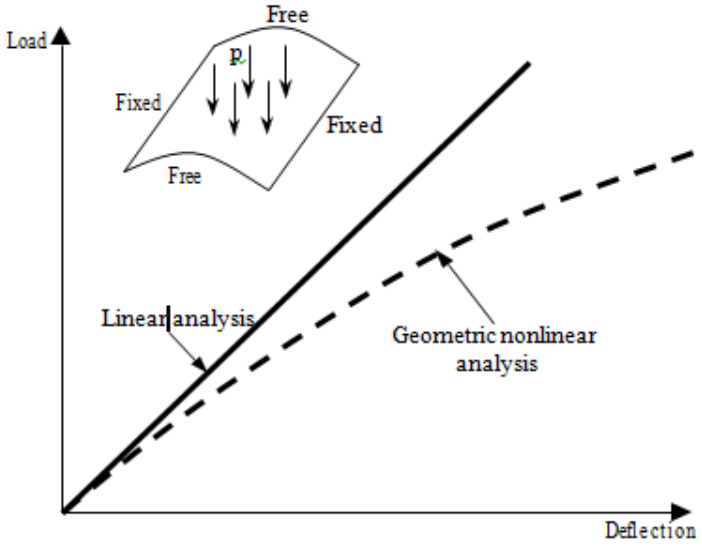

Fig. 5.4 Central deflection of cylindrical shell under uniform pressure (Softening behaviour)

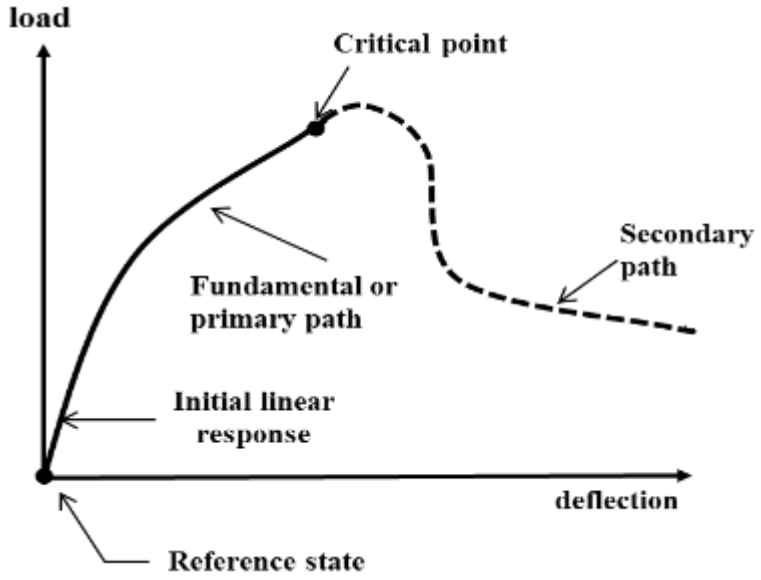

Fig. 5.5 Primary and secondary equilibrium paths

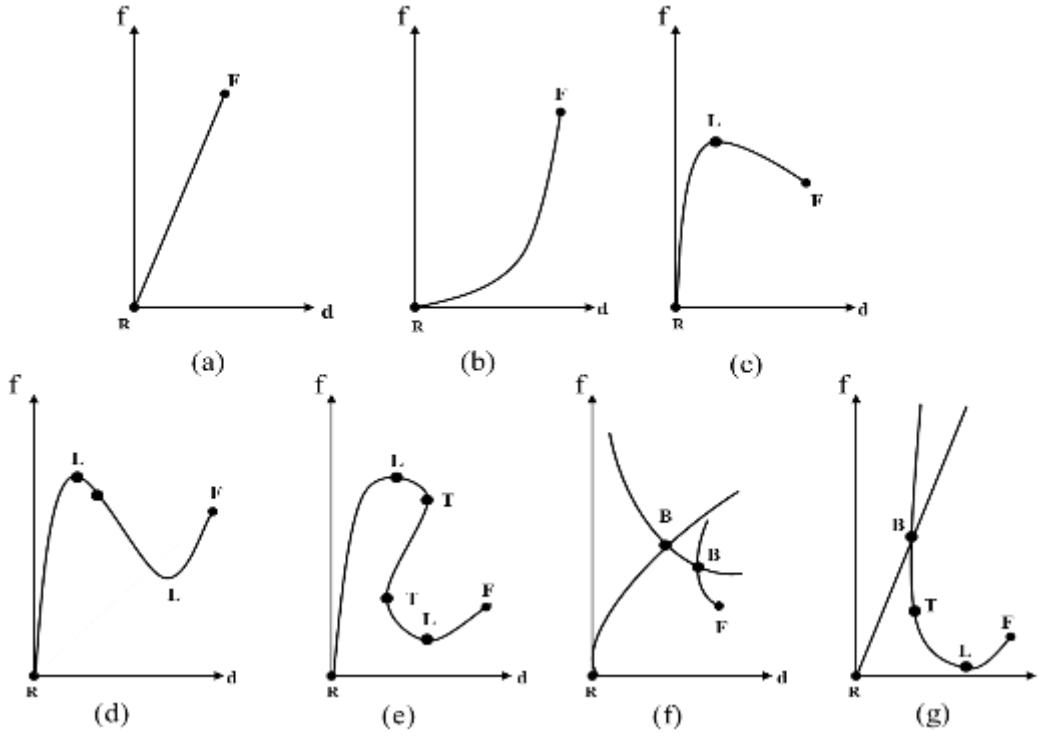

Fig. 5.6 Different types of load-deflection (f-d) curves

Reference state

The reference state is the origin of the f–d curve as it is the state from which the loads and deflection starts and also measured.

Primary and secondary path

The path that originates from the reference state is termed as the primary or fundamental path. It continues from the reference state until a state called critical point is

reached. The paths that are not primary but links with it at a critical point is called secondary path.

Various types of f-d curves are shown in Figure.5.6. Some important locations in these curves are discussed below.

Critical Point

The critical point is a location in equilibrium path at which the structure becomes physically uncontrollable or marginally controllable. The relation between the load and deflection is not unique at critical points. Two types of critical points are discussed here:

- Parallel to defection axis and at the location which is tangential to the to the equilibrium path horizontally is called the Limit point (L)
- The crossing point of two or more equilibrium paths is called the Bifurcation point (B)

Turning Point (T)

Parallel to the load axis and at the location which is tangential to the equilibrium path vertically is called as turning points. As such points have potential to affect the performance of certain solution methods; they are only of some computational significance and are not critical points.

Failure Points (F)

Some points at which a path suddenly stops or break due to because of physical failure are called failure points. The functional equilibrium of the structure would be regained if the failure is local in nature even after moving to another equilibrium path dynamically. On the other hand, it would be detrimental if the failure is global in nature and the functional equilibrium of the structure is never regained.

Different possible types of equilibrium paths are given in Figure.5.6. Symbols F and L denotes the failure and limit points respectively. Composites and glassy crystals exhibit linear responses as in Figure.5.6 (a). A stiffening response shown in Figure.5.6 (b) is typical of structures under tensile loadings. The stiffness effect comes from the geometry transformations in response to the applied loads. Many common structures exhibit response as in figure.5.6(c) wherein immediately after softening a linear response is followed. Curved

structures like shallow arches exhibit snap through response as shown in Figure.5.6 (d) where in after the second limit the softening response is combined with hardening behaviour. These responses are unstable and have negative stiffness's between the limit points. Typical structures like trusses, domed shaped members, exhibit snap-back responses shown in Figure.5.6 (e) where in the response curve reverses back in itself with resurfacing of turning points. The state between the two turning points may be in equilibrium and stable which can be of physical possibility.

In all the responses discussed so far, the response behaviour itself is unique in nature. In Figure.5.6 (f) and (g), interesting points called as bifurcation points exist which are popularly known as buckling points. These points provide more than one response path and proceeds towards a path based on least energy over the others. Typically thin structures under compressive loads exhibit such bifurcation points. Many combinations of bifurcation and turning points may occur under compressive load as shown in Figure.5.6 (g). Thin cylindrical shells under axial compression exhibit such a complicate response.

5.8 Finite element formulation

Whether the displacement (or strain) is small or large, it is an inherent requirement that the conditions of equilibrium between internal and external forces have to be met. If the displacements are defined in the usual manner by 'a', the equilibrium condition can be obtained using virtual work principle Crisfield MA, Bathe and Cook [8, 12, 13]. However different definition of stresses and strains which are conjugate to each other must be used in the formulation. For example in the Total Lagrangian formulation the measures of Second – Piola Kirchhoff stress and Green strain are considered and for the Updated Lagrangian formulation the measures of Cauchy stress and Almansi strain (for large displacement – small strain problems) or logarithmic strain (for large displacement – large strain problems) are considered. In all cases we can write,

$$\prod(a) = \int_V \bar{B}^T \sigma dV - f = 0 \qquad \text{... (5.34)}$$

where Π(a) represents the sum of external and internal forces and $\overline{B}$ is the strain-displacement matrix and defined as:

$$d\varepsilon = \overline{B} da = (B_L + B_{NL}) da \qquad \text{... (5.35)}$$

Here B_L is the same matrix used in linear infinitesimal strain analysis and B_{NL} is the nonlinear strain – displacement relation.

Taking the variation of equation (5.34) with respect to 'da', we have:

$$d\prod = \int_V d\bar{B}^T \sigma dV + \int_V \bar{B}^T d\sigma dV = K_T\, da \quad \text{....(5.36)}$$

The stress – strain relation is defined as:

$$d\sigma = D d\varepsilon \quad \text{…(5.37)}$$

where D is the constitutive matrix which is constant for linear elastic materials.

$$d\sigma = D\bar{B}da \quad \text{…(5.38)}$$

$$d\bar{B} = dB_{NL} \quad \text{...(5.39)}$$

From equation (5.36), (5.37) and (5.38), we can write

$$d\prod = \int_V dB_{NL}^T \sigma\, dV + \bar{K} da \quad \text{...(5.40)}$$

where $\bar{K} = \int_V \bar{B}^T D \bar{B} dV = K_L + K_{NL}$ …(5.41)

K_L represents the conventional small displacement linear stiffness matrix,

$$K_L = \int_V B_L^T D B_L dV \quad \text{...(5.42)}$$

The matrix K_{NL} is due to the large displacement effect and is given by,

$$K_{NL} = \int_V \left[B_L^T D B_{NL} + B_{NL}^T D B_L + B_{NL}^T D B_{NL}\right] dV \quad \text{…(5.43)}$$

K_{NL} is known as the initial displacement matrix or large displacement matrix and it contains the terms which are linear and quadratic in 'a'. This matrix is calculated only for the Total Lagrangian formulation and in the case of Updated Lagrangian formulation this effect is obtained by updating the nodal coordinates in the computation of the stiffness matrix.

The first term in the right hand side of equation (5.36) can be generally written as:

$$d\bar{B}^T \sigma\, dV = K_\sigma da \quad \text{... (5.44)}$$

K_σ is known as the initial stress matrix or geometric stiffness matrix and it is a symmetric matrix that depends on the stress levels.

The equation (5.36) can be written as:

$$d\prod = (K_L + K_{NL} + K_\sigma) da = K_T\, da \quad \text{... (5.45)}$$

where K_T is the total tangential stiffness matrix.

5.9 Buckling Analysis

The displacement (or stress) response in any structure for a given loading is evaluated by establishing and solving the equilibrium between the internal and external forces. In some situations it is very important to find whether the equilibrium of the structure under the given loading is stable or not. A structure is said to be in stable equilibrium if it returns to the original configuration upon being subjected to a small disturbance. On the other hand if the structure undergoes an uncontrollable amount of deformation leading to its collapse upon being subjected to a small disturbance, its equilibrium is said to be

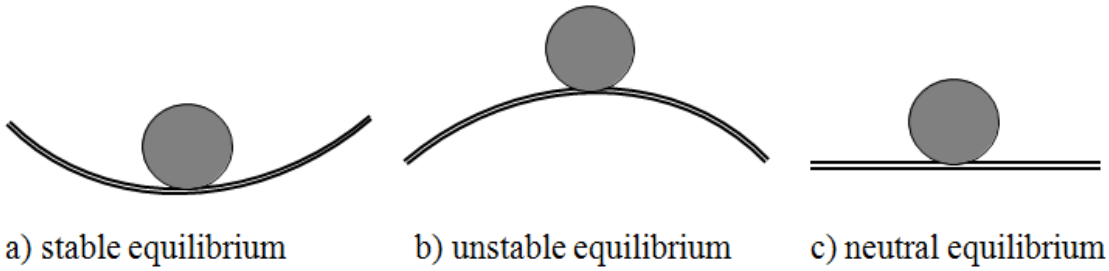

Fig. 5.7 Three types of equilibrium configurations

unstable. Upon a small disturbance, if the structure moves from equilibrium to an adjacent position it is said to be in neutral equilibrium. These three types of equilibrium configuration are shown in Figure-5.7.

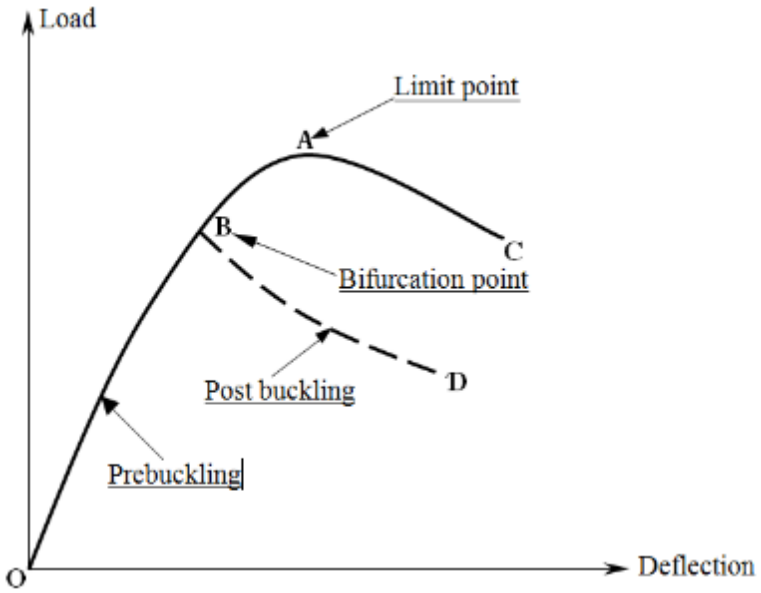

Fig. 5.8 Load-Deflection curve of cylinder under external pressure

The point at which the structure loses the stability is identified by a bifurcation point in load – deflection curves. At this point the structure undergoes large deformation, which is different from the small deformation behaviour prior to bifurcation. This phenomenon is termed as 'bucking'. The load – deflection curve of cylinder under external pressure is shown in Figure-5.8. The equilibrium path OAC corresponds to the axisymmetric deformation of cylinder. Upon reaching the bifurcation point the structure prefers the non-axisymmetric deformation path BD instead of the path BAC. It can be observed that the load at bifurcation point is less than the load at the limit point and hence the cylinder undergoes buckling deformation before the collapse. The paths OB and BD are defined as pre and post buckling paths and the onset of buckling occurs at the intersection bifurcation point B. The different buckling behaviours of various structures are shown in Fig. 8. While the plate structures exhibits the stable post buckling behaviour, the shell structures in general exhibit unstable post buckling behaviour. Neutral post buckling path is normally seen in beam buckling Criesfield MA [13].

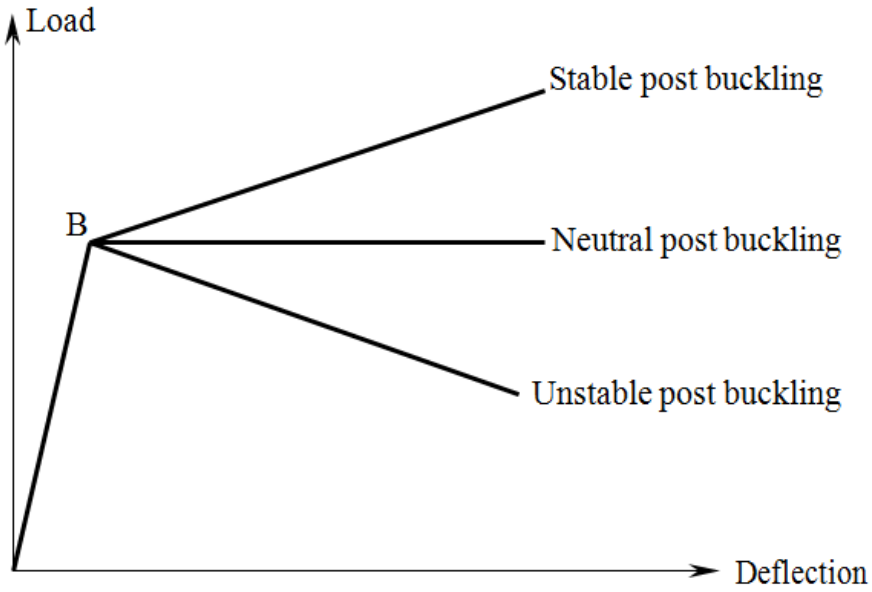

Fig. 5.9 Different post buckling phenomena

It is important to understand why the structures lose stability at some particular load. Generally, structures can carry a great deal of strain energy during the membrane deformation. This means that, the structures undergo very small membrane deformation for carrying a particular amount of strain energy and it has to undergo very large bending deformation to carry the same amount of strain energy. If the structure undergoes the membrane deformation, its stiffness decreases with the increase in membrane compressive

load. At one stage, the stiffness reduces to such an extent that it can no longer be able to carry strain energy for membrane deformation and it suddenly undergoes a large bending deformation. At this point, bifurcation occurs and the membrane strain energy is converted in to bending strain energy. Different approaches are used to predict the linear and nonlinear buckling loads of structures. They are discussed in the following paragraphs.

5.10 Linear Buckling

Consider a structure that is subjected to a reference level of loading $\{f\}_{ref}$. By carrying out a standard linear static analysis, we can obtain membrane stress distribution in the structure. From this stress distribution we can calculate the geometric stiffness (initial stress) matrix $[K_\sigma]_{ref}$ as per equation (5.44). For another load level $\{f\}=\lambda\{f\}_{ref}$, where λ is a scalar parameter, the geometric stiffness matrix $[K_\sigma]$ is calculated as $[K_\sigma] = \lambda[K_\sigma]_{ref}$. This implies that multiplying all loads in $\{f\}_{ref}$ by λ also multiplies the intensity of stress field by λ without changing the distribution of stresses. For the load $\lambda\{f\}_{ref}$, the equilibrium equation is written as:

$$[[K_L]+\lambda[K_\sigma]_{ref}]\{a\}=\lambda\{f\}_{ref} \quad ...(5.46)$$

It is to be noted that the effect of large displacement is not yet accounted in the above equation. If we increase the displacement vector {a} by infinitesimal displacement {da} without any increase in the force, the equation (5.46) can be rewritten as:

$$[[K_L]+\lambda[K_\sigma]_{ref}]\{a+da\}=\lambda\{f\}_{ref} \quad ...(5.47)$$

Subtracting equation (5.46) from (5.47) will give:

$$[[K_L]+\lambda[K_\sigma]_{ref}]\{da\}=\lambda\{f\}_{ref} \quad ...(5.48)$$

The equation (5.48) defines an Eigen value problem whose lowest Eigen value λ_{cr} is termed as buckling load factor and the buckling load is given as:

$$\{f\}_{cr}=\lambda_{cr}\{f\}_{ref} \quad ...(5.49)$$

The Eigen vector {da} associated with λ_{cr} defines the buckling mode. The magnitude of {da} is indeterminate and it identifies buckling mode shape but not amplitude. The terms in

parenthesis of equation (5.48) comprise a total or net stiffness matrix $[K_T]$ and since the forces $[K_T]\{da\}$ are zero, we can say that membrane stresses at bifurcation point reduce the stiffness of the structure to zero with respect to buckling mode $\{da\}$.

Various computational methods are available for determining λ_{cr}. Eigen values methods used to compute natural frequencies and modes of vibration can also be applied to buckling problems. In most of the practical situation it is required to calculate only the minimum value of λ_{cr} and in such cases it is unnecessary and wasteful to use a method that automatically extracts several Eigen values. However, at times it is required to know the several lowest Eigen values and their associated buckling modes in order to get insight into ways of stiffening or supporting the structure so as to make buckling less likely.

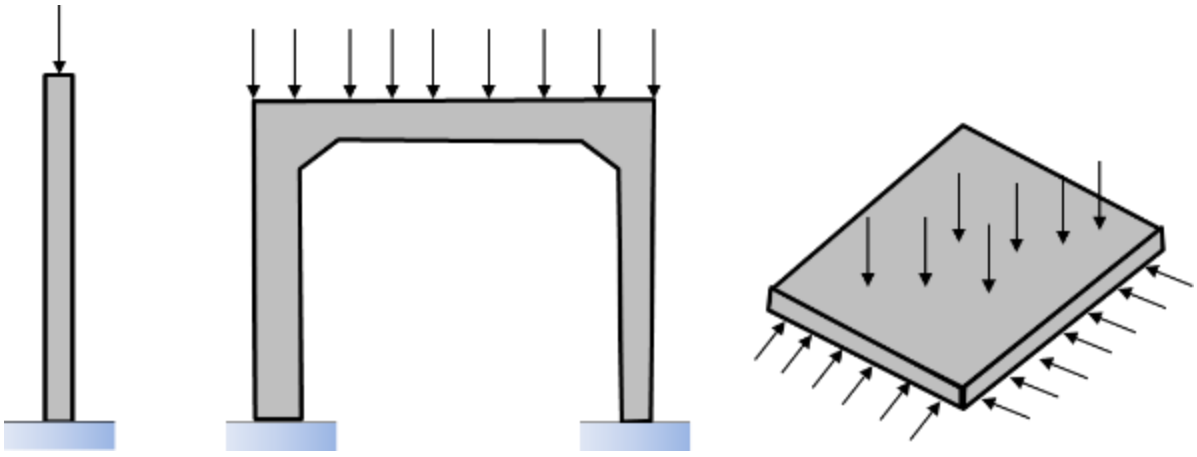

Fig. 5.10 Structures that are adequately modeled by linear buckling

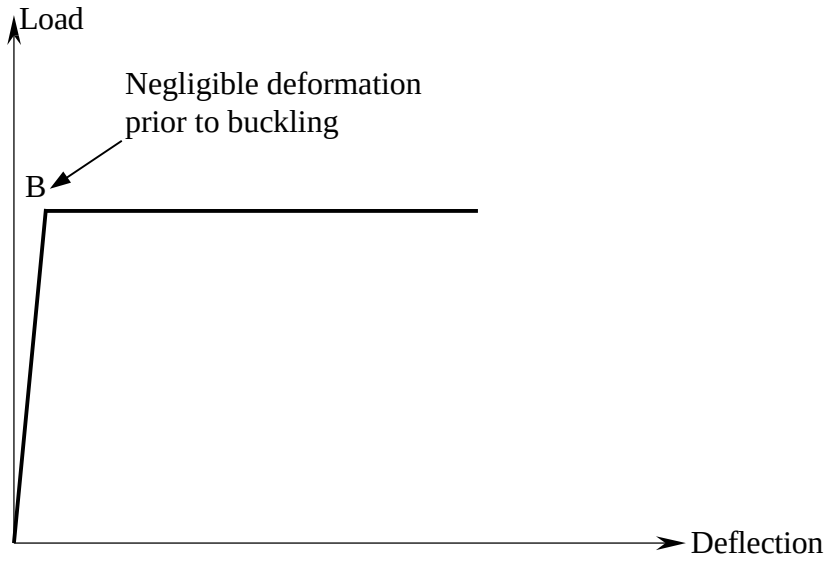

Fig. 5.11 Typical response for linear buckling

Linear buckling analysis is used extensively in engineering design and most of the general purpose finite element programs have the capability for solving linear buckling problems. Symmetrically loaded structures such as plates loaded in-plane and straight columns which are not slender represent as good examples for linear buckling. Figure-5.10 shows some examples for which linear buckling predictions are adequate. The post buckling of these structures occurs following very small pre-buckling deformations as shown in Figure-5.11. However, linear buckling analysis should not be used for the cases where it is not applicable. The limitations of linear buckling analysis are:

1. Pre-buckling displacements must be small.
2. Elastic material behaviour.
3. Negligible effect of imperfections.
4. Loads independent of displacement.

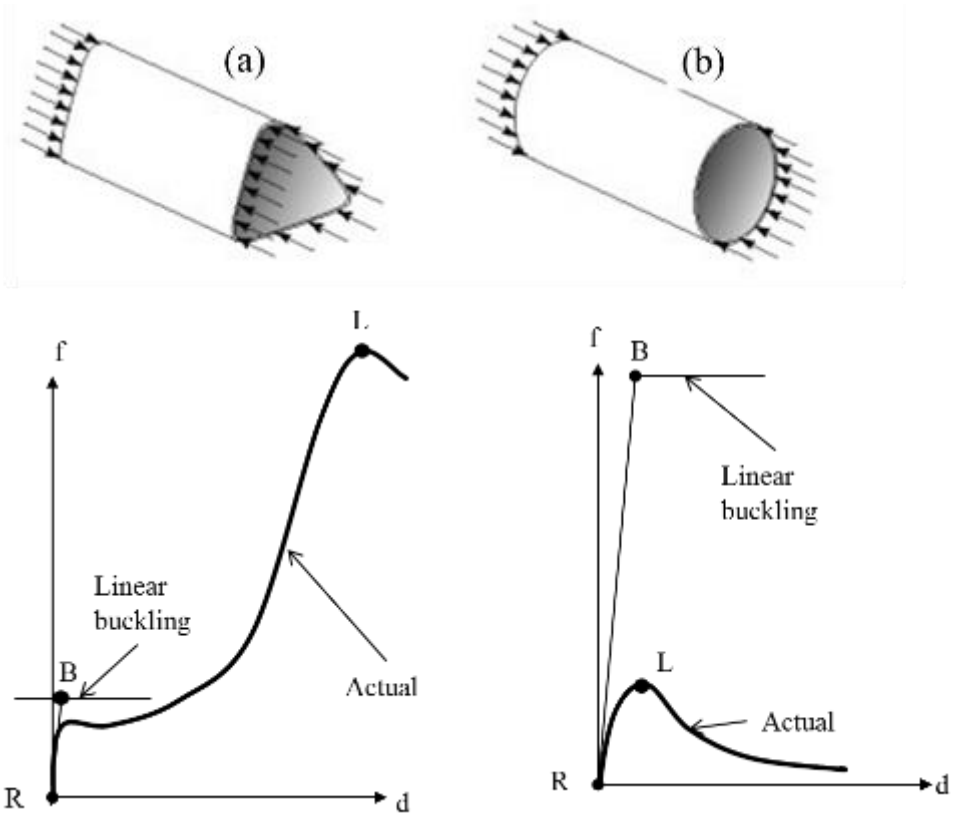

Fig. 5.12 Examples where linear buckling is not applicable

Figure-5.12 depicts tow cases where in the linear analysis of buckling fail to characterise the responses. Case (a), represents an axially loaded prismatic cylindrical shell with triangular section as seen in some in fuselages of helicopters and space vehicles. The response curve depicts adaption of geometry to the compressive load and redistribution of stresses accordingly. When the limit point is reached the structure eventually collapses at a load substantially higher than the predicted linear buckling load. Case (b) represents axially compressed circular cylindrical shell which is sensitive to the imperfections and tends to fail at a lower load than that estimated by linear buckling analysis. In such cases it is required to evaluate the buckling load by a nonlinear buckling analysis.

5.11 Nonlinear Buckling Analysis

When the pre-buckling deformation involves nonlinearities resulting from large displacement, plasticity or displacement – dependent load, linear buckling analysis fails to predict the correct buckling load. In this case, bifurcation analysis is preceded by a nonlinear pre-buckling analysis. Then at any load step t, the equation (5.34) is written as:

$$[\{[K_L] + [K_{NL}]\}_t + \lambda_t [K_\sigma]_t]\{da\}_t = 0 \quad \ldots(5.50)$$

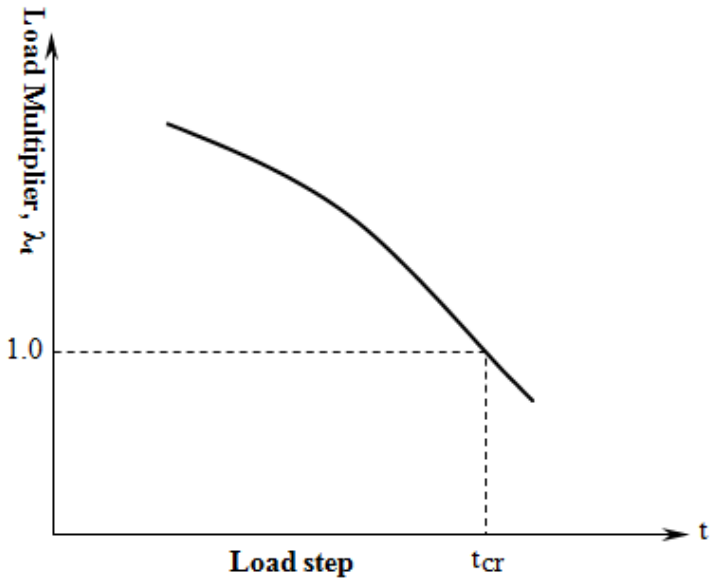

Fig. 5.13 Nonlinear buckling analysis

The suffix‘t’ in Equation-5.50 represent the matrices at the load step ‘t’. The matrix $[K_{NL}]$ in this case includes the effect of all nonlinearities. The Equation-5.50 once again represent an eigen value problem and now the Eigen value analysis is to be repeated for several load steps and the load step t_{cr} at which $\Delta t = 1$ is considered as the nonlinear buckling load. This is shown in the Figure-5.13. The Eigen vector $\{a\}_t$ at $\Delta t = 1$ represents the nonlinear critical buckling mode.

5.11.1 Effect of Imperfections

Geometric imperfection resulting from the fabrication tolerances can significantly reduce the buckling strength of structures. The amount of reduction depends on the geometric shape and type of loading. Very thin structures are more imperfection sensitive compared to thick structures. The reduction in buckling load is around 80% for an axially compressed thin cylindrical shell when the imperfection is of the order of shell thickness. For the same imperfection, the buckling load of cylindrical shell reduces by nearly 20% when it is subjected to external pressure. Hence the effect of geometric imperfection should be properly taken into account in the analysis.

5.12 General approach to buckling analysis

The approach to be followed for the buckling analysis depends on various aspects such as the geometry, loading and material. The following points provide some direction towards approaching a solution to the buckling problem based on the category of loading Crisfield, Kleiber [13,14].

1. Evaluate the linear elastic buckling load λ_E of the structure from the bifurcation analysis.
2. Find out the load λ_y at which the maximum stress in the structure reaches the yield stress. This can be found from the results of linear static analysis.
3. Evaluate the ratio (λ_E/λ_y).
4. If the ratio $(\lambda_E/\lambda_y) < 0.2$, the buckling is in the elastic range. The effect of imperfection should be included in the analysis. The effect of geometric nonlinear effect should be included in the analysis, if the prebuckling deformation is more.
5. If the ratio $(\lambda_E/\lambda_y) > 0.2$ and $(\lambda_E/\lambda_y) < 5.0$, the buckling occurs in the elastic - plastic range and effect of imperfections should be considered in the nonlinear analysis.
6. If the ratio $(\lambda_E/\lambda_y) > 5.0$, the structure undergoes plastic buckling and imperfections has less influence on buckling.
7. If the ratio $(\lambda_E/\lambda_t) > 20.0$, the structure is considered to be very rigid and failure occurs mainly by plastic collapse instead of buckling. The imperfections effects need not be considered in the evaluation of collapse load.

5.13 Material non-linear analysis

Material non-linearity could be various types viz. Nonlinear elastic, Hyperelastic, Elastic- Perfectly Plastic, Time independent Plastic, Time dependent plastic(creep), Visco-elastic, Visco- plastic, Temperature dependent elasticity, Temperature dependent plasticity.

Non-linear elastic

Stress strain relation is nonlinear with small strain (order of 20%) within elastic limit.

Loading and unloading occurs along same path.

Hyperelastic

Stress strain relation is nonlinear with large strain. Used for elastomers.

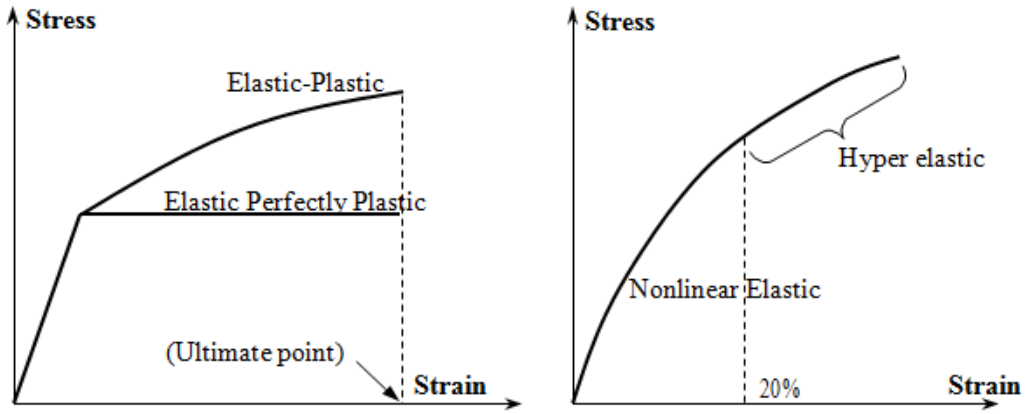

Fig. 5.14 Some stress-strain behaviours

Time independent plastic

The stress strain relation is nonlinear after material point stress exceeds yield value. Plastic strain grows with increasing stress.

Time dependent plastic

Creep phenomenon that occurs under high temperature, leads to increasing plastic strain at constant stress. Plastic strain is function of time and stress.

This note will deal extensively with elasto-plasticity.

Elasto-plasticity deals with elasto-plastic behaviour of materials undergoing small and large strains where stress at any point crosses the yield limit.

This analysis primarily consists of computing the elasto-plastic constitutive matrix, [$_t$ D] used to compute tangent stiffness matrix, [K_T]. The incremental stress-stress relation is calculated from the equation $\{\Delta\sigma\} = [{}_t d]\{\Delta\varepsilon\}$. The currently used analysis procedures are based on mathematical models obtained by some assumptions on macro deformation behaviour during post yielding response.

5.13.1 Assumptions in plasticity theory

Yield Criteria

It is an initial condition of yield defining the elastic limit of material in a multi axial state of stress. This leads to yield criteria viz. Von-Mises and Tresca., Jones, Bathe, Crisfield [7, 8, 13].

Von-Mises Yield Criteria

A point in material undergoes inelastic action if distortion strain energy per unit volume in multi- axial state of stress is more than the distortion energy developed in a bar uniaxially stressed to elastic limit.

This criteria implies > Von–Mises stress > uniaxial yield stress.

$$\text{Von-Mises Stress} = = \frac{1}{\sqrt{2}}\left\{(\sigma_1-\sigma_2)^2+(\sigma_2-\sigma_3)^2+(\sigma_3-\sigma_1)^2\right\}^{\frac{1}{2}} \quad ...(5.51)$$

where σ_1 , σ_2 and σ_3 are the stresses in principal direction.

Tresca Yield Criteria

Inelastic action occurs if maximum shear stress in any plane passing through the material point maximum shear stress at same point yielded under uniaxial tension.

$$\text{Tresca Stress} = \text{maximum } \{|(\sigma_1-\sigma_2)|, |(\sigma_2-\sigma_3)|, |(\sigma_3-\sigma_1)|\} \text{ yield surfaces}$$

Existences of loading surfaces define the limits of elastic and plastic after initial yield during post yielding response. The use of yield surface to model strain hardening is a mathematical idealization of some macroscopically observed behaviour.

Flow rules

Flow rules are used to describe post-yielding response. In this regard Prandtl-Reuss assumption says that the increment in plastic strain is directly proportional to deviotoric stress components.

The general concept of flow rule is $\Delta\varepsilon_{ef}^{p} = \lambda \frac{\partial \phi}{\partial \sigma_{ij}}$

where λ is defined as $\lambda = (\Delta\varepsilon_{ef}^{p} / \sigma_{eff})$ and ϕ is scalar quantity and is function of σ_{ij} . The concept of effective stress or effective plastic is used to describe post-yielding response under multi-axial state of stress.

Plastic incompressibility

Hydrostatic pressure has some influence on plastic deformation of metals, which is ignored in this assumption. Incompressibility is treated by using variable Poisson's ratio in elastic and plastic range. Poison's ration is 0.5 in plastic range.

Elastic unloading and coincidence of loading and yield surfaces implying that during loading from one plastic state to neighbouring state there is change in elastic state only. This also implies that post yielding response after unloading from a plastic state is insensitive to reverse yielding. It means no hysteresis in material is assumed.

In liner flow theory based on earlier mentioned flow rules, total kinematic strain is decomposed in to elastic and plastic strains but this is valid for small strain problems undergoing monotonic and Proportional loading. This means the ratio of various components remains constant throughout the loading process.

Based on the above assumptions the models to describe plastic behaviour are presented below. Further plastic behaviour is modelled by three important characteristics.

a. Flow rule

Few rules have already been discussed.

b. Yield criteria.

Von-Mises, Tresca, Drucker-Prager, Mohr-Coulumb etc.

c. Strain Hardening rule

Isotropic, Kinematic, Mixed, Mechanical sublayer model etc.

d. Integration of stress strain law and stress updates.

A vast literature is available on different schemes of integration out of which we will discuss the incremental approach using Forward Euler subincrement method which is efficient one from convergence point of view.

5.14 Hardening rules

a. Isotropic hardening

The load surface expands uniformly in stress space about the origin maintaining the shape, centre and orientation as that of the yield surface during plastic straining. This theory is not realistic in case of complex loading path involving change in direction of stress vector in stress space. Yield surface is the locus of points satisfying yield function. The hardening rule is as in Figure-5.15

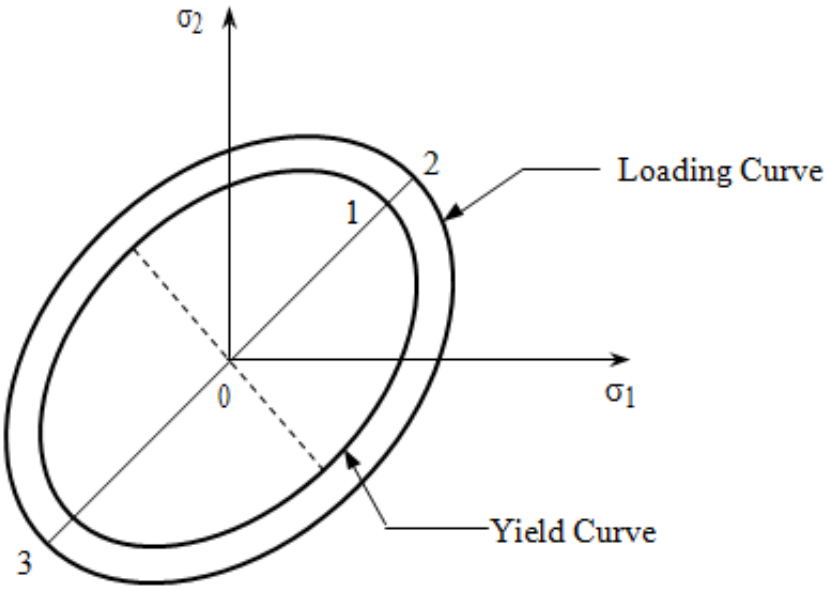

Fig. 5.15 Isotropic Hardening

b. Slip theory of hardening

Predicts corners on yield surface instead of smooth surface. Not used because of mathematically complicated constitutive matrix.

c. Kinematic hardening

This theory assumes that the loading surface moves in a rigid fashion in stress space maintaining the same size, shape and orientation of the yield surface during plastic deformation.

It accounts for Bauschinger effect implying that at material point yields at lesser stress value in one direction if it has seen prior yielding in reverse direction. The model based on this theory is suitable for cyclic work hardening and softening materials. The hardening model is as in Figure-5.16

d. Mixed hardening

The load surface moves rigidly as well as expands in stress space. In general all problems of material nonlinearity undergoing non-proportional and reversed loading need to be modeled using this theory.

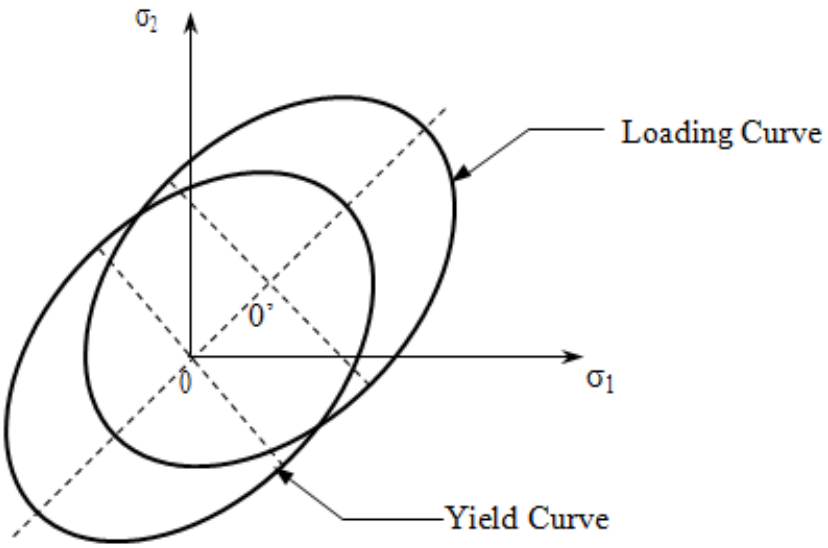

Fig. 5.16 Kinematic Hardening

5.15 Anisotropic Plasticity

All the above theories assume isotropic plasticity hence the prediction of response under large strain condition is hardly realistic. Hill's model in this regard uses the yield function, f which is a function of six yield stresses in three principal directions of anisotropy. So this model is computationally difficult to model. Hence the conventional plasticity algorithms use the isotropic models, Bathe, Crisfield, Kleiber [8, 13,14].

5.16 Computation of Standard Tangential modular (Elasto-plastic Constitutive) matrix, $[{}_t D]$

a. Von_mises Yield Criteria and Isotropic strain hardening

Using associated flow theory,

$$d\varepsilon_{ij}^{P} = d\lambda \frac{\partial f}{\partial \sigma_{ij}} \qquad \ldots (5.53)$$

where $d\lambda$ is known as plastic multiplier.

The yield function is defined as

$$f = \sigma_e - \sigma_y(\varepsilon_{ps}) = 0 \qquad \ldots (5.54)$$

and σ_e = Effective stress or Von-Mises stress

$$= \sqrt{\frac{3}{2}} \left(\{S\}^T [L] \{S\} \right)^{0.5}$$

where $\{S\} = \{ S_X, S_Y, S_Z, \tau_{xy}, \tau_{YZ}, \tau_{ZX} \}$ are deviotoric components of stresses and [L] is a 6x6 diagonal matrix, which is defined as:

$L_{ii} = 1$ for $i = 1,...3$ $L_{ii} = 2$ for $I = 4,...6$

Putting the value of Effective stress in yield function, we obtain $S = \sqrt{\frac{3}{2}}\sigma_y$ which is the radius of the cylinder representing the yield surface.

For the occurrence of the plastic flow and to keep the new state of stress on yield surface.

$$df = \frac{\partial f^T}{\partial \sigma_{ij}} d\sigma_{ij} + \frac{\partial f}{\partial \varepsilon_{ij}^p} d\varepsilon_{ij}^p = 0 \qquad \ldots (5.55)$$

Let $a = \frac{\partial f}{\partial \sigma_{ij}}$ and $A = -\frac{1}{d\lambda} \frac{\partial f}{\partial \varepsilon_{eff}^p} d\varepsilon_{eff}^p$

Then substituting a and A in eqn. (5.55), we get $a^T d\sigma - A d\lambda = 0$ … (5.56)

Linear decomposition of strain component gives,

$$d\varepsilon = d\varepsilon_e + d\varepsilon_p$$

$$= [D]^{-1} \{d\sigma\} + d\lambda \frac{\partial f}{\partial \sigma_{ij}} \qquad \ldots (5.57)$$

Putting the value of $d\lambda$ from eqn. (5.57) into eqn(5.56) we get,

$$d\lambda = \frac{1}{(A+a^T Da)} a^T D d\varepsilon \quad \ldots (5.58)$$

This is an important equation to be used for plastic strain computation.

$d\sigma = d\varepsilon\left[D - \frac{a^T DDa}{A + a^T Da} \right]$ Which means, tangential modular matrix or elasto-plastic constitutive matrix is $\left[{}_t D^{ep} \right] = \left[D - \frac{a^T DDa}{A + a^T Da} \right]$ … (5.59)

To calculate, A

$$A = \frac{1}{d\lambda} \frac{\partial \sigma_y}{\partial \varepsilon^p_{eff}} d\varepsilon^p_{eff} \qquad d\varepsilon^p_{ij} = d\lambda \frac{\partial f}{\partial \sigma_{ij}} = d\lambda S_{ij}$$

Effective plastic strain, $\varepsilon^p_{eff} = \sqrt{\frac{2}{3}}\left[\varepsilon^2_{px} + \varepsilon^2_{py} + \varepsilon^2_{pz} + \frac{1}{2}(\gamma^2_{xy} + \gamma^2_{yz} + \gamma^2_{xz}) \right]^{\frac{1}{2}}$ … (5.60)

Using $S_{ij} S_{ij} = \sqrt{\frac{2}{3}} \sigma_y$, we get $d\varepsilon^p_{eff} = \frac{2}{3} d\lambda \sigma_y$

Hardening modulus, $H = \frac{\partial \sigma_y}{\partial \varepsilon^p_{eff}}$, so , $A = \frac{2}{3} H \sigma_y$

b. <u>Strain Rate dependent hardening model</u>

The yield stress in yield function, f is written as, $\sigma_y = \sigma_s + H\varepsilon^p_{eff}$ … (5.61)

σ_s is the static yield strength.

where, $\dot{\varepsilon}_{eff}$ is instantaneous time rate of change of Effective strain.

$\dot{\varepsilon}_{eff} = \sqrt{\frac{2}{3}\left\{ (\dot{\varepsilon}_{ij} d)(\dot{\varepsilon}_{ij} d) \right\}}$ and the suffix 'd' is for deviotoric components

<u>Mixed hardening model</u>

Yield function, $f = \frac{1}{2}(S_{ij} - \alpha_{ij})(S_{ij} - \alpha_{ij}) - \sigma_y^2 / 3 = 0$ … (5.62)

where α_{ij} is the kinematic shift of the center of the yield surface = $(1-\beta)(2/3)\left(D^{ep} \right)\varepsilon^p_{ij}$

$$\sigma_y = \sigma_o + \beta H \varepsilon^p_{eff}$$

For β = 0 it is kinematic hardening

= 1 it is isotropic hardening.

5.17 Integration of Stress strain law and stress update

1. During solution at any iteration level, i , $\Delta U$is computed.
2. Total strain increment , $\Delta\varepsilon = B\Delta U$ is calculated
3. Aim is to calculate , $\Delta\sigma$
   i. An elastic stress increment for iteration 'i', $\Delta\sigma^e = D\Delta\varepsilon$ is calculated.
   ii. Total Stress $f(\sigma_i) = \sigma_{i-1} + \Delta\sigma^e$
   iii. If $f(\sigma_i) - \sigma_o \leq 0$ thenelastic behaviour assumptions holds. Otherwise the yield surface has been crossed during trial stress incrementation.
   iv. The contact stress $\sigma_c = \sigma_i + q\Delta\sigma$ where $0 \leq q \leq 1$ and $f(\sigma_c) - (\sigma_o) = 0$. This equation is quadratic in q. It is observed that the path from σ_i to σ_c is fully elastic.
   v. A stress state $\sigma_{ti} = \sigma_c + D(\Delta\varepsilon_i - d\lambda.a)$, $\Delta\varepsilon_i = \Delta\varepsilon / m$

where m is the no of sub steps in to which the total increment $\Delta\varepsilon$ is divided. This approach is known as Forward Euler integration with sub increment approach. If the above increment is repeated up to m steps a stress state σ_t which will have very less drift from the updated yield surface. $d\lambda$ at each sub step is evaluated using stress at previous sub step.

Vi. Updated yield stress, $\sigma_{yi} = \sigma_{yi-1} + H_{i-1}\Delta\varepsilon_{eff}^P$

$$\Delta\varepsilon_{eff}^P = \frac{2}{3} d\lambda \sigma_{yi-1}$$

Vii. Scaling of the stress $\sigma_f = \sigma_t \frac{\sigma_{yi}}{\sigma_{eff(t)}}$

Viii. Updated yield surface $= \sigma_f - \sigma_{yi} = 0$

For all the above steps refer the following Figure-5.17

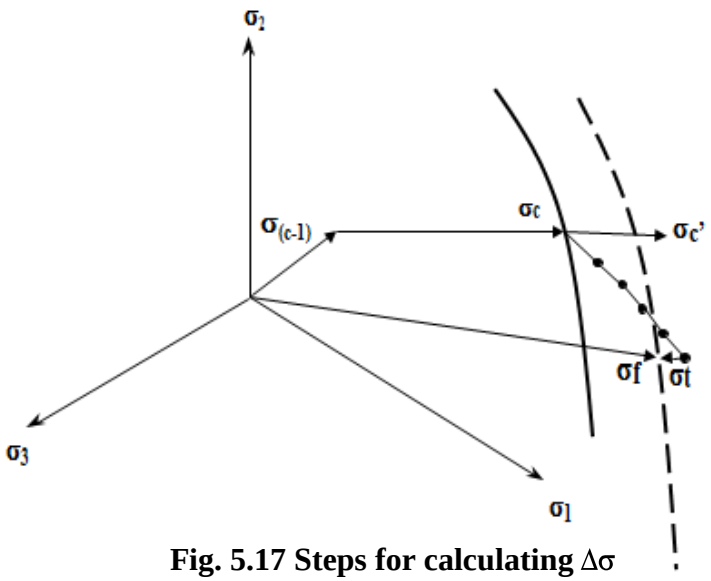

Fig. 5.17 Steps for calculating Δσ

5.17.1 Application of material non-linear analysis

1.Metal forming processes.

2.Deformation of any component under abnormal loading conditions.

3.Collapse load evaluation of structures.

4.Impact simulation of deformable bodies under fast transient events

5.18 Non-Linear Transient Analysis

Usually all high energy transient events such as high velocity impact, blast, crash cause non-linear response in structures in form of large displacement, plasticity or change of contact conditions at different interfaces. These events are of short duration and the frequency content is greater than 100 times the lowest natural frequency of the structure and hence involves the propagation of stress wave through the structure. In these types of problems the equation of motion is time integrated by direct time integration schemes such as Explicit time marching. Belytschko, Huges, Moran [9, 10].

5.18.1 Equation of motion

$$[M]\{\ddot{U}_n\}+[C]\{\dot{U}_n\}+[K]\{U_n\}=\{F_n^{ext}\} \quad \ldots (5.63)$$

For nonlinear problems, $[K]=f\{U_n\}$ and $[K]\{U_n\}=\{F_n^{\text{int}}\}$ is internal force vector.
Using 2nd order accurate explicit central difference scheme, we get

$$\{\dot{U}_n\}=\left(\frac{1}{2\Delta t}\right)\left[\{U_{n+1}\}-\{U_{n-1}\}\right] \quad \ldots (5.64)$$

$$\{\ddot{U}\}=\left(\frac{1}{\Delta t^2}\right)\left[\{U_{n+1}\}-2\{U_n\}+\{U_{n-1}\}\right] \quad \ldots(5.65)$$

Substituting the above equations into equation 5.63, we get

$$\left(\frac{1}{\Delta t^2}[M]+\frac{1}{2\Delta t}[C]\right)\{U_{n+1}\}=\{F_n^{ext}\}-\{F_n^{\text{int}}\}+\frac{1}{\Delta t^2}[M]\left(2\{U_n\}-\{U_{n-1}\}\right)+\frac{1}{2\Delta t}[C]\{U_{n-1}\} \quad \ldots(5.66)$$

For nonlinear problems [K] is computed every time step.

[M] and [C] must be diagonal to make the explicit scheme economical since this scheme is conditionally stable, critical $\Delta t = (2 / \omega_{max})$ w_{max} *is* maximum free element frequency over the whole model.

Writing the frequency in terms of material property and characteristic size of the element, we get, *critical* Δt *=(Le / Elastic Wave speed)* …(5.67)
this condition is known as Courant Stability criteria.

5.18.2 Selection of time step

Depends on following factors

1. Plasticity
2. Presence of Contact interfaces
3. Wave propagation effect
4. Types of elements used

5.18.3 Effect of plasticity on time step

In general it is observed that for stiffening behaviour of structures where tangent modulus decreases with increasing strain, w_{max} decreases with increasing strain. So w_{max} at any time during nonlinear deformation is less than that for the linear elastic response. Thus a time step stable for purely elastic response is also stable and accurate for non-linear response. Further special care should be taken to make the integration stable since the instability caused by improper time step may be suppressed by energy dissipating mechanism viz. Plasticity and damping.

5.18.4 Effect of Contact interfaces

Treatment of Contact conditions using Penalty algorithms, which is the most usual method, external force vector contains normal and tangential force on slave nodes calculated from interface stiffness. Similarly the normal and tangential forces obtained at contact point on master segment are extrapolated to master nodes and included in external force vector. In case of large interface pressure the interface stiffness required is very large which leads to high *Wmax* for inter face elements. This means a small stable time step is required for integration.

5.18.5 Effect of wave propagation phenomena

In case of suddenly applied loads characterized by high frequency content, stresses develop at point of application instantaneously. But because stress is transmitted through material in form of interaction between metal atoms, it takes fine time for the other portion of structure to see the stress. It implies the information is passed in terms of a wave, which reflects, from a fixed boundary in same sign and from a free boundary in reverse sign. These phenomena are important in case of blast, hydro forming, impact and crash problems.

Choice of mesh:

- Lower order elements are preferred to higher order elements because strain discontinuities propagate through the model leading to numerical oscillations.
- Element sizes should not change drastically since the discrete representation of a continuous mass distribution by mass matrix will be improper leading to artificial

reflection at element boundaries where size transition occurs. The reflection causes numerical noise.

5.18.6 Types of element used for discretization.

Continuum elements:

Continuum elements are used to simulate both structural solid and fluid domain. In fluid domain calculation pressure is an element state variable, which can develop in to strong spatial discontinuity because of increasing sound wave speed with time. This discontinuity is known as shock. To treat this numerically the discontinuity has to be smeared by using artificial viscosity. This leads to alteration in wave speed. Hence, all other elements will not develop shock rather they will see the stress wave. Belytschko, Bonet, Cook [10, 11, 12].

wave speed used in eqn(5.67) = f (adiabatic sound speed, C , viscosity coefficients) for fluids.

$$C = \left(\frac{4G}{3\rho_0} + \frac{dp}{d\rho}\}_E + \frac{pv^2}{\rho_0}\frac{dp}{dE}\}_\rho \right)^{0.5} \quad \ldots(5.68)$$

where G is bulk modulus. An EOS is to be used for defining pressure, p = f (ρ, E)

E= internal energy = pv

Elastic wave speed $= \sqrt{\frac{E(1-\nu)}{(1+\nu)(1-2\nu)}}$

Characteristic length, Le =(Element volume / Area of the largest face)

Truss elements

Le = Length of the element

Elastic dilational wave speed = $\sqrt{\frac{E}{\rho}}$

Beam elements

Beam elements sees flexural stress wave. Hence, $\Delta t = \frac{o.5L}{\sqrt{\frac{3EI}{\rho}\left(\frac{3}{12I + AL^2} + \frac{1}{AL^2}\right)}}$

Shell elements

Wave speed = $\sqrt{\frac{E}{\rho(1-\nu^2)}}$

5.18.7 Energy Balance check

Ensure stable and accurate computation using Explicit scheme energy balance check is needed.

$$W_{\text{int}}^{n+1} + T^{n+1} = W_{ext}^{n+1} \quad \ldots(5.69)$$

Internal energy+ Kinetic energy= External energy at current time step

$$W_{\text{int}}^{n+1} = W_{\text{int}}^{n} + \Delta W_{\text{int}} \quad \ldots(5.70)$$

$$W_{ext}^{n+1} = W_{ext}^{n} + \Delta W_{ext} \quad \ldots(5.71)$$

$$\Delta W_{\text{int}} = \frac{\Delta t}{2}(U^n R_{\text{int}}^n + U^{n+1} R_{\text{int}}^{n+1}) \quad \ldots(5.72)$$

$$\Delta W_{ext} = \frac{\Delta t}{2}(U^n R_{ext}^n + U^{n+1} R_{ext}^{n+1}) \quad \ldots(5.73)$$

Explicit scheme is economical and efficient for problems involving high frequency loadings, since these problems require small time-step to capture the associated phenomena and this scheme is stable for small time steps only. Whereas Implicit schemes are efficient for structural dynamics problems having moderate frequency contents since this problems are of long duration and characteristically slow hence allows larger time step to be used. All commercial programs have algorithms to compute the time-step, which is a function of amount of non-linearities and element sizes. Ls-Dyna the code of choice using extensively this transient dynamics with vast library of material models with good treatment as discussed above for material strain hardening with and without rate effects complimented with robust contact treatments as discussed in next chapter.

5.19 Contact Analysis

Apart from the systems of nonlinearity due to deformation, strain and material behaviour, contact is another source of nonlinearity that can be observed in the buckling problems. In a typical axial collapse process the deformation modes and collapse progression is heavily due to the contact bother internal and external. Contact between two bodies appears when they come towards each other during the deformation process. In these problems a force normal to the contacting surface acts on the two bodies when they touch each other. If there is friction between the surfaces, shear forces may be created that resists the tangential motion (sliding) of the bodies. Contact analysis focuses mainly to identify the areas in contact and evaluate the contact pressure so generated. Zhong [17]

The high nonlinearity arising from the contact problems require high computing resources to provide a solution. As discussed in the previous sections it's a category of boundary non linearity with discontinuous boundaries and force transmittal only when the two bodies are in contact. No constraints are applied when the bodies are out of contact. The contact algorithm should be capable of identifying when the two surfaces are coming into contact with each other and apply the appropriate constraint at the point of contact. It also should be capable in doing reverse thing in identifying when the contact is lost between the two contacting surfaces and remove the constraints accordingly.

This chapter deals with the various aspects that are relevant for contact analysis. The terminologies commonly encountered in contact analysis are discussed briefly.

Classifications of contact analysis based on several criteria are explained. The continuum mechanics equation for contact analysis and the solution approach for contact analysis are discussed in this chapter.

5.19.1 Terminology in Contact Analysis

Master and slave bodies: Two bodies, which can contact each other during deformation process, are called as master and slave bodies. Both of these bodies may be deformable or the master body is rigid and slave body is flexible. Sometimes they are also referred as 'contactor body' and 'target body'.

Master and slave surfaces: The participating surfaces in the master and slave bodies, which are likely to contact each other during the deformation process, is called Master and Slave surfaces.

Master and Slave lines: A master line is an imaginary line formed through the list of grid points in an order at the interface on the master body in a topological manner. Similar thing applies to the slave line which based of grid points on the slave body.

Master and Slave nodes: The points on the master and slave lines which form the grid are called master and slave nodes respectively.

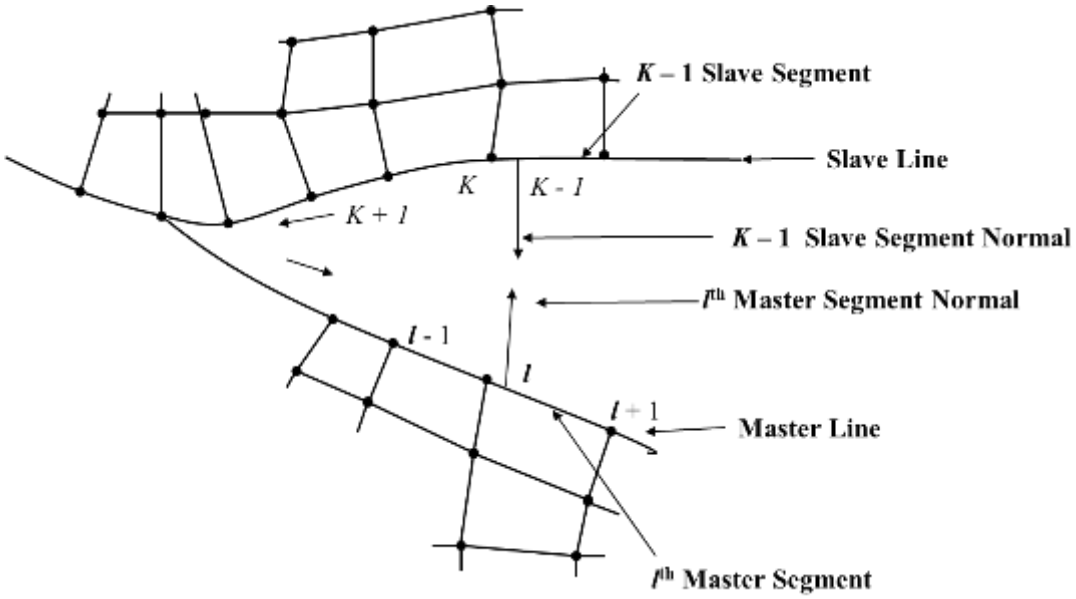

Fig. 5.18 segments and lines in master and slave bodies

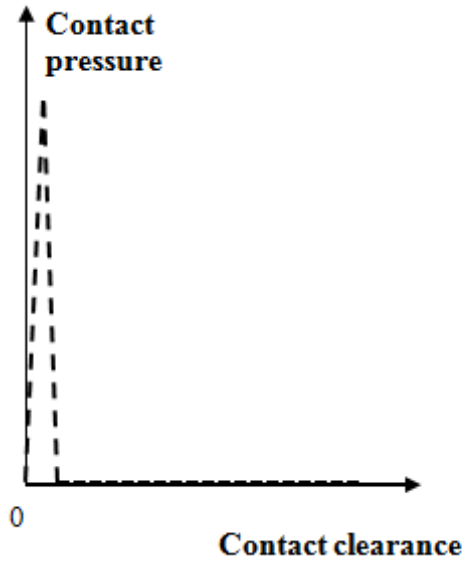

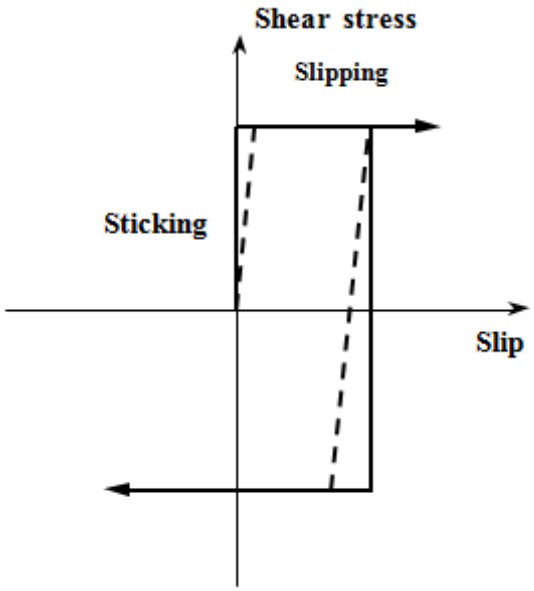

Fig. 5.19 Contact pressure – clearance relation **Fig. 5.20 Friction models for contact analysis**

Master and slave lines are further broken down to segments which are lines joining adjacent grid points. The line segment between master grid points is master segment and the one between slave points is slave segment. A master segment contains two master nodes at the minimum to form a master line while the slave line might contain many slave segments or no slave segment with just a node. Figure-5.18 shows the nodes, segments and lines in a master and slave bodies.

Contact pair:

The pair of surfaces that may likely to contact each other during the deformation is called as contact pair.

Contact clearance and contact pressure:

The distance separating the two surfaces in a contact pair is known as the clearance. When the clearance between the participating surfaces is zero, constraints are applied and contact pressure can be transmitted between the bodies in contact without any limit. When this pressure drops down to zero or negative the surfaces separate from each other with constraints removal. The figire-5.19 depicts the contact pressure – clearance relation.

The dramatic change in contact pressure that occurs when a contact condition changes from ‘open’ to ‘closed’ some time makes it difficult to compute the contact simulation.

Contact Sliding:

The relative sliding of the two surfaces with respect to each other after they establish contact is termed as contact sliding. Hence, in addition to determining whether contact occurred at a particular point, the contact analysis must calculate the relative sliding of the two surfaces. The magnitude of slide can be either small or finite and it is computationally less expensive to model contact problem with small sliding.

Contact Friction:

If the two interacting surfaces that participate in the contact are rough, the relative sliding between the surfaces is affected by the friction and needs to be taken into account. The analysis generally should address this behaviour through simple coulombs frictional model with coefficient of friction, μ. The limiting frictional shear force is computed by the product μ* p, where p is the contact pressure between the two surfaces. The Figure-5.20 depicts such a relative motion between two surfaces in contact.

Convergence problems might arise during simulations due to the discontinuous states between the surfaces of the contact while sticking and slipping. Penalty based friction formulation can be used to avoid difficulties while capturing the frictional behaviour. Elastic slip can be included to have stable behaviours. This slip allows small amounts of relative motion when the surfaces are supposed to be sticking. This is indicated by the dotted line in Figure-5.20. The penalty stiffness is selected in such a way that the maximum elastic slip is a very small fraction of the characteristic element length. The penalty friction formulation works well for most problems, including most metal forming application. For the problem with ideal stick-slip frictional behaviour, the more expensive, Lagrange frictional model is used. This model is more expensive, as the solution converges more slowly and solution needs more iteration for convergence.

5.19.2 Contact classification

Contact problems are classified depending on the stiffness and type of the contacting bodies. Based on the stiffness, contact problems are classified as:

1. Rigid to flexible contact
2. Flexible to flexible contact.
3. Surface to surface contact

Rigid to flexible contact

In this type of problem, one of the contacting bodies is considered as rigid compared to other body. This means that the stiffness of the rigid body is much higher compared to the other body and hence it undergoes very less deformation and strain. In general, whenever the soft material is coming into contact with a hard material the problem can be classified as, rigid to flexible. In this type of contact analysis, the rigid surface is considered as master surface and the flexible surface is treated as slave surface. This situation is predominant in many metal forming problems.

Flexible to flexible contact

In this type of contact problem, the stiffness of both contacting surfaces is of the same order and hence both of them are deformable. This is a more common type of contact problem that is used between deformable surfaces and typical example of this type of contact is the bolted flanges under loads, bending or crushing of sheet metal sections Surface-to-surface contact.

If the interaction is taking place at surface level for both the contacting bodies, the problem can be classified as surface-to-surface contact. It provides better contact results, such as normal pressure and friction stress for a typical engineering problem. It supports large deformation with friction with inclusion of sliding in an efficient manner. The potential surfaces which form the contact pair are identified and processed for sticking and sliding while applying constrains. Typical examples are welded and fit assemblies, airbag to dummy interfaces, belts to occupants and deep-drawing problems.

5.19.3 Continuum mechanics equations

Applying the principle of virtual work for N bodies which are in contact at any time "t" with ${}^{t}S_C$ as the area of contact for each body M, M=1,2,…N,

$$\sum_{M=1}^{N}\left\{\int_{t_v}^{t}\sigma_{ij}\delta\varepsilon_{ij}d^tV\right\}=\sum_{M=1}^{N}\left\{\int_{t_v}\delta u_i^{\,t}f_i^{\,B}d^tV+\int_{t_{Sf}}\delta u_i^{\,St}f_i^{\,S}d^tS\right\}+\sum_{M=1}^{N}\int_{t_{S_C}}\delta u_i^{\,Ct}f_i^{\,C}d^tS \qquad \ldots(5.74)$$

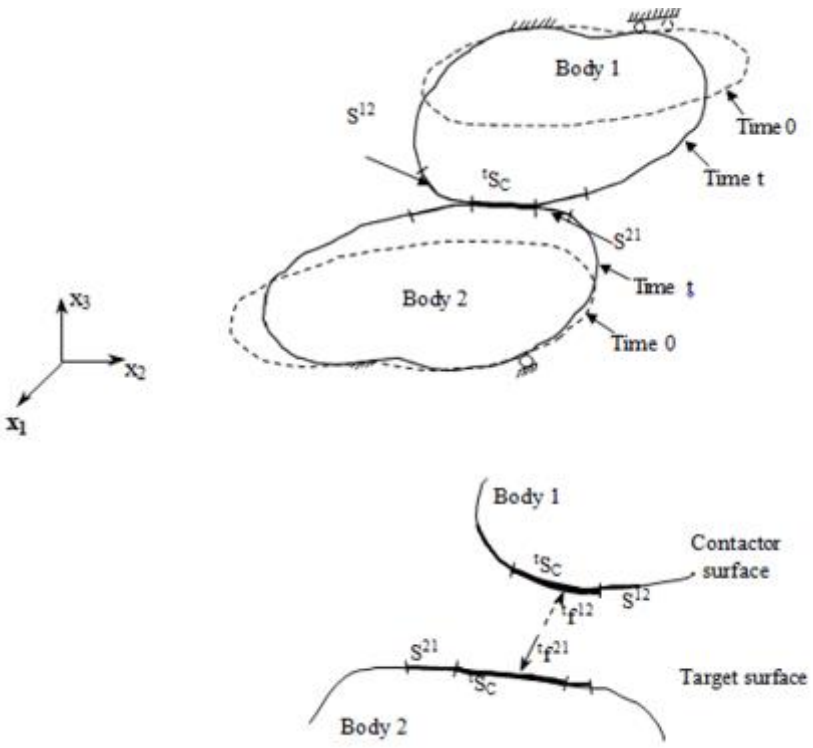

Fig. 5.21 Bodies 1 and 2 in contact at time "t"

The expressions in braces corresponds to the usual terms and the ones on the right side with summations indicate the contribution of the contact forces as a contribution of externally applied tractions which are denoted as $t_{f_i^c}$ and act over the areas $t_{S_i^c}$ the components of the known externally applied tractions are denoted as $t_{f_i^s}$ and act over the areas t_{S_f}. Fig-5.21 shows two bodies 1 and 2, which are in contact with each other. No rigid body motion is possible without contact and each body needs to support each other.

Assuming the vector contact surface tractions on body-1 which is in contact with body-2as $t_f 12$, then $t_f 12 = 1_f 21$. The virtual work done due to the tractions in contact as in the Equation-5.74 can be written as:

$$\int_{S^{12}} \delta u_i^{1t} f_i^{12} dS^{12} + \int_{S^{21}} \delta u_i^{2t} f_i^{21} dS^{21} = \int_{S^{12}} \delta u_i^{12t} f_i^{12} dS^{12} \qquad \ldots(5.75)$$

where δu^1 and δu^2 represent the virtual displacements of bodies 1 and 2 on the contact surfaces respectively, while

$$\delta u^{12} = \delta u^1 - \delta u^2 \qquad \ldots(5.76)$$

The contact surface pair in this case is made up with pair of surfaces S^{12} and S^{21} which can be of unequal sizes. At time 't', the interface area of body 1 one body 2 is t SC of body 2, and body 2's interface area on body 1 is $^t S_C$ which are parts of surface pair S^{12} and S^{21}.

The expressions on the right side of Equation-5.75 indicate the summation of virtual work over the relative virtual displacements of the contact pair coming from the contact tractions. At S^{21} surface we can assume 'n' as an unit vector in outward directions while 's' be another vector such that the cross product of **n**, **s** forms a right hand basis as shown in Figure-5.22. The contact traction ${}^{t}f^{12}$ acting on S^{12} can be decomposed in to normal and tangential components corresponding to 's' and 'n' on the surface S^{21} as per below:

$$ {}^{t}f^{12} = \lambda n + ts \qquad \text{....(5.77)} $$

The expressions λ and t represent the normal and tangential traction components which can further be decomposed as

$$ \lambda = ({}^{t}f^{12})^{T} n \text{ and } t = ({}^{t}f^{12})^{T} s \qquad \text{...(5.78)} $$

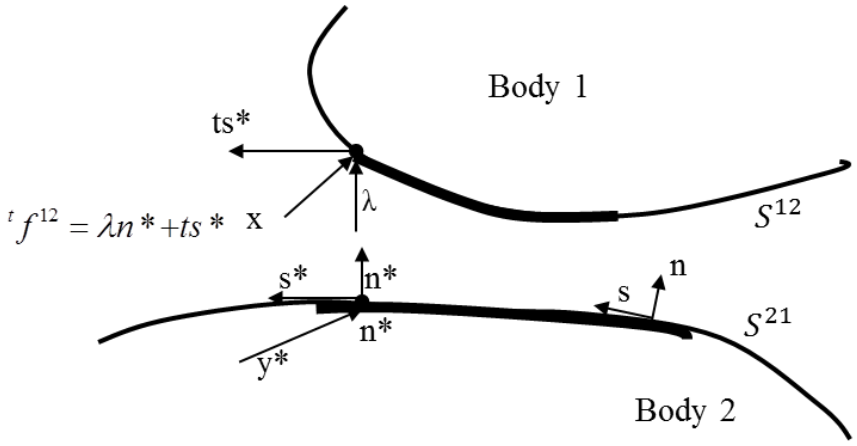

Fig. 5.22 Surface and Vector representation in a contact pair

The values of 's' and 'n' vectors are defined further with consideration of point **x** on surface S^{12} and **y***(**x**,t) on the surface S^{21}. From 'x' the distance to S^{21} can be written as ,

$$g(\boldsymbol{x},t) = (\boldsymbol{x} - \boldsymbol{y}^*)^T \boldsymbol{n}^* \qquad \ldots(5.79)$$

The unit normal vector used in the point **y***(**x**,t) is **n*** and its correspondence at point 'x' with **s*** is as per Equation- 5.79. The gap function for the contact pair can be represented as 'g' and the conditions for a normal contact can be formulated as:

$$\begin{aligned} g &\geq 0 \\ \lambda &\geq 0 \\ g\lambda &\geq 0 \end{aligned} \qquad \ldots(5.80)$$

The last expression interlinks gap function and normal tractions which indicates the fact that if the gap function 'g' is greater than zero then $\lambda = 0$, and vice versa.

Coulomb's law of friction can be applied if frictional conditions are desired with the introduction of μ the coefficient of friction. The non- dimensional variable τ can then be defined as:

$$\tau = \frac{t}{\mu\lambda} \qquad \ldots(5.81)$$

The product '$\mu\lambda$' represents the resistance due to friction and tangential velocity which is relative can be computed for its magnitude as

$$\dot{u}(x,t) = \dot{u}^2\big|_{y^*(x,t)} - \dot{u}^1\big|_{(x,t)} s^* \qquad \ldots(5.82)$$

The unit vector's' at point **y***(**x**,t) in tangential direction is $u(\boldsymbol{x}, t)$ and the relative tangential velocity at the point **y*** with respect to point 'x' is the product $\mathrm{u}(\mathbf{x}, \mathrm{t}) \,.\, \mathbf{s}^*$

Applying the frictional conditions from Coulombs law

$$\left.\begin{aligned} &|\tau| \leq 1 \\ &\text{and } |\tau| < 1 \quad \text{implies } \dot{u} = 0 \\ &\text{while } |\tau| = 1 \text{ implies } sign(\dot{u}) = sign(\tau) \end{aligned}\right\} \qquad \ldots(5.83)$$

The interface conditions for normal conditions and tangential conditions are better depicted in Figure-5.23.

The contact problem in Figure-5.21 thus can be resolved to the conditions (5.80) and (5.83) through the fundamental principle of virtual work Equation-5.74 as applied on onto bodies 1 and 2 .

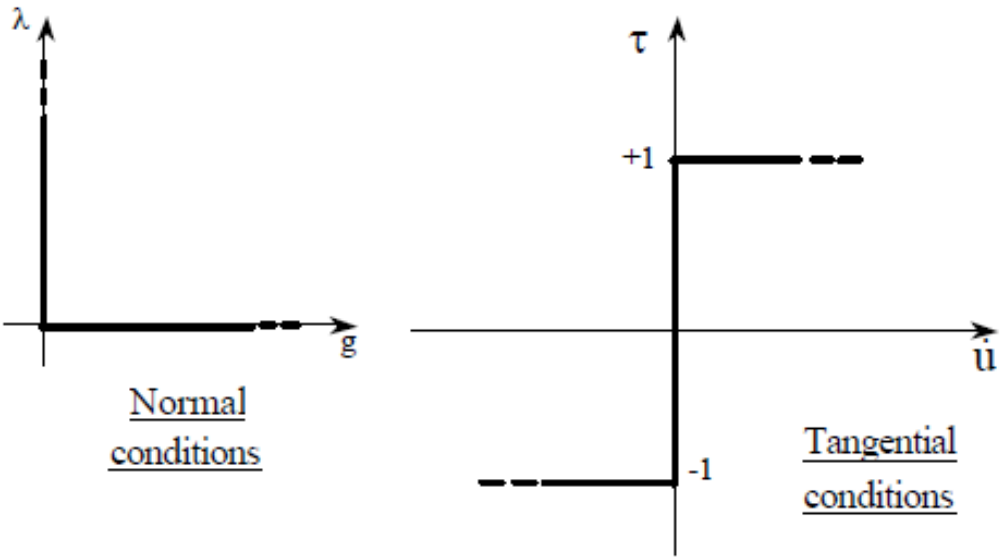

Fig. 5.23 Interface conditions in contact analysis

In the preceding section, we considered in essence static (or pseudo-static) contact conditions. In dynamic analysis, the distributed body force includes the inertial force effects, and kinematic interface conditions must be satisfied at all instances of time, requiring displacement, velocity and acceleration compatibility between the contacting bodies. The time integration of derivatives, in general does not automatically satisfy that the time derivatives of displacements are also compatible in the contact area and this compatibility must be separately imposed on the step-by-step solution.

5.19.4 Solution Approach for contact problems

This section explains how the contact constraints are imposed in a solution approach referred as the constraint function method.

Satisfying the condition in Equation -5.80, let's assume '**w**' to be a function of gap function 'g' and normal traction component 'λ' as w(g, λ) while satisfying the condition in Equation -5.83, let's assume '**v**' to be a function of τ the non-dimensional variable and relative tangential velocity $\dot{u}$ as v($\dot{u}$,τ). The conditions of the contact can be written as:

$$w(g, \lambda) = 0 \qquad \ldots(5.84)$$

and $$v(\dot{u}, \tau) = 0 \qquad \ldots(5.85)$$

The principle of virtual work can be applied with imposition of above conditions and can be resolved either by penalty method or Lagrange multiplier methods. Considering the

Langrangian method, the variable λ and τ can be used as Lagrange multipliers while the variations of the variables can be assumed to be with $\delta\lambda$ and $\delta\tau$.

Applying the variables onto Equations -5.84 and Equation-5.85 by $\delta\lambda$ and by $\delta\tau$ and integrating over the surface area of S^{12}, the constraint Equation can be written as :

$$\int_{S^{12}} \left[\delta\lambda w(g,\lambda)+\delta\tau v(\dot{u},\tau)\right] dS^{12} = 0 \qquad \ldots(5.86)$$

Now for the contact problem with two bodies as depicted in Figure-5.21 the governing equations to be resolved are from the principle of virtual work equation while the effect of tractions in the contact pair are considered through unknown externally applied forces with Equations-5.86 as the constraint.

To simplify the formulation of governing finite element equation, consider the two-dimensional case of the contactor and target bodies shown in Figure-5.24. The node k_1 and k_2 define a straight boundary but are not necessarily the corner nodes of an element. Instead, they are any two adjacent nodes on the corner bodies.

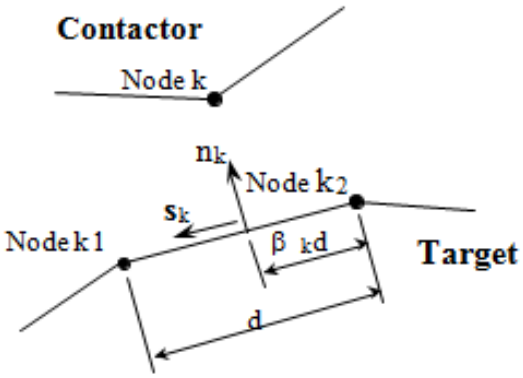

Fig. 5.24 Two-dimensional case of contact

The discretization of the continuum mechanics Equations-5.74 and 5.86 corresponding to the conditions at time t + Δt gives:

$$^{t+\Delta t}F(^{t+\Delta t}U) = {}^{t+\Delta t}R - {}^{t+\Delta t}R_c(^{t+\Delta t}U, {}^{t+\Delta t}\tau) \qquad \ldots(5.87)$$

and $$^{t+\Delta t}F_c(^{t+\Delta t}U, {}^{t+\Delta t}\tau) = 0 \qquad \ldots(5.88)$$

applying this to 'm' nodes of the contactor,

$$^{t+\Delta t}\tau^T = \left[\lambda_1,\tau_1,\ldots\lambda_k\tau_k,\ldots\lambda_m,\tau_m\right] \qquad \ldots(5.89)$$

Nodal point displacements are used to express the relative velocity and gap functions.

The vectors $^{t+\Delta t}R$ obtained by assembling for all 'm' contactor nodes k = 1,…,m, the nodal point force vectors due to contact. For the contactor node k and the corresponding target nodes, the nodal force vector is:

$$^{t+\Delta t}R_k^c = \begin{bmatrix} -\lambda_k(n_k + u\tau_k S_k) \\ (1-\beta_k)\lambda_k(n_k + u\tau_k S_k) \\ \beta_k\lambda_k(n_k + u\tau_k S_k) \end{bmatrix} \quad \ldots(5.90)$$

where β_k, $\mathbf{n}_k$, s_k are defined in Figure-5.24

The vector $^{t+\Delta t}F_c$ can be written as:

$$^{t+\Delta t}F_c^T = \begin{bmatrix} ^{t+\Delta t}F_1^{cT}, ..., ^{t+\Delta t}F_m^{cT} \end{bmatrix} \quad \ldots(5.91)$$

where

$$^{t+\Delta t}F_k^c = \begin{bmatrix} w(g_k, \lambda_k) \\ v(\dot{u}_k, \tau_k) \end{bmatrix} \quad \ldots(5.92)$$

By linearization of the last computed state, the solution equations in incremental form for Equations-5.87 and 5.88 can be obtained. At a state of time 't' the linearized equations then can be written as:

$$\begin{bmatrix} ^tk + ^tk_{uu}^c & ^tk_{u\tau}^c \\ ^tk_{\tau u}^c & ^tk_{\tau\tau}^c \end{bmatrix} \begin{bmatrix} \Delta u \\ \Delta\tau \end{bmatrix} = \begin{bmatrix} ^{t+\Delta t}R - ^tF - ^tR_C \\ -^tF_C \end{bmatrix} \quad \ldots(5.93)$$

The increments in the solution variables ^{t}U and $^t\tau$ and $^tK^c_{uu}$, $^tK^c_{u\tau}$ are ΔU and $\Delta\tau$ while $^tK^C$ and $^tK^C_{\tau\tau}$ are contact stiffness matrices and defined as below and their detailed expressions depend on the constraint functions used.

$$\left\{ \begin{array}{ll} ^tK^c_{uu} = \dfrac{\partial^t R_C}{\partial^t U}; & ^tK^c_{u\tau} = \dfrac{\partial^t R_C}{\partial^t \tau}; \\ ^tK^c_{\tau u} = \dfrac{\partial^t F_C}{\partial^t U}; & ^tK^c_{\tau\tau} = \dfrac{\partial^t F_C}{\partial^t \tau}; \end{array} \right\} \quad \ldots(5.94)$$

The flow chart shown in Figure-5.24 gives a typical algorithm used for contact analysis and this is based on Newton-Raphson technique. Its starts with careful detection of the state, in which the defined contact pairs exist to evaluate the open and close condition of slave nodes. Based on the contact conditions it determines whether the node is sliding or sticking and applies appropriate contact conditions. In a similar fashion it removes the constraints when it detects an open condition for the nodes. The configuration of the model gets updated using the correction calculated from the iterations.

The changes in the contact conditions at the slave nodes is the first check the algorithm does before the checking for equilibrium checks in forces and moments. The contact status changes form close to open when the contact pressures are negative or zero while it becomes open to close when the clearance is negative or zero. The algorithm updates the conditions of the contact depending on the status at the end of every first iteration and proceeds to the second iteration towards subsequent iterations until no changes in contact status are detected. The iteration where no changes are detected becomes the first equilibrium iteration to be followed by convergence checks. Further iteration are performed if the convergence check fails. The process repeats subsequently for the next load steps.

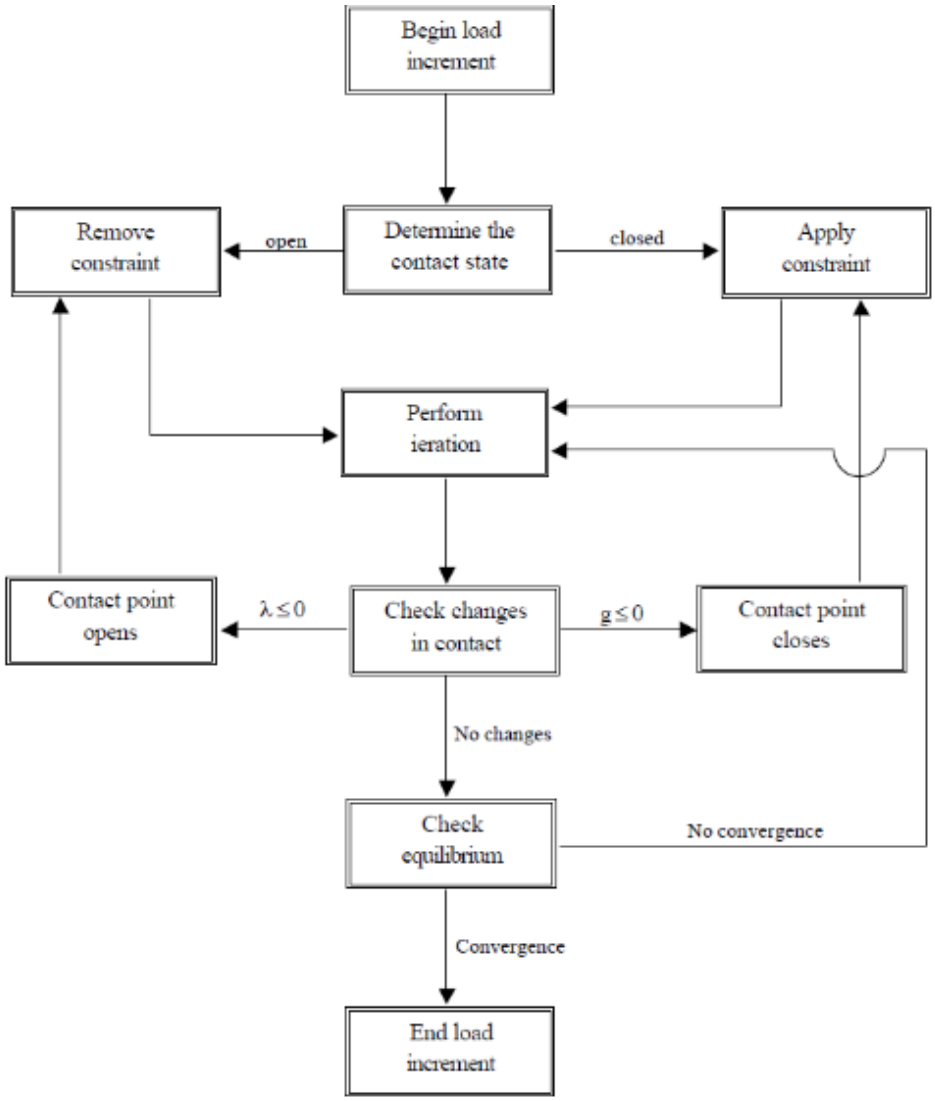

Fig. 5.25 Typical algorithm for contact analysis

Equipped with the detailed know how of the nonlinearity aspects and their formulations, it becomes necessary to understand the basic of the crash mechanics pertaining to the collapse of the thin wall sections which is well introduced and explained in the next chapter which forms major basis for this research.

CHAPTER 6

6.0 Crushing Mechanics of thin wall members and Analytical characterizations

During a typical frontal impact, occupants within the vehicle undergo rapid changes in velocity. This is primarily due to rapid vehicle deceleration caused by the rigid nature of the vehicle's metal frame components and body assembly. Many of today's vehicles incorporate deformable, energy-absorbing (EA) structures within the vehicle structure to manage the collision energy and slow the deceleration which in turn can lower the occupant velocity relative to the vehicle. Occupant velocities can be higher in Light-duty trucks and MPVs having a full-frame structure resulting in increased demands on the supplemental restraint system (SRS). In these types of vehicles an energy management system can be installed between the bumper and the vehicle structure to help absorb some of the collision energy and reduce occupant velocities.

The major energy management comes from the upfront crash energy absorption which can be designed to fit into the available packaging space without affecting the cost- weight effectiveness. This desire for components with light weight and higher energy absorbing capacity for various ground mobility systems has led to renewed interest in thin-walled sections. Abramowicz, Jones, Wierzbicki [23–25]. Solutions to the competing design goals of safety and light weightiness lie in the origination of innovative upfront energy absorption designs involving innovative designs which can be compounded by new materials, such as High Strength Low Alloys (HSLA), Dual Phase steels (DP), as well as Aluminium. Many of today's vehicles incorporate deformable, energy-absorbing (EA) structures within the vehicle structure to manage the collision energy and slow the deceleration which in turn can lower the occupant velocity relative to the vehicle. For the improvement in vehicle crashworthiness without mass offset these lightweight structures are very important. The direct consequence would be to design a cross-section which has the potential to minimize the force levels that occupants would get exposed. Many efforts have been focussed in developing design criteria for safety by utilizing collapse of thin walled structures with plastic hinge mechanisms. White, Jones [28-29].

Collapse of thin-walled sections has been known for its excellent energy absorption mechanism. It has been utilised widely in modern day structures in wide domains of

Automotive, Aerospace, Defence, Civil structures and others primarily due to high load bearing capacity with low weight. Under normal loading conditions these structures are exposed to compressive loads in axial directions and their energy absorption capacity varies on their design response characteristics and collapse modes. In Automotive domains thin-walled sections are used commonly for energy absorption and the usage of square shaped sections is of preferred choice primarily due to its low cost, ease of manufacture and has reasonable energy absorbing capability. Axial collapse of the thin walled structures has been studied in detail over decades and the understanding was limited primarily to circular tubes.

The foundational work on the axial collapse of thin walled members and its energy absorption was done by Alexander [30] and developed an approximate model to predict predict the mean crushing force and energy absorption. His work was further enhanced by Wierzbicki and Abramowicz [25,31], Abramowicz and Jones [23,24] and others through static and dynamic characterizations on circular and square tubes. Following this interesting researches studies were conducted with experimental and theoretical predictions by others (e.g. Guillow et al.[32], Langseth et al.[21], Huang and Lu [33], Tarigopula et al.[34]) with the main focus being on square and circular cross-sections. It was found that the collapse of these members under axial load displayed similar trends. The fundamental characteristic is in terms of force- displacement curve where the axial force experiences a high peak initially which is followed by a drop and then oscillated around a mean value. Though they collapsed similar they exhibited different collapse modes with different shapes. The circular members collapsed with diamond mode, concertina mode, mixed modes and in some cases unstable modes of global bending or buckling. It was also found from their researches that these modes functionally depend on the geometrical parameters of the members like that of thickness, length and diameter. Similarly for a square tube, modes of symmetric, asymmetric, global bending and buckling tend to appear during their collapse.

6.1 Basis for the Core research methodology

The geometrical configurations of the thin walled members like thickness, material, cross-sectional layout etc., influence the collapse and there by its efficiency in energy absorption. The cross-section configuration of a collapsing member was found to be a dominant factor and considered for this research. Many accomplished researches [24, 25, 30, 31, 35] were performed and efforts were put to describe theoretically, experimentally and numerically the collapse behaviours in metal columns with different cross sectional layouts, such as circular

[24, 30, 32], Square and their derivatives like that of top-hat [26] cross sections. The findings of these researches confluence towards a fact that heavy deformations happen near the corners edges of the sections and the crush energy is dissipated through bending and membrane deformations occurring in corner zones. The higher the deformation higher is the plastic work done and higher would be the energy absorbed. This aspect in the collapse process drives down an important inference **that the energy absorbing capacity of the collapsing structures depends on its "corners"** [25,31]. The number of corners participating in the collapse decides the energy absorbing efficiency and this forms the core principle to this research. In addition to the influence of corners it is also noted that the number of side flanges enclosing one corner element has to be even in numbers to form a prismatic configuration with favourable angle aiding in stability of the collapse and for achieving highest crush energy absorption efficiency [36].

6.2 Analytical considerations

The deformation behavior and associated energy absorption characteristics of circular cross-sections in axial compression has been studied for long time by pioneering researchers (Abramowicz and Jones, 1984, 1986 [23,24]; Grzebieta, 1990 [32]; Wierzbicki et al., 1992[38]; Singace et al., 1995 [39]) and basic analytical models were developed to estimate the folding wavelength and associated mean collapse force. These models were rudimentary to the fact that the folding mechanism was an assumption from which the bending and stretching energies were derived to be equated with external work done by the mean axial collapse force denoted as $\overline{P}$. Although simple, these models seriously neglect coupling of bending and membrane stresses during the collapse process along with effects of reactions loading in the folds. The deformation of the member in a repeatable lobed pattern was observed and the folding wavelength was defined. The minimization of the mean crush force $\overline{P}$ with wavelength (2λ) was performed while in some cases another parameter 'm' was used to achieve the required effect on $\overline{P}$. The proposed mechanisms were presented through three models which describe the folding mechanism at different levels of complexity in an increasing order towards a realistic representation.

The basic model proposed by Alexander, 1960 [30] was very approximate in describing the collapse behavior and Figure-6.1 illustrates the folding process. It misses out significant response points due to its prediction of folds without any curvature effects with unidirectional

folding from its mid surface deviating from the actual folding process where lobes are form inwards and outwards. Because of this for each fold the corresponding two peaks and two troughs is missed. This also affects the deformation progression at any point in the fold. The manner in which the tube collapses is as shown in the Figure-6.1.

The expressions for the mean load $\overline{P}$ and the half wavelength λ from the basic model proposed by Alexander [30] are expressed as below

$$\frac{\lambda}{R} = \sqrt{\frac{\pi}{\sqrt{3}}}\left(\frac{t}{R}\right)^{\frac{1}{2}} \cong 1.347\left(\frac{t}{R}\right)^{\frac{1}{2}} \quad \ldots(6.0a)$$

$$\overline{P} \cong \overline{\sigma_0}\, t^2\left[8.462\left(\frac{R}{t}\right)^{\frac{1}{2}} + 1.814\right] \quad \ldots(6.0b)$$

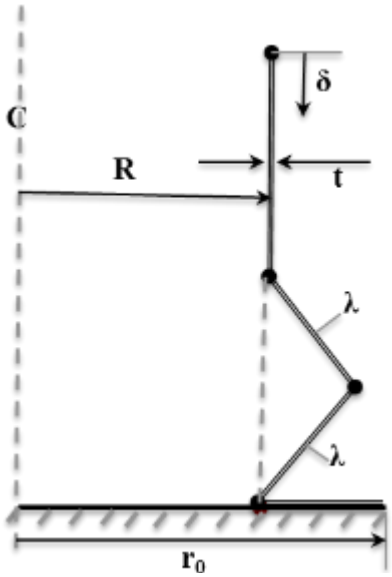

Fig. 6.1 Basic folding of Alexander

The predictions for mean load $\overline{P}$ based of above theory was later found to be grossly lower by 65 to 73% as compared to the measured values from the experiments of Bardi et al.[37]. On the other hand it was also under predicting the wavelength λ range from 10 to 23%. Abramowicz and Jones (1984) [23, 24] provided modifications to the above model to predict the mean load better but struggled to get better predictions for the folding wavelengths. Further refinement to the linear folding model of Alexander model was by Wierzbicki et al. [38] where it was proposed that the folding mechanism progresses with partial inward and outward folding from the original mid surface as described in the Figure-6.2. The missing gap in predictions was later adjusted through a factor '*m*' and a detailed extension was put by Singace et al. [39]. The value of m was found to have a value of 0.65 as fixed entity. The expressions for mean load $\overline{P}$ and half wavelength λ is as per below equations.

$$\frac{\lambda}{R} = \sqrt{\frac{\pi}{2}}\left(\frac{t}{R}\right)^{\frac{1}{2}} \cong 1.253\left(\frac{t}{R}\right)^{\frac{1}{2}} \quad \text{and} \quad m = 0.65 \qquad \ldots(6.0c)$$

$$\overline{P} \cong \overline{\sigma_0}\, t^2\left[7.874\left(\frac{R}{t}\right)^{\frac{1}{2}} + 1.408\right] \qquad \ldots(6.0d)$$

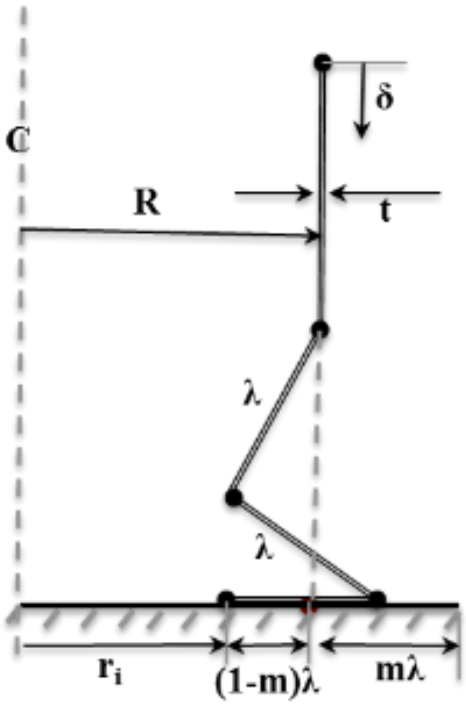

Fig. 6.2 Improved Basic folding- Wierzbicki

The predictions for these key variables of the folding process were investigated by Bardi et al.[37] and their estimations for the mean load was even lower that the initial prediction from Alexander which when compared to the experimental values was far worse at about 60–67% of the measured values. The same trend was found for wavelength as well and are in the range of 17 to 32% under predictive than the measured values.

The difficulties of predicting the folding process parameter from the above linear models was addressed by Wierzbicki et al. [38] through a model with concertina folding as per the Figure-6.3. This provided the initial break through to correctly represent the folding process. In this model the folding progression is through formation of circular arcs alternating partially inward and outward with constant radius ρ from the original middle surface without any correction factors.

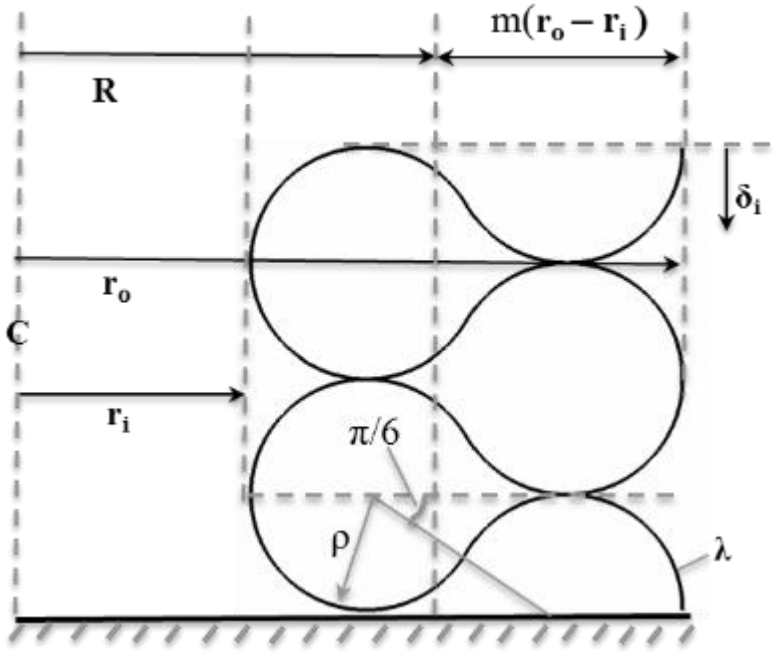

Fig. 6.3 Concertina folding- Wierzbicki

The expressions for the for mean load $\overline{P}$ and half wavelength λ is as per below equations.

$$\rho = \frac{3\lambda}{5\pi}\ ,\ r_0 - r_i = 2\rho\left(1+\frac{\sqrt{3}}{2}\right) \text{ and } \frac{\lambda}{R} \cong 1.853\left(\frac{t}{R}\right)^{\frac{1}{2}} \qquad \ldots(6.0e)$$

$$\overline{P} \cong 11.22\ \overline{\sigma_0}\ t^2\left(\frac{R}{t}\right)^{\frac{1}{2}} \qquad \ldots(6.0f)$$

which was later refined by Abramowicz and W, Jones[23] for *Non-axisymmetric* collapse with a strain hardening material to be

$$\overline{P} \cong \{\ C_1\left(\frac{R}{t}\right)^{\frac{1}{2}} + C_2\ \} * \ \overline{\sigma_0} t^2 \Big/ 4 \qquad \ldots(6.0g)$$

where C_1 and C_2 are evaluated depending on the number of corners formed in the circumferential direction in the crushing process.
These values are tabulated as below:

No. of corners	C_1	C_2
2	31.01	17.22
3	28.86	44.74
4	28.23	83.13
5	27.95	132.49

Further studies by Bardi et al.[37] found that the predicted values for these variables values provided the mean load $\overline{P}$ values to be of 81–91% of the measured values within reasonable accuracy levels. The initial linear models although were kinematically admissible their predictions for mean load mean load $\overline{P}$ and folding half wavelength λ were grossly deficient and can be considered to be of foundational value. The third model of Wierzbicki being more

realistic in the folding pattern predicted values which are closer within reasonable accuracy for the mean loads. However for the half wave lengths all the three models were under predictive and poor. This indicates the underlying deficiency in predicting the deformation energy per unit length of the undeformed member as compared to the experimental values.

With advent of low cycle time design developments in the automotive industry the need for simplified crush models to predict the crash response for thin walled front end structures used as Energy absorbers have become more profound. The above models can predict crash responses to a limited extent and restricted to simplified geometry such as circular and rectangular columns. The major limitation which restrict their wide spread usage comes from their inability in predictiveness beyond circular elements and simple box shapes.

The following section presents a complete analytical treatment with derivation for the mean crushing force in progressive crushing of thin-walled sections with an arbitrary angle between the adjacent plates forming corners. The present analysis is based on the consideration of a generalized folding mode which combines features of the quasi-in extensional and extensional collapse mechanisms as in the Figure-6.4.The present problem poses a considerable modelling and computational challenge because the process of progressive crushing involves large plastic strains, curvatures, displacements, and rotation. A closed-form solution is achieved by following the theory of plasticity in combination with quasi-in extensional and extensional collapse mechanisms with a travelling hinge line.

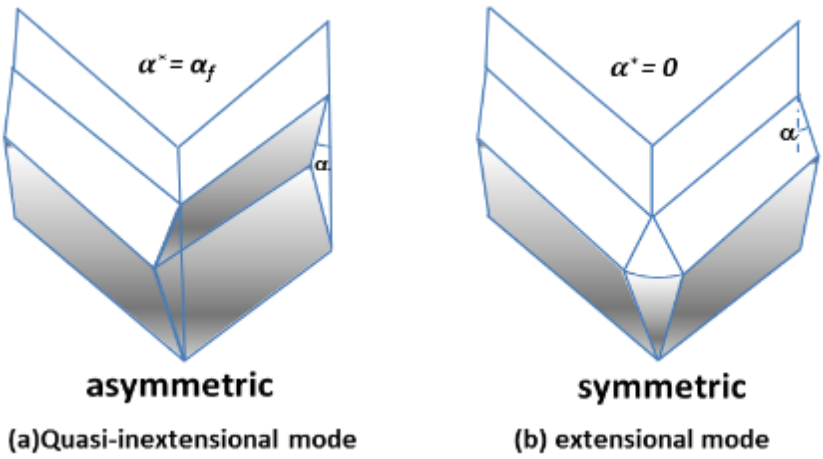

Fig. 6.4 Two Basic Collapse Mechanisms controlled by α^*

6.3 Formulation of Super Folding Element

The failure of the linear line segment models in predicting and describing the basic folding mechanism [30], instigated further detailed research which has led to the development of **S**uper **F**olding **E**lement theory as proposed by Wierzbicki and Abramowicz [25,31]. Using this theory, the plastic collapse process was analyzed for prismatic members. The enhancements include adoption of rigid-plastic material and kinematic continuity conditions as applied between rigid and deformable boundaries. The model was constructed using complex combination of surfaces such as cylindrical, conical, trapezoidal and toroidal surfaces with deformations along the stationary and moving lines of plastic hinges. The dissipation of the energy due to plastic deformation in the walls of thin walled sections was also considered in the model. Abramowicz and Jones [23] later validated the theory by valuable experimental studies.

According to the super folding element theory, the folding starts initially with elastic or elastic-plastic buckling and proceeds to the plastic collapse in relatively small parts of a structure in narrow hinge lines. The overall deformation of the structure is due to the rigid body motion of the wall segments which could be slightly deformed or might be undeformed while severe plastic deformations are contained to small areas. Most importantly this theory has enabled to clearly characterize the folding patterns with symmetric macro elements where in the folding patterns are having geometrical similarity. The complete folding mechanism can be constructed from the folding of a single folding element as illustrated in Figure-6.5. This small folding element is called the Super folding Element (SFE) with special reference to Wierzbicki and Abramowicz [25,31].

The generalized representation of SFE is as depicted in Figure-6.5 with its dimensional assumptions. The folding of this element in plastic mode can be categorized into five distinct deformation mechanisms.

1. Toroidal surface with moving boundaries and quasi-inextensional deformation
2. Bending deformations along stationary hinge lines
3. Rolling deformations with floating boundaries and undergo inextensional deformation.
4. Opening of conical surfaces that undergo extensional deformation.
5. After the travelling hinge line is locked the bending deformations along inclined and stationary hinge lines.

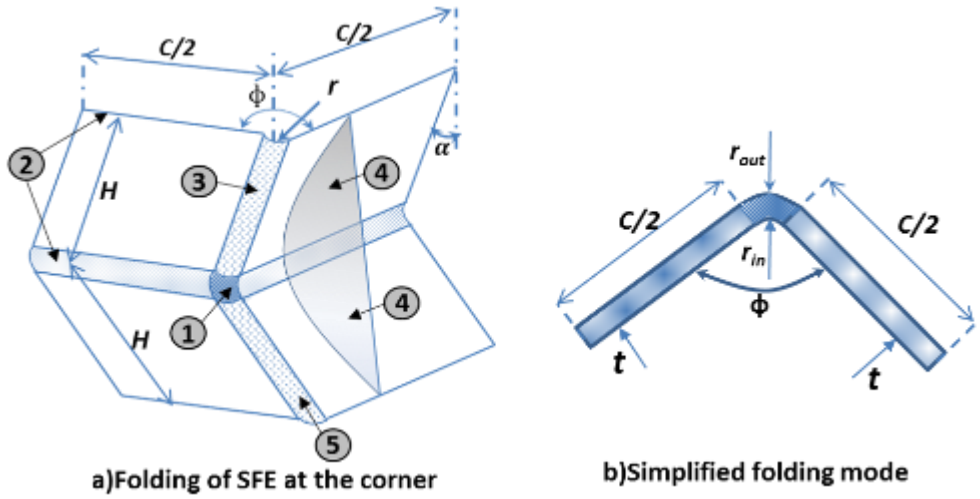

Fig. 6.5 Idealized collapse mechanism and Dimensional assumptions for SFE

Simpler folding mechanisms from smaller elements as indicated in Figure 6.5b form the foundational construction for the global generalized folding mechanism. The mechanism in in Figure-6.5a is assembled from two simplified modes of Figure-6.5b which are asymmetric and symmetric in nature, respectively. A time like parameter α^* is introduced to define the status of the element in consideration from its initial undeformed upright position. The progression of the deformation process in each mode is decided by α^* which could be, $0 \le \alpha^* \le \alpha_f$ as depicted in Figure-6.4. For the condition when $\alpha^* = \alpha_f$, the folding of SFE is dominated by an asymmetric mode while the case $\alpha^* = 0$ refers to a symmetric mode. For a condition between the limits $0 \le \alpha^* \le \alpha_f$ both mechanisms participate in the folding process which initially starts as an asymmetric mode until when the moving hinge line 3 gets locked within an element. At this juncture the conical surface 4 gets initiated to grow in an extensional manner there by confining the plastic deformations.

The switching parameter, α^*, is found to be dependent on the geometric parameters of side wall total length '*C*', wall thickness '*t*', and the corner angle 'ϕ '. It also depends on the constraint conditions imposed on the faces of super macro element that are deforming. In the cases of SFE with $\phi = \pi/2$ and acute angles the switching parameter $\alpha^* = 0$, the asymmetric mode of deformation is predominant, while for elements with obtuse values for the central angle, ϕ larger than 120 degrees, the symmetric mode controls the folding process depending on the *C/t* ratios [25]. Both the modes operate when the central angle is in the intermediate ranges while their individual contribution to the folding process and there by energy dissipation is dependent on the central angle, ϕ and the width to thickness aspect ratio, *C/t*

Wierzbicki and Abramowicz[25]. These folding modes which are occurring without any constraints on the deforming faces are referred to as natural folding modes.

6.4 The solution procedure

The kinematically formulated crushing problem can be resolved in three steps following the simillar method of Abramowicz [25,27]. Its start with the postulation of the deformation pattern of the macro element either in displacement or velocity field based on observations from the experiments. This deformation pattern of SFE is vectorized with geometrical parameters as depicted in Figure-6.5 which are the switching point parameter α^*, average rolling radius, *r*, length of the plastic folding wave, 2*H* which will be evaluated during the solution process. As a second step, after the postulation of the deformation pattern is the adoption of the theory of plasticity and determination of the functionals associated with energy dissipation and total energy dissipation to the vector β. Setting a minimum condition to obtain the optimal values of the vector β forms the third step to the solution process. In the following sections a detailed discussion and derivation for the closed form solution is revisited based on initial pioneering works of Wierzbicki and Abramowicz.[31]

The known input parameters for the present generalized folding mode are: the length of the cross-section *C*, the wall thickness *t*, and the angle ψ_o of a given element. In the abbreviated notation, these parameters can be represented by the vector:

$$\boldsymbol{\xi} = \{\boldsymbol{C}, \boldsymbol{t}, \boldsymbol{\psi_o}\}$$

The time like parameter α^* *is* considered to be an independent variable which controls the crushing process. The effective crushing distance, δ_{ef}, and the terminal value of time like parameter α_f were calculated separately and are also known parameters of the process. Finally, the length of the buckling wave *2H*, the small bending radius ***r***, as well as the "switching" parameter α^* are all unknown and will be determined as a part of the solution. For the sake of simplicity, it is convenient to introduce the vector of unknown parameters:

$$\boldsymbol{\chi} = \{\boldsymbol{r}, \boldsymbol{H}, \alpha^*\}$$

Basic Assumptions:

- Rigid/perfectly plastic, isotropic and independent of time with a suitably adjusted flow stress σ_0 to account for the work-hardening properties of the material.

- The plastic dissipation $\sigma * \dot{\varepsilon}$ is uniquely defined by a strain rate tensor $\dot{\varepsilon}$ assuming the usual normality convexity properties of the yield function,
- It is assumed that the constitutive equations are not affected by the rotation of the shell element (the co-rotational yield condition).
- The Cauchy stress tensor,σ and velocity strain rate tensor, $\dot{\varepsilon}$, will be used to assure work conjugation of stress and strain rate measures.
- The effect of variable thickness is retained in the analysis of continuously deforming regions, but is neglected on stationary or moving hinge lines

Formulating the displacement field for a given vector $\boldsymbol{\xi}$,

$$U^* = U^*(x, \chi, \alpha) \tag{6.1}$$

where * denotes kinematical admissibility of a given variable. The velocity field:

$$\dot{U}^* = \dot{U}^*(x, \chi, \alpha)\dot{\alpha} \tag{6.2}$$

which is obtained from the displacement field $\mathbf{u}^*$ by time differentiation.

In the current deformed configuration α^*, the relations between the strain rate and the velocities are linear (Equation-6.2). In the continuously deforming regions, the strain rate is defined as a symmetric gradient of the velocity field (the so-called velocity strain) while honouring the kinematic continuity conditions at the hinge lines.

Considering the current configuration of the basic folding mechanism described by the parameter α^* from the theory of plasticity, the best set of parameters {H, b} is obtained by extremizing the internal rate of energy dissipation which can be written as

$$\frac{\partial}{\partial x}\int_v \sigma^* \dot{\varepsilon}^* dv = 0$$

. . . (6.3)

The resulting optimum parameter of the velocity field will change from one configuration to the other, so that, in general, $\chi = \chi(\alpha^*)$ and based on further observation form the tests the length of the plastic folding wave *2H,* as well as the magnitude of the rolling radius *b,* undergo only slight changes following which we can treat the vector of unknown parameters χ as independent of the process parameter α^*. The above assumption considerably simplifies the calculations and renders a closed-form solution possible.

Integrating Equation-6.3 with respect to time (or α^*) from t = α^* = *0* to the end of the process $t=t_f$, α^* = α_f and changing the order of integration, we obtain:

$$\frac{\partial}{\partial x}\int_0^{\alpha f} d\alpha \int_v \sigma^* \dot{\varepsilon}^* dv = 0$$

⋯(6.4)

The total plastic work which is proportional to the mean crushing force *Pm*, can then be defined as :

$$P_m \delta_f = \int_0^{\alpha f} d\alpha \int_v \sigma^* \dot{\varepsilon}^* dv \qquad \ldots(6.5)$$

where the product $Pm\delta_f$ represents the total plastic work of external forces and is equilibrated by the system of internal stresses.

Considering the Energy balance, for shells made of rigid-perfectly plastic isotropic materials, the rate of internal energy dissipation is divided into continuous and discontinuous velocity fields

$$\dot{E}_{\text{int}} = \int_s (M_{\alpha\beta}\dot{k}_{\alpha\beta} + N_{\alpha\beta}\dot{\varepsilon}_{\alpha\beta})dS + \sum_{i=1}^{n}\int_{\varsigma^i} M_0{}^i \left[\dot{\theta}^i\right] dl^i \qquad \ldots(6.6)$$

where the extent of plastic deformation which is continuous is defined as *S* while, L^i denotes the length of the ith hinge line with the number of stationary or moving hinge lines denoted by n. The symbol $\left[\dot{\theta}^i\right]$ denotes the rotation rate jump across the moving hinge line. The components of the rotation rate and extension rate tensors are denoted, respectively, by $\dot{k}_{\alpha\beta}$ and $\dot{\varepsilon}_{\alpha\beta}$. The bending moments $M_{\alpha\beta}$ and membrane forces $N_{\alpha\beta}$ are the corresponding conjugate generalized stresses. The total internal plastic dissipation is obtained by integrating Equation-6.6 in the interval $0 \le \alpha \le \alpha_f$ Since the total dissipation is obtained as a result of two different folding modes acting "in series," the expression for the rate of energy splits into two parts.

$$E_{\text{int}} = \int_0^{\alpha^*} \dot{E}_{\text{int}}{}^{(1)} d\alpha + \int_{\alpha^*}^{\alpha_f} \dot{E}_{\text{int}}{}^{(2)} d\alpha$$

(6.7)

where α denotes a configuration at which the extensional mode of deformation takes over the quasi-inextentional mode. During the first phase of the deformation $0 \le \alpha \le \alpha_f$, the crushing process is controlled by a quasi-in extensional folding mode and the corresponding dissipation is due to plastic flow over the toroidal surface, as well as the bending along stationary and traveling hinge lines.

Consider first the plastic flow over toroidal surfaces (Figures-6.5*a and 6.6).* The integrand in the first integral of Equation-6.7 has in general six components as below:

$$\int_0^{\alpha^*} \dot{E}_{\text{int}}{}^{(1)} d\alpha = E_1 + E_2 + E_3 \quad \text{And} \quad \int_{\alpha^*}^{\alpha f} \dot{E}_{\text{int}}{}^{(2)} d\alpha = E_4 + E_5 + E_6 \qquad \text{...(6.8)}$$

In view of the rotational symmetry and the assumed radial plastic flow along with plastic flow the rate of energy dissipation due to the plastic flow over the toroidal surface is reduced to

$$\dot{E}_1 = \int_s N_0 \dot{\lambda}_{\Phi\Phi} dS$$

where $\dot{\lambda}\phi\phi$ represents the stretch in the circumferential direction and the final expression for the energy $\dot{E}_1$, is written as

$$E_1 = \int_0^{\alpha^*} \dot{E}_1 = d\alpha = 16 M_0 \frac{Hr}{h} I_1(\psi_0, \alpha^*)$$

$$\cdots(6.9)$$

where I_1 is defined as

$$I_1(\psi_0, \alpha^*) = \frac{\pi}{(\pi - 2\psi_0)\tan\psi_0} \int_0^{\alpha^*} \cos\alpha \left\{ \sin\psi_0 \sin\left(\frac{\pi - 2\psi_0}{\pi}\beta\right) + \cos\psi_0 \left[1 - \cos\left(\frac{\pi - 2\psi_0}{\pi}\beta\right)\right] \right\} d\alpha$$

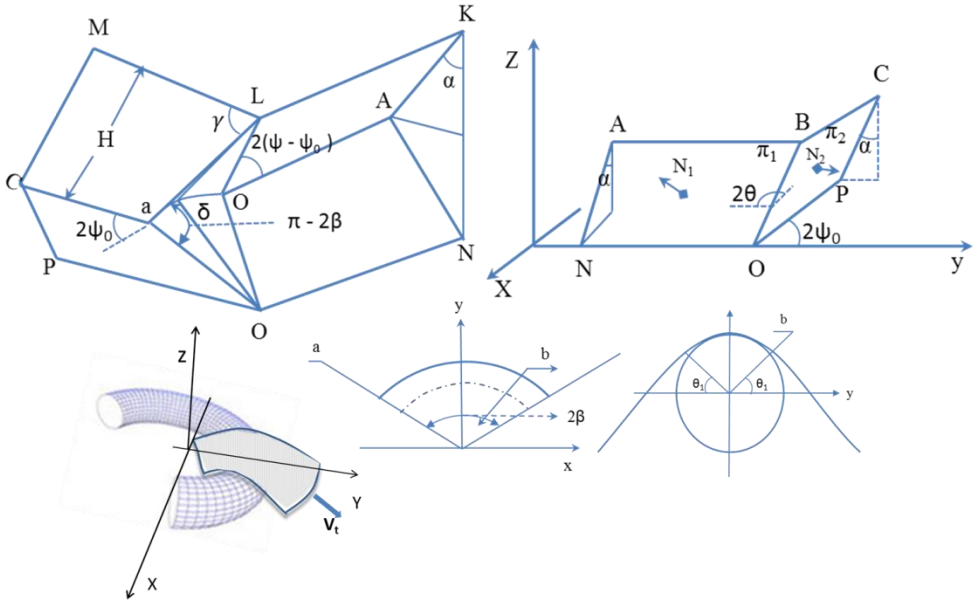

Fig. 6.6 Geometry of folding and plastic flow over toroidal surface

The rate of energy dissipated for the two moving hinge lines $\dot{E}_2$ equals to the limit bending moment per unit length M_0 *t*imes the rate of rotation *a* times the length of the hinge *C.*

Because the hinge line is split, there will be two such hinge lines in the folding mechanisms as shown in Figures 6.5a and 6.6

$$\dot{E}_2 = 2M_0 C\dot{\alpha} \quad \ldots (6.10)$$

The total energy dissipation by integrating the Equation-6.10 in the limits (0, α^{*}) gives

$$E_2 = 2M_0 C\alpha^* \quad \ldots (6.11)$$

The rate of energy due to the inclined traveling hinge lines is equal to the fully plastic bending moment times the rate of rotation $\dot{\omega}$ times the variable length of the hinge line $l = 2H/\sin\gamma$ gives

$$\dot{E}_3 = 4M_0 \frac{H^2}{r} ctg\psi_0 \cos\alpha \sqrt{(tg^2\psi_0 + \sin^2\alpha)}\dot{\alpha} \quad \ldots (6.12)$$

Integrating it further gives

$E_3 = 4M_0 \frac{H^2}{r} I_3(\psi_0, \alpha^*)$ where I_3 is a function of a and α^* which is represented as

$$I_3(\psi_0, \alpha^*) = ctg\psi_0 \int_0^{\alpha^*} \cos\alpha \sqrt{tg^2\psi_0 + \sin^2\alpha}\, d\alpha \quad ...(6.13)$$

In the second phase of the crushing process $\alpha \le \alpha \le \alpha_f$ the initially straight line at the hinge , is bent to accommodate the newly formed conical surface area 4 in Figure-6.5a. It is assumed that the material within the conical zone undergoes stretching in the meridional direction and can be defined as

$$\dot{E}_4 = \int_S N_0 \dot{\lambda}_{\theta\theta} dS \quad \ldots(6.14)$$

where S is a current area of the growing cone which uniquely depends on α^* . The final expression can be rewritten as (Abramowicz and Jones (1984))

$$\dot{E}_4 = 2M_0 V_t \frac{H}{t} \quad \ldots (6.15)$$

where V_t, corresponds to the rate of stretching of the arc in area 4 in Figure-6.5a and equals to

$$V_t = 2H\phi(\alpha, \alpha^*, \psi_0)\dot{\alpha} \quad \ldots (6.16)$$

where

$$\phi(\alpha, \alpha^*, \psi_0) = \frac{\sin\alpha^* tg\psi_0 \sin 2\alpha}{2(\sin^2\alpha^* + tg^2\psi_0 \sin^2\alpha} + (\psi - \psi_0)\cos\alpha$$

The total energy dissipation obtained by integrating Equation-6.16 in the limits (0, α^*) is:

$$E_4 = 4M_0 \frac{H^2}{t} I_4(\psi_0, \alpha^*) \quad \ldots (6.17)$$

where

$$I_4(\psi_0, \alpha^*) = \int_{\bar{\alpha}}^{\alpha} \left\{ \frac{\sin\alpha^* \sin 2\alpha \tan\psi_0}{2(\sin^2\alpha^* + \tan^2\psi_0 \sin^2\alpha)} + \left(\frac{\pi - 2\psi_0}{\pi} \beta \right) \cos\alpha \right\} d\alpha \quad \ldots (6.18)$$

Which is again a known function of ψ_0 and α^*

The rate of energy dissipation on the horizontal hinge line is the same as in phase I, Equation-6.10. The total energy then can be written as

$$\mathrm{E}_2 = 2M_0 C(\alpha_f - \alpha^*) \quad \cdots (6.19)$$

During the second phase of deformation, the inclined hinge B0 in Figure-5.6 is fixed in a material coordinate system and has constant length. The corresponding contribution to the rate of energy dissipation comes from bending in the stationary hinge line BO and equals to the fully plastic bending moment M_0 times the length of the hinge L times the rate of angular velocity $2\theta_1$ and equals to

$$\dot{E}_6 = 2M_0 H ctg\psi_0 \frac{\sin\alpha^* (\sin^2\alpha^* + tg^2\psi)_0}{\sin^2\alpha^* + tg\psi_0 \sin^2\alpha} \dot{\alpha} \quad \ldots (6.21)$$

while the total energy, obtained by integrating (21) in the limits (α^*, α_f) is

$$E_6 = M_0 H I_6(\psi_0, \alpha^*) \quad \ldots (6.22)$$

where

$$I_6(\psi_0, \alpha^*) = \frac{2}{\tan\psi_0} \int_{\alpha^*}^{\alpha f} \frac{\sin\alpha^* (\sin^2\alpha^* + \tan^2\psi_0)}{\sin^2\alpha^* + \tan^2\psi_0 \sin^2\alpha} d\alpha \quad \cdots (6.23)$$

For each given value of the angle ψ_0 the definite integrals I_1 through I_6 can be evaluated numerically if the magnitude of switching point $\alpha = \alpha^*$ is known. In general, α^* is defined by the optimality condition for a given structure and is unknown a priori. It can be noticed that remarkably that the concept of elements with floating boundaries has been decoupled from complex calculation of the rate of internal energy dissipation Equation-6.7 into a set of relatively simple "uniaxial" equations -6.9 and 6.22.

The global energy balance equation -6.5 for a given assembly of corner elements can be obtained by summing up the contributions of plastic mechanisms in a single corner element and then adding the energies of individual corner elements. Each contributing term has a different functional dependence on unknown parameters *r*, *H* and α^* and the generalised governing Equation-6.7 can finally be written in the form:

$$\frac{P_m}{M_o} = \left\{ B_1 \frac{r}{t} + (B_2 + B_5)\frac{C}{H} + B_3 \frac{H}{r} + B_4 \frac{H}{t} + B_6 \right\} - \frac{2H}{\delta_{eff}} \qquad \ldots(6.24)$$

where P_m represents the mean crushing force and M_o represents plastic moment per unit length, the coefficient B_1 through B_6 depend on α^* and ψ_0 . The corresponding coefficients take the form as $B_1 = 8I_1$, $(B_2+B_5) = 2\alpha_f$ which represents a total contribution of bending along horizontal hinge lines, $B_3 = 2I_3$, $B_4 = 4I_4$ and $B_6 = I_6$. The mean crushing load ***Pm*** is thus a function of three unknown parameters H, r, and C which are determined from the condition defined in Equation-6.3 in the range $0 < \alpha^* < \alpha_f$.

For the folding element as shown in the Figure- 6.5a and 6.6 assuming the clamped boundary condition on horizontal planes, the bending energy $(B_2 + B_5)$ should be doubled. Similarly the energies E_4 and E_6 should also be doubled because there are two conical surfaces and two inclined hinge lines in Figure-6.6. Then, the energy balance Equation-6.5 can be written in the form of Equation-6.24 with corresponding constants equal to $B_1 = 8I_1$, $(B_2+B_5) = 2\alpha_f$, $B_3 = 2I_3$, $B_4 = 4I_4$ and $B_6 = I_6$, respectively. It should be pointed out that the basic folding elements with clamped boundary conditions represent only one possible deformation path to reach the final fully crushed configuration. The magnitude of the switching point parameter α^* , which controls relative contributions of a quasi-inextensional and an extensional modes of deformations, depends strongly on the angle ψ_0 and the aspect ratio *C/t*. For complete corner element of SFE with acute angles of $\phi \leq \pi/2$ the corner angle($\phi = 2\psi_0$) the inextensional/asymmetric mode deformation would be dominant mode depending on the *C/t* ratio. While for obtuse angles of corner ϕ larger than 120 deg extensional/symmetric mode of deformation starts to control the crushing process. For the angles in the intermediate range both the modes exists with each mode contributing to the energy dissipation depending on the corner angle and C/t ratios [25].

For energy absorption purposes the quasi-inextensional mode is preferred as most of the plastic work is done by this mode and most of that crushing happens in the angular element with acute angles of corner angle ϕ (i.e $2\psi_0$) between 90 deg and 120deg. **Hence for**

maximum energy absorption with carefully chosen C/t ratio it can be inferred that the corner angles of thin walled members need to fall in the range of 90 deg and 120deg. This foundational understanding on the collapse of the corner element with SFE would not be complete if the understanding is extended beyond the single corner element towards multi corners which the next chapter would address. It also provides detailed explanation of the comparators for the designers and different measures of efficiencies for addressing the effectiveness of an energy absorbing device.

CHAPTER-7

7.0 Extension of the SFE to Multi cornered Sections

Having identified the basic mechanisms of Plastic energy dissipation in the previous chapter and developing the generalized form of emery balance equation, the calculation of the crushing resistance of thin-walled structural members can be assembled from the basic folding mechanism as in Figure-7.1. for most of the acute values of the central angle ϕ ($\phi = 2\psi_o$) , the switching point parameter α^*, which controls relative contributions collapse modes, approaches 90^0 and instigates the inextensional mode of collapse. The extensional model of collapse would be minuscule and confined to a small area which then has a small contribution to the energy dissipation process. However for the obtuse values of the central angle the extensional modes become predominant and would take over as the primary mode of energy dissipation.

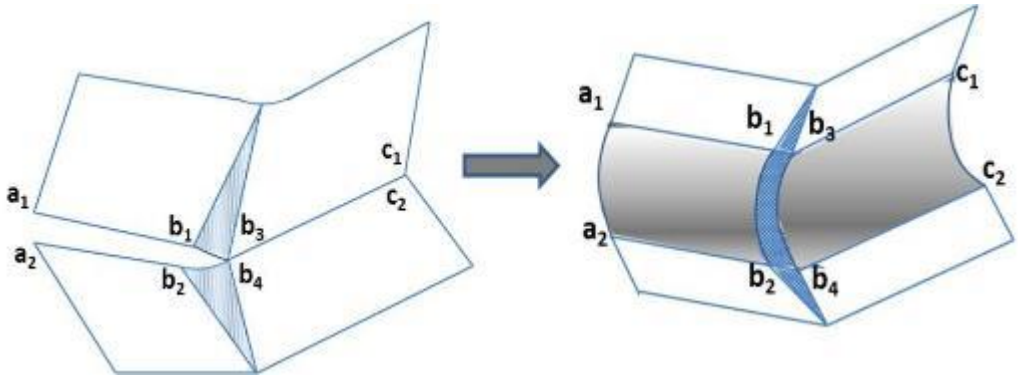

Fig. 7.1 Assemblage of two asymmetric modes with material discontinuity and fully consistent collapse

For the primary need of energy absorption, the quasi-inextensional mode is preferred as most of the plastic work is done by this mode with majority of crushing happening in the angular element with acute angles of corner angle ϕ (i.e 2 ψ_0) between 90 deg and 120deg [31,38]. In the design of the thin walled sections for energy absorption purposes the central angle is thus, should be confined to the range 90 deg and 120deg for maximum effect.

The global energy balance equation by Abramowicz [25, 27] for a given assembly of corner elements can be obtained by summing up the contributions of plastic mechanisms in a single corner element and then adding the energies of individual corner elements. Each contributing term has a different functional dependence on unknown parameters, average rolling radius**, *b***, plastic folding wave ,2*H*, and switching point parameter α^* so that the governing equation (6.24) can be written in the form:

$$\frac{P_m}{M_o} = \left\{ B_1 \frac{r}{t} + (B_2 + B_5)\frac{C}{H} + B_3 \frac{H}{r} + B_4 \frac{H}{t} + B_6 \right\} - \frac{2H}{\delta_{eff}}$$ where P_m represents the mean crushing force and M_o represents plastic moment per unit length while coefficients B_1 through B_6 are dependent on α^* and ϕ. This equation is further simplified by setting the switching parameter $\alpha^* = \alpha_f = \pi/2$ and assuming the clamped boundary conditions on horizontal planes Figure-7.1 , The balance equation then can be re written to the form:

$$\frac{P_m}{M_o} = \left\{ B_1 \frac{r}{t} + B_2 \frac{C}{H} + B_3 \frac{H}{r} \right\} - \frac{2H}{\delta_{eff}} \qquad \ldots(7.1)$$

The coefficients B_4 and B_6 vanish due to lower and upper limits of integration in evaluating of α^* while the coefficient (B_2+$B5$) representing the bending contributions becomes 2 α_f. This expression involves two unknown parameters of H and r which can be further determined by setting minimum conditions for least mean crushing force

$\frac{\partial P_m}{\partial H} = 0$, $\frac{\partial P_m}{\partial r} = 0$ and the solution is obtained as

$$r = \sqrt[3]{B_1 B_3 / B_1^2}\ \sqrt[3]{Ct^2}\ , \quad H = \sqrt[3]{B_2^2 / B_1 B_3}\ \sqrt[3]{C^2 t}$$

Putting back in to the equation -7.1 we obtain , $\frac{P_m}{M_o} = 3\ \sqrt[3]{B_1 B_2 B_3}\ \sqrt[3]{C/t}$ … (7.2)

while M_0 can be related to energy equivalent flow stress flow stress σ_0 as $M_0 = \frac{\sigma_0 t^2}{4}$

where σ_0 can be approximated to $0.92\sigma_u$.

This is an important result which explains major contribution of the inextensional deformation mode in dissipating two thirds of plastic energy at stationary and moving plastic hinge lines. The extensional deformations are confined to small fractional area of the shell and dissipates remaining one third of the energy. The expression (7.2) can be used in conjunction with the rate of energy balance equation to derive the load-deflection characteristics of the structural member there by its energy absorbing characteristics

7.1 Extension to multi-corner Sections

As indicated in the above consideration for the single corner element, **the efficiency of the structure in energy absorption is majorly dependent on the number of corner elements that are capable of collapsing predominantly in inextensional mode, accommodated into**

the section of consideration. It is therefore desirable to develop and design thin-walled structures for energy absorption with multiple corners for weight efficient energy absorption. For multi-corner columns, due to the complicacy in dealing with achieving the desired multi cornered feasible members into a production phase not much study was focused in practically achieving such compatible progressive buckling structures. With good advancements in recent Design and manufacturing technologies and efficient use of CAE techniques an attempt is made in this research on multi cornered structures of the energy absorption.

Wierzbicki and Abramowicz[25] presented theoretical basis and according to them the above method can be used to predict the crushing resistance of prismatic columns (square, hexagonal, rhomboidal etc.) composed of *n* identical corner elements. For such columns, the compatibility conditions on horizontal and vertical planes are always fulfilled and the final crushing resistance would be made of one element's crushing force times the number of corner elements, *n.*

7.2 Square/Rectangular Sections

Extending this single corner element theory received a great deal of attention in the literature in view of its obvious application in controlling the process of energy absorption by automobile bodies during a front or rear-end collision. The collapse mechanism of a rectangular column can be modeled with a good accuracy by an assembly of four basic folding mechanisms, each of the length C. The crumpling process of a rectangular tube is progressive, each new fold is being formed after the previous one is completed, Figure-7.2. The corresponding force-shortening characteristics exhibits fluctuations around a mean value with peaks and valleys positioned at regular intervals 2H

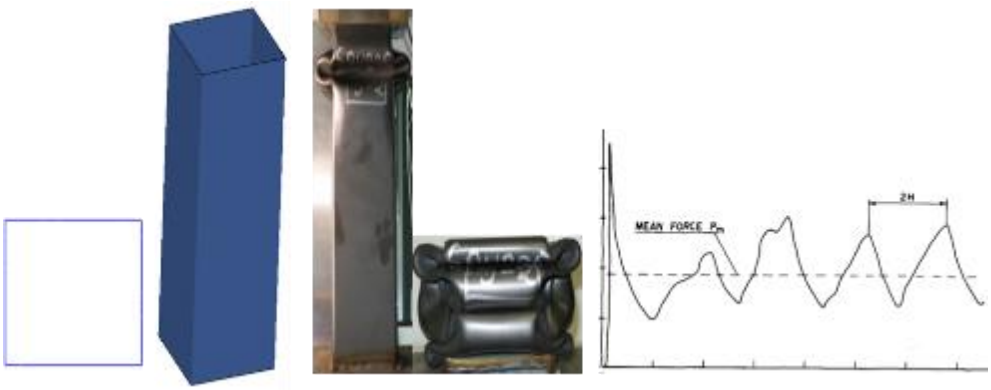

Fig. 7.2 Crumpling of Rectangular column and Force-displacement characteristics

The energy absorption of the member is thus well characterized by the mean crushing for *Pm.* The dimensions of the rectangular cross section C x *d,* the wall thickness t, the corner angle ϕ = 90 deg between plates, and the flow stress σ_0 are all considered known. The sought-off quantities are the mean crushing force *Pm, the* wavelength *H,* and the rolling radius *r.*

Since four basic folding elements make up the rectangular section, all energies, calculated above should be multiplied by four. In the particular case of an inextensional mode of deformation ($\alpha_f = \pi/2$) the solution to Equation-6.24 can be obtained in a simple analytical form, In this case, the coefficients B_1 through B_3 in Equation-6.24 equal to B_1 =4.44, B_2 = π and B_3 =2.30, respectively and the numerical solution for ***Pm/M₀*** can be written as :

$$\frac{P_m}{M_o} = 52.22\,(C/t)^{0.33} \qquad \ldots(7.3)$$

and this result can be applied for all quasi-in extensional, symmetric mode of deformations.

Substituting for energy equivalent flow stress flow stress σ_0 as $M_0 = \frac{\sigma_0 t^2}{4}$ the equation for mean crushing force can be further simplified to

` $$P_m = \mathbf{13.055}\ \sigma_0\ t^{5/3} C^{1/3} \qquad \ldots(7.4)$$

While the length of plastic fold wave can be calculated from Equation-6.26 as H= 0.97 $\sqrt[3]{tC^2}$

A higher fractional power in the present improved solution, equation (7.4), reflects a larger contribution of extensional deformation into the total energy dissipation

7.3 Hexagonal Sections

The previous research done by Abramowicz, Wierzbicki and Norman Jones [24, 25, 26, 27, 29, 36] was pretty much limited to circular tube and Square columns. However utilizing the generalized governing equation developed for Single corned element, the SFE concept cam be further extended for increased collapse efficiency towards regular shapes of Hexagon, Octagon and multi edged columns with a clear focus on achieving the asymmetric collapse within the between 90 deg and 120deg. The collapse mechanism of a Hexagonal column can be modeled with a good accuracy by an assembly of six basic folding mechanisms, each of the length C and with corner angle ϕ = 30 deg., and is shown in Figure-7.3

Fig. 7.3 Crumpling of Hexagonal thin walled section with 6 corner elements

Similar to the Square columns the mean crushing force for a hexagonal column the non-dimensional solution P_m / M_0 for various C/t aspect ratios can be approximated by the function :

$$\frac{P_m}{M_o} = 78.34\left(C/t\right)^{0.4} \qquad ...(7.5)$$

It can be noted that this expression as compared to the square columns has slightly higher fractional power indicating larger contribution of extensional deformations to the crushing resistance of hexagonal columns. Substituting for energy equivalent flow stress flow stress σ_0 as $M_0 = \frac{\sigma_0 t^2}{4}$ the equation for mean crushing force can be written as :

$$P_m = 19.58\ \sigma_0\ t^{1.6} C^{0.4} \qquad ...(7.6)$$

While the length of plastic fold wave can be calculated from Equation-7.2 as

$H = 0.988\ \sqrt[3]{tC^2}$

7.4 Octagonal Sections

The collapse mechanism of an Octagonal column can be modeled with a good accuracy by an assembly of eight basic folding mechanisms, each of the length C and the angle ϕ = 135 deg., as shown in Figure-7.4.The collapse might then be a mixed mode.

Fig. 7.4 Crumpling of Octagonal thin walled section with 8 corner elements

Similar to the Square columns the mean crushing force for an Octagonal column can be obtained by multiplying 8 the mean crushing strength of angle elements. The non-dimensional solution P_m / M_0 for various C/t aspect ratios can be approximated by the function:

$$\frac{P_m}{M_o} = 104.3\left(C/t\right)^{0.4} \qquad \ldots(7.7)$$

It can be noted that this expression as compared to the square columns has slightly higher fractional power indicating larger contribution of extensional deformations to the crushing resistance of octagonal columns. Substituting for energy equivalent flow stress flow stress σ_0 as $M_0 = \frac{\sigma_0 t^2}{4}$ the equation for mean crushing force can be written as:

$$P_m = 26.11\ \sigma_0\ t^{1.6} C^{0.4} \qquad \ldots(7.8)$$

While the length of plastic fold wave can be calculated from Equation-7.2 as H= 0.988 $\sqrt[3]{tC^2}$

7.5 Ideation and Design of 12-Edge- Section

With the current trends and future road map of crash regulatory and public domain requirements on Vehicle Crash & occupant Safety from NHTSA, ENCAP and IIHS it's very much evident that there is tremendous need for improving vehicle crash energy performance of vehicles. With the advent of Electric & hybrid vehicles it becomes more of a challenge and with trends to keep the vehicle structure lighter the need for enhanced vehicle safety is inevitable. These modern day vehicles target to be lighter which aggravates occupant responses to crash and also restrict the crash energy absorption to front end structure only. The slight sharing of this energy as possible in conventional vehicle is not possible due to the fact that the occupant compartments floor is utilized to package the battery packs which have to protected at all times.

With this in back ground and utilizing the best capabilities of thin walled sections under dynamic progressive buckling with the inferences of this research (section 6.1) motive to develop prismatic multi edge sections with maximum number of stable corner elements within the package space, an ideation of 12 edge section was considered. The ideation was then developed into mature concept using the powerful tools of CAE with Ls-Dyna as the code for explicit FE analysis.

Starting from the package space of the octagon section as discussed in the previous section, the number of corner elements can be increased twelve keeping the same thickness and length of the specimen. This increase in number of corner elements should also provide stable

crushing mechanism in predominantly asymmetric mode for high plastic work. Keeping this as the aim the corner angle was targeting to be around 90 and 120 deg (as derived in the previous chapter). The Figure-7.5 below indicates the process by which the corner angle and stable response was achieved.

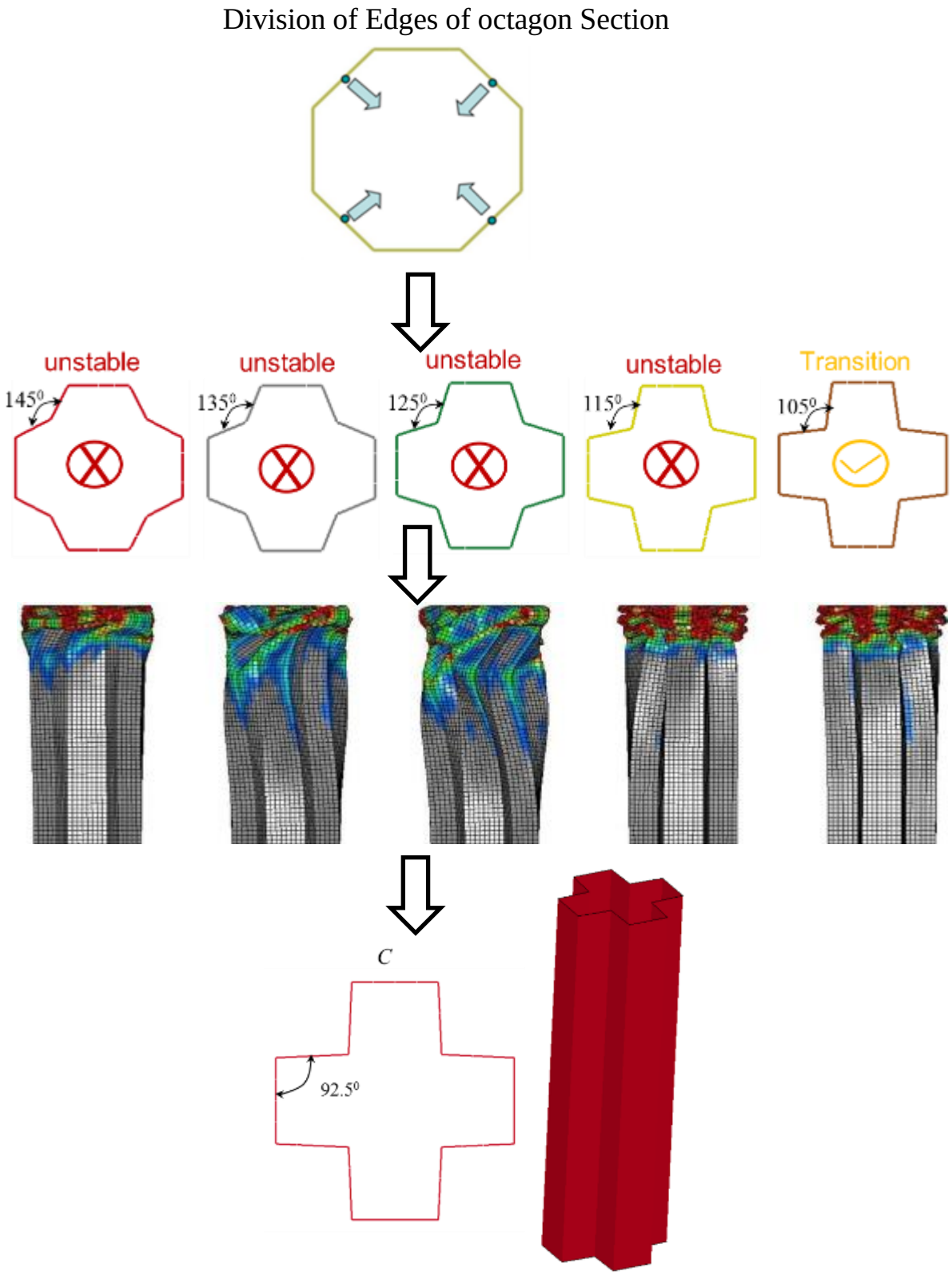

Fig. 7.5 Development of stable corner elements for 12-edge sections from the package space of octagon section

With the division of the edges of an octagon section a new 12 edged section was developed and this sections can be treated similar to the previous sections and the expression for mean force can be derived with assemblage of 12 corner elements. The non- dimensional solution P_m / M_0 for various C/t aspect ratios can be approximated by the function:

$$\frac{P_m}{M_o} = 156.48\left(C/t\right)^{0.334} \quad \ldots(7.9)$$

It can be noted that this expression closely resembles the rectangular column with corner angles closer to 90deg and ensure the dominance of asymmetric mode of collapse. The equation for mean crushing force can then be written as

$$P_m = \mathbf{39.12}\ \sigma_0\ t^{1.67} C^{0.34} \quad \mathbf{...}(7.10)$$

While the length of the plastic fold wave can be still calculated with H= 0.9889 $\sqrt[3]{tC^2}$.

This is an extremely important derivation as it clearly shows at theoretical level the this section has a capacity potential of about 50% higher than octagon and more than double than equivalent rectangular sections. The developed section holds the corner angle at 92.5 deg and ensures asymmetric mode of collapse for a properly chosen *C/ t* ratio. Further discussion on the performance of this section and practical achievement of this section is presented in the next chapters.

7.6 Design Parameter evolution and Analysis

Within the framework of design for energy absorption and weight reduction there are two key parameters which most of the OEMS consider in developing their front end energy absorbing structures. The most important term, the specific energy absorption, can be defined as the ratio of the total energy that is dissipated to the specimen mass. For an ideal energy absorber it is related to the mean collapse load P_m by the relation:

$$SEA = E_s^c = \frac{\int P dx}{V\rho} = \frac{P_m}{A_s \rho} \quad ...(7.11)$$

where V is the volume of the specimen, A_s is the material area of the section and ρ is the density of the material. Although SEA serves as good comparator for the effectiveness of the

section in consideration, usage of this expression for design seriously ignores the contribution of material parameters and for thin walled structures absorbing energy it is necessary to identify both material and geometric contributions to specific energy absorption. Structures of a given weight and made from same materials are not necessarily equally effective in their resistance to deformation. Since at fixed geometry, the energy absorbing capacity increases linearly with specific ultimate tensile strength. A parameter ***"structural effectiveness"*** can be defined at this juncture to address this as $\eta = E_s^c / \sigma_u^s$ to eliminate the contribution of material to the specific energy absorption there by geometric factor alone can be assessed.. This can be further simplified as:

$$\eta = E_s^c / \sigma_u^s = \frac{P_m}{A\sigma_0} \qquad ...(7.12)$$

where, σ_0 is characteristic stress (Abramowitz and Jones [23]) and can approximated to $(\sigma_y + \sigma_u)/2$ where σ_y and σ_u are the yield and ultimate tensile stresses, respectively. Pugsley, Magee and Thornton [41 42] further enhanced this structural effectiveness by linking this to structural density or solidity ratio ϕ=(Volume of the material / volume enclosed by the structure). Since $\sigma_u^s = \sigma_u / \rho$ and the collapse load can be written as:

$$P_m = \eta\ \sigma_u \mathrm{A} = \eta\ \sigma_u\ \phi\ A_0 \qquad ...(7.13)$$

The structural effectiveness relations based of the mean force estimations from previous sections and their linking expressions to solidity ratios are derived and refined further to be tabulated in table-7.1 as below;

Table-7.1 Derived expressions for solidity ratio ϕ and structural effectiveness *n*

Section Type	Dimension	Mean Peak force(P_m)	Solidity ratio(ϕ)	Structural effectiveness(η)
Square	**Side C**	**13.055** $\sigma_0\ t^{1.6} C^{0.3}$	$4t/C$	**1.29** $\phi^{0.6}$
Hexagon	**Side C**	**19.58** $\sigma_0\ t^{1.6} C^{0.4}$	$4t/(\sqrt{3}C)$	**1.97** $\phi^{0.6}$
Octagon	**Side C**	**26.11** $\sigma_0\ t^{1.6} C^{0.4}$	$8t/5C$	**2.54** $\phi^{0.6}$
12 Edge	**Side C**	**39.12** $\sigma_0\ t^{1.67} C^{0.34}$	$12t/5C$	**1.93** $\phi^{0.6}$

The second parameter is the Collapse efficiency, which is a measure of how much of the structure is available to absorb the energy. Collapse efficiencies can be defined either on Geometry, load or energy absorbing basis. Because of the nature of buckling process, not all

of the energy absorbing structure is usable; ultimately a point is reached where the structure has completely flattened and the load rises rapidly. Three measures of energy absorbing efficiency, which can be identified as:

The geometric or Crush efficiency $\boldsymbol{S_E}$ is a measure of the packing of the folds during collapse and is given by the ratio of the actual compression to the original length as

$$S_E = \frac{\delta_{\max}}{l_0} \qquad ...(7.14)$$

where l_0 is the original length of the member. The second measure of efficiency is related to the load fluctuations which can occur during the collapse process. The Crush force efficiency $\boldsymbol{A_E}$ is defined by

$$A_E = \frac{P_m}{P_{\max}} \qquad ...(7.15)$$

where P_m is the mean collapse load while $P_{\max}$ is referred to the highest force on the force-displacement curve. The third measure is Energy efficiency $\boldsymbol{E_E}$ which is related to the actual energy absorbed, given by the area A under the force deflection curve and can be written by

$$E_E = \frac{A_{f-d}}{P_\delta l_0} \cong \frac{P_m \delta_c}{P_\delta l_0} \qquad ...(7.16)$$

The magnitude of these measures will be affected by the magnitude and number of fluctuations in the load which occur during the collapse process. Hence, these efficiencies will provide a good direction to the design of collapse structures for energy absorption.

The detailed theoretical foundations from this chapter needs to be evaluated and refined through state of art analytical methods using the numerical simulations using the nonlinear finite element code Ls-Dyna. Usage of the code without any assessments of the inbuilt capabilities of the shell elements would not be logical. Benchmark tests for assessing their stability, reliability, accuracy and robustness are to be done for selection of right elements which forms the core of the next chapter along with aspects for material characterisations.

CHAPTER 8

8.0 Numerical characterization & validations with CAE

(Non-linear finite element analysis)

8.1 Performance evaluation and Selection of Ls-Dyna shell elements

With the usage of Ls-Dyna explicit code for numerical characterization, it is imperative to explore and establish the robustness of the shell elements. The development of a reliable and simple to use shell elements for modeling thin shell structures has been a challenging task for researches, for several decades. Shell elements should be able to model both plane stress and plate bending phenomena and should pass the tests used to evaluate plane and plate elements Due to increasing importance and extensive use of these shell structures in many of the automobile, Nuclear, aerospace and ordnance companies, by Govt., and Corporate labs and research organizations, good amount research has been carried out and many elements have been formulated based on three distinct approaches. They are as follows:

1. Facet representation using flat plate elements.
2. Shell element based on shell theory.
3. Degenerated shell element.

Among these three types of elements, the degenerated shell element has become very popular due to its efficiency, generality and simplicity compared to other shell elements. The concepts, advantages and disadvantages of these shell elements are discussed in the following chapters.

8.2 Shell Formulations

8. 2.1 Flat Elements

The earliest attempt at constructing suitable shell element was based on the superposition of stretching behavior (membrane element) and bending behavior (plate bending element that enforces Kirchhoff's hypothesis). In uncoupled condition adequate response can be derived for either membrane or bending. It grossly under performs in the cases where the membrane and bending stiffness are strongly coupled. The advantages and disadvantages of using the flat element for modeling the shell behavior are:

Advantages:

- Simple to formulate.
- Easy to define input data for geometric description.
- Blending with other element types
- Rigid body motions could be modeled without inclusion of strains

Disadvantages:

- Exclude the coupling of membrane and bending effects due to absence of curvature.
- Being a flat element the bending moment at element boundaries are not continuous.
- General shells treatment is with triangular shaped elements only
- Cannot be applied to imperfection sensitive structures due to geometric approximation.

8.2.2 Shell Theory and Elements

Curved shell elements based on specific shell theories have been developed to overcome the limitation of flat elements. Different shell theories are available and by carrying out approximation to different degree, while reducing the 3-D field equations to a particular class of shell equations using analytical integration over the thickness. These elements involve three displacements and their derivatives w.r.t the local coordinates. This resulted in an element with 12 d.o.f for each of four nodes. The advantages and disadvantages of shell theory based elements are summarized below:

Advantages
- Includes the coupling of membrane and bending effects.
- No discontinuity of geometries in representing a curved surface.

Disadvantages

- Difficulties in choosing an appropriate shell theory as there are a very large number of such theories being available.
- Applicable for a particular type of geometry, either cylindrical or spherical.
- Difficulties in achieving the inter element compatibility condition, as the shell theory elements needed C^1 continuity.

8.2.3 Degenerated Shell Element

The concept of degenerated shell element was first introduced by Ahmad (1970) to extend the parametric element concept. By discretizing the three dimensional equations of continuum mechanics the process of degeneration begins. By introducing the assumption that original normal to the middle surface are inextensible and remain straight, and the stress in the normal direction is zero, the three dimensional formulation can be degenerated.

The element retains a measure of transverse shear deformation and hence it is a Mindlin type of element requiring only C^0 continuity. The displacements and rotations of the shell mid-surface are taken as degrees of freedom. The degenerated shell element was considered as an important breakthrough in the finite element analysis of shells. The different integration schemes for the numerical integration in the *r-s* plane for evaluating the element matrices are shown in Figure- 8.1 below. The advantages and disadvantages of the degenerated shell element are given below:

Advantages

- Simple to formulate.
- Applicable for any geometry and shape.
- Capture the coupling effect between membrane and bending actions.
- Independent of complex shell theories.

Disadvantages

- Applicable for thick shells, when full integration is used to evaluate the stiffness matrix.
- Suffers the problem of membrane and shear locking, when the element is used for thin shells, with full integration.

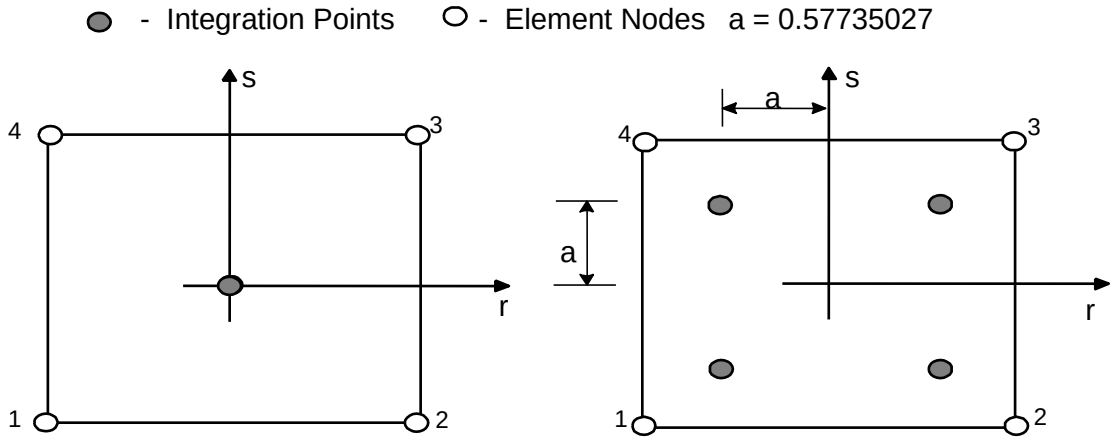

Reduced Integration Full Integration

Fig. 8.1Integration schemes for Shell Elements

8.3.0 LS-DYNA Shell Formulations

Before going on great guns with the usage of elements there is a need to understand the behavior of different elements. One should make an attempt to test the elements in the software to be sure of their validity, Sensitivity to shape distortion and behavior in example

problems for which the results are known in advance. LS-Dyna has eight shell elements of different formulations [72]. They are:

ELFORM1: HUGHES - LIU
ELFORM2: BELYTCHKO - TSAY (DEFAULT)
ELFORM6: S/R HUGHES - LIU
ELFORM7: S/R CO-ROTATIONAL HUGHES - LIU,
ELFORM8: BELYTCHKO - LEVIATHAN SHELL
ELFORM10: BELYTCHKO - WONG - CHIANG
ELFORM11: FAST (CO-ROTATIONAL) HUGHES-LIU
ELFORM16: FULLY INTEGRATED SHELL ELEMENT

8.3.1 Formulations: HUGHES – LIU

In Ls-Dyna the first shell element to be implemented was the HUGHES-LIU SHELL **(ELEFORM1)**. It is a made up of four nodes with uniformly reduced integration. This element is developed from by degenerating the standard 8-node brick element formulation as shown in Figure-8.2. The Qualities of this element are:

- computational efficiency and robustness due to its simplicity
- Compatibility with brick elements due to its generation from 3D brick element.
- Inclusion of finite transverse shear strains
- Good treatment of finite strains due to its incrementally objectivity with rigid body rotations generating no strains

The spurious energy mode sand zero energy modes issue which become active due to in sufficient boundary conditions and has been overcome by a refinement and its termed as **HUGHES –LIU WITH SELECTIVELY REDUCED INTEGRATIN (ELFORM6)** as shown in Figure-8.3 below. And also an inner loop 3 is added to increase the reliability and accuracy as shown below

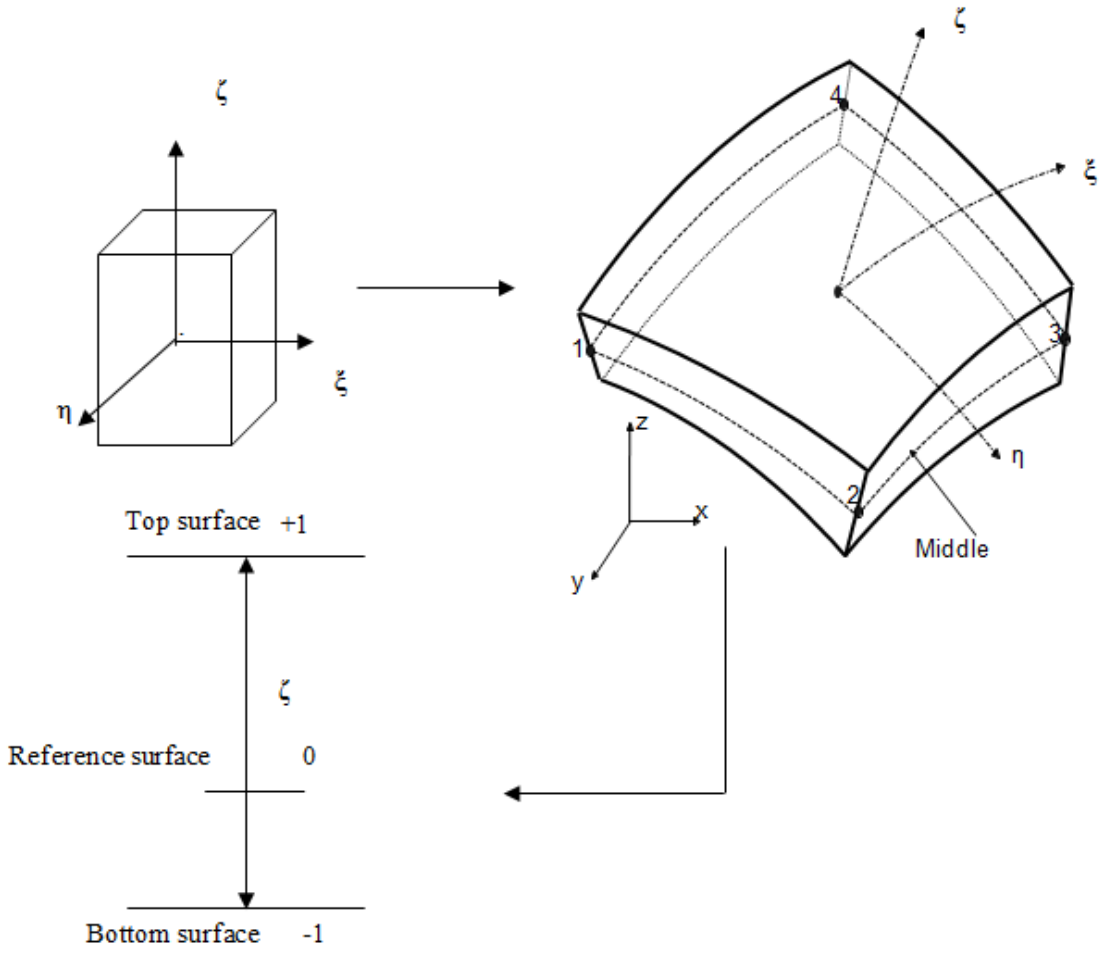

Fig-8.2 Mapping of bi-unit cube into Hughes-Liu shell element

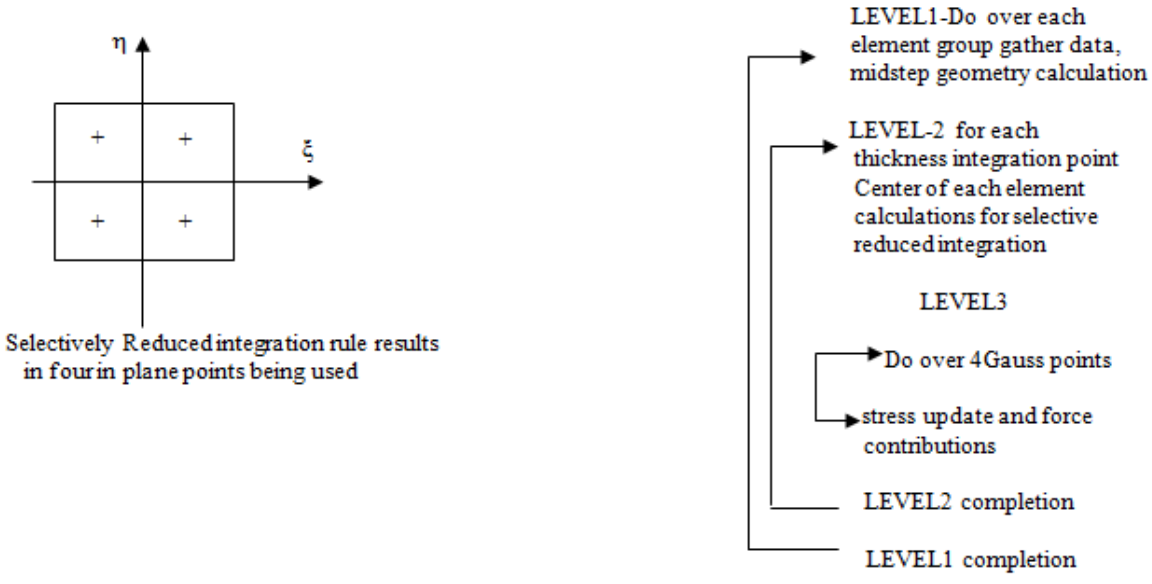

Fig. 8.3Inner loop for increased reliability of Elements

Further refinement to improve the speed and the reduction in number of operation was done and it is referred as the **S/R CO-ROTATIONAL HUGHES – LIU (ELFORM7) AND FAST CO-ROTATIONAL HUGHES SHELLS (ELFORM11).** Simplifications make this shell effective and cheaper:

- Strain rates updates are not central. The computation of the strain displacement matrix only happens at time n+1 and not at time n+1/2
- The transformations between the local and global coordinate systems is removed by storing the stresses in local shell system
- To avoid more computations the Jaumann rate rotation is also not performed

The Hughes-Liu shell element formulation is available in four variations as below

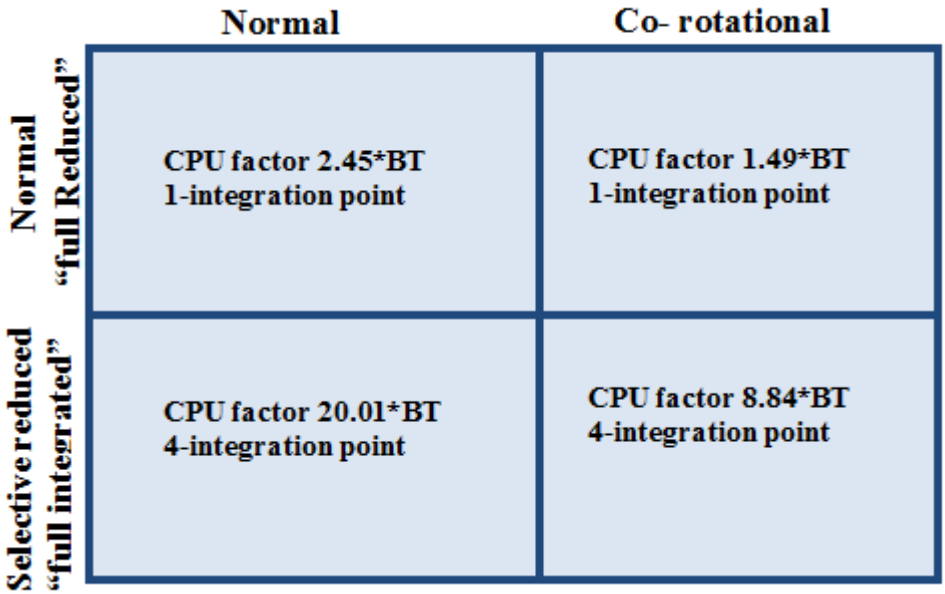

8.3.2 Belytchko - Tsay (default): ELFORM2

To improve the computational efficiency and robustness an alternative to Hughes-Liu shell element in the form of **Belystschko-Lin-Tsay** shell element was implemented [10]. The simplicity of these elements comes from a combined C0-rotational and velocity strain formulation and predominantly flat geometry. Two kinematic assumptions lead to mathematical simplification and made this element very efficient. A coordinate system was embedded into the element to avoid the complexities of nonlinear mechanics the constitutive evaluation is reduced to Cauchy Stress by providing the choice of velocity Strain or rate of deformation in the formulation. To suppress the serious zero energy modes or spurious energy modes termed as Hourglass energy modes that come inherently with one point quadrature, the physical stresses are added with hourglass viscosity stresses at the local element level. Though this element is computationally fast, this element will give wrong

results for warping due its flat geometry assumption and should not be used where there is warping. A further improvement to this element is the **BELYSTSCHKO-WONG-CHIANG (ELEFORM10) ELEMENT.** This element is improved version of the default formulation with warping stiffness and also an improved transverse shear treatment is given. Still further improvement is made to the Default element with physical hourglass control. This element is **BELYSTSCHKO-LEVIATHAN (ELFORM8)**. Infact this is new element and is still in development.

8.3.3 Fully integrated Shell Element (ELFORM 16)

The load of hourglass modes comes along with the usage of reduced integration elements which are with one point integration. There are nine zero energy modes for the reduced integrations element shell with four nodes and with six degrees of freedom per node. If these are not properly constrained or controlled then they propagate erroneous results affecting the overall response and accuracy of the solution. One way of it is by using full integration scheme. Though this element is free of spurious energy modes, it exhibits serious locking phenomena for these plates/beam/shell applications. Though this element is computationally costlier it however yields results with accuracy when good mesh density and selective application is employed.

8.4.0 Problem Description

In order to evaluate the performance of these shell elements, numerical testing was carried out involving all the eight different formulations of shell elements. The standard benchmark Problem of Pinched hemisphere [12] with concentrated load is selected to assess the performance of the program. The effectiveness of these elements is compared with the exact analytical solution.

The pinched hemispherical shell is widely used to test shell elements. It is used as test problem for the analysis of doubly curved shell. The shell is subjected to self-equilibrating concentrated load. Rigid body rotations constitute significant amount of deformation for this problem. The geometric and loading details are shown in Figure-8.4. The mesh pattern specified for this problem is obtained by dividing the quadrant of the hemisphere into three pieces, each of which is modelled by an n x n mesh. The loading is given to the model in a ramped for 0.2sec and continued till 0.4secs. The convergence of displacement of these elements are compared with each other and depicted in graphical form.

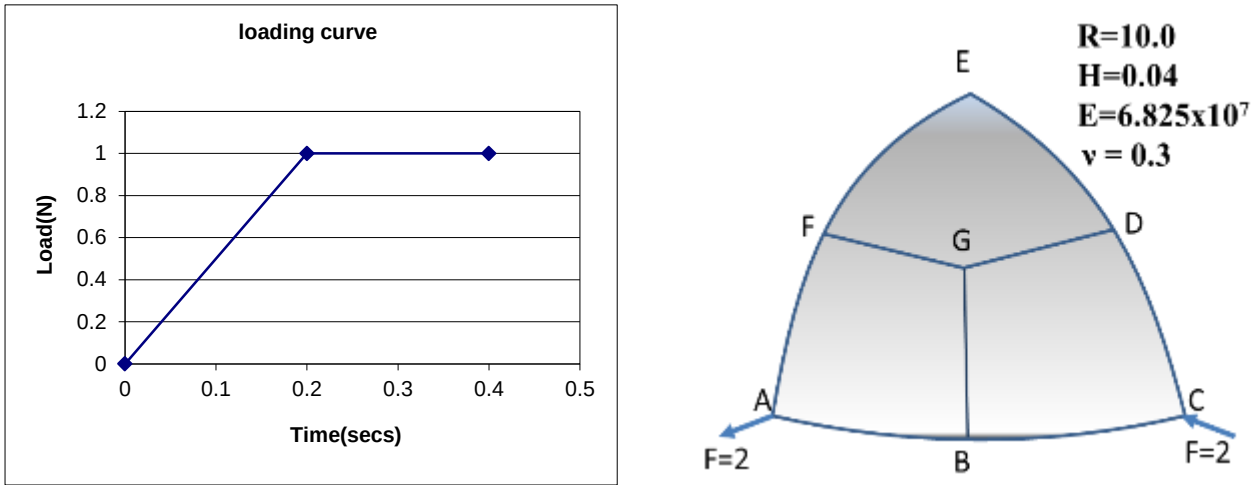

Fig. 8.4 Geometry and loading of pinched hemispherical shell

8.5.0 Investigation-Results and Discussion

The problem is run with different elements formulations for different mesh sizes. A typical FE model with 4x4 mesh density is as shown in the Figure-8.5. LS-Dyna971 with one CPU is used as the solver. The displacement at the loading point along with respective CPU timings are tabulated in tables-8.1 and 8.2 and also presented in graphical form Figures-8.7, 8.8 and 8.9.

- It is found from the results, though it is fast, the **Elform2**, which is the default element exhibits a behavior, which is not confirming to the exact result. It is not able predict the results due to the warping associated with the problem.
- The **Eleform16**, which is a fully integrated Shell element, exhibits serious locking problem when it is used for lower mesh densities. Its performance with higher mesh densities is good and in conformance with the theoretical result.
- The **Eleform8** which is a new element and still under development also deviates from the exact result to a considerable extent.
- The **Elform10** which takes in warping and also the transverse shear effect predicts the results in conformance with the theoretical value very fast even ate lower mesh densities and is recommended for the problems with serious warping considerations.
- The **Elform6** though it converges near to the exact value it is computationally expensive as it takes more CPU time.
- In this testing process the **Elform1**, **Elform7** and **Elform11** also converged to the exact value but with varying CPU timings.

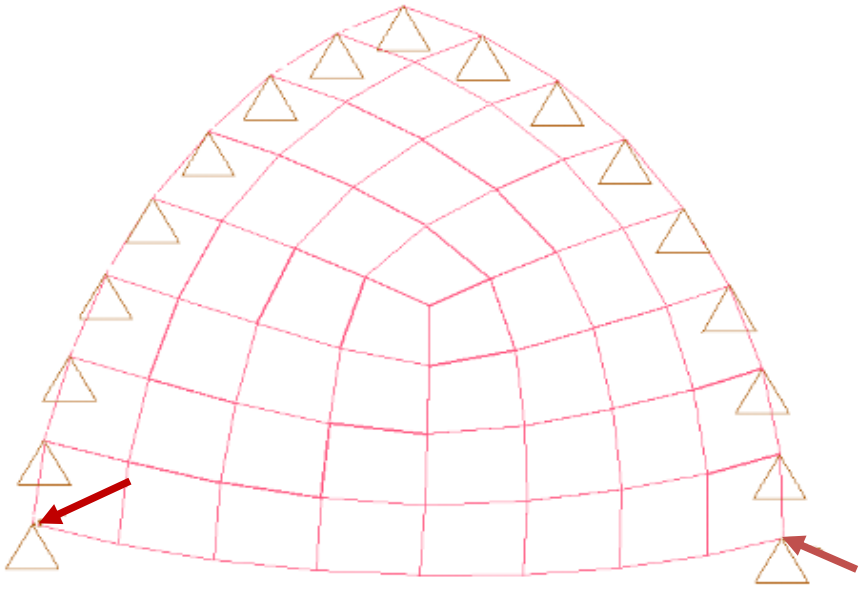

Fig. 8.5 Finite element Model with 4x4 mesh pattern of Pinched Hemisphere

Table-8.1 Displacement convergence for Element formulations for NxN mesh

Mesh	ELFORM1		ELFORM2		ELFORM6		ELFORM7	
	Disp.	Norm.Disp	Disp.	Norm.Disp	Disp.	Norm.Disp	Disp.	Norm.Disp
2	0.10141	1.0975	0.13177	1.426082	0.06912	0.748052	0.055702	0.60284
3	0.09625	1.041667	0.14658	1.586364	0.09225	0.998377	0.088295	0.95557
4	0.09546	1.033095	0.14874	1.60974	0.09342	1.011039	0.091771	0.99319
5	0.09440	1.021645	0.14862	1.608442	0.09317	1.008333	0.096784	1.04745
6	0.09322	1.008874	0.13902	1.504545	0.09202	0.995887	0.090977	0.9846
8	0.09465	1.024351	0.1399	1.514069	0.09375	1.01461	0.093065	1.0072

Mesh	ELFORM8		ELFORM10		ELFORM11		ELFORM16	
	Disp.	Norm.Disp	Disp.	Norm.Disp	Disp.	Norm.Disp	Disp.	Norm.Disp
2	0.12427	1.344913	0.092751	1.003799	0.101424	1.097662	0.03542	0.383333
3	0.120515	1.304275	0.092988	1.006364	0.096775	1.047348	0.07568	0.819048
4	0.1208	1.307359	0.092565	1.001786	0.095453	1.033041	0.08714	0.943117
5	0.12187	1.318939	0.092212	0.997965	0.09442	1.021861	0.08974	0.971169
6	0.12621	1.365909	0.09371	1.014177	0.09583	1.037121	0.08916	0.964881
8	0.124055	1.342587	0.093154	1.00816	0.094658	1.024437	0.09117	0.986699

Table-8.2 Comparison of CPU timings for Element Formulations for a 4x4 mesh

Elements	**Cpu. Time (sec)**	**Comparison with ELform2**
ELFORM1	153.98	2.44064
ELFORM2	63.09	1
ELFORM6	1238.8	19.63544
ELFORM7	654.78	10.37851
ELFORM8	99.92	1.583769
ELFORM10	88.21	1.398161
ELFORM11	122.07	1.934855
ELFORM16	196.7	3.117768

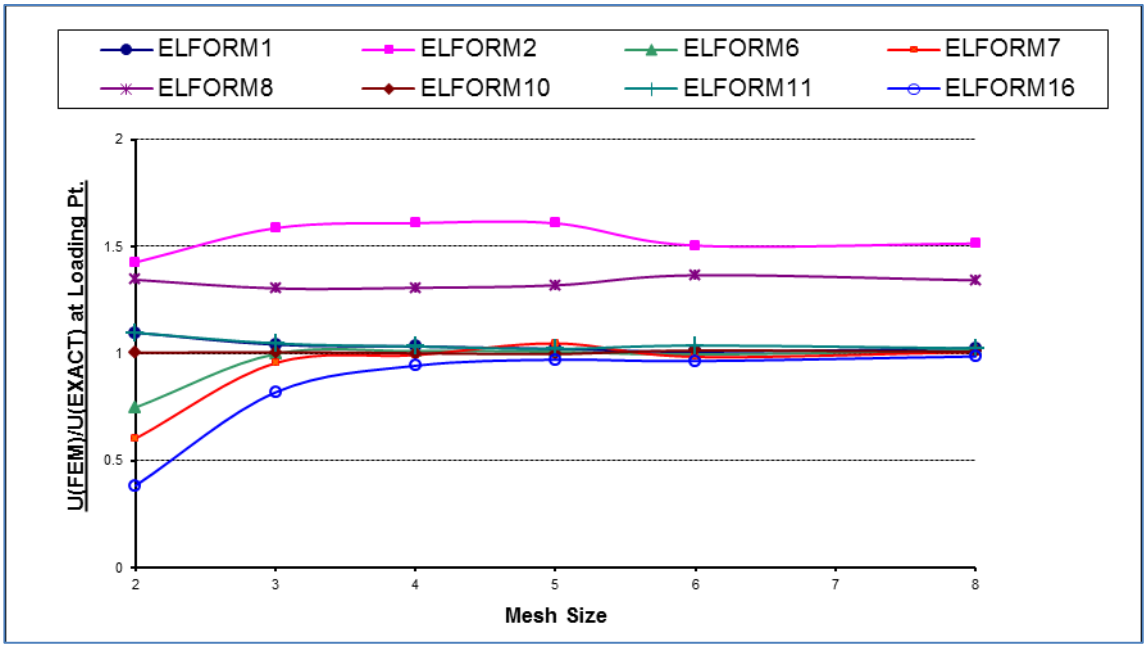

Fig. 8.6 Displacement Convergence for Pinched Hemisphere

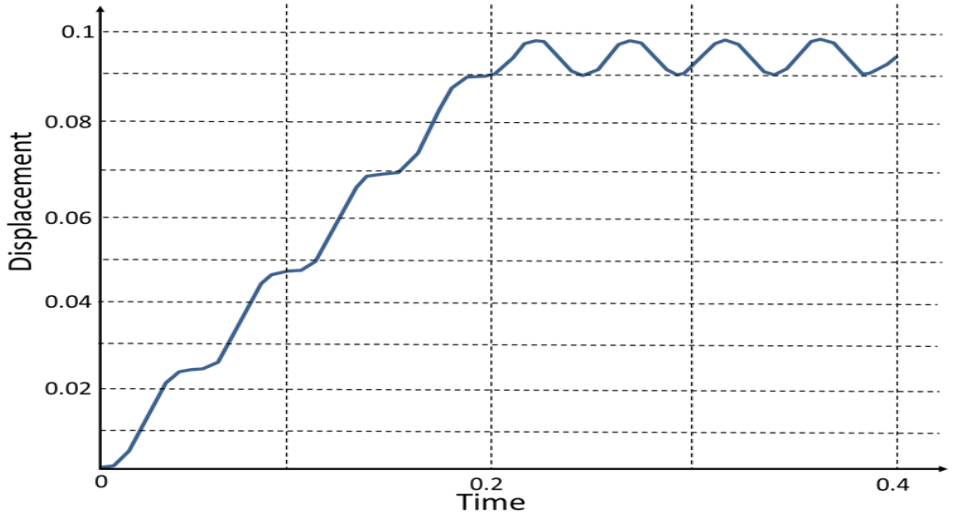

Fig. 8.7 Plot of Output Displacement Vs Time at the loading Point for (ELFORM10)

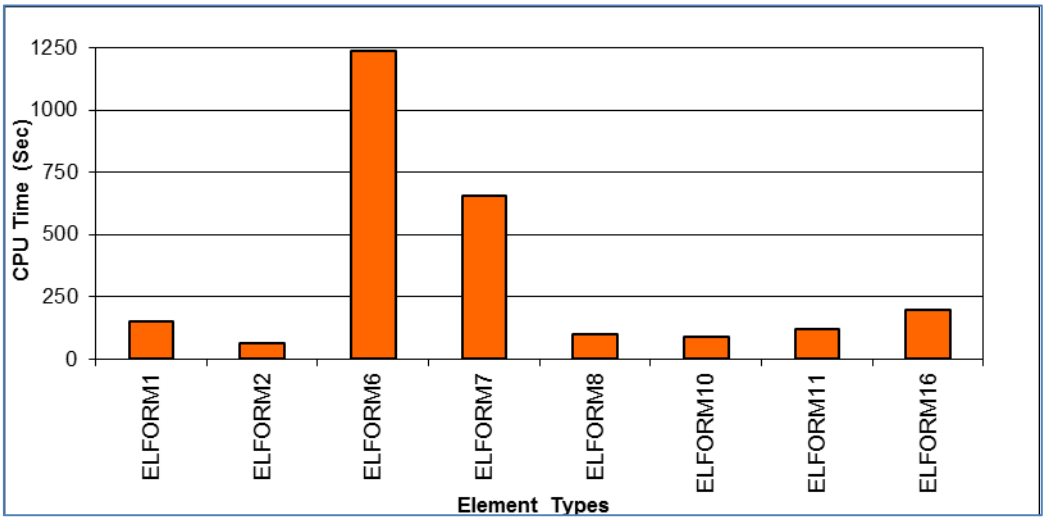

Fig. 8.8 Comparison of CPU Time For Different Elements

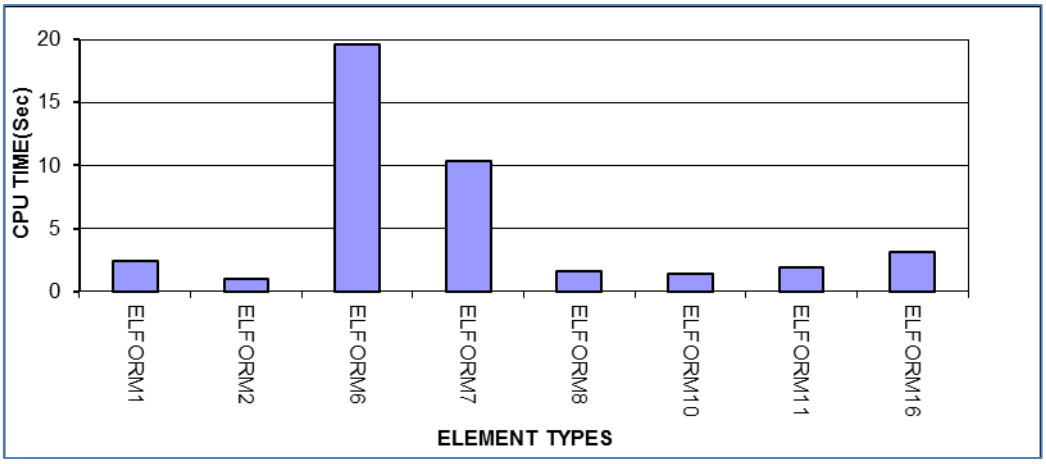

Fig. 8.9 Comparison of Elements with respect to ELFORM2

8.6.0 Conclusion and Shell Element selection

The Shell elements of Ls-Dyna with various formulations has been tested with standard pinched hemispherical problem for different mesh densities and found that though the **Elform2**, which is fast and default element is not converging and its behavior is in non-conformance to the exact value. The **Elform10**,which is an improved version of **Elform2** Behaves well in conformance with the theoretical value and is comparable with Elform16. Though the **Elform16**, which is based on full integration, predicts good results it exhibits locking phenomena with coarse mesh densities. However with proper mesh density it is the best one for accuracy point of view devoid of any spurious behaviors of hour glassing and instabilities. It is preferred as the best element with Good computational speed and accuracy in the industry provide the mesh is fine enough.. The elform6, which also behaves well in conformance with the theoretical value, is not recommended unless specified, as it is highly expensive among all the elements. **Elform1, Elform7**, **Elform8** and **Elform11** also behave well with reasonable accuracy and with reasonable cost. For the purpose of this research **ELFORM16** is chosen and used and being in line with industry with regards to Crash and Safety CAE.

8.8.0 Finite Element model formulation and Simulations

The characteristic understanding of the process, in which thin-walled structures are compressed using state of art, CAE methodologies can help to elucidate effectively their responses under quasi-static and dynamic loadings. Non-linear finite element code, Ls-Dyna, was actively used in this research to study the collapse patterns and analyze the energy absorbing characteristics of thin-walled sections with various sections subjected to axial impact loading. Tarigopula [34].

The specimens were modelled using the quadrilateral Full-Integration (ELFOR16) shell element with four nodes and with five integration points through the thickness. To accurately capture the folding pattern with characteristic wavelength, the mesh size and density has to be chosen in such way that it should be smaller than the length of the plastic hinge. The deformation has to display correct buckling pattern and be consistent in it responses for wide variety of variations with compressive interactions in deformed configurations. Mark [40]. The mesh size is therefore carefully chosen keeping into account of Courant's stability criteria for explicit time integration as:

Within above stability limits the time step and mesh length for shell elements is calculated as:

$$\Delta t = \frac{l_s}{C} \qquad \ldots (8.1)$$

where l_s is the characteristic length and C is the acoustic wave speed which is defined as

$$C = \sqrt{\frac{E}{\rho(1-\upsilon^2)}}$$

where E is the Young's modulus, ρ is the density of the material and υ denotes the Poison ratio of the material while the half-length of the stress wavelength for a Square member is calculated from Equation-7.2. An optimal mesh size of 4 mm x 4 mm was derived using Equations -8.1 and 7.2 and also from the mesh convergence study. Typically the meshed shell elements representing the thin walled FE model would be placed at the mid fiber location along the neutral axis. The thickness then offsets on both side of the mesh by half. The stiffness-type hourglass control model is adopted to eliminate the zero-energy modes.

8.8.1 Quasi-static Simulations

The upper end of the specimen was loaded using a moving rigid plate using Shell elements and *MAT_RIGID material model. The length of the section in consideration was at 350 mm and the sheet thickness was at 1.6 mm. The rigid clamped condition at the bottom end of the

model is by constraining of all degrees of freedom. "AUTOMATIC_SURFACE_TO_SURFACE" contact algorithm was used to simulate the contact between the rigid plate and the specimen with a friction coefficient of 0.3 to avoid lateral movements. To account for the internal contact between the faces and lobes during deformation, an "AUTOMATIC_SINGLE_SURFACE" contact algorithm was used. The thin walled sections were designed to be composed of two parts close to symmetry about a longitudinal axis and have about 8mm of overlapping welding flange along the side. The sides were welded by using a constrained spot-weld option in LS-DYNA, replicating the MIG welded condition as in the experimental MIG welding.

The material model used to replicate the isotropic high-strength steel alloy is through Type 24 Piecewise Linear Plasticity constitutive law of LS-DYNA. The quasi-static simulations have been carried out using this isotropic material. Table-8.1 in the next chapter presents the parameters of the materials that are used in the constitutive law. The load was applied using a rigid block which was given a boundary prescribed motion in order to simulate the quasi-static compression with a displacement control as in Figure-8.10. Standardized control cards were used to minimize the inertia effect.

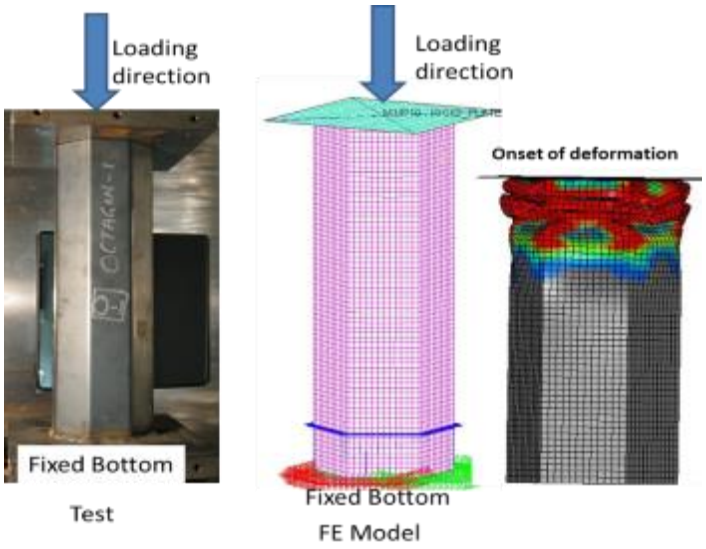

Fig. 8.10 Quasi-static setup Physical Test and CAE Model

A rigid block was used to apply the load on the specimen and it was also given a boundary prescribed motion in order to simulate the quasi-static compression with a displacement control. Enough care is taken in the model to minimize the inertia effect, with standard control cards. The ramp step in the loading was chosen to minimize the overall effect and does not induce strain rate or dynamic effects. The calculated kinetic energy was found to be insignificant when compared to the strain energy absorbed by the specimen.

The simulation works were carried out initially for developing stable sections which would provide robust repeatable collapse and then refined for production representative designs. The designs are further matured through addition manufacturing tolerances and provisions to aid in physical sample development. The simulation works are then continued for the intended cross sections across the material range from low strength steel with yield about135MPa to High strength Steel with yield about 1200MPa. The results of the simulations in terms of their force-displacement characteristics were extracted and discussed further in the results sections. The Figure-8.8.2 represents a typical quasi-static crush process and final deformation shapes with repeatable lobed pattern on the specimens with intended cross-sections.

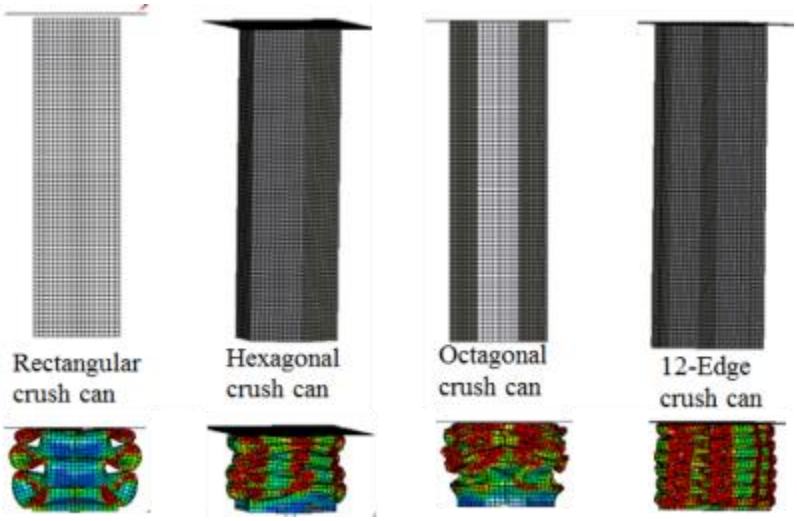

Fig. 8.11 Quasi-static crush simulations of specimens of different Cross-sections

8.8.2 Dynamic Simulations

The crush behavior of thin-walled sections under quasi-static loading enables to capture the fundamental characteristics of collapse process with Mean crushing force (P_m) and Energy Absorption (E_{abs}) as dominant parameters. However crush behavior is devoid of any dynamics effect which is the main feature of dynamic impact load cases. Most of the energy absorbing devices are developed for structures that are designed to withstand impact load conditions. The important feature of dynamic impact is that the loading occurs within a short duration of time. Its due to this transient nature of the process, the deformations are predominantly dynamic in nature.

Previous studies on the dynamic crushing process by Jones, Abramowicz W and White MD [23,24,27] are indicative of two major influential factors that affect the crushing process. The first one is the rate sensitivity property of the material where in the yield and flow stress are

dependent on strain rate. Steels are rate sensitive materials and for typical mild steel the value of yield stress nearly doubles in dynamic case than its quasi-static cases. Rate sensitivity effect is generally represented by Cowper-Symonds relations and used by Abramowicz and Jones [23] to modify the energy flow stress which is used to derive the mean crushing force.

In automotive domains of impact assessments the most commonly used strain rate dependent material model is the piecewise linear plasticity model where in the true stress-strain curves are directly fed into the material model. By scaling the static yield stress with a factor described by Cowper – Symonds relation using isotropic and kinematic hardening plasticity, the dynamic effects of strain rates are considered. The model uses plastic-kinematic hardening as below:

$$\sigma_y = \left[1 + \left(\frac{\dot{\varepsilon}}{C}\right)^{\frac{1}{p}}\right] . \sigma_0 \qquad \ldots(8.2)$$

where $\sigma_0$is the initial yield stress, $\dot{\varepsilon}$ is the strain rate while *C* and *P* are the Cowper-Symonds strain rate parameters. In Ls-Dyna a table is used to define each strain rate value with load curve giving the stress vs effective plastic strain curves. During the course of deformation process if the strain rate falls below that of minimal value the lowest strain rate curve is taken while the highest for high strain rates. In the intermediate range the strain rate for each element is calculated and a linear interpolation between the strains rates determined experimentally is used for the resulting stress states in the plastic regions. The implementation is through *MAT_PIECEWISE_LINEAR_PLASTICITY material model.

The second influential factor is the inertia which develops in the structure due to rapid accelerations that are involved in impact load case. This factor is generally explained in terms of the Stress wave propagations in the structural media which is dependent on the initial load and boundary conditions in terms of Mass and velocity. Reflecting the two influential factors a dynamic load case for the characterizing the crush cans is developed using a sled vehicle as shown in the Figure 8.12.

The FE model is constructed similar to the Quasi-static model with 1.6mm thickness and 350mm length using Type 24 Piecewise Linear Plasticity constitutive law for the material and AUTOMATIC SURFACE_TO_ SURFACE contact algorithm for self and contact with rigid wall. The Specimen in this case is attached to a rigid plate with mass of 250 kg and

accelerated with *INITIAL_VELOCITY option at 15m/s (with responses at lower velocities being similar). The responses were extracted and compared with experimental values. The responses of the dynamic crushing are strongly influenced by the material rate sensitivity properties which are in turn dependent on material characterization at different strain rates. Once these strain rate responses are extracted for the intended materials then the dynamic responses of the section under impact loading are deemed to be assured. The assessments then would limit to evaluate the material strain rate sensitivity and robust performances of the FEA models in predicting the dynamic crush force characteristics which later are evaluated in full vehicle tests.

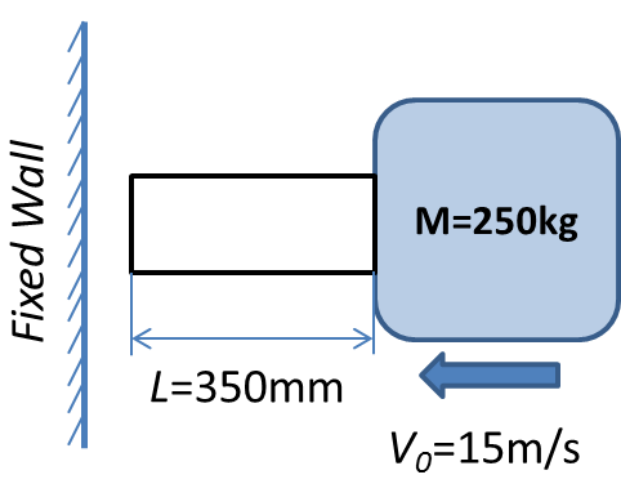

Conceptual-Setup

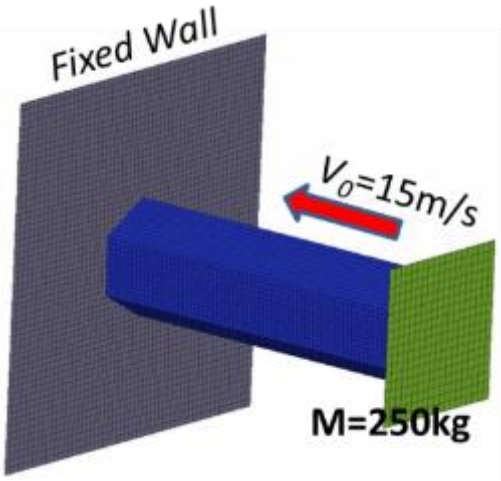

FE Model Set-up

Experimental Set-up

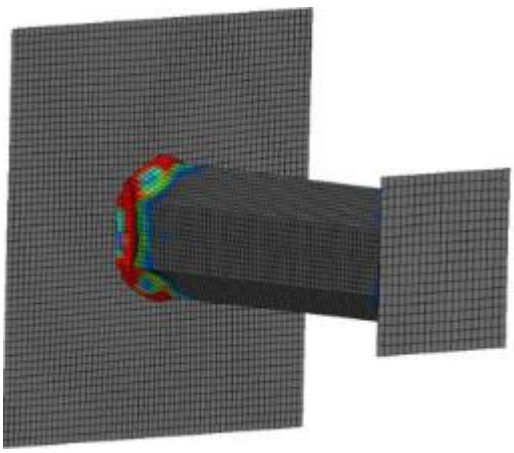

Onset of deformation in FE Model

Fig. 8.12 Dynamic crush test setup and CAE Model

From the material characterizations, shapes and parameters from the previous chapters the dominant aspect identification would be beneficial to focus efforts towards an optimal combination for best SEA. The next chapter introduces a new methodology through DOE and multi-objective optimization towards achieving an optimal set.

CHAPTER 9

9.0 Sensitivity study (DOE) of thin wall sections and Multi-objective Optimization

In the design of thin walled sections, maximizing crashworthiness performance should always be a major objective. The design options present two approaches for enhancing the performance of the multi-corner thin-walled structures. One is by employing advanced material with better mechanical properties and other is by developing an optimized set of values for wall thickness and cross-sectional configuration. In this chapter, to achieve optimal crashworthiness performance, a set of simulation tests which had different wall thicknesses, material properties, and cross-section configurations was designed using a four-level design of experiments (DOE) based on Taguchi [47] method. These designs were analyzed for crashworthiness with high fidelity Finite element (FE) models and solutions are sought through explicit finite element code of LS-DYNA. The design responses of those samples are extracted for crash responses extracted from the results. Similar design approach was followed as that of previous sections for deriving the optimal designs. Parametric studies were also performed apart from design optimization, to determine the influences of the cross-section configuration, material properties, and wall thickness on the crashworthiness performance.

Specific energy absorption (SEA), which is absorbed energy per unit structural mass, and crush force efficiency ($\boldsymbol{A_E}$), which is ratio of mean crushing load to peak crushing are considered as Design objectives in crashworthiness optimization. SEA and $\boldsymbol{A_E}$ should always be maximized to improve crashworthiness performance. To deal with these multiple objectives, multi-objective optimization design method was utilized in the investigations for crashworthiness design of thin-walled members under axial loading and Pareto-optimal set of designs was extracted.

9.1 Problem description

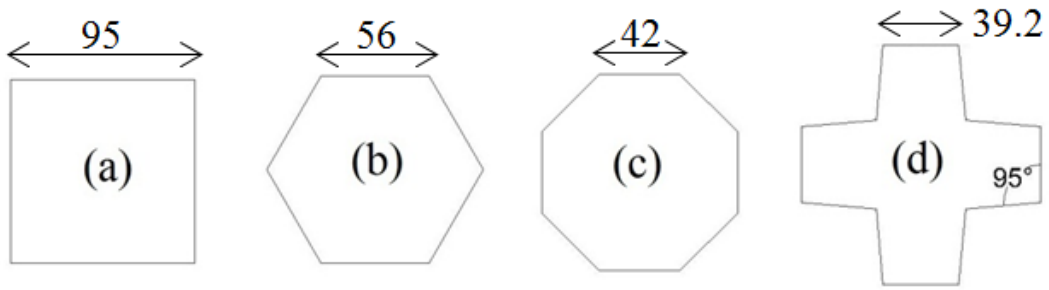

Fig. 9.1. Cross-section of members: (a) square, (b) hexagonal, (c) octagonal, and (d) 12-edge

The sections considered in this study were prismatic thin walled sheet metal multi cornered members. Schematic diagram of the computational models is shown in Figure-8.10 and 8.11 of chapter-8. Identical loading condition and boundary conditions were maintained for all four FE models including rectangular, hexagonal, octagonal, and 12-edged cross-sectional members. Moreover, all the members had the same normalized length equal to 250 mm. The members differ only in their cross-section configuration, which is as depicted in Figure-9.1.

As described in the previous section 7.8.1 in chapter-7 calculations were performed using non-linear explicit finite element code LS-DYNA and the results were post-processed using LS-PREPOST. Elastic-plastic material model of MAT24 was used with materials ranging from low strength steel CA5 with the yield stress of 130 MPa to high strength steel DP600 with the yield stress of 445 MPa and their constitutive behavior in the sections in consideration was utilized in the investigation. Mechanical properties of these material samples are as summarized in chapter -10

9.2 Design objectives

In the design for crashworthiness, specific energy absorption (SEA) is considered to be the first measure of energy-absorption capacity of a thin-walled section and is therefore, the first objective of this optimum design was to maximize SEA. SEA for this purposes can be defined as:

$$SEA = E_{int} / m, \qquad ...(9.1)$$

where E_{int} the internal energy and m is total mass of the member.

Typically, the collapse process involves forces which are fluctuating around mean value before they escalate to higher value when deformation is bottomed out at the end of effective stroke length, which is considered to be equal to 250 mm for all cases. Therefore, mean crushing force P_{mean} was defined by:

$$P_{mean} = \frac{1}{S_E}\int_0^{S_E} P(s)ds, \qquad \ldots(9.2)$$

where S_E is effective stroke length.

The second objective was crush force efficiency (A_E), as is an indicator for characterizing load consistency, which was defined as:

$$A_E = \frac{P_{mean}}{P_{max}} = \frac{1}{P_{\max} S_E}\int_0^{S_E} P(s)ds, \qquad \ldots(9.3)$$

where P_{max} refers to the highest force on the force-displacement curve. The higher the A_E value, the better would be the stability and load consistency. For an ideal member, A_E is equal to %100.

In multi-objective problems to compare the candidate solutions the concepts of Pareto dominance and Pareto optimality are the commonly used. Francis Ysidro introduced these concepts while Vilfredo Pareto [48] generalized them. The selected solution would be part of Pareto set when there is no other solution which can degrade any other objective and improve at least one of the objectives. Multi-objective problems are more complex than single objective problems, due to the fact that no unique solution is available that can satisfy the multi objectives. It would rather be a set of optimal solutions, which is called Pareto front [49] with acceptable trade-offs.

Formally, a vector $\vec{u} = [u_1, u_2, ..., u_N]^T$ is considered to *Pareto-dominate* the vector $\vec{v} = [v_1, v_2, ..., v_N]^T$ in a minimization context if and only if:

$$\begin{aligned} &\forall i \in \{1, ..., N\} : f_i(\vec{u}) \le f_i(\vec{v}), \\ &\exists j \in \{1, ..., N\} : f_i(\vec{u}) < f_i(\vec{v}) \end{aligned} \qquad \ldots(9.4)$$

In multi-objective optimization context, to compare and rank vectors Pareto dominance is used. Vector $\vec{u}$ dominates vector $\vec{v}$ in the Pareto sense, meaning that $F(\vec{u})$ is superior to $F(\vec{v})$ while among all objectives there is at least one objective function, for which $F(\vec{u})$ is strictly better than $F(\vec{v})$.

A solution is said to be belonging to Pareto set or termed Pareto optimal only if no another solution is available which can dominate it. In other words, it puts out a condition that a solution cannot adversely affect an objective and improve the other objectives. The objective vector which corresponds to the Pareto set Pareto dominant vector, or non-inferior or non-dominated vector. Pareto optimal set is the grouping of all Pareto optimal solutions

and their objective vectors are called Pareto front. As its am amalgamation solution sets it becomes impossible to fit an analytical expression for of the Pareto front.

9.3 Taguchi method

To systematically optimize with small testing time and low experimental costs, Taguchi method has been used most commonly. This method utilizes small number of experiments to study a large number of variables by utilizing orthogonal (balance) arrays (OAs) from experimental design theory. It is considered to be a matured and fully developed formulation due to the fact that there is independence of target value from the ratio of signal factors or controllable factors to noise factors or uncontrollable factors and is consistent with Taguchi quality objective. To express the scatter around a target value this method uses signal-to-noise ratio (S/N) wherein high value of S/N indicates that the random effects of the noise factors are lower than the signal. Uncontrollable factors contribute to the noise and often cannot be eliminated and they co-exist in the environment causing the variations in the output. In this study, the main goal of design experiments was to maximize the SEA and the A_E values; the S/N ratio for HB (i.e. higher is better) characteristics are required which is as per below:

$$S/N_S = -10\log_{10}\frac{1}{n}\left(\sum_{i=1}^{n} 1/Y_i^{\,2}\right) \qquad \ldots(9.5)$$

Under the same experimental conditions, n denotes the number of repetitions and while Y denotes the result of measurements for SEA and A_E and becomes our design objective.

Three controllable factors with each factor having four levels is considered in this study. Therefore, the experimental conditions with L_{16} (4^3) orthogonal array was chosen and listed in **Table** 9.1

Table 9.1. Experimental tests' conditions

	A (Cross-sectional configuration)	B (Material type)	C (Wall thickness)
Test 1	Level 1	Level 1	Level 1
Test 2	Level 1	Level 2	Level 2
Test 3	Level 1	Level 3	Level 3
Test 4	Level 1	Level 4	Level 4
Test 5	Level 2	Level 1	Level 2
Test 6	Level 2	Level 2	Level 1
Test 7	Level 2	Level 3	Level 4

Test 8	Level 2	Level 4	Level 3
Test 9	Level 3	Level 1	Level 3
Test 10	Level 3	Level 2	Level 4
Test 11	Level 3	Level 3	Level 1
Test 12	Level 3	Level 4	Level 2
Test 13	Level 4	Level 1	Level 4
Test 14	Level 4	Level 2	Level 3
Test 15	Level 4	Level 3	Level 2
Test 16	Level 4	Level 4	Level 1

In order to construct the optimal conditions the approach of the analysis of mean (ANOM) statistical approach was adopted. Initially, for each controllable factor at a certain level the mean of the S/N ratio must be calculated. For example, for factor I at level i, $\left(\mathrm{M}\right)_{\mathrm{factor=I}}^{\mathrm{level=i}}$ the mean of the S/N ratio is given by:

$$(M)_{factor=I}^{level=i} = \frac{1}{n_{Ii}} \sum_{j=1}^{n_{Ii}} [(\frac{S}{N})_{factor=I}^{level=i}]_j \qquad \ldots(9.6)$$

In Equation-9.6, n_{Ii} n_{Ii} represents the number of instances of factor I at level i and $[(S/N)_{factor=I}^{level=i}]_j$ is the corresponding S/N ratio of factor I at level I; its appearance sequence in Table-9.1 is the *j*th. Similarly using the same measure at a certain level, the mean of the S/N ratios of other factors can be determined. Once the optimal condition is established, the S/N response table and Figure can be obtained. Finally, the crush simulations were carried out under these optimal conditions. for analyzing the influence of each controllable factor on the process of simulation the analysis of variance (ANOVA) statistical method was also used in addition to ANOM. The contribution of each factor ρ_F in percentage is given by:

$$\rho_F = \frac{SS_F - (DOF_F V_{ER})}{SS_T} \times 100 \qquad \ldots(9.7)$$

In Equation-9.7, by subtracting one from the number of the level of each factor (L), the the degree of freedom for each factor as represented by DOF_F is obtained. The total sum of squares, SS_T , was given by:

$$\mathrm{SS_T} = \sum_{j=1}^{m} \left(\sum_{i=1}^{n} \mathrm{Y_i^2} \right) - \mathrm{mn}\left(\overline{\mathrm{Y_T}}\right)^2 \qquad \ldots(9.8)$$

Where $\overline{\mathrm{Y_T}} = \sum_{j=1}^{m} \left(\sum_{i=1}^{n} \mathrm{Y_i} \right)_j / (\mathrm{mn})$, under the same experimental conditions n represents the number of repetitions while m represents the number of experiments carried out in this study The factorial sum of squares, $\mathrm{SS_F}$, was given by:

$$SS_F = \frac{mn}{L}\sum_{k=1}^{L}\left(\bar{Y}_k^F - \bar{Y}_T\right)^2 \quad \ldots(9.9)$$

where $\bar{Y}_k^F$ represents the average value of the measurement results of a certain factor at the *k*th level. The variance of error V_{Er} is as given by:

$$V_{Er} = \frac{SS_T - \sum_{F=A}^{D} SS_F}{m(n-1)} \quad \ldots(9.10)$$

Full factorial of this process based on selection of the three factors with the four levels is calculated as:

$$N = L^m \quad \ldots(9.11)$$

where N is number of possible design, L number of levels for each factor and m is number of factors. For this study N is 64 (4^3) tests. Contrastingly this is where the power of Taguchi method comes into play. In this case it chooses only 16 tests. Other tests based on these S/N ratios can be predicted as [50]:

$$(S/N)_P = (S/N)_m + \sum_{i=1}^{n}\left[(S/N)_i - (S/N)_m\right] \quad \ldots(9.12)$$

where $(S/N)_m$ is the total mean S/N ratio, $(S/N)_i$ is the mean S/N ratio at the predicted level, and n is the number of the main design parameters that affect the quality characteristic.

Therefore, this study focused on optimization of crush absorbers, in case that, cross-sectional configuration, material property and wall thickness are considered as the design variables and SEA and A_E are considered as the design objectives, according to which the optimization levels were arranged as shown in **Table** 2.

Table 9.2. Controllable factors and their levels

Factor	Level 1	Level 2	Level 3	Level 4
Cross-sectional configuration	Rectangle	Hexagonal	Octagonal	12-edge
Material type (steel)	CA5	HA3	SAPH440	DP600
Wall thickness (mm)	1	1.2	1.4	1.6

Therefore, the experimental conditions were obtained by choosing an L_{16} (4^3) orthogonal array and by combining **Table** 9.1 with **Table** .

9.4 Results and discussion

The SEA and A_E of each crush absorber prepared in simulation tests 1-16 were then measured as shown in the previous section, the values of which are presented in **Table-9.3**.

Table-9.3. SEA and A_E for 16 test conditions

Test number	Mass (kg)	Total energy absorbed (kJ)	Pmax (kN)	Pmean (kN)	SEA (kJ/kg)	A_E
Test 1	0.992	3.011	44.014	12.043	3.036	0.274
Test 2	1.190	5.963	76.531	25.850	5.010	0.338
Test 3	1.388	8.992	117.290	35.967	6.476	0.307
Test 4	1.573	15.985	189.830	63.940	10.164	0.337
Test 5	1.190	5.331	55.344	21.322	4.480	0.385
Test 6	0.992	5.246	58.657	20.984	5.291	0.358
Test 7	1.586	14.500	167.100	58.000	9.140	0.347
Test 8	1.376	16.230	165.410	64.924	11.797	0.393
Test 9	1.234	8.947	70.040	35.788	7.250	0.511
Test 10	1.410	13.850	127.440	55.400	9.820	0.435
Test 11	0.881	7.712	67.865	30.846	8.749	0.455
Test 12	1.048	14.583	121.210	58.332	13.910	0.481
Test 13	1.854	17.822	118.460	71.284	9.611	0.602
Test 14	1.623	18.229	150.750	72.916	11.233	0.484
Test 15	1.391	16.902	167.380	67.608	12.151	0.404
Test 16	1.149	17.353	190.070	69.416	15.106	0.365

Substituting By inserting the number of simulation repetitions and results in Equation-9.6, S/N ratio of each simulation condition was determined (**Table 9.4**9.4).

Table 9.4. Results of the measurement and the S/N ratio of each simulation condition

	SEA_i	$(S/N)_{SEA}$	A_E	$(S/N)A_E$
Test 1	3.036	9.6457	0.274	-11.2570
Test 2	5.010	13.9971	0.338	-9.4274
Test 3	6.476	16.2264	0.307	-10.2672
Test 4	10.164	20.1416	0.337	-9.4518
Test 5	4.480	13.0254	0.385	-8.2849
Test 6	5.291	14.4703	0.358	-8.9286
Test 7	9.140	19.2186	0.347	-9.1910
Test 8	11.797	21.4351	0.393	-8.1231
Test 9	7.250	17.2070	0.511	-5.8322
Test 10	9.820	19.8425	0.435	-7.2359
Test 11	8.749	18.8387	0.455	-6.8489
Test 12	13.910	22.8668	0.481	-6.3526
Test 13	9.611	19.6553	0.602	-4.4116
Test 14	11.233	21.0100	0.484	-6.3087
Test 15	12.151	21.6925	0.404	-7.8741
Test 16	15.106	23.5828	0.365	-8.7491

Subsequently, values of S/N ratio were inserted in Equation-9.6 and mean of S/N ratios of a certain factor was obtained and presented in **Table 9.5** and **Table 9.6**9.6 for SEA and A_E, respectively. The contents in bold face in Tables-9.6 and 9.7, refer to the maximum value of mean of S/N ratios of a certain factor among four levels, thus indicating optimum conditions for SEA and A_E values.

Table 9.5. The mean of the S/N ratios of a certain factor for SEA

$\frac{Factor}{Level}$	$(S/N)^{Level}_{factor}$				$\left[(M)^{Level}_{factor}\right]$
	j = 1	j = 2	j = 3	j = 4	
A/1	9.646	13.997	16.226	20.142	15.003
A/2	13.025	14.470	19.219	21.435	17.037
A/3	17.207	19.842	18.839	22.867	19.689
A/4	19.655	21.010	21.692	23.583	21.485
B/1	9.646	13.025	17.207	19.655	14.883
B/2	13.997	14.470	19.842	21.010	17.330
B/3	16.226	19.219	18.839	21.692	18.994
B/4	20.142	21.435	22.867	23.583	22.007
C/1	9.646	14.470	18.839	23.583	16.634
C/2	13.997	13.025	22.867	21.692	17.895
C/3	16.226	21.435	17.207	21.010	18.970
C/4	20.142	19.219	19.842	19.655	19.714

Table 9.6. The mean of the S/N ratios of a certain factor for A_E

$\frac{Factor}{Level}$	$(S/N)^{Level}_{factor}$				$\left[(M)^{Level}_{factor}\right]$
	j = 1	j = 2	j = 3	j = 4	
A/1	-11.257	-9.427	-10.267	-9.452	-10.101
A/2	-8.285	-8.929	-9.191	-8.123	-8.632
A/3	-5.832	-7.236	-6.849	-6.353	-6.567
A/4	-4.412	-6.309	-7.874	-8.749	-6.836
B/1	-11.257	-8.285	-5.832	-4.412	-7.446
B/2	-9.427	-8.929	-7.236	-6.309	-7.975
B/3	-10.267	-9.191	-6.849	-7.874	-8.545
B/4	-9.452	-8.123	-6.353	-8.749	-8.169
C/1	-11.257	-8.929	-6.849	-8.749	-8.946
C/2	-9.427	-8.285	-6.353	-7.874	-7.985
C/3	-10.267	-8.123	-5.832	-6.309	-7.633
C/4	-9.452	-9.191	-7.236	-4.412	-7.573

Initially, Y_K^F (average value of the measurement results of a certain factor at the *k*th level) was obtained from SEA_i and A_{Ei} in Table-9.3, as listed in Table-9.7 for SEA and A_E values, respectively.

Table 9.7. The average value of the measurement results of a certain factor in the kth level for SEA and A_E

	SEA			A_E		
	$\bar{Y}_K^A$	$\bar{Y}_K^B$	$\bar{Y}_K^C$	$\bar{Y}_K^A$	$\bar{Y}_K^B$	$\bar{Y}_K^C$
Level 1	6.172	6.094	8.045	0.314	0.443	0.363
Level 2	7.677	7.839	8.888	0.371	0.403	0.402
Level 3	9.932	9.129	9.189	0.470	0.378	0.423
Level 4	12.025	12.744	9.684	0.464	0.394	0.430

By Through substituting $Y_T = 8.9515$ by SEA and $Y_T = 66.1088$ by A_E in Equation-9.9, the factorial sum of squares, SS_F, was calculated individually for each factor, as listed in Tables 6 and 7. Using Equation-9.8, the total sum of squares, SS_T, was determined. Through substituting SS_F and SS_T= 545.0632 by SEA and SS_T= 0.3273 by A_E in Equation-9.10, the variance of error, V_{Er}, was derived. Finally, by the substitution of SS_F, SS_T, V_{Er}, and DOF_F = 3 in Equation-9.7, the percentage contribution of each factor, ρ_F, was sequentially evaluated; these values are presented in Table-9.8.

Table 9.8. The factorial sum of squares and the percentage of contribution of each factor

Factor	$(SS_F)_{SEA}$	$(\rho_F)_{SEA}$	$(SS_F)_{AE}$	$(\rho_F)_{AE}$
Cross-sectional configuration	237.153	43.422	0.207	80.300
Material type	285.829	52.353	0.027	8.713
Wall thickness	17.017	3.035	0.033	10.988

Rank orders of the contribution percentage of each factor on the SEA value as per their magnitudes, were as follows: (1) material type (52.35%), (2) cross-sectional configuration (43.42%), and (3) wall thickness (3.04%). On the other side, rank orders of the contribution percentage of each factor on the A_E value were as follows: (1) cross-sectional configuration (80.30%), (2) wall thickness (10.99%), and (1) material type (8.71%). Results were pretty exciting: material type was the most influential factors for SEA value and the least influential factor for A_E value, while the influence of wall thickness on SEA value was almost negligible and, most interestingly, cross-sectional configuration played a dominant role in both design objectives: SEA and A_E. According to Tables-9.5 and 9.6, optimum conditions for obtaining the maximum SEA value were as follows: 12-edge cross-section of steel type DP600 and wall thickness of 1.6 mm. Furthermore, the optimum conditions for obtaining the maximum A_E value were as following: octagonal cross-section of steel type CA5 and wall thickness of 1.6 mm; According to aforementioned optimal condition the confirmation simulated test was carried out and maximum SEA=21.38 kJ/kg and maximum A_E =0.53 were calculated (Figure-9.2).

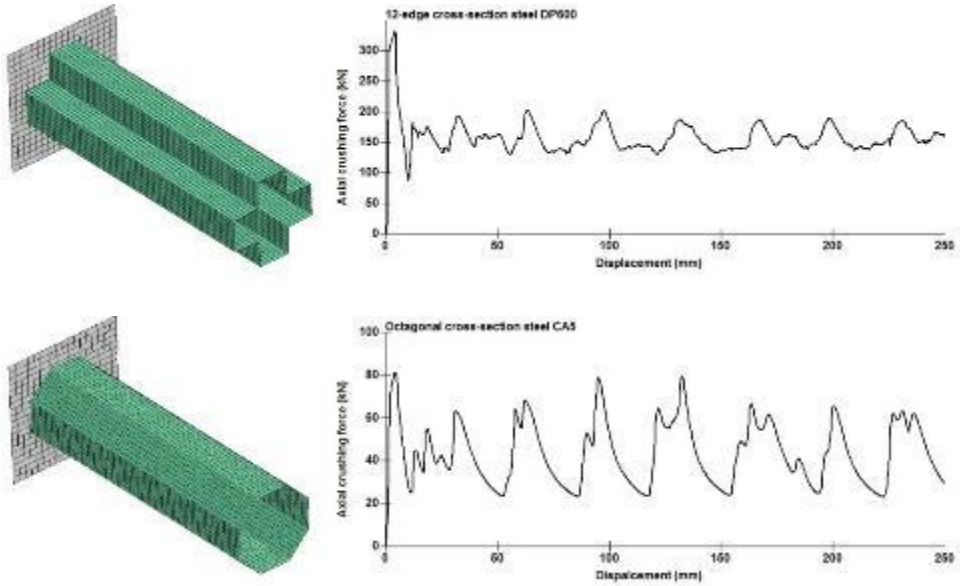

Fig. 9.2. Axial crushing force-displacement curves of 12-edge DP600 and octagonal CA5

The first comparator for the effectiveness of a crush absorber is specific energy absorption (SEA), which provided a choice to design the sections with minimum mass with regard to energy absorption capacity. **Fig.** -9.3 which is a bar chart provides a clear comparison for SEA values for all sections in terms of cross-sectional configuration, wall thickness, and material type.

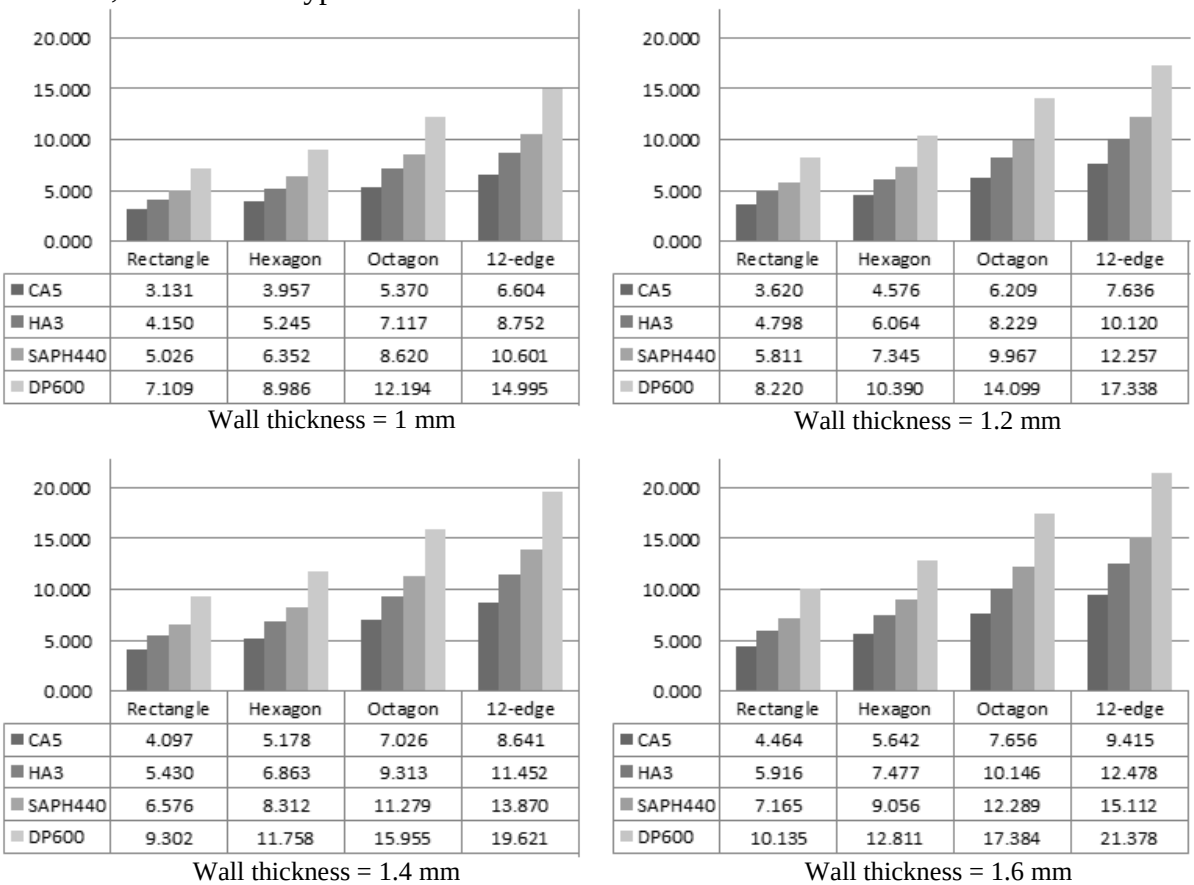

Fig. 9.3. SEA values for all design conditions (kJ/kg)

According to the Fig. 3, it is clearly obvious that there was a direct relationship between SEA and design objectives (i.e. cross-sectional configuration, material type, and wall thickness).

Also, it can be concluded that rectangle cross-section had significantly lower energy absorption capacity than others. Hexagonal and octagonal configurations were better, while the 12-edge configuration showed the best SEA capacity of all. Another important trend which can be inferred from the charts is the dependency of SEA on the material characteristics. For the same section configuration, higher strength material led to higher SEA value. Clearly, the 12-edge cross-sectional member made of high yield strength steel (DP600) was observed to lead the pack with the highest SEA as compared to the rest of the sections.

The second significant comparator for the effectiveness of an energy absorber is crush force efficiency (A_E). **Fig. 9.**4 as a bar chart provides a clear comparison of the A_E value for different cross sections, material types, and wall thicknesses.

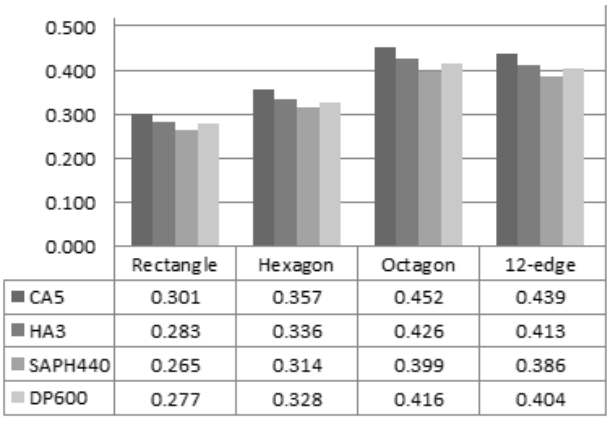

	Rectangle	Hexagon	Octagon	12-edge
CA5	0.301	0.357	0.452	0.439
HA3	0.283	0.336	0.426	0.413
SAPH440	0.265	0.314	0.399	0.386
DP600	0.277	0.328	0.416	0.404

Wall thickness = 1 mm

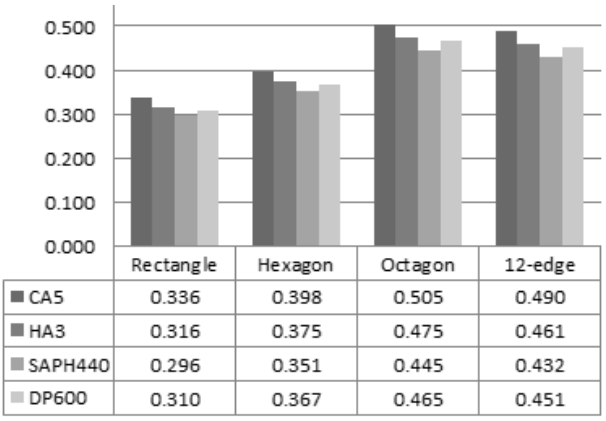

	Rectangle	Hexagon	Octagon	12-edge
CA5	0.336	0.398	0.505	0.490
HA3	0.316	0.375	0.475	0.461
SAPH440	0.296	0.351	0.445	0.432
DP600	0.310	0.367	0.465	0.451

Wall thickness = 1.2 mm

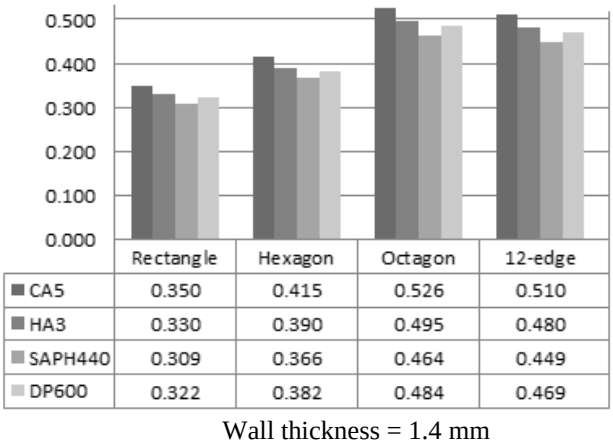

	Rectangle	Hexagon	Octagon	12-edge
CA5	0.350	0.415	0.526	0.510
HA3	0.330	0.390	0.495	0.480
SAPH440	0.309	0.366	0.464	0.449
DP600	0.322	0.382	0.484	0.469

Wall thickness = 1.4 mm

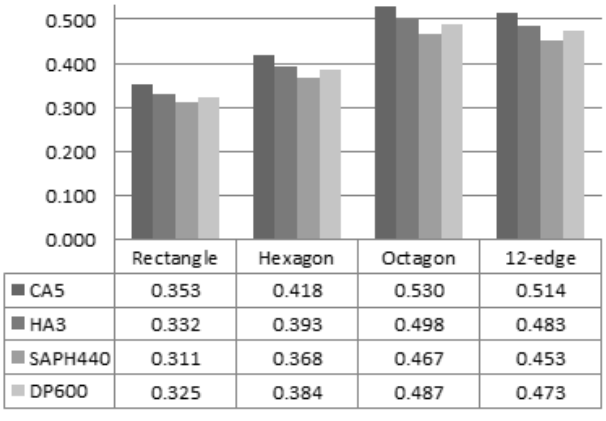

	Rectangle	Hexagon	Octagon	12-edge
CA5	0.353	0.418	0.530	0.514
HA3	0.332	0.393	0.498	0.483
SAPH440	0.311	0.368	0.467	0.453
DP600	0.325	0.384	0.487	0.473

Wall thickness = 1.6 mm

Fig. 9.4. A_E value for all design conditions

For crush force efficiency (A_E), an interesting trend can be observed for the sections. Similar to SEA trend, the bigger the wall thickness, the larger the value of A_E. Thus, the same as SEA, there was a direct relationship between A_E and wall thickness. A similar pattern could be seen for each cross-sectional configuration and material type, which was is not the same as that of SEA. For material range starting from steel CA5 to steel SAPH440, A_E value

gradually decreased and, afterward, increased for steel DP600; but, it was still lower than the result of steel CA5. Consequently, octagonal cross-section performed outstanding in terms of crush force efficiency and A_E value reached its peak for these cross-sections for material type of steel CA5.

Although treating one criterion as constraint and optimizing the other criterion generates meaningful results, the interaction features of these criteria are lacking. From a practical application point of view, multi-objective design appears to be more meaningful. The task now is to select the best multi-corner thin-walled member(s) based on specific energy absorption (SEA) and crush force efficiency (A_E) capacity.

This multi-objective optimization problem can be expressed as follows:

$$\begin{cases} Minimize: 1/SEA \;\&\; 1/CFE \\ s.t. \begin{cases} Cross-sectional\ \ configuration \in \{Rectangle,\ Hexagonal,\ Octagonal\ and\ 12-edge\} \\ Material\,(steel)\ type \in \{CA5,\ HA3,\ SAPH\,440,\ P\,600\} \\ Wall\ \ thickness \in \{1\,mm,\ 1.2\,mm,\ 1.4\,mm,\ 1.6\,mm\} \end{cases} \end{cases} \quad ...(9.13)$$

To fully understand the solution for the multi-objective optimization problems, the exploration of the Pareto sets is crucial space. For more flexibility to the designers in making the decisions the Pareto front provides the designer with a range of optimal solutions. It is shown from the Pareto plots that SEA and A_E are in competition with each other. Any point in the Pareto frontier can be an optimum and to seek further improvement in one objective means to some extent it must sacrifice the other objective.

All possible conditions including 64 full-factorial designs are plotted in **Fig. 9.**-9.5, where x and y axes are 1/SEA and 1/ A_E, respectively. By employing a code in MATLAB based on *Pareto-domination* concept of Equation-9.4 for all the possible conditions, Pareto points were illustrated.

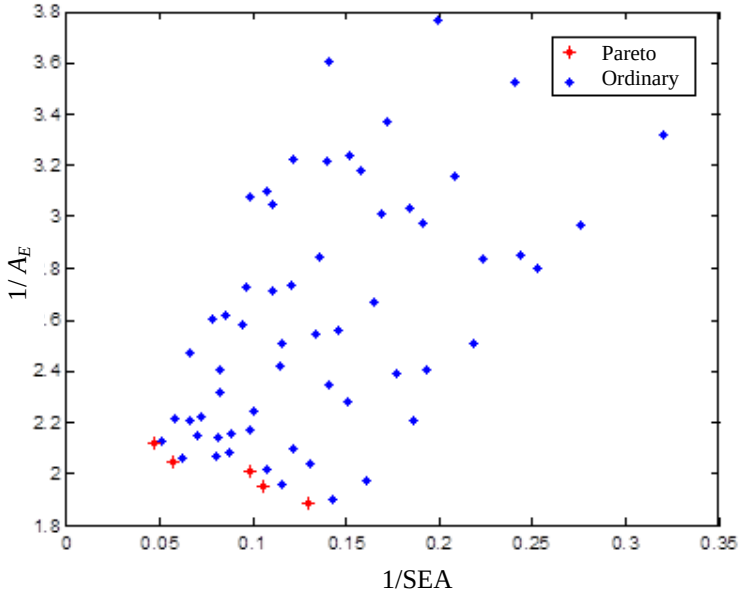

Fig. 9.5. Illustration of the Pareto points in the design space

Finally, the Pareto points which were un-dominated solutions were extracted, as tabulated in Table-9.9.

Table 9.9. SEA and A_E comparison of the Pareto points

	Cross-sectional configuration	Material type	Wall thickness (mm)	SEA (kJ/kg)	A_E
1	Octagonal	CA5	1.6	7.656	0.530
2	Octagonal	SAPH440	1.6	10.146	0.498
3	Octagonal	DP600	1.6	17.384	0.487
4	12-edge	CA5	1.6	9.415	0.514
5	12-edge	DP600	1.6	21.378	0.472

Two out of five Pareto points were the results of the single objective study, which was predictable. The rest are 12-edge cross-section member of steel CA5 and octagonal cross-section members of steel SAPH440 and DP600 (**Fig. 9.**-9.6). All Pareto solutions had the largest wall thickness. The existence of both low strength steel (CA5) and high strength steel (DP600) in Pareto solutions were noticeable. SEA domain from the lowest to the highest values varied by around 180% while, for A_E, it was 12%, meaning that as a single objective study, SEA value had a priority to be selected as the design objective.

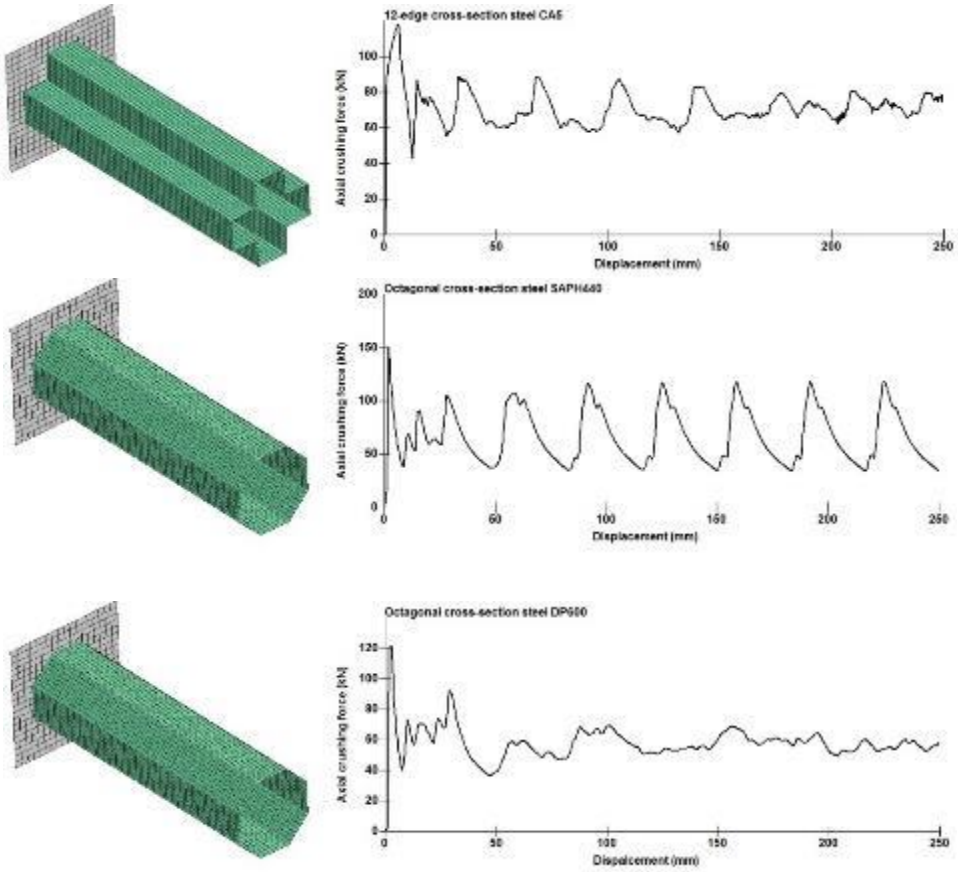

Fig. 9.6. Axial crushing force-displacement curves of 12-edge DP600, octagonal CA5, and octagonal SAPH440 members

9.5 Directional conclusion

This chapter presented the crashworthiness design optimization of thin-walled multi-corner members, including the rectangular, hexagonal, octagonal, and 12-edge cross-sectional profiles made of the materials ranging from low to high strength steel. The main objective of this chapter was to show how parametric method optimization coupled with multi-objective optimization which was applied to a discontinuous design space would lead to an efficient and effective design optimization approach for the crashworthiness investigation of the energy absorbers.

For the optimum design, specific energy absorption (SEA) and crush force efficiency (A_E) were set as the design objectives and the cross-sectional configuration, wall thickness, and material type were selected as three design variables. Design of experiment based on Taguchi method and multi-objective optimization were employed to formulate the optimum design problems and the optimal designs were finally solved using the derived formulations. The investigation was broken up into two phases: (1) investigation of the members to achieve

maximum SEA and A_E values separately as a single objective study, and (2) investigation of the member for maximum SEA and A_E performance simultaneously as a multi-objective study.

It was found that, in order to reach the maximum SEA value, 12-edge section made of high strength steel DP600 was the best choice; while octagonal section made of low strength steel CA5 performed the best in achieving the maximum A_E value. Then, based on the DOE results, a parametric study was presented and it was found that the cross-sectional configuration as well as material type had significant effects on SEA, while cross-sectional configuration had the only dominant effect on A_E. Meanwhile, wall thickness and design objectives were in a linear relationship, i.e. bigger wall thickness always leads to higher SEA and A_E values for each cross-sectional configuration and material type. Moreover, steel's yield and ultimate stresses show conflicting effects on SEA and A_E, which results in undergoing a multi-objective optimization study for obtaining a Pareto optimal solution.

Its thus directionally made clear from the above, the dominant performance of 12-edge specimen with corner angle closer to 90^0 over the other cross-sectional specimens along with new methodology for selection through parametric coupled with multi-objective optimization. The dominance of 12 edge specimen established so far needs to be further ascertained through experimental validations and the behavior correlations through numerical studies which the next chapters would address in detail. With the shape aspects well understood and established the performances clearly relies on the material characterization which has to be profoundly extracted in term of stress-strain properties to be fed directly into the simulations. The quality of the data decides the quality of the numerical predications which is well explained in the next chapter.

CHAPTER-10

10.0 Material characterization (Static and Dynamic)

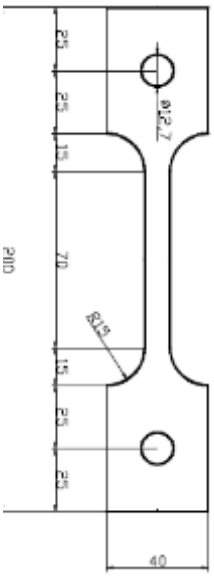

Fig. 10.1 AS1391-2007 Tensile Test Sample

In this study, materials ranging from low strength steel with yield about135MPa to High strength Steel with yield about 1200MPa were investigated. The average thickness of the material is 1.6mm. In order to define material parameters for numerical simulations and also to obtain accurate material information uniaxial tensile tests on these material sample as shown in Figure-10.1 were performed in accordance with AS1391-2007 standards in three different angles (0^0,45^0 & 90^0) with respect to the rolling direction at ambient temperature of 23 deg in a standard laboratory conditions using Instron hydraulic testing machine under displacement control at 1mm/min in a closed loop control mode. The true stress strain curves so obtained along with the test Apparatus were laid out in the Figure-10.2

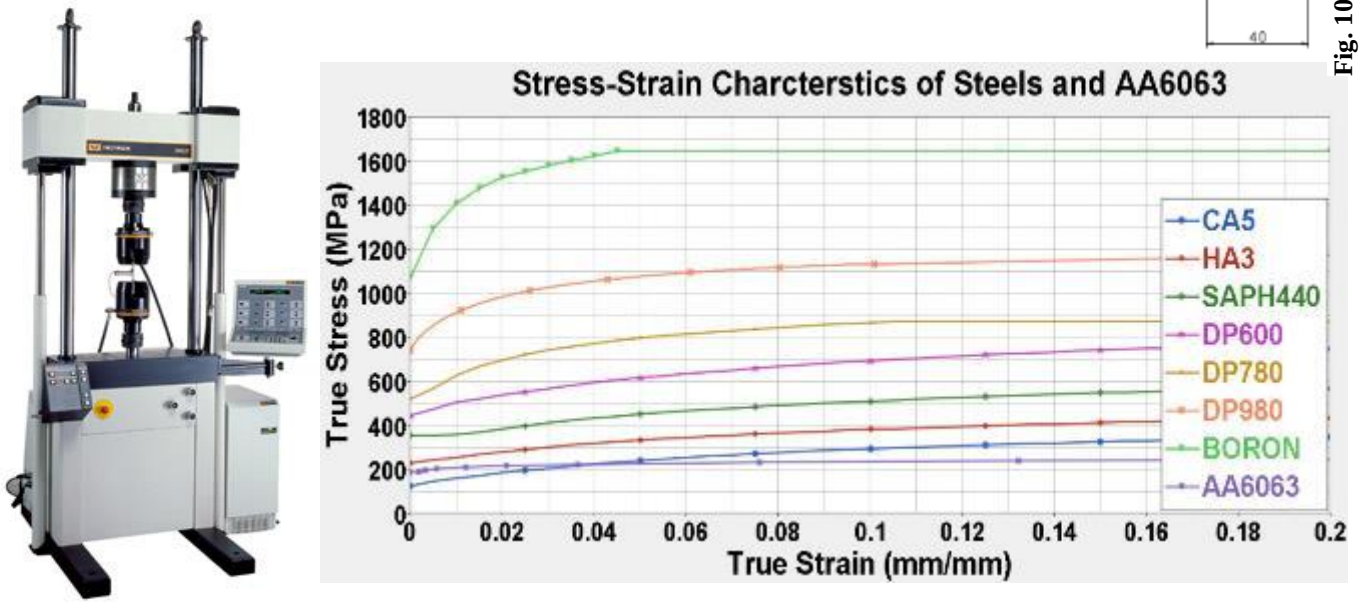

Fig. 10.2: Test apparatus and True stress-strain curves for the materials in consideration

The mechanical properties of these material samples are also summarized in the table 10.1.

The deformation of the structures involved in vehicle collisions can be considered predominantly as high deformation process where the structure gets loaded dynamically under different strain rates. Inherent sensitivity of steels to strain rates influences significantly the tensile properties and thereby crash behavior of the vehicle structure. Although its impractical to evaluate the strain rate properties of every grade of steel used in automotive domains, the guidelines provided by Auto/steel partnership (Cooperative group with Ford Motor Company, General Motors, Chrysler and US steel mills)provided direction in the selection of the material gardes. In this study seven different strain rate sensitive steel grades starting from HA3 to Boron steel are considered and their dynamic characteristics are extracted at different strain rates starting from the Quasi-static uniaxial tensile test as discussed above section with strain rate as low as 0.0001/s.

Coupons were prepared under tight tolerances as prescribed by AS1391-2007 (Figure-10.1) standards and care has been taken to minimize the load oscillations. The thickness of the coupons were maintained at 1.6mm and the desired loading rates were obtained by controlled Hydraulics of the machine .The data quality of the high strain rate test has been enhanced using DIC (Digital Image Correlation) due to accuracy and reliability limitations with strain gauges and Doppler extensometers. The DIC technique provided reliable non-contact measurements and accurate measurements of displacement and strains.

Table 10.1 –Mechanical properties of the Materials

Material Name	Density (kg/mm^3)	Poisson's ratio	Yield Stress (Mpa)	Ultimate Stress (Mpa)
Steel - CA5	7.80E-06	0.30	130	270
Steel -HA3	7.80E-06	0.30	235	340
Steel -SAPH440	7.80E-06	0.30	358	460
Steel -DP600	7.80E-06	0.30	445	673
Steel -DP780	7.80E-06	0.30	521	857
Steel -DP980	7.80E-06	0.30	742	1003
Steel -Boron	7.80E-06	0.30	1076	1625
AA6063 (Aluminium Alloy)	2.70E-06	0.33	192	235

The results of the coupon tests under different strain rates are extracted and the following Figure-10.3 depicts the strain rate responses for Low strength steel HA3, medium strength

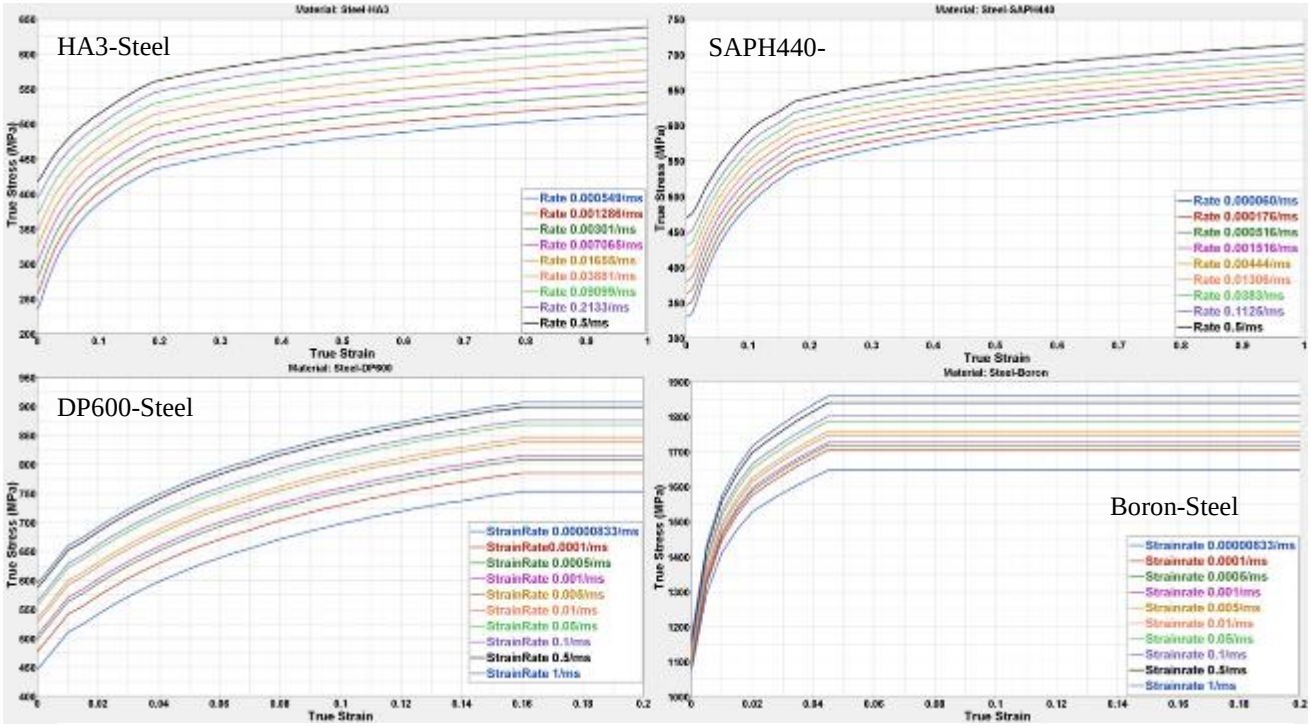

Fig. 10.3: Dynamic True stress-strain curves for the materials in consideration

SAPH440 steel through DP600 steel to high strength Boron Steel. The maximum strain rate achieved was 1/ms. From the data curves it can be observed that at even lower strain rates for lower strength materials a rapid increase of dynamic yield stress while it tends to be asymptotic at higher strength materials as seen in Boron Steel. On the other hand the tensile strength increases with strain rates all across the range in line with existing assumption on steel strain rate sensitivity. The data so obtained from quasi-static and dynamic tests feed directly into Numerical models which greatly enable the response predictions in a realistic manner.

The numerical models provide the needed prediction but their validity relies on the level of replication in the physical tests. The design space and performances so far understood and established needs their validation through their correlations to good test data. The next chapter provides the basis for this through quasi-static and dynamic tests which are critical to the research objective.

CHAPTER-11

11.0 Experimental characterisation through Quasi-static & Dynamic tests:

11.1 Design of Physical samples

In this study, thin walled specimens with different cross sections were designed based of initial confidence gained through upfront numerical simulation works with all the constraints and tolerances coming from welding, stamping and other manufacturing processes. The designs were then processed through standard manufacturing process which is vehicle production representative in terms of dimensioning, tolerances, material specs. etc.; These specimens are sourced from standard steel rolls and stamped in a controlled environment with tight tolerances. The thickness and mechanical properties are constant along the section length and MIG welded to form the intended sections. The dimensions of these specimens were carefully chosen to prevent the Euler buckling Abramowicz [43] and within the limits of suggested overall Length to Section size ratios. The following Figure-11.1 depicts the cross sectional dimensions of these specimens. The length is maintained at 350±0.1mm and thickness at 1.6 ± 0.1mm

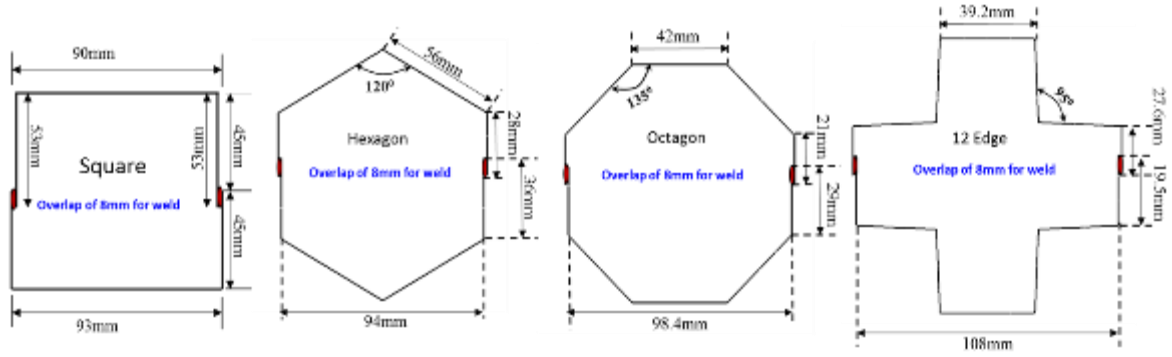

Fig. 11.1: Cross-sections and Dimensional details of the test specimens

11.2 Quasi-static Testing

Quasi-static tests on thin-walled Specimens were performed on a universal computer servo-control testing machine machine with 250kN capacity. The machine was operated at a constant cross-head speed of 0.1 mm/s. During the tests, the compressive load and displacement were measured using a strain-gauge load-cell. The machine was controlled by a PC that also recorded and processed the measured data from the test machine. As illustrated in the Figure-11.2 the specimens were placed between the loading platens and subjected to

axial compressive load at an ambient temperature of 23^0 C. The test specimens pre-crush and post crush under quasistatic conditions are also depicted.

Fig. 11.2: Quasi-static test apparatus and test specimens

11.3 Dynamic Testing

Dynamic test setup is as per the Figure-8.8.3 where in the physical samples are welded to a rigid plate and installed onto a sled vehicle. The sled frame is mounted onto a propulsion trolley and accelerated through high strength cables with controls by electric motors. The total weight of the sled vehicle is about 250kg and the speed targeted is 15m/s (54kph). All the kinetic energy of the systems is expected to be absorbed by crushing of the intended samples. The crush forces and displacements over time domain were recorded from the sled vehicle to a reasonable accuracy. The Figure-11.3 displays the sled vehicle upon which the frame with the samples welded is mounted. The data acquisition system along with the emergency brake system is also displayed in the Figure. The tests were done only Hexagon and Octagon shaped samples which are prepared with DP600 steel. The results of these tests are used to correlate the CAE models and establish the predictive capability with robustness of the finite element models along with methodology. These models were then further utilized to conduct more design experiments with different sections and with range of steel grades and Aluminum. The results of which are discussed in in the following sections.

Fig. 11.3: Dynamic test sled vehicle and Data acquisition systems

The tests so performed provide crucial data sets needed for the evaluation of the design responses. These responses provide an insight into the differences between reality and virtuality which are well discussed in the next chapter.

CHAPTER-12

12.0 Results and Discussions

12.1 Quasi-Static crush tests and CAE Simulation

For all the specimens in the crush tests, fundamental basic characteristic of each specimen in terms of Force-Displacement data were recorded and plotted. The deformation patterns were carefully analysed and from the collected data, Energy absorption parameters were obtained .The crush tests were repeated twice for most of the specimens to assure results repeatability and accuracy. Within in the data limits, a discrepancy of two to four percent was observed in the results related to identical specimens tested under same conditions. The physical test results obtained are as in the table-12.1 and compared with corresponding theoretical and analytical FEA values.

Table-12.1 Comparison of Results of quasi-static tests, CAE and theory

Material: Steel-HA3 Specimen Length:350mm			*Mean Force P_m (kN)*			*Peak Force P_{max} (kN)*		*Crush δ_m (mm)*		*Total Absorbed Energy E_{abs} (kJ)*		*Specific Energy Absorbtion SEA (kJ/kg)*	
CROSS-SECTION	*Dimension 'C' (mm)*	*Thickness 't' (mm)*	*CAE*	*TEST*	*THEORY*	*CAE*	*TEST*	*CAE*	*TEST*	*CAE*	*TEST*	*CAE*	*TEST*
Square	90	1.6	27	28	27.6	116	112	243	254	6.56	7.16	4.17	4.56
Hexagon	56	1.6	48	44	45.6	137	134	252	266	12.34	11.74	8.41	8
Octagon	42	1.6	58	59	56	140	141	267	277	15.48	15.78	10.55	10.76
12-Edge	39	1.6	92	93	89	186	196	250	248	23	23.56	12.51	12.4

12.1.1 Deformation mode, Mean Force, P_m and Crush, δ_m

The deformed sections and pattern of deformations from both test and CAE are compared in the Figure-12.1. It can been seen that all the sepcimens collpased in a regular repeatable lobed pattern which is the characterstic of an ***inextensional*** mode of collapse except for Octagonal section which collapsed in a mixed mode of ***inextensional and extensional***. The Square shape sample collapsed with 3 lobes while Hexagonal shape with 4 and Octagonal shape with 5 lobes. Due to its close package of section with corner angles closer to 90 deg, the 12 edge shape collapsed forming 6 lobes thereby having the higehst plastic work done

which has direct bearing on energy absorbed. The test curves and curves from CAE agree to a good extent at initial peaks while to a reasonalble extent through the crushing process.

The first comparator for effectivenss of an energy absorber in terms of force is the Mean force $\boldsymbol{P_m}$ which provides a quick first view of its straining capacity toward crushing.With highest number of edges to its package, the 12-edged sample definetly leads the pack with 93 kN followed by Octagon with 59kN, Hexagion with 44kN and lowest from Square section with 28kN. The relative performances can be viewed through the Figure- 12.2 in terms of bar chart highlighting the Mean force values for different cross sections. Extending further, the crush experiments were continued on for material range chosen in the previous sections starting from low yield strength steel CA5 to highest with Boron steel including Aluminium alloy AA6063.

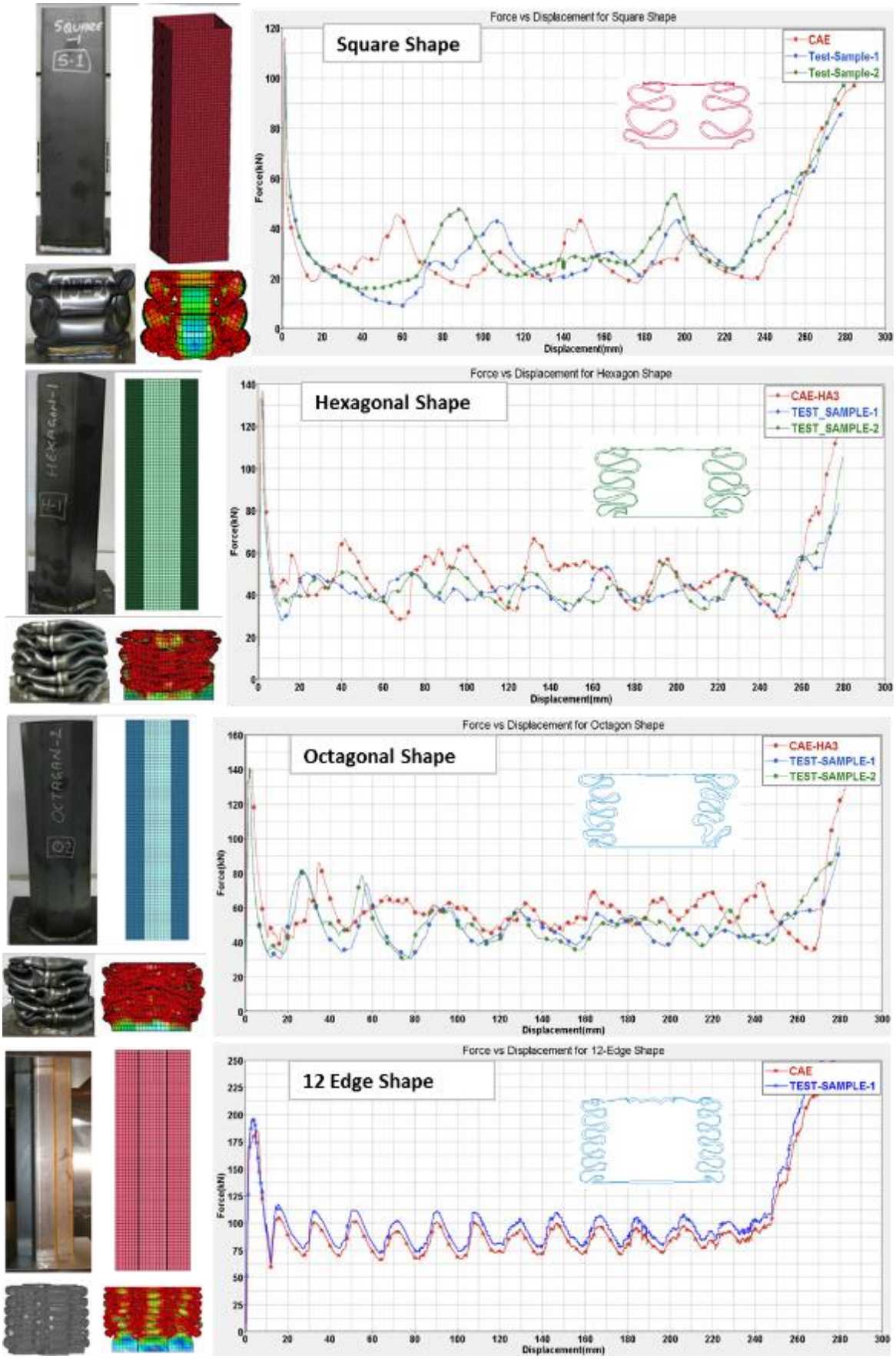

Fig. 12.1: Force-Displacement characterstic curves of the samples and their deformation modes

The responses for different materials can be viewed from the Figure-12.2 where an interesting trend can be observed. At lower yields the force capacity of the sections are in close proximity while at higer yeilds they distribute distinctly from each other indicating their strong dependency on material characterstics.

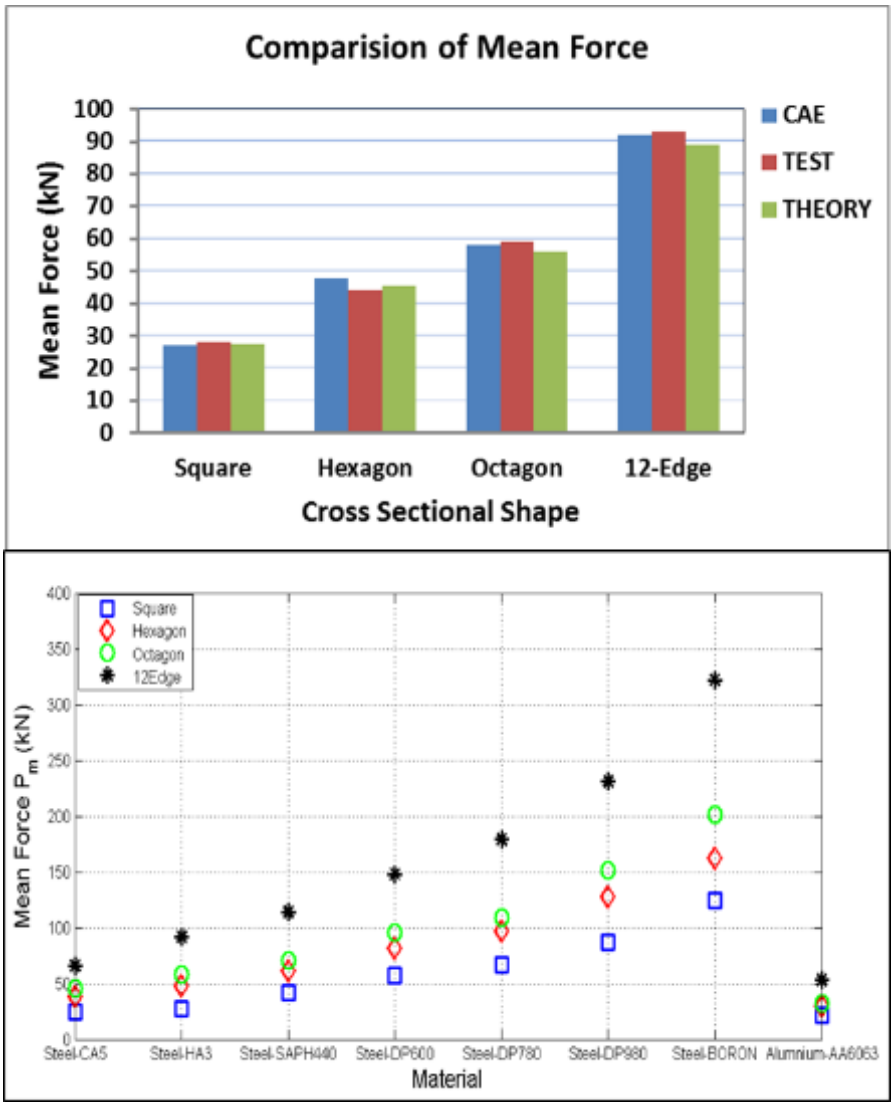

Fig. 12.2: Mean force comparison for different cross section and different Materials

Peak force P_{max} is another force measure which provides an indication of the amount of initial force needed to form the first lobe. Once the first lobe formation is initated the force levels drops down to oscilate around the mean value.In its natural condition without triggers the peak force significes the initial stiffeness of the section to collpase. The tabulated values in table-12.1, indicates highest peak value for the 12 edge section which descends to square section.

Another measure which is of significance the total amount of crush δ_m which is indicative of displacement domain of the crush process. Depending on the crushing mode and packaging of the corners with corner angles and material stiffnes, the crush value varies. For simple package of corners with less material distribution along with obtuse include corners angles provide the maximum crush as they tend to have more spatial space to accommodate the material flow between the lobes due to the mixed mode of collapse in inextensional and extensional modes. For the sections with increased material distribution with acute corner angles the spatial space would be constrained between the lobes due to inextensional mode and can lead to lower crush values. This can be clearly evident from the fact that the section with obtuse corner angle of 120^0 which is the Octagon section has the highest amount of crush oweing to its mixed mode collpase followed by hexagon and then by Square . For 12 edged section which has collpase pattern with maximum lobes at 12 corners the material stack up is higher and there by lower crush which lead to a condition of higher stiffness with maximum mean force in smallest crush which inturn provides a higher slope in the energy characterstic of the crush can.

12.1.2 Total energy E_{abs}, Specific Energy Absorbtion *SEA* and Weight Effectivenes W_E

The second significant comparator for the effectivenss of an energy aborber is with the energy domain. The table-12.1, provides a clear comparion of the energy absorbing capacities of the different section in consideration with clear leader being the 12 edged section with 23kJ of energy aborbstion for an effective crush of 250mm followed by Octagon section with mixed mode collapse and descending down to square section. The Figure-12.3 below provide the energy plot of the tested cross sectional shapes and its evident that 12 edged shape with maximum material distribution along with favourable corner angle provides highest energy absorption. It also indicates the highest slope (stiffness) to collapse due to the modes of deformation at the corners initiating maximum plastic work.

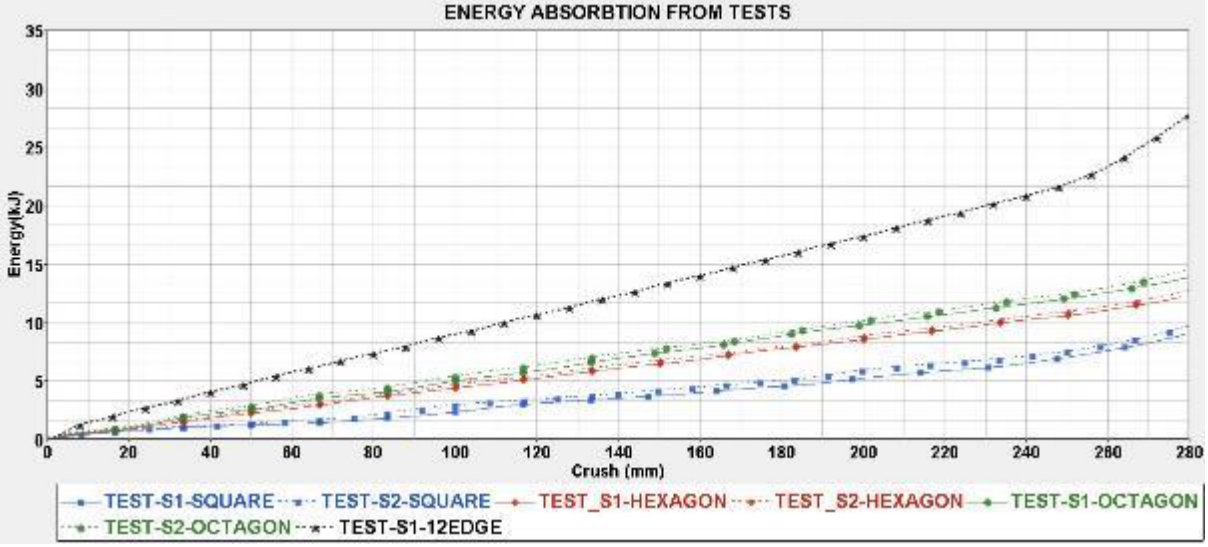

Fig. 12.3: Total energy (E_{abs}) comparison for the specimens with different cross sections

The desire for an enegry absorber with highest capacity is often limted by the package spacing in the subsystems into which they are integrated. Designing such a system with in the allocated space is of big challenge for the designers. This contraining limitation would be further more complicated if mass limitation also gets added to the list. For practical applications the total energy provides only gross energy but, with limitation of space and mass it becomes difficult to select and layout the section within the allocated space. So a more practical measure of energy which is Specifc Energy Absorbtion in short ***SEA*** is more useful. This provides a choice for the designers to rightly layout the sections with minimum mass. The tabulated values form the table provide a direction with clarity and enables selection of the section for maximum energy aborbtion with minium mass. Clearly the 12-edge is leading the pack with highest ***SEA*** as compared to the rest of the sections. Its high SEA also indicates of the section's potential to downsize and provide similar performnace as that of other sectional shapes there by providing felxibity for the designers.The following Figure-12.4 illustrate the factual description of the above disucssion. The Figure-12.4 also presents the SEA data from further set of crush experiments done on secimens with material range as described previously. The imperative performance of the 12 edge section for SEA can be observed with every material.

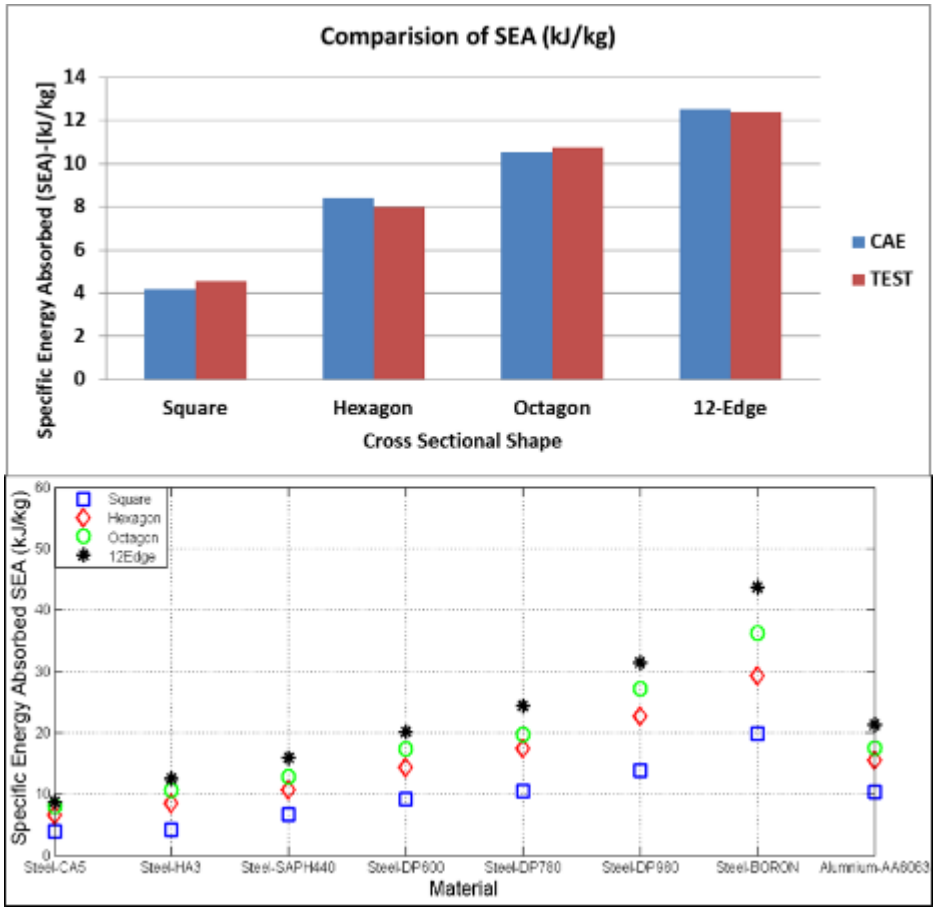

Fig. 12.4: SEA comparison for different cross-sections and materials

Its also interesting to note the SEA for Alumnium alloy which provides better value than low end steels due to its lighter density and indicative of better alternative choice for energy absorption than corresponding steels when mass becomes dominant factor.This aspect is getting a closer attention for hybrid and elctric vehicles where mass become a dominant factor.

Another important trend which can be inferred from the plots is the dependency of SEA on the material charterstics. For the same section shapes with higher strength material gives higher SEA and this could potentially become a limitation in using SEA as a comparator between sections with different materials however, within the same material range SEA can provide clear direction and choice of selection. The acheivement of desired collapse is often constrainted by the intervention of the other failure modes like global bending, manufacturing defects and other vehicle systems interferences into ideal collapse behaviour. Quantitative assessments of such collpase modes with infusion of other failure modes limits the definition of SEA and its application. However SEA in combination with crush efficiency can become a powerful comparator and it serves to be an appropriate parameter for defining the

effectiveness of a section. This product can be nomenclatured as ***"Weight Effectivenes , W_E***". The description of crush efficiency is through full collapse process and it doesnot vary widely in thin walled columns when collpase modes stability is achieved. In other words, crush efficency must be ascertained before W_E can be assumed to be convergent with SEA. Table-12.2 provides the quantitative evaluation of weight effectiveness for different cross

sections for a tested material of HA3 where in one can observe the dominance of 12 edge section and the same trend is continued even for different materials of steel and alumnium as seen in Figure-12.5. One interesting observation can be clealry noticable that the W_E of

Table-12.2: Quantitative evaluation of Weight effectiveness (W_E), solidity ratio ϕ and structural effectiveness η

Material: Steel-HA3 Specimen Length:350mm			*Specific Energy Absorbtion SEA (kJ/kg)*		*Weight effectiveness W_E*		*Solidity ratio(ϕ)*	*Structural Effectiveness (η)*
CROSS-SECTION	*Dimension 'C' (mm)*	*Thickness 't' (mm)*	*CAE*	*TEST*	*CAE*	*TEST*		
Square	90	1.6	4.17	4.56	2.90	3.33	0.071	0.25
Hexagon	56	1.6	8.41	8	6.06	6.11	0.066	0.39
Octagon	42	1.6	10.55	10.76	8.05	8.51	0.061	0.47
12-Edge	39	1.6	12.51	12.4	8.94	9.08	0.106	0.50

Alumnium being higher than low to mid range steels and provides a choice for Energy absorbers with lighter mass.

Another derivative measure of SEA for desensitising its dependence on material strength is the structural effectivness which was discussed in detail in the previou sections. Over wide range of material strength preperties provided the structural geometry and the collpase mode are same the SEA is linerly dependent on the Ultimate tensile strnegth.The parameter of Structural effectiveness "η" desensitises the dependency and provides a measure which is dependent on structural Geometry alone. For a given solidity ratio **(ϕ)** the table-12.2 provides the effectiveness of collapse structure purely from geometrical perspective which serves as an important comparator tool to designers when selecting the shape and dimensions of the energy absorber. For the given dimensions of the specimens it can be seen that 12 edge section is twice geometrically effective than conventional square section.

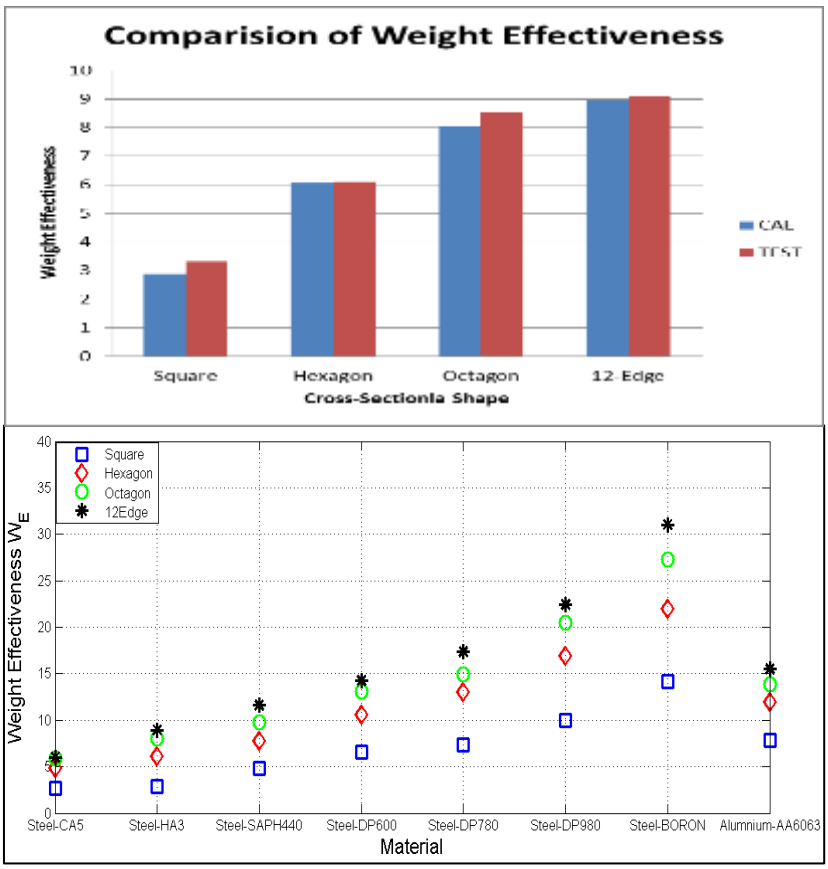

Fig. 12.5: Weight effectiveness (W_E) comparison for different Cross-sections and Materials

12.1.3 Crush Efficiency *(S_E)*, Crush force Efficiency *(A_E)* and Energy Efficiency *(E_E)*

In addition to above comparators which provide charactertsic measure to compare different energy aborbing devices it is also important to consider the measure of space utilisation and effectiveness of packing the folds during the collpase process. The C***rush efficiency*** S_E provides the displacement treatment to the collpase process and follows the discussion on total crush δ_m from the previous sections. It gives the measure of packaing the folds within the allocated space. With in the wide material range and thickness the sections with proper corner angle collapsing through inextensional modes to a simillar level as evident in the Figure-12.1 where it can be observed that the all the section collapse with 75 % crush efficency when there is no intervening spurious failure modes.

Material: Steel-HA3 *Specimen Length:350mm*			*Crush Efficiency* S_E *(%)*		*Crush Force Efficiency* A_E *(%)*		*Energy Efficiency* E_E *(%)*	
CROSS-SECTION	*Dimension 'C' (mm)*	*Thickness 't' (mm)*	*CAE*	*TEST*	*CAE*	*TEST*	*CAE*	*TEST*
Square	90	1.6	69	73	23	25	16	18
Hexagon	56	1.6	72	76	36	33	26	25
Octagon	42	1.6	76	79	41	40	32	32
12-Edge	39	1.6	71	71	53	48	35	34

Table-12.3: Comparison data for Crush Efficiency ($S_{E)}$, Crush force Efficiency ($A_{E)}$ and Energy Efficiency ($E_{E)}$

The ***Crush force efficiency*** A_E which is a relative measure of load fluctuation happenening between the Mean and Maximum forces during the collapse process.Interesting trend can be observed for the sections tested with the range of materials as in the Figure-12.6 where at low strength materials the crush force efficiency tend to be divergent between the sections where geometrical layout of the material would be dominant in initiation of collapse process towards fully crushed configuration. This influence of geometry tend to diminish as the material becomes stronger and stiffer where corners become stronge and thereby reducing the effect of geometry. In actual designs, most of the designers come over this problem through careful placement of triggers to initiate the collapse proces at lower forces there by maintaining a decent crushforce efficiency for stability and robustness.

The last measure of the effciency is the ***Energy Efficiency*** E_E which is the measure of the energy absorbers's ability to maximise the energy absorbtion as compared to the ideal condition of full collpase at the peak load. It can be observed that the sections tested within the material range the E_E averages to about 26% in untriggered condition. This effieciency leans heavily towards the peak force level at the initiation of collapse process. However in triggered condition as peak forces smoothen out towards mean forces the Energy efficiency get improved to a greater extent and can go as high as 70 to 80%. Table-12.3 provides the quantative details for the comparsions for a tested material of HA3 for all the three efficiency measures.

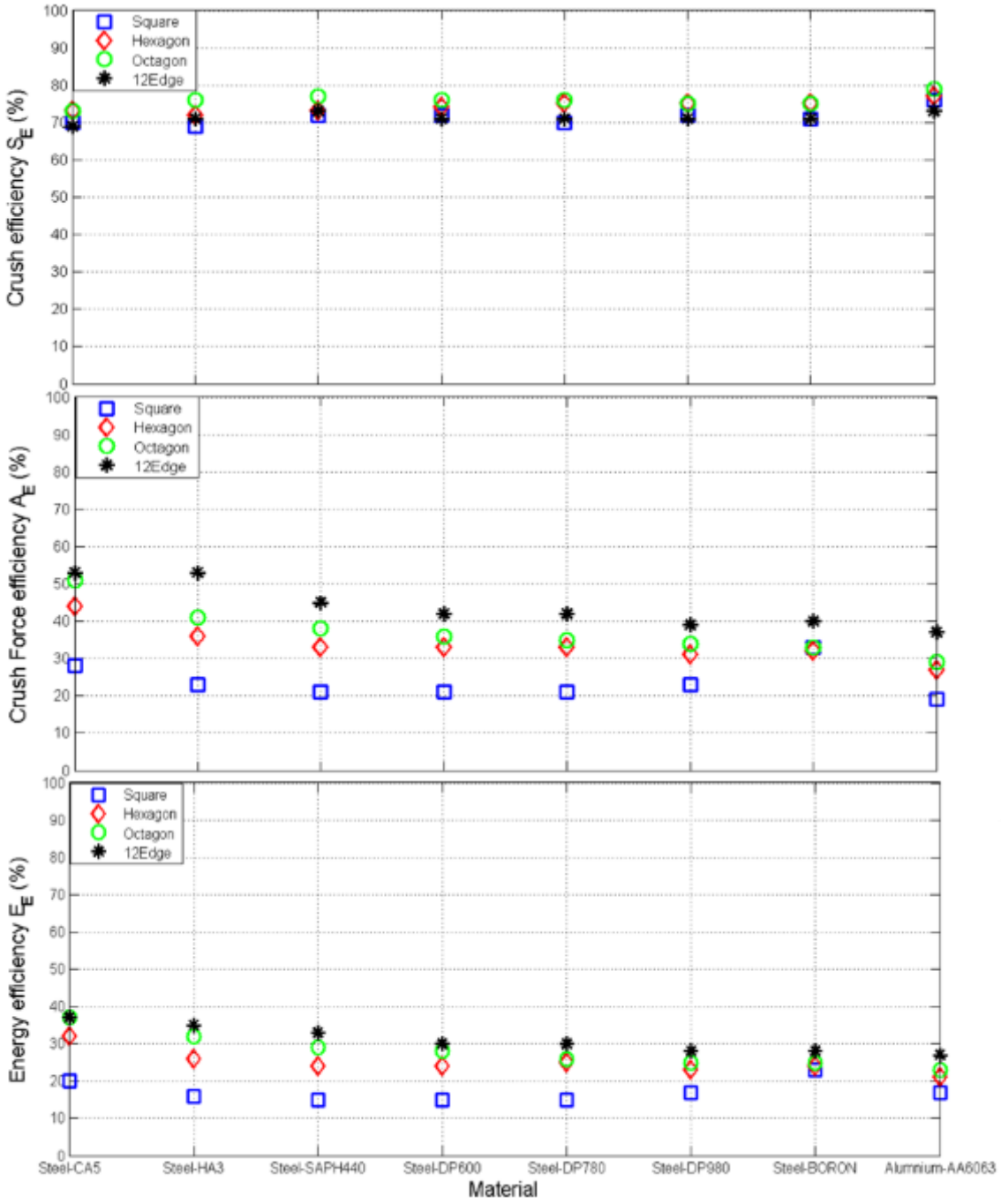

Fig. 12.6: Crush Efficiency ($S_{E)}$, Crush force Efficiency ($A_{E)}$ and Energy Efficiency ($E_{E)}$ for different materials

12.2 Dynamic crush tests and CAE Simulation

For all the specimens in the crush tests, fundamental basic characteristic of each specimen in terms of Dynamic force and displacement data were recorded and plotted. The deformation patterns were carefully analysed and from the collected data, Energy absorption parameters were obtained .The crush tests were repeated twice for most of the specimens to assure results repeatability and accuracy. Within in the data limits, a discrepancy of two to four percent was observed in the results related to identical specimens tested under same conditions. The

physical test results obtained are as in the table-12.4 and compared with corresponding analytical FEA values.

Table-12.4 Comparison of results: Dynamic tests and CAE

Material: Steel-DP600								
	Peak Force P_{max} (kN)		**Max., Dynamic Crush δ_c (mm)**		**Crush Energy E_{dyn} (kJ)**		**Kinetic Energy Absorbed (%)**	
CROSS-SECTION	**CAE**	**TEST**	**CAE**	**TEST**	**CAE**	**TEST**	**CAE**	**TEST**
Hexagon	343	330	121	120	13.81	14.02	50.53	49.55
Octagon	331	340	125	126	14.29	14.37	48.80	50.71

12.2.1 Deformation mode, Max Force P_{max}, Dynamic crush δ_c and Crush Energy E_{dyn}

The deformed sections and the pattern of deformations from both test and CAE are compared in the Figure-12.7. It can be observed that both the specimens collapsed in a consistent manner with regular repeatable lobes with mixed modes involving ***inextensional and extensional modes.*** The specimens are without any triggers and targeted to collapse in their natural folding modes. The test and CAE curves agree with each other to a reasonable extent at their peaks and also through the crushing process. The first comparator for the effectiveness of the sections in consideration for energy absorption is initial peak force P_{max} needed for initiation of the collapse process. The specimens of Hexagon specimen collapsed with higher peak force at 343kN than that of Octagon due the differences in packaging of the corner elements in the edges which in Octagon is unfavourable and so is the lower initiation force. Although the main deformation mode of repeatable collapse was initiated at the contact point, a late instability due the elasto-plastic stress wave propagation caused the octagon specimen to deviate from regular crushing process at the end as indicated in the Figure 12.7.

The second comparative parameter which is indicative of crushing progression along the specimen is the dynamic crush $\boldsymbol{\delta_c}$ **.** The test results for the hexagon and octagon specimens indicates the simillar progression of the deformation process and agree to a good extent with the corresponding CAE values. The similarity is in crushing process and its progression should provide simillar energy absorbtion which is the case as the specimens are designed to simillar dimensions. The Crush energy E_{dyn} absorbed stands at about 14kJ and both sepcimens absorb about 50% of the initial kinetic energy. The results comparison of dynamic

test and CAE provides close predictiveness in a reliable way with reasonable accuracy. The CAE models were able to predict and describe the plastic behaviour with inclusion of strain rate effects. The predictiveness of both static and dynamic behaviours of the crush process is at higher note, mainly due to good material model description through eloborate testing and incorporation of the test data within material models of Ls-Dyna.

The results conformance between test and CAE provided foundational step upon which further investigations were performed. More experiments were conducted numerically across the intended sections with selcted materials ranging from low end HA3 steel to high end Boron- steel along with Alumnium-AA6063. The numerical experiments were done under same loading condtions of 15m/s amd with same boudary conditions. The results so obtained are discussed further.

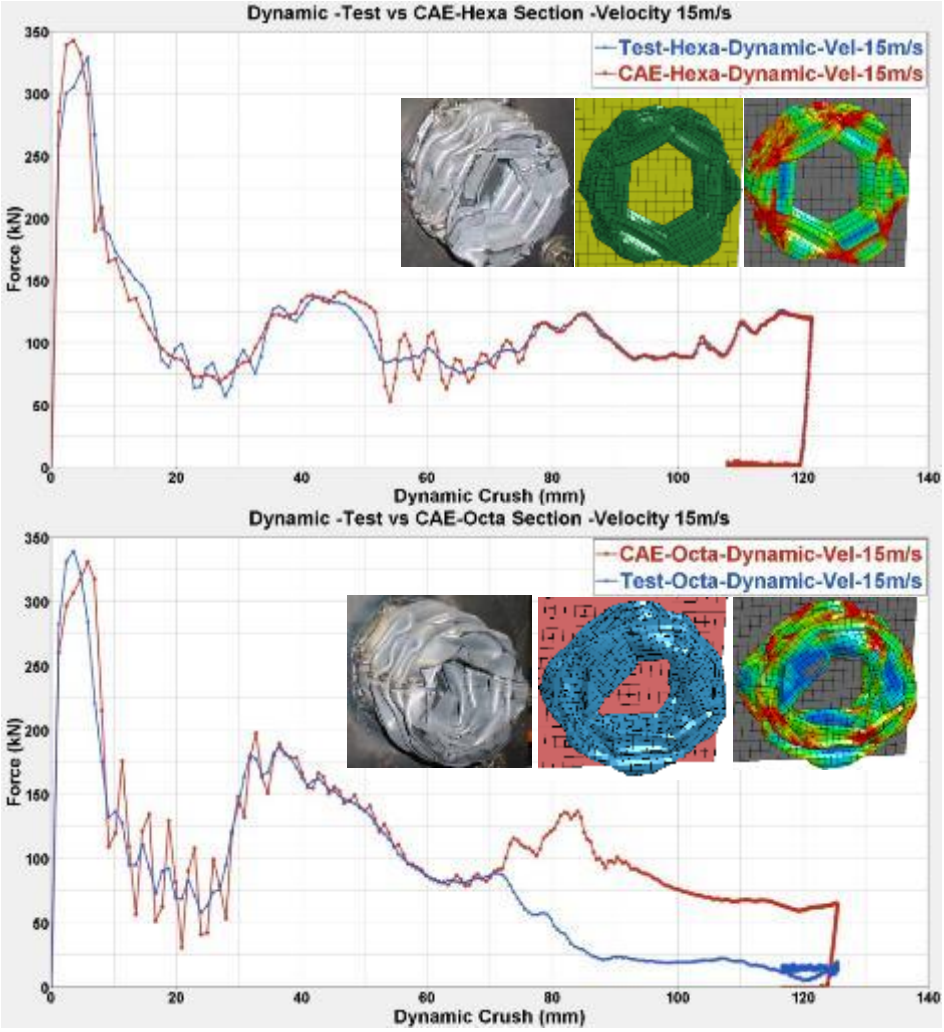

Fig. 12.7: Force-Displacement characterstic curves of the samples and their deformation modes

The intended specimens with sections of Square, Hexagon, Octagon and the newly developed 12-edge are subjected to dynamic crush tests at 15m/s with different materials of steel and Aluminium as mentioned before and their responses are extracted in a similar fashion. The fundamental characteristic of the crush process is as in the Figure-12.8. The force oscillation characterises the crushing process within the package domain in terms of crush. The velocity of impact invokes the strain rate loading on the specimens while an appropriate material stress-strain curve is selected corresponding to the loading rate to describe the state of stress in the plastic collapse process.

The force-displacements curves (Figure-12.8) indicate the dominance of 12-edged section over rest of the specimens with highest peak forces and shortest dynamic crush. The design of 12-edge section with corner angle of 95^0 provides an ideal corner element and collapse of that element provides highest energy absorption. With its tight packaging of edges the lobes collapse with shortest wavelength and there less collapse. The data curves of the peak crush force P_{max} and dynamic crush $\boldsymbol{\delta_c}$ as in Figure-12.9 provides the overlay with other sections with different materials.

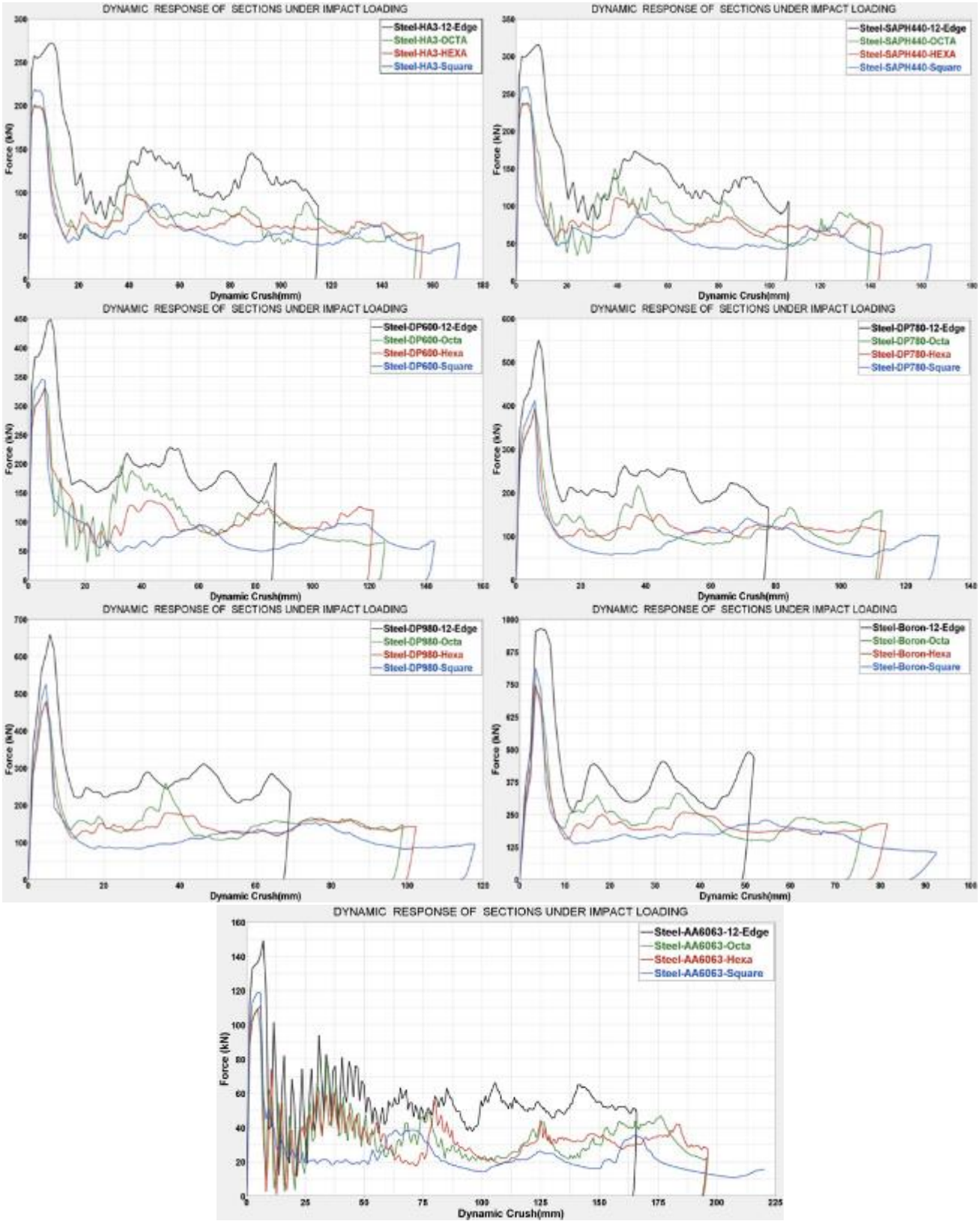

Fig. 12.8: Dynamic crush responses of thin walled sections tested at 15m/s

The sections of Octagon and Hexagon performed similar to each other for the same reason as discussed previously. The Square section which performed inferior in the quasi-static crush tests performed better in the dynamic crush. The favourable corner angle closer to 90deg in

the square sections gets attenuated by the higher strain rate effects during the crushing process. The sections with Aluminium collapsed in a similar fashion as that of Quasi-static tests due to insensitiveness of Aluminium to the rate effects which makes a unique material choice for energy absorption where energy absorption at constant force without getting affected by loading rate is desired.

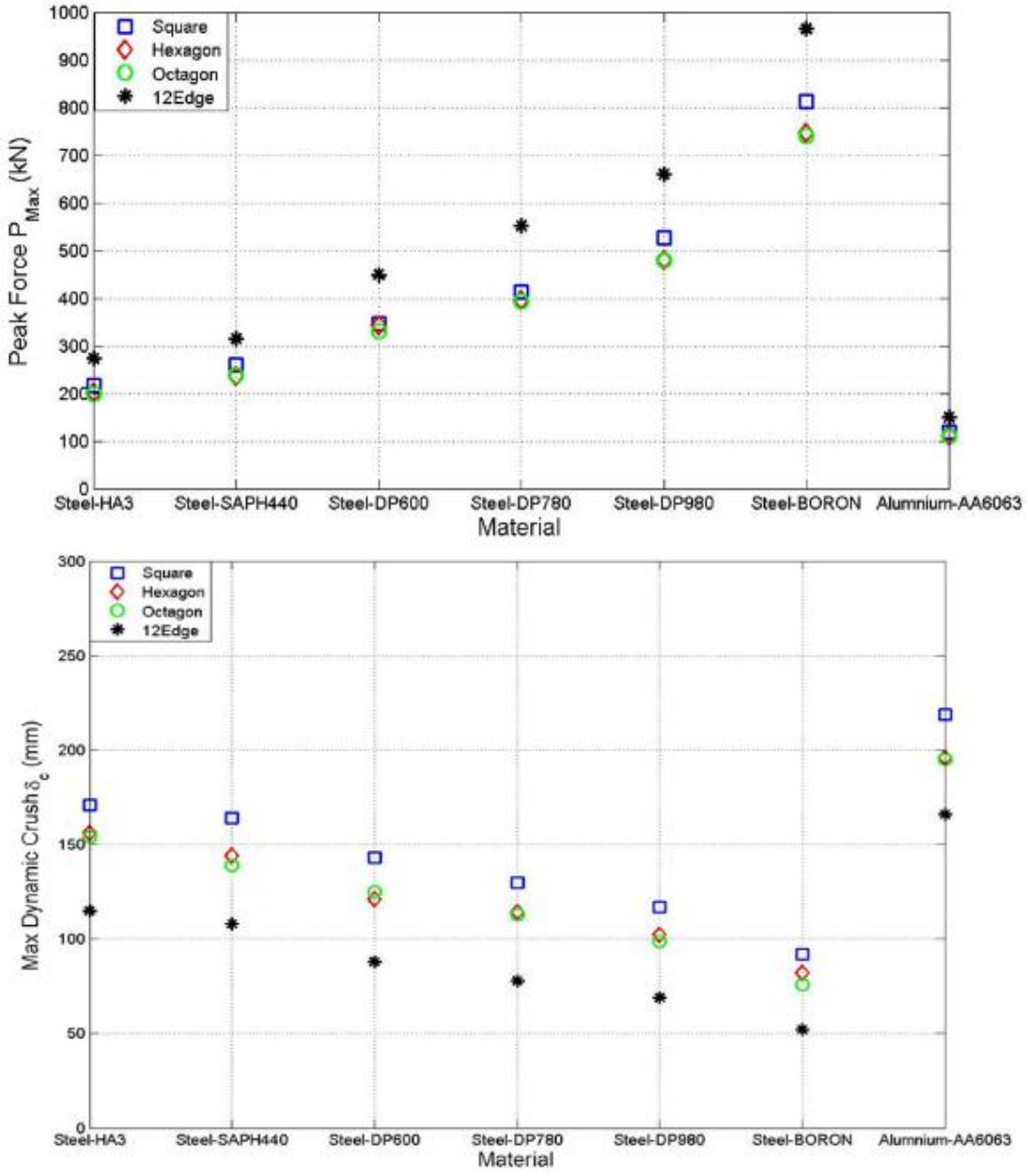

Fig. 12.9: Dynamic crush responses of thin walled sections tested at 15m/s

The dynamic crush responses indicate very low crush for 12– edge sections across the material range indicative of it continuous dominant response. As the strength of the material increases the dynamic crush reduces indicative of increase in corner wall stiffness and there by higher force to initiate collapse. Square Section with lowest number of corners performed lowest in the ladder.

The energy responses in term of Dynamic crush energy and percentage of Initial kinetic energy is an important parameter in characterising the performance of the thin walled sections. The energy absorbing capability of the sections decides the choice of the sections for designers to develop the crash compatible structure. The responses in Figure-12.10 indicates again the dominant performance of the 12-edge sections across all material ranges and has indicated to absorb about 70% of initial kinetic energy with the current design space and dimensions. This is about 52 % higher than convention square sections, 37% higher than Hexa and 32% higher than Octagon sections with same material, thickness and packaging spaces. The trends indicate increase in the energy absorption with material strength due to stiffness enhancements and higher force requirements for collapse initiation and progression.

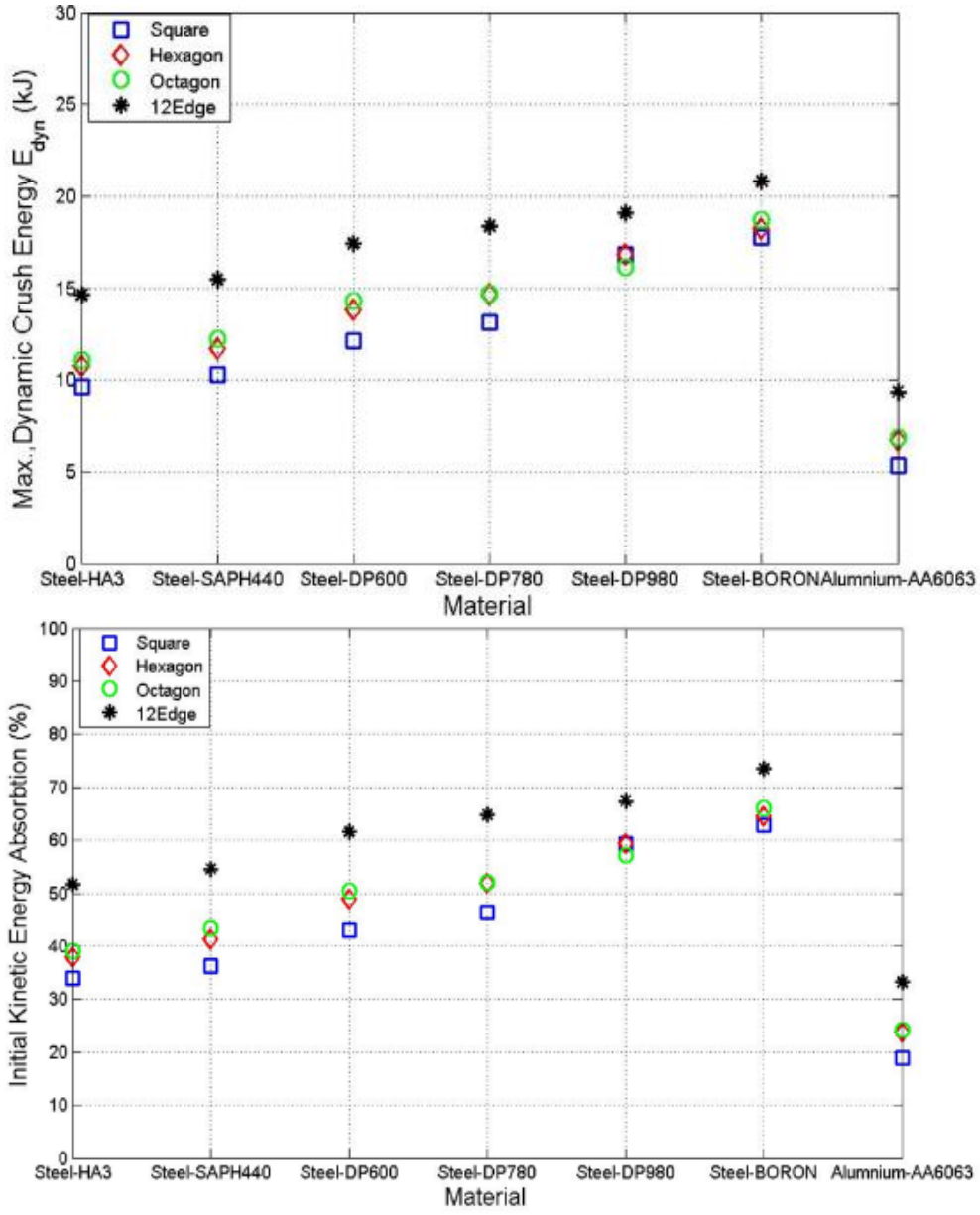

Fig. 12.10: Dynamic Energy responses of thin walled sections tested at 15m/s

12.2.2 Effect of impact velocity on the dynamic responses

One important aspect of the thinwalled sections without triggers under dynamic impact loading is the effect of impact velocity on the crushing process. This aspect is investigated and the results are as in the Figure-12.11. Though the main crush deformation of assymteric mode is initiated at the initial contact point, the inertial effect in the form of impact stress wave propogation can cause tube to quickly experience instbility which can lead to global bending. The sections under considerations are investigated further for different impact velocities starting from 5m/s to 100m/s. The previosuly tested material DP600-steel is considered for the material and thickness of 1.6mm. The responses indicate robust pefromnces under variable velocities. The sections collapsed in a repeated lobed fashion with similar Peak force (P_{max}) and follwed simillar crush progression up until the velocities of 40m/s. The rapidity of loading under 100m/s is of extreme and the 12 edge section provided good crush progression with ***inextensional*** mode of deformation thereby establishing its dominance in multitude of static and dynamic load cases.

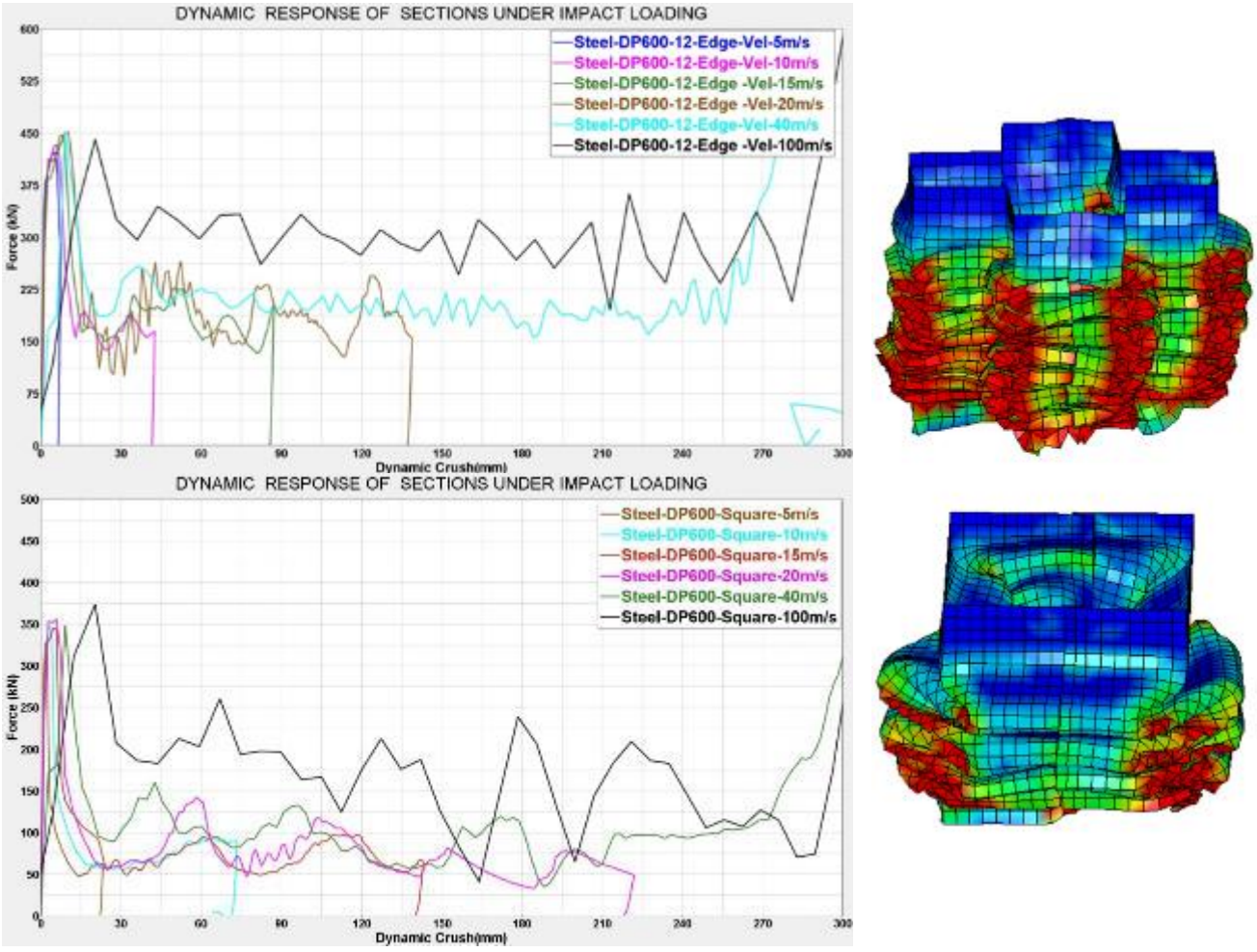

Fig. 12.11: Dynamic responses of thin walled sections tested at variable velocities

CHAPTER 13

13.0 Extension to an AutomotiveVehicle towards crash performance

In the domains of automotive industry, vehicle crashworthiness and occupant safety remain among the most tangible, important and challenging design considerations. The response of vehicle structure in a crash event greatly affects the occupant's injury performance and fatalities. For the vehicle structure to be more effective in a crash event, it has to have good energy compliance systems to manage the crash loads and its propagation to the occupant compartment. In most of the modern day vehicles an energy management system would be installed between the bumper and the vehicle structure to help absorb some of the collision energy and reduce occupant excursion velocities.

From the safety facts from NHTSA data for the year 2007 the distribution of fatalities by different type of vehicle crashes was plotted (Figure-13.0) where it can be observed that majority of the crashes are happening in a head on fashion typically termed as frontal impacts. The pie distribution of the fatalities indicates a phenomenal value of 53% towards drivers of the vehicles while 22% is attributed to passengers.

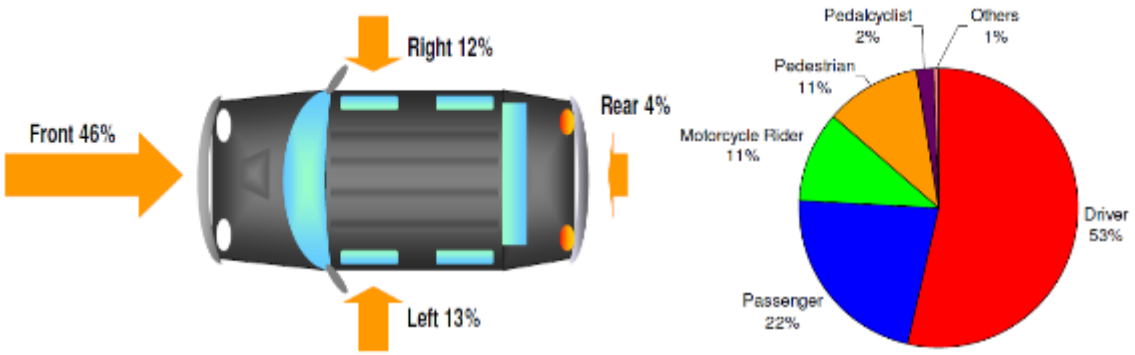

Fig. 13.0 Fatal distribution of vehicle crash types from Safety facts- NHTSA 2007

Asymmetric or concentrated loading across the vehicle front along with lack of enough structural capacity to specifically take these loads is the main reason for high intrusions into passenger compartments and associated injuries. When these injuries attributed to intrusions, NHTSA's injury data shows many occupants had serious chest injuries than any other injury type. These chest injuries are found to be on higher level when old passengers above 60 are involved. It is for this reason chest injury performance is considered for evaluating the design responses on full vehicle level simulations.

Moreover when a crash situation is unavoidable, it is the crash energy and the manner in which vehicle occupants experience the associated forces that will determine the extent of injury to those occupants. So improving the vehicle crashworthiness reduces the magnitude of the forces experienced by the occupants while on other hand the everlasting desire to improve the fuel efficiency in conventional and charge range in Electric/Hybrid vehicle creates a great desire for of light structures. Often this lightening exercise aggravates exercises aggravates the risks for occupant protection. The Solution to this competing design goals of safety and fuel efficiency through light weight structures lie in the origination of innovative upfront energy absorption designs.

The understanding and characterization of thin walled structural columns with multi cross sections developed in previous sections fit well into the domain of upfront energy absorption motive and would not complete if their ultimate responses are analyzed at a full vehicle level in terms of their capacitance for crash energy absorption. The data from IIHS (Insurance institute of Highway safety) [44] indicates that the overall driver death rate in midsize cars is 23% lower than in small cars which shows the vulnerability of small cars with light bodies towards frontal crashes. Keeping in view light weighted bodies, a full vehicle CAE model was purposefully chosen where in very tight package space constraints are prevalent with smallest space availability for the energy absorbing devices within the category of small cars. The interlying idea is to establish the fact that the energy absorbing devices successfully working in such a tight space constraint domain would be definitely be able to perform at a higher degree when used in a larger space domains of medium and large segment of vehicles.

13.1 Automotive Vehicle-CAE model and crash simulation

A full vehicle CAE model of a small car which is resonably correlated was loaned from an OEM and its is considered for evaluation of the previously developed multi corner sections for energy absorbtion in a dynamic loading environment following the test conditions specified in the FMVSS 208 (Federal Motor Vehicle Safety Standards) standard. This standard also serves as the basis for the NHTSA's New Car Assessment Program (NCAP) rating the new cars for their crash performances. The intended test vehicle is decked with ATDs (Anthropomorphic Test Dummy) mimicking a human occupant in un-restrained without seat belt conditions and subjected to a velocity of 56kph into a rigid wall as depicted in the Figure-13.3

The critical injury criteria, which are generally assessed, include chest deceleration, chest deflection, and femur/Tibia (proximal) lower leg. For the purpose of assessing the effectiveness of energy absorption in the devices so developed in previous section, only chest deceleration and dash intrusion, which is indicative of Femur/Tibia Loading [45], is considered

Fig. 13.1: Package layout of the front-end structure of an automotive vehicle

The full vehicle CAE model is made up of 1759948 nodes and 1814462 elements with 1282 parts. The vehicle length is 3724mm with a mass of 1100kg. The package space available for the energy-absorbing device is just 100mm, which amounts for only 2.7 % of the total length. The Figure-13.1 shows the layout and packaging of the front-end structure comprising of the bumper and energy absorbing devices or "***crush cans***". The assemblage of these crush cans to the bumper system is as depicted in Figure-13.2

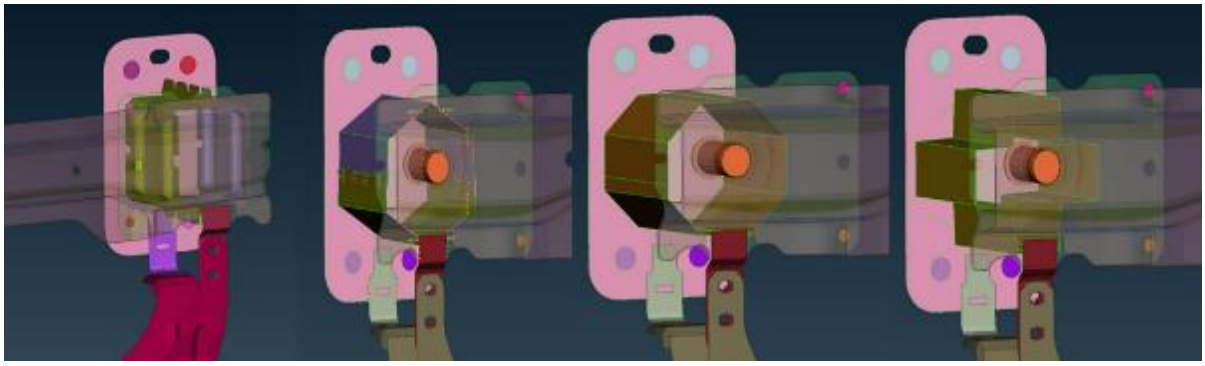

Fig. 13.2: Assemblage of crush cans to bumper system

In full frontal crash scenario, this front-end structure is designed to be the primary load path and do the crash energy management in such a way that it decelerates the vehicle by

absorbing the crash kinetic energy in a controlled manner. This controlled absorption and deceleration of the vehicle should produce a safe deceleration to the occupant of the vehicle. This safe deceleration of the occupant can only be possible if the kinetic energy absorption in the front-end structure is maximised. Figure-13.3 displays the dynamic collapsing of the crush cans of different cross section in their characteristic manner and thereby affecting the vehicle's deceleration and dynamic crush. The whole simulation event of Full-frontal impact to a rigid wall at 56kph is completed in 90 ms and the responses are extracted accordingly.

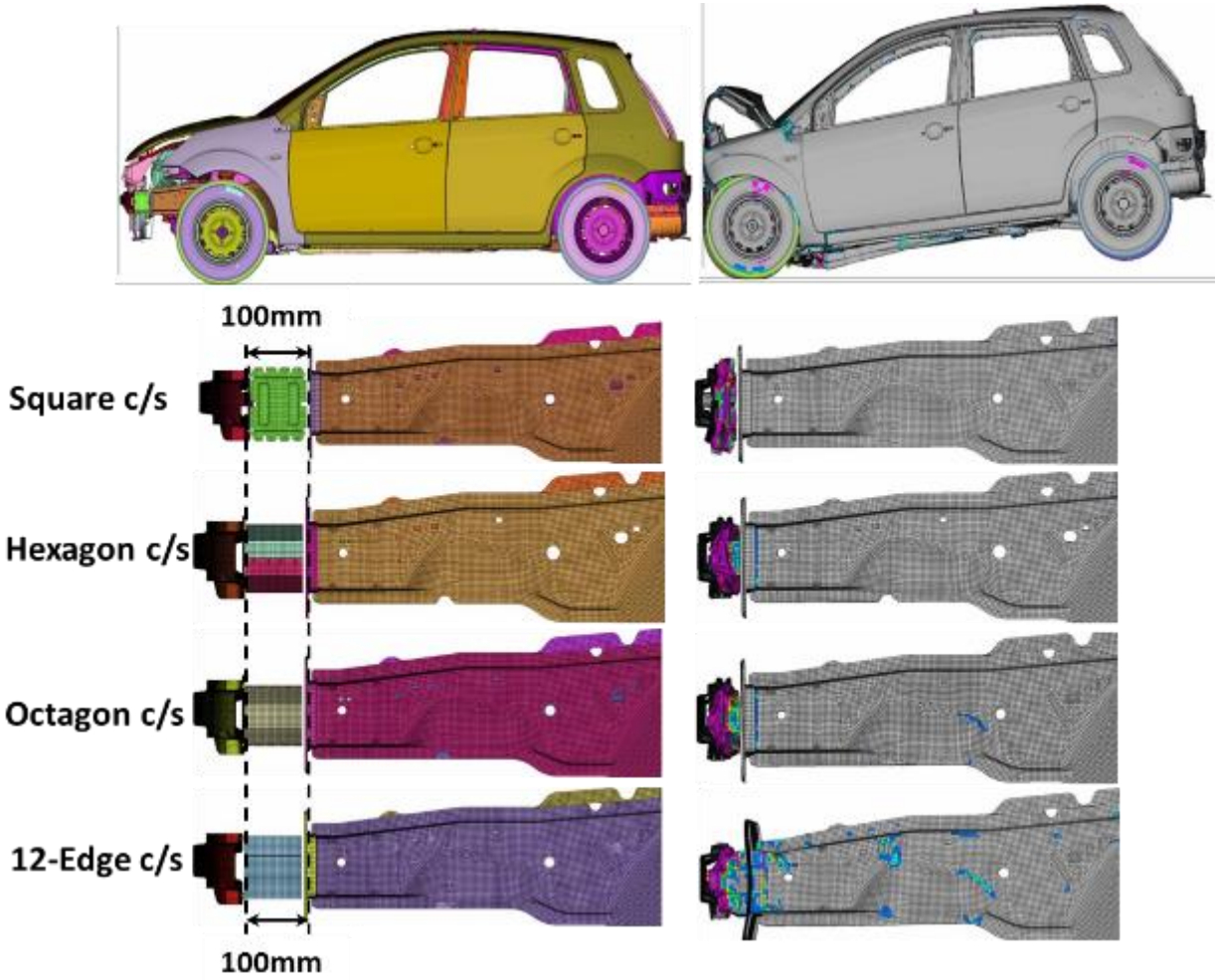

Fig. 13.3: Full frontal Impact and deformation modes of the vehicle and crush cans

13.2 Investigation of impact Resposnes

The characterstic responses of the vehicle in terms of deceleration pulse and crush are extracted at the B-pillar bottom [SAE J211-"Instrumentation for impact tests" –March 1995] and ploted for four load cases of crush cans subject to same impact velocity and boundary conditions. The crash pulses of the vehicle so extracted is overlaid in time domain and crush domain and displayed in Figure-13.4. The acceleration trends in all the four load casess with different crush cans remained simillar which indicates that the vehilce deformations

followed simillar collpase patterns. From these plots it can be inferred that the deceleration responses from 0 -25ms are clearly attributed to the effect of crush cans in absorbing the crash kinetic energy very upfront. The effectiveness of 12-Edge crash can is dominating in the pack followed by the Octagonal and getting descended to Square. The higher the upfront energy aborbtion the lower it becomes in the second stage where occupant starts responding to the vehicle decelerations. This effect can be seen in the later part of the pulse and where significant drops can be observed. The overall dynamic crush varied from 448mm for the vehicle with Sqaure crush cans to a maximum reduction of 435mm for the vehicle with 12-edged crush cans.Given the smallest packaging space of 100mm in the category of small vehicles this reduction of dynamic crush is very significant as it can greatly alleviate the safety of occupants.

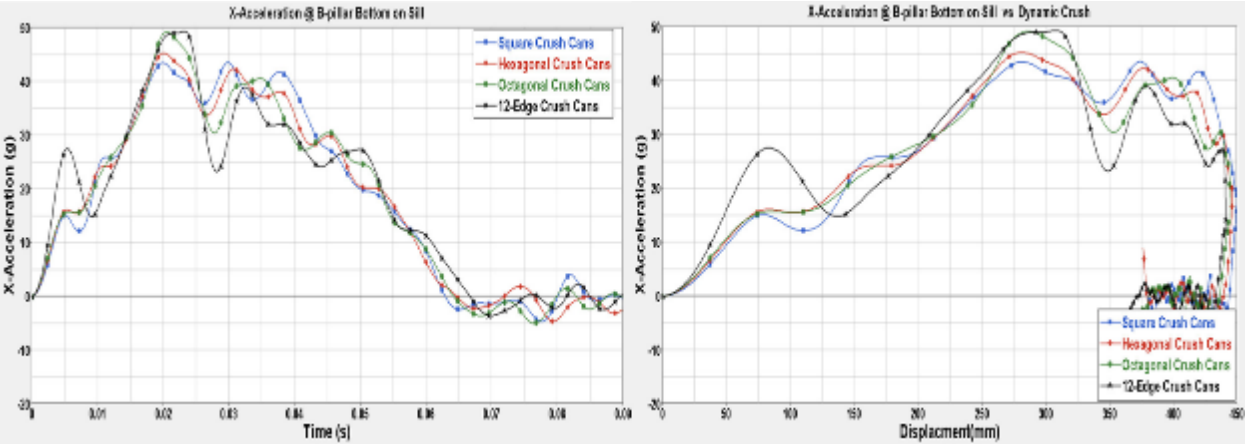

Fig. 13.4: Vehicle deceleration pulse (g) with respect to time(s) and displacement (mm)

Table-13.1 provides data on the contribution of crush cans to the energy absorbtion and it can observed that for simillar mass and similar material of the crush cans 12-Edge cross-section contributes to 10.8 % of initial vehicle kinetic energy.It is 38% higher than conventional square crushcans. The Specific Energy Absorbtion data also leans heavily towards 12-Edge crushcan with a value 20.21kJ/kg which is 39% higher than conventional square crushcans.

Table-13.1: Crash cans contribution towards vehicle Kinetic Energy absorption and their *SEA*

Crash Can Cross Section	*Mass (kg)*	*Vehicle Kinetic Energy (kJ)*	*Energy Absorbed by Crush cans (kJ)*	*Kinetic energy absorbed by crush cans(%)*	*SEA (kJ/kg)*
Square	0.84	155.28	10.37	6.68	12.34
Hexagon	0.78	155.28	12.14	7.82	15.56
Octagon	0.80	155.28	13.41	8.64	16.76
12-Edge	0.83	155.28	16.78	10.80	20.21

13.3 Maximum occupant chest deceleration

In this section we present basic notions and terms needed to assess the crash severity for an occupant (Huang 2002) [46]. As the crash pulse approximation, from vehicle's equation of motion, we use Equivalent Square Wave (ESW):

$$ESW = 0.4\frac{v_0^2}{\delta_c} \quad \ldots(13.1)$$

where v_0 the initial is impact velocity and δ_c is maximum dynamic crush. Dynamic Amplification Factor (DAF) defines as the ratio maximum occupant chest deceleration to the equivalent square wave:

$$DAF = 1+\sqrt{1+(\omega t^*)^2} = 1+\sqrt{1+(2\pi f t^*)^2}\ ;\ \omega = 2\pi f\ ,\ t^* = \sqrt{\frac{\delta_r}{\delta_c}}t_m \quad \ldots(13.2)$$

where f is restraint natural frequency, t^* is the time when occupant contact restraint, δ_r is restraint slack, δ_c is maximum dynamic crush and t_m is the time when maximum dynamic crush occurs. Also the maximum occupant chest deceleration is given by:

$$a = ESW \times DAF \quad \ldots(13.3)$$

Knowing initial impact velocity V_0 = 56kph and with the assumption of the distance between an occupant and vehicle (restraint slack) δ_r = 0.4m and restraint natural frequency f = 6Hz (Huang 2002); by substituting δ_c (Maximum dynamic crush) and $\boldsymbol{t_m}$ (time when maximum dynamic crush occurs) in equations 13.1-13.2, ESW (equivalent square wave), DAF (Dynamic Amplification Factor) and a (Maximum occupant chest deceleration) can be calculated.The results of the vehicle and occupant decelerations along with Intrusions are presented in Table- 13.2 .

Table-13.2: Effect of Crash can with different cross sections on Dash intrusion and Occupant injury in FMVSS 208- full frontal impact @56kph

Crash Can Cross Section	*Peak Acceleration (g) 0-25ms*	*Peak Acceleration (g) 25-90ms*	*Max., Dynamic Crush (mm)*	*Dash Intrusion @ Brake Pedal C/L (mm)*	*Estimated Occupant Chest deceleration (g)*	*Reduction in Dash Intrusion (%)*	*Reduction in chest deceleration (%)*
Square	43	43	448	18	70.91		
Hexagon	45	42	445	15.8	70.44	12.22	0.66
Octagon	49	40	443	14.9	70.38	17.22	0.75
12-Edge	49	38	437	13.8	68.09	23.33	4.01

The data clearly indicates the advantageous effect of Crash can with 12-edge cross section over other cross sections. Any increase in upfront energy absorbtion of crash kinetic energy aids in reduction of its propogation into occupant compartment. One important resposne

which gets greatly affected by this reduction is dynamic dash intrusion which, has its direct bearing on the Femur/Tibia loading *NHTSA Report* [45]. The tabulated data shows 23% reduction in dash intrusion measured at the centreline of Brake Pedal and this is an important direct benefit which can be reaped from enhanced upfront energy absorbtion of the front-end structure. Another important response which has been positivey affected is the chest deceleration.

It can be observed that a reduction of 4% has been achieved with this 12-Edged Crash can although only a small space of 100mm was provided thus indicative of the potential of the multi-cornered sections for enhancement in crashworthiness of Automtive vehicles and reduction in occupant fatalities in severe crash events. **These multi cornered designs if extended to other vehicle categories with heavier mass and sizes, the effect would be greatly pronounced and has good potential to improve occupant compartment safety from severe imapact scenarios.**

CHAPTER-14

14.0 Conclusions

The collpase behaviour and energy aborbtion characterstics of multi cornered thin walled sections with cross sections of Square, Hexagon, Octagon were investigated in this research. The design of section with 12-Edges to improve the performance was developed.Analystical foundations for characterising the collapsing behaviour were developed based on the SFE (Super folding Element) and was further extended to multi cornered sections to develeop important collpase parameters and provide a direction for designers in developing efficient energy absorbing devices.

Experimental specimens were designed and manufactured with chosen Steel-HA3 material to the production standards based on numerous studies using the state of art CAE and analytical methods. Range of materials in Steel and Alumnium were selected based on their applicability in real world and characterised to for their behaviours through standard tests for their responses statically and dynamically with strain rates. A new methodology utilising parametric and multiobjective optimisation was proposed for selection of optimum parameters for energy abosurbing sections.

All the specimens were Quasi-statically and dynamically crushed under compressive loading to study their fundamental charaterstics in terms of Force-Displacement, energy absorbtion, efficiencies both in CAE and tests. The results obtained were comapred with their analytical values and were observed to be in good agreement within numerical tolerance limits. This coherence of reults were further utislised in testing the multi cornered sections with variance of material grades using CAE methodologies under tight numerical controls.

The results so obtained were also analysed to further enhance the understanding and establish the superiority of multi cornered sections especially 12-edged specimen in their functionality of energy absorbtion.The learning and conclusions from the Quasi static tests and Dynamic tests at component elevels would not be complete if these designs of multi cornered members are tested in a dynamic environment using full scale, full vehicle conditions and establish their effects toward achieving the ultimate goal of enhanced occupant safety.

A logical choice was made in the selection of category of vehicle to test the energy absorbing behaviour of the sections in discussion to replicate a worst case scenario in terms of package space, size, mass and velocity of the vehicle. The designs were tailored to suit the smallest package space of 100mm in the front end structure and subjected to 56kph full frontal impact into a rigid wall following FMVSS standards using a decently correlated Full vehicle CAE model. The results so obtained were analysed and proved beyond doubt the effectivenss of the multi-cornered section especially the 12-Edge section which has lead the pack and proven to be the best in the class outshining all other sections in every category of performances either static or dynamic, either low speed or high speed. It even outshined other conventional sections in enhancing the Crashworthiness of the vehicle and there by occupant safety even in smallest package space of 100mm.This design has great potential to enhance the pccupant safety in a great way if adopted to higher segment vehicles where package space and size would not be restricted.

The following points could be highlighted from this study:

- The collpase of an angular element is heavily dependent on the corner angle ϕ for the given size parameter "*C*" and wall thickness "*t*". For acute angles of the corner with $\phi \leq \pi/2$ the inextensional/asymmetric mode deformation would be dominant mode depending on the *C/t* ratio. While for obtuse angles of corner ϕ larger than 120 deg extensional/symmetric mode of deformation starts to control the crushing process

- For energy absorption purposes, the quasi-inextensional mode is preferred due to maximum plastic work done by this mode through localised buckling with moving hinge lines. The plastic collapse at the corners would be maximised if the corner angle ϕ (i.e 2 ψ_0) is maintained between 90 deg and 120deg

- The maximation of plastic work is through mean collapse force P_m and higher this paremeter the higher would be the energy absorbtion. The specimen with maximum number of uniform corners packaged within the boundary limits of C, t and σ_0 (the characteristic flow stress) provides the best performnace.

- The 12-Edge section with its corners unformly packed and crushed in a controlled inextensional mode to deliver a staggering value 89kN as mean crush force which is three times than conventional Square section.

- All the specimens with equivalent mass collpased in a simillar manner to 75% of their orginal length, the dominance of 12-Edge specimen is observed by three times the performance of the Square section in total energy aborbed and SEA with *23.5kJ* and *12.4 kJ/kg* respectively.

- SEA for the range of grades of steel showed ascending trend with strength while Aluminium Alloy 6063 showed better SEA performanace than low to mid level steels due to its lighter density and fit better for Energy aborbtion where mass is a constraint.

- Weight Effectivenss "W_E" definition was proposed for qualitative assessment of SEA to avoid its masking of failure infusions from unstable collpase modes. Simillar trend as that of SEA with dominance from 12-edge specimen was observed. Alumnium Alloy 6063 showed good weight effectiveness as compared to that of low and medium strength steels

- All the specimens collapsed with 75 % crush efficency in stable collpase modes without any intervening failures while with Crush force eefficency and Energy efficiency showede convergent trend with material strength with AluminiumAl6063 performing betetr than low and medium strength steels

- The dominance of 12-edge section continued on to dynamic performnace at 15m/s velocity with peak load standing at across all material ranges and has indicated to absorb about 70% of initial kinetic energy with the current design space and dimensions. This is about 52 % higher than convention square sections, 37% higher than Hexa and 32% higher than Octagon sections with same material , thickness and packaging spaces.

- The rapidity of loading under extreme 100m/s veoclity did not alter thecollpase of 12 edge section which provided good crush progression with ***inextensional*** mode of

deformation thereby establishing its dominance in multitude of static and dynamic load cases

- The collpase of multi cornered sections while extended further to dynamic load cases with full vehicle impact at 56kph as per FMVSS208 showed 10.8 % absorbtion of initial vehicle kinetic energy with 12-Edge cross-section crush cans which is 38% higher than conventional square crushcans.

- The Specific Energy Absorbtion data also leans heavily towards 12-Edge crushcan with a value 20.21kJ/kg which is 39% higher than conventional square crushcans.

- The dynamic dash intrusion measured at centerline of brake pedal on firewall into the occupant compartment reduced by 23% with 12-Edged crush cans which is direct reduction on Femur loading of the occupant

- The occupant chest deceleration reduced by 4% inspite of very small package space for the crush can within the front-end structure

- These designs have great potential to improve occupant compartment safety from severe imapact scenarios if further extended to other vehicle categories with heavier mass and sizes.

- This methodology does not limit itself to automotive domains and can further be applied to any ground transport, Aero-space domains wherever energy absorbtion is needed in a controlled manner.

CHAPTER-15

15 Recommendations and scope for future works

15.1 Recommendations for a good design of the thin walled sections for efficient energy absorption

The efficient energy absorbing mechanism in an automotive or any ground transportation vehicle is through the collapse of thin walled sheet metal sections. The members are generally designed in two parts and are assembled at sub-assembly stations to form full sections. The collapse of these sections in crash events provides the intended purpose of crash energy abortion as per their designed intent to collapse in a controlled manner. A general consideration that must be considered for better crash energy management is the designed section's capacity to absorb the total amount of energy which is available.

The energy dissipation in a simplified format of Equation-6.5 is defined as

$$E= \int_0^{\delta_{max}} P(\delta)\ d\delta \qquad \ldots(15.1)$$

where in the instantaneous crushing force is represented as $P(\delta)$ for given member while δ and δ_{max} are the current crush distance and maximum achievable crush distance respectively. The mean crushing force is then represented by Pm .

In developing a good design for energy absorbing devices it should be noted that the product of Pm and d_{max} which represents the crush energy absorbed should be maximized. The individual components individual components of Equation-15.1 are of low relevance. From the inferences of the previous chapters we can deduce that the mean crushing force depends primarily on the ***number of corners in a given member***, the wall thickness t and average flow stress σ_0 of the material in consideration.

For the design of the crush members it's easy to adjust the parameters (t and σ_0) to achieve the required level of the mean crush force Pm as the starting target point. This average force level is however difficult to remain at the same level and consistent over the entire available crushing distance d_{max} of the member. This consistency in the crushing process is possible

only if a steady, progressive collapse pattern is sustained in the member throughout the entire collapse process. For a well-designed crash sections, the intended folding patterns and modes would be initiated straightway into the collapse process with a stable, repeatable mode. If any this stability is disturbed by any inclusions either external or internal the process gets disturbed and the section might jump to a premature bending collapse rather than progressive collapse. For good energy absorption it is always better to design the members in such a way that a repeatable asymmetric folding mode is targeted.

There may be instances during the progression of desired asymmetric folding, where the repeatable process gets disturbed and incubation of symmetric or inverted modes . As far as possible these modes need be avoided as it can seriously lower the energy absorption capacity of the collapsing member. If one of these modes is induced either during the initiation or later in the progressive collapse process, the overall stability of the collapse process is lost and global bending takes over. In order to achieve the design of a good structural member it requires a diligent designed approach with conditions:

- The topology of the intended cross-section to be designed in such a way that the localized plastic deformation of the section in the formation each folding lobe can be accommodated without interferences and penetrations while maintaining the compatibility with other neighboring lobes.

- The local plastic deformations of the section should be free from interferences coming joining methods like Spot welds (rivets or MIG welds)

- The member need to be initiated for a stable repeatable collapse pattern by usage of properly designed ‘triggers’ which can initiate or force a desired folding mode while also reducing the high initial peak loads to a level that it no longer induces unstable plastic deformations in initiation process. The lower the peak to mean force ratio the consistent the section becomes in its collapse.

- Boundary conditions of these members should provide stable loading conditions (Bumper, bumper plates, stiffness of joints, loading direction) should be packaged in a way that they do alter the axial loading of the section. Any deviation of direction the loads axially would lead to instability and there by global bending of the members.

- **Although this research study established beyond doubt the dominance of 12-edge sections, sections with higher edges are possible to develop. This development can be practically possible through multi cell extrusions to which Aluminum material would be great candidate and have practical significance to EV and Hybrid vehicles where light weight is very dominant requirement.**

15.2 Scope for future works

The collapse process and associated energy absorbing process is of at most importance for the engineers working in automotive crash and safety domains. The energy absorption and the rate at which he vehicle is decelerated directly influences the occupant's injury in inevitable crashes. Any attempt to mitigate the injuries and protect the occupants is extremely valuable and needs continuous attention to the ongoing challenges. As discussed and presented in this research the collapse of thin walled sections provide excellent mechanism for energy absorption. With carefully designed sections in a prismatic fashion and with even edges robust and repeatable collapse can be achieved.

In practicality these thin walled sections should function robustly with progressive collapse devoid of any spurious modes inclusions which can lead to global bending. They have to deal with multitude of crashes at different velocities, different modes (front, side, rear..), different masses etc., to ensure the collapse of these thin wall members collapse robustly

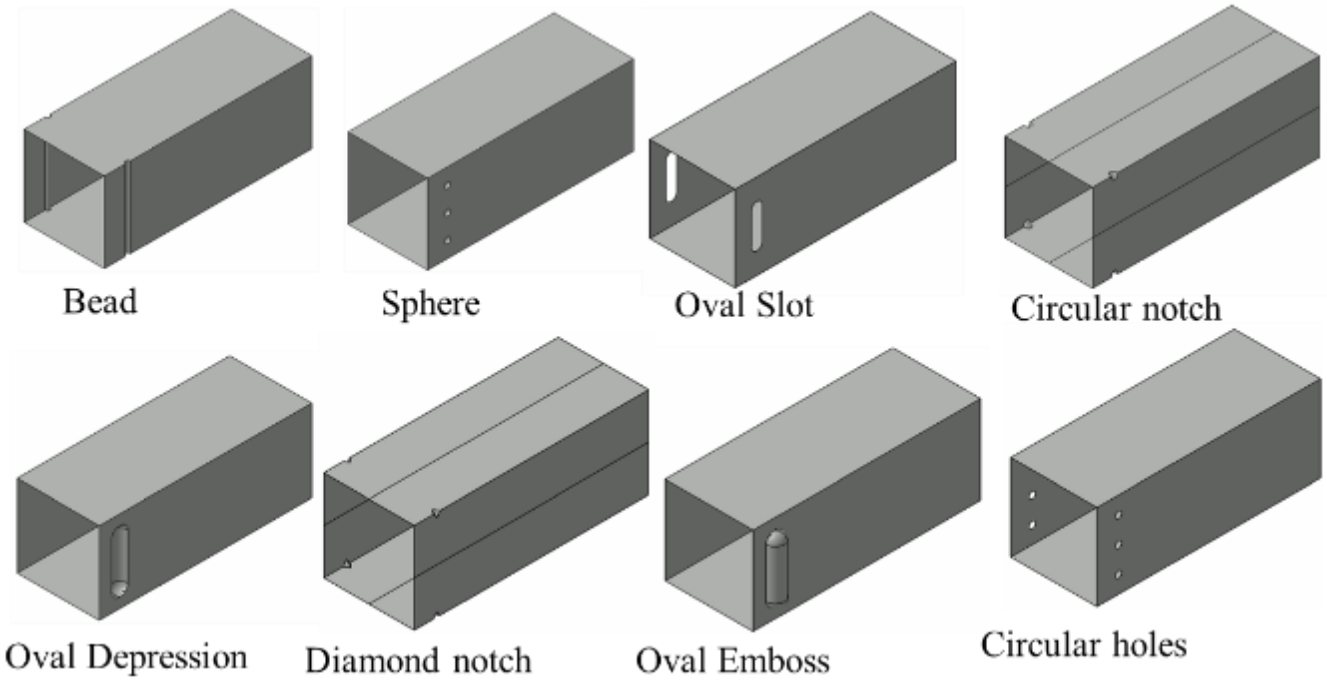

Fig. 15 Different types of triggers for robust collapse of thin walled sections

without incursion of unstable modes, OEMS prefer to use stable force crushing columns with specially designed initiators where in a complete collapse of is achieved by triggering the initial mode. These initiators are triggers and they work in initiating the folding mode by creating a specific weakness at a carefully chosen location. They reduce initial peak load and improve the crush force efficiency especially when the material strength dominates the effect of the cross-sectional geometry. They also aid in reducing high loads which could cause bending collapse.

In order to make the triggers work effectively they have to be positioned at right locations. This position is dependent on the position of the first fold which again is the function of wall thickness and dimensions. As discussed in the analytical sections the folding wavelength of the section can be calculated and the locations of the first fold can be determined. For efficient design and robust collapse, the design of triggers can take eight different types and can be placed appropriately. The Figure-15 provides a snapshot of the shapes and can be very useful in establishing robust collapses at different conditions. The primary focus in this research was on characterizing the collapse processes in natural modes without any triggers. This can be further extended and investigated further with the triggers and provide characterization to improve the existing knowledge in the area. The investigation can provide the optimum design of the trigger and its effects in multitude of load cases of frontal ODB (offset deformable barrier) impacts, Angular impacts, 25% small offset impacts and other impact modes.

References:

1. NHTSA Safety Facts 2007- DOT HS 810 993.
2. "Traffic Safety Facts 1994 ", DOT-HS-808-292, US Department of Transportation, 1991.
3. Wdlentowitz, H. and Adam, H., "Predicting the Crashworthiness of Vehicle Structures made by Light weight Design Materials and Innovative Joining Methods", Occupant Protection in Transportation Systems, pp 33 1-352, 1995.
4. Evans, L., "Passive Compared to Active Approaches to Reducing Occupant Fatalities", Proceedings of Twelfth International Technical Conference on Experimental Safety Vehicles, pp. 1149-1 157, 1989.
5. Abramowicz W, Jones N. "Dynamic axial crushing of square tubes". Int J Impact Eng 1984;2(2):179–208
6. Auto steel partnership & American Iron and Steel Institute (AISI) Safety,
7. N. Jones, Structural Impact, Cambridge University Press, 1989.
8. Bathe KJ (1996), Finite Element Procedures, Prentice-Hall, Eaglewood Cliffs, NJ.
9. Belytschko T and Huges TJR (1983), Computational Methods for Transient Analysis, North Holland, Amsterdam.
10. Belytschko T, Liu WK and Moran B (2000), Nonlinear Finite Elements for Continua and Structures, Wiley, Chichester.
11. Bonet J and Wood RD (1997), Nonlinear Continuum Mechanics for Finite Element Analysis, P.632, Cambridge University Press, New York.
12. Cook RD, Malkus DS and Plesha ME (1989), Concepts and Applications of Finite Element Analysis, 3rd edn. Wiley, Chichester.
13. Crisfield MA (1991), Nonlinear Finite Element Analysis of Solid and Structures, Vol. 1, Wiley, New York.
14. Kleiber M (1989), Incremental Finite Element Modeling in Nonlinear Solid Mechanics, Ellis Horwood, Chichester.
15. Oden JT (1972), Finite Elements of Nonlinear Continua, McGraw-Hill, New York.
16. Simo JC and Hughes TJR (1998), Computational Inelasticity, Spring–Verlag, New York.
17. Zhong ZH (1993), Finite Element Procedures for Contact-Impact Problems, Oxford.University Press, New York.Zienkiewicz OC and Taylor RL (1991), The Finite Element Method, McGraw-Hill, New York
18. "Traffic Safety Facts 1994 ", DOT-HS-808-292, US Department of Transportation, 1991

19. Wdlentowitz, H. and Adam, H., "Predicting the Crashworthiness of Vehicle Structures made by Light weight t Design Materials and Innovative Joining Methods", Occupant Protection in Transportation Systems, pp 33 1-352, 1995.
20. Langerak, N.A.J. and Kragtwijk, S.P., "The Application of Steel and Aluninum in a New Lightweight Car Body Design", SAE Technical Paper Series 982285, 1998.
21. Langseth, M. and Hoppentad, O.S., "Static and Dynamic Axial Crushing of Square Thin-Walled Aluminum Extrusions ", International Journal of Impact Engineering, 18(7), pp. 949-968, 1996.
22. Evans, L., "Passive Compared to Active Approaches to Reducing Occupant Fatalities", Proceedings of Twelfth International Technical Conference on Experimental Safety Vehicles, pp. 1149-1 157, 1989.
23. Abramowicz W, Jones N. “Dynamic axial crushing of square tubes”. Int., J Impact Eng.1984;2(2):179–208.
24. Abramowicz W, Jones N. “Dynamic progressive buckling of circular and square tubes”. Int., J Impact Eng. 1986;4(4):243–70.
25. Abramowicz W, Wierzbicki T. “Axial crushing of multicorner sheet metal columns”. J Appl., Mechanics 1989;56(3):113–20.
26. WhiteMD, Jones N. “Experimental quasi-static axial crushing of top-hat and double-hat Thin-walled sections”. Int., J Mech., Sci., 1999;41(2):179–208.
27. White M D, Jones N. “Experimental study into the energy absorbing characteristics of top-hat and double-hat thin-sections subjected to dynamic axial crushing.” Proc., Instn., Mech.,Engrs., Part D, J Automobile Engineering 1999;213(3):259–78.
28. White M D, Jones N, Abramowicz W. “A theoretical analysis for the quasi-static axial crushing of top-hat and double-hat thin-walled sections.” Int., J Mech., Sci., 1999;41(2):209–33.
29. Jones N. “Structural impact”. Cambridge: Cambridge University Press; 1989 [Paperback ed., 1997].
30. Alexander JM. “An approximate analysis of the collapse of thin cylindrical shells under axial loading”. Q J Mech., Appl., Math 1960; 13(1):10–5.
31. Wierzbicki T, Abramowicz W. “On the crushing mechanics of thin walled structures” J Appl., Mech., Trans ASME 1983;50(4 a):727–34.
32. Guillow SR, Lu G, Grzebieta RH. “Quasi-static axial compression of thin-walled circular aluminum tubes”. Int., J Mech., Sci., 2001;43(9): 2103–23.

33. Huang X, Lu G. “Axisymmetric progressive crushing of circular tubes. Int., J Crashworthiness” 2003;8(1):87–95.
34. Tarigopula V, et al. “Axial crushing of thin-walled high-strength steel sections”. Int., J Impact Eng. 2006;32(5):847–82.
35. Mamalis AG, Manolakos DE, Baldoukas AK, Viegelahn GL. “Energy dissipation and associated failure modes when axially loading polygonal thin-walled cylinders”. Thin-Walled Structures 1991;12:17–34.
36. Wierzbicki T, Jones N. “Structural failure”. New York: John Wiley and Sons; 1989.
37. F.C. Bardi, H.D. Yun, S. Kyriakides. “On the axisymmetric progressive crushing of circular tubes under axial compression International Journal of Solids and Structures” 40 (2003) 3137–3155
38. Wierzbicki, T., Bhat, S.U., Abramowicz, W., Brodkin, D., 1992. “Alexander revisited—A two folding elements model of progressive crushing of tubes. International Journal of Solids and Structures” 29, 3269–3288.
39. Singace, A.A., Elsobky, H., Reddy, T.Y.,1995. “On the eccentricity factor in the progressive crushing of tubes. International Journal of Solids and Structures” 32, 3589–3602
40. J. Mark, F.G. Holst, J. Michael Rotter, “Axially compressed cylindrical shells with local settlement, Thin-Walled Structures” 43 (2005) 811–825.
41. C.L.Magee and P.H.Thornton “Design considerations in energy Absorbtion by structural Collapse”
42. A. PUGSLEY “The crumpling of tubular structures under impact conditions”. Prec. Symp., on the Use of Aluminium in Railway Rolling Stock, Institute of Locomotive] Engineers, The Aluminium Development Association, London 33-41 1960
43. Abramowicz W, Jones N. “Transition from initial global bending to progressive buckling of tubes loaded statically and dynamically”. International Journal of Impact Engineering 1997; 19(5–6):415–37.
44. “IIHS safety Report” Vol 44, No.4, April 14 2009
45. “NHTSA Report” DOT HS 809 676 –“The Relationship between Occupant Compartment Deformation and Occupant Injury”, November 2003.
46. Huang M (2002) “Vehicle crash mechanics”. CRC,
47. G. Taguchi, “Introduction to quality engineering: designing quality into products and Processes”, 1986.

48. C.A.C. Coello, D.A. Van Veldhuizen, G.B. Lamont, “Evolutionary algorithms for solving multi-objective problems”, Springer, 2002.
49. A. Ben-Tal, “Characterization of Pareto and lexicographic optimal solutions, in:Multiple Criteria Decision Making Theory and Application”, Springer, 1980, pp. 1-11.
50. R. Roy, “A primer on the Taguchi method”, 1990, New York, (1990).
51. Yu-Cheng Lu. “Improved concept models for straight thin-walled columns with box cross section” Journal of Zhejiang University 2008; 9(11):1473-1479
52. W. Abramowicz. “Thin-walled structures as impact energy absorbers” Journal of Thin walled Structures 2003 41 91-107
53. Weigang Chen, Tomasz Wierzbicki. “Relative merits of single-cell, multi-cell and foam-filled thin-walled structures in energy absorption” Journal of Thin-Walled Structures 39 (2001) 287–306
54. Glenn F, Syrowik, Mark A. Huber. “Energy-Absorbing Polyurethane Foam to Improve Vehicle Crashworthiness” SAE International Congress and Exposition Detroit, 1995-950553
55. A.G. Mamalis, D.E. Manolakos, M.B. Ioannidis. “Finite element simulation of the axial collapse of metallic thin-walled tubes with octagonal cross-section” Journal of Thin-Walled Structures 41(2003) 891–900
56. F Schneider , N Jones “Impact of thin-walled high-strength steel structural sections” Proceedings of the Institution of Mechanical Engineers, Part D: Journal of Automobile Engineering 2004 218: 131
57. Xiong Zhang, Gengdong Cheng, Hui Zhang “Theoretical prediction and numerical simulation of multi-cell square thin-walled structures” Journal of Thin-Walled Structures 44 (2006) 1185–1191
58. Fyllingen , O.S.Hopperstad , A.G.Hanssen, M.Langseth. “Modelling of tubes subjected to axialcrushing” Journal of Thin-Walled Structures Thin-Walled Structures 48 (2010) 134–142
59. B. Yan, C. Kantner, H. Zhu and G. Nadkarni, “Evaluation of Crush Performance of a Hat Section Component Using Dual Phase and MartensiticSteels” SAE International Congress and Exposition Detroit, 2005-01-0837
60. Sanjeev Kumar. “A Numerical Study on the Axial Crush Characteristics of Thin Walled Rectangular Tubes Subjected to Dynamic Impact” SAE International Congress and Exposition Detroit, 2008-01-0242

61. Marian Królak, Katarzyna Kowal, Radosław J. Mania, Jacek Świniarski. “Stability and Load carrying capacity of Multi-Cell Thin walled columns of Rectangular cross-sections” Journal of Theoretical and Applied Mechanics 47, 2, pp. 435-456, Warsaw 2009
62. Heung-Soo Kim and Tomasz Wierzbicki, “Crash Optimization of an Aluminum foam filled Front side Rail” 9th ASME Symposium on Crashworthiness, Occupant Protection, and Biomechanics in Transportation, Orlando, Florida, 2000
63. Ali Najafi , Masoud Rais-Rohani “Influence of Cross-Sectional Geometry on Crush Characteristics of Multi-cell Prismatic Columns” 49th AIAA/ASME/ASCE/AHS/ASC Structures, Structural Dynamics, and Materials Conference AIAA 2008-2014
64. Y.S. Tai, M.Y. Huang, H.T. Hu. “Axial compression and energy absorption characteristics of high-strength thin-walled cylinders under impact load” Journal of Theoretical and Applied Fracture Mechanics 53 (2010) 1–8
65. Denis Wood. “Consideration of the Elastic Compressive Properties of Cars in Frontal Impact” SAE International Congress and Exposition Detroit, 1999-01-0095
66. Sigit P.Santosa, Tomasz Wierzbicki, Arve G.Hanssen", Magnus Langseth. “Experimental and numerical studies of foam filled sections under axial compressive loading” International Journal of Impact Engineering 24 (2000) 509534
67. Dai-Heng Chen, KenichiMasuda. “Crushing Behavior of Thin-Walled Hexagonal Tubes with Partition Plates” ISRN Mechanical Engineering Volume 2011, Article ID 503973
68. Guofei Chen, Ming F. Shi. “Mass Efficient Cross-Sections Using Dual Phase Steels For Axial and Bending Crushes” SAE International Congress and Exposition Detroit, 2007-01-0978
69. V. Jandaghi Shahi, J. Marzbanrad, “Analytical and experimental studies on quasi-static axial crush behavior of thin-walled tailor-made aluminum tubes” Journal Thin-Walled Structures 60 (2012) 24–37
70. Hallquist. L. and Benson (1986). “Dyna 3D. a computer code for crashworthiness engineering”. Proc., of International Fem conference Germany. Nov. I7 I8. pp. I69 -188
71. Haug,E. et al.(1986). “Numerical techiniques. Experimental validation of structural impact and crashworthiness analysis with supercomputers for the automotive industry”. Proc., of International conference on super computer applications in the automotive industry. A Computational Mechanics Publication, pp. I27 -136.
72. Ls-Dyna971 Theory Manual- Livermore Software Technology Corporation 2008

Annexure-1

Derivation of Mean Crush force for 12-edge section:

The methodology for analyzing thin walled sections under axial crush load was developed by Wierzbicki and Abramowicz [25, 31] through **S**uper **F**olding **E**lement theory. The detailed mathematical treatment is presented in Chapter-6 of this thesis. The foundational construction of generalized folding mechanism is from simple element as displayed in the Figure 6.5 below.

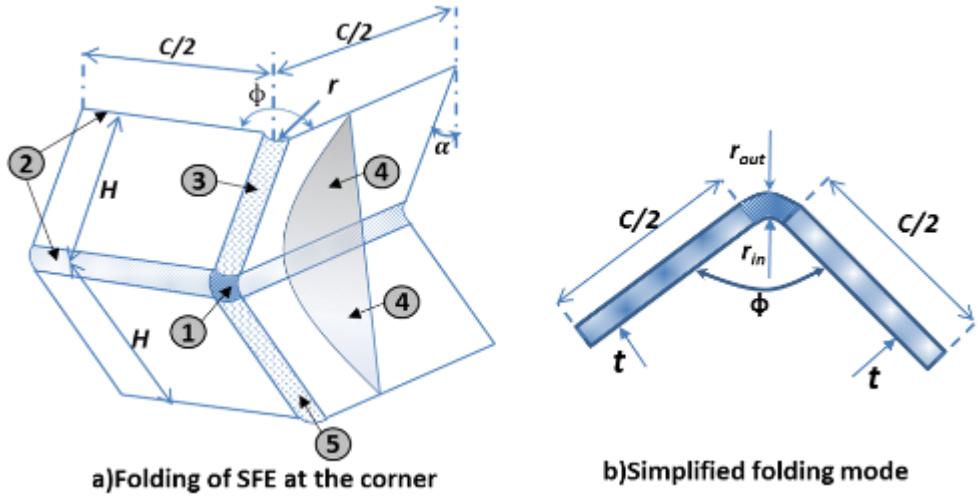

Rigorous kinematical approach was employed in the solution process for obtaining energy dissipation through inextensional and extensional modes. The configuration of 12-edge section is such that there are 12 corner elements with corner angles targeted around 90 degrees and the solution for Mean force (P_m) needs to be constructed from the assemblage of 12 corner elements. The corners in the cross section can be categorized into two as shown in the figure below Convex corners (Cv) and the concave corners (Cc) depending on whether they point outward or inward in the section.

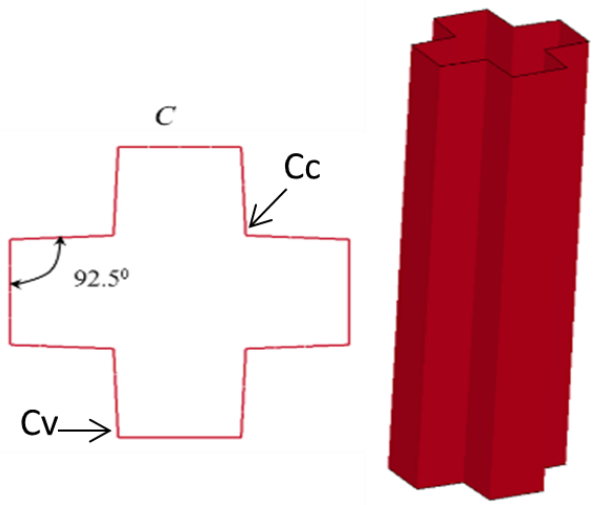

Due to the favorable angle for the inextensional mode at the corner the collapse process would be dominated by this mode which is most effective for energy dissipation through maximum plastic work. From the global energy balance Equation-6.5, the generalized formulation for internal energy absorption is equated to the external work in folding wave length of *2H* gives

$$\frac{P_m}{M_o} = \left\{ B_1 \frac{r}{t} + (B_2 + B_5)\frac{C}{H} + B_3 \frac{H}{r} + B_4 \frac{H}{t} + B_6 \right\} - \frac{2H}{\delta_{eff}} \qquad \text{--- (a)}$$

where P_m represents the mean crushing force and M_o represents plastic moment per unit length, the coefficient B_1 through B_6 depend on α^* and ψ_0. The corresponding coefficients take the form as $B_1 = 8I_1$, $(B2+B5) = 2\alpha_f$ which represents a total contribution of bending along horizontal hinge lines, $B_3 = 2I_3$, $B_4 = 4I_4$ and $B_6 = I_6$ due to the clamped boundary condition on horizontal planes. The coefficients are well described in the chapter -6 and when substituted in the above equation while arranging the terms as per the convex and concave corners the equation takes the form

$$\frac{P_m}{M_o} 2H\delta_{eff} = N_{Cv}(16I_1 \frac{r}{t} H + 2\pi C_{Cv} + 4I_3 \frac{H^2}{r}) + N_{Cc}(16I_1 \frac{r}{t} H + 2\pi C_{Cv} + 4I_3 \frac{H^2}{r}) \qquad \text{---(b)}$$

Where δ_{eff} the effective crushing distance which can be equated to 0.73 for inextensional collapse. N_{Cv} and N_{Cc} are the numbers of concave and convex corners in the cross section respectively. C_{Cv} and C_{Cc} are the flange lengths of the convex and concave corners respectively.

Since 12-edge section is symmetric with corner angle close to 92.5degrees and taking into account of the number of concave and convex corners behaving in the same fashion the equation further reduces to

$$\frac{P_m}{M_0} = \frac{1}{\delta}\left\{ N\left(8I_1 \frac{r}{t} + 2I_3 \frac{H}{r} \right) + \pi \frac{L_c}{H} \right\} \qquad \text{---(c)}$$

where N is the total number of corners inclusive of the concave and convex while L_c is the perimeter of the section. This expression has two unknown parameters of *H* and *r* which can be further determined by setting minimum conditions for least mean crushing force

$\frac{\partial P_m}{\partial H} = 0$, $\frac{\partial P_m}{\partial r} = 0$ and the solution is obtained as

$2NI_3 \frac{1}{r/t} - \pi \frac{L_c/t}{(H/t)^2} = 0$ and $16I_1 - 4I_3 \frac{H/t}{(r/t)^2} = 0$ which when solved we get the dimensionless half wavelength as

$$\frac{H}{t} = 4\frac{I_1}{I_3}\left(\frac{r}{t}\right)^2 = 4\frac{I_1}{I_3}A_0^2\left(\frac{L_c}{t}\right)^{2/3} = H_c\left(\frac{L_c}{t}\right)^{2/3} \quad \text{--(c)}$$

The dimensionless mean crushing force reduces to

$$\frac{P_m}{M_0} = \frac{1}{\delta}\left\{\left(16NI_1A_0 + \frac{\pi}{4}\frac{I_3}{I_1}\frac{1}{A_0^2}\right)\left(\frac{L_c}{t}\right)^{1/3}\right\} = P_s\left(\frac{L_c}{t}\right)^{1/3} \text{ where } A_0 = \left(\frac{\pi I_3}{32NI_1^2}\right)^{1/3} \quad \text{-- (d)}$$

Applying these to the current 12 corned section with ($\alpha_f = \pi/2$) the expressions for the I_1 and I_3 from chapter-6 become $I_1 = 4.44$ and $I_3 = 2.3$. The coefficient H_c then reduces to *0.19* and the P_s *to 68.4.*

The half wavelength of the folding then becomes

$$\frac{H}{t} = 0.19\left(\frac{12C}{t}\right)^{2/3}$$

$$H = 0.98t^{1/3}c^{2/3}$$ where ***t*** is the thickness and ***C*** the corner length.

The expression for the mean crushing force becomes

$$\frac{P_m}{M_0} = 68.4\left(\frac{L_c}{t}\right)^{1/3} = 68.4\left(\frac{12C}{t}\right)^{1/3} = 68.4 * 2.288C^{1/3}t^{-1/3} = 156.48\,C^{1/3}t^{-1/3}$$

Substituting for energy equivalent flow stress flow stress σ_0 as $M_0 = \frac{\sigma_0 t^2}{4}$ the equation for mean crushing force can be finally be written as:

$$P_m = \mathbf{39.12}\ \sigma_0\ t^{1.67}C^{0.34}$$ where ***t*** is the thickness and ***C*** the corner length.